



ISAS - INTERNATIONAL SCHOOL FOR ADVANCED STUDIES

*Thesis submitted for the attainment
of the Degree of
"Doctor Philosophiae"*

Protostellar Collapse Models: Development of a Multi-Dimensional Numerical Code

Candidate:

Leonardo SIGALOTTI

Supervisors:

Prof. F. DE FELICE

Prof. D. W. SCIAMA

Academic Year 1987/88

*Thesis submitted for the attainment
of the Degree of
“Doctor Philosophiae”*

**Protostellar Collapse Models:
Development
of a
Multi-Dimensional Numerical Code**

Candidate:

Leonardo SIGALOTTI

Supervisors:

Prof. F. DE FELICE

Prof. D. W. SCIAMA

Academic Year 1987/88

Ai miei genitori Girolamo e Dora

A mia moglie Aura

Acknowledgements

I would like to express my gratitude to Professors D. W. Sciama and F. de Felice for their constant guidance and assistance throughout this investigation as well as for their encouragement and help in the preparation of the manuscript. I am also especially indebted to Dr. A. Lanza and Prof. J. C. Miller for their friendly collaboration. Without their experience this work could probably not have been done. In particular Dr. Lanza has contributed by giving valuable advice at critical phases in the construction of the codes, while Prof. Miller helped me with many useful discussions as well as reading and correcting the final manuscript.

I would like to thank Dr. A. P. Boss for his suggestions and words of encouragement during the testing of the codes and I also appreciate the interest of Dr. M. H. Ibáñez during his short stay at Trieste. His critical comments have undoubtedly contributed to improving part of the manuscript. I am very grateful to Mr. R. Innocente for his help and advice regarding some critical technical points at the programming stage. His experience and computational knowledge have eased my work.

My thanks also go to Miss F. Sadutto for helping me to type part of this thesis and to Mrs. A. Zinner for her moral support and much else besides. I will never forget her help during these four years.

Finally, I would like to express my gratitude to all of the SISSA staff, especially to Mrs. D. Orlandini for her attention and industry during my stay at the school.

Contents

1	Introduction	1
2	The Physical Problem	7
2.1	The Early Stellar Evolution Period	8
2.2	The Angular Momentum Problem	16
2.3	The Ratio a/m	22
3	The Mathematical Problem	32
3.1	Physical Assumptions	33
3.2	Basic Equations	34
3.3	The Concept of Grid Motion	36
3.4	Spherically Symmetric Flows: The 1-D Problem	37
3.5	Axisymmetric Flows: The 2-D Problem	38
3.6	Non-Axisymmetric Flows: The 3-D Problem	40
3.7	Initial and Boundary Conditions	41
4	The Computational Grid	46
4.1	Description	46
4.2	Geometrical Grid Properties	49

4.3	Grid Motion Routine	53
4.4	Grid Velocity	56
5	Poisson Solver	58
5.1	Solution Method	58
5.2	Determination of the Density Coefficients	61
5.3	Calculation of the Potential Coefficients	67
5.4	Gravitational Potential for the Main Grid-Cells	74
5.5	Gravitational Potential for the Axial Cells	75
5.6	Gravitational Potential at the Centre	76
5.7	Accuracy and Tests	78
6	Hydrodynamics	87
6.1	General Method	87
6.2	One-Step Solution Procedure	92
6.3	Compact Radial Quotients	94
6.4	Donor Cell Assignments	95
6.5	Grid Contraction Effects	98
6.6	Numerical Stability and Accuracy	100
6.7	Finite-Difference Hydrodynamic Equations	108
6.8	The Angular Momentum Transport	111
6.9	Hydrodynamical Boundary Conditions	116
6.10	Artificial Viscosity	127
7	Spherically Symmetric Collapse	135
7.1	Pressureless Collapse	136

7.2	Isothermal and Adiabatic Collapse	144
7.3	Conclusions	154
8	Axisymmetric Collapse	156
8.1	Consistent Advection of Angular Momentum	159
8.2	Ring Formation	163
8.3	Conclusions	185
9	Further Research	188
 Appendices		
A	Solution of the Poisson Equation in Two Space Dimensions	191
A.1	Determination of the Density and Potential Coefficients	193
A.2	Gravitational Potential at the Cloud Centre	194
B	Abscissae and Weight Coefficients of the 21-Point Gauss-Legendre	
	Quadrature Formula	196
C	Finite-Difference Approximations	201
C.1	A Three-Point Finite-Difference Scheme	201
C.2	Acceleration Gradients	204
C.3	Finite-Difference Representations for the Advective Terms	206
C.4	Time Differencing	209
	 Bibliography	 210

Chapter 1

Introduction

It is commonly believed that star formation is a process which occurs naturally in the overall evolution of initially diffuse, low-density, interstellar clouds. In this view, the origin of stars has been associated with the collapse of individual protostellar subcondensations, which eventually form inside such primeval clouds. This very early phase of the evolution is poorly supported by observations and, hence, the physical details of this initial fragmentation stage into protostellar subclouds are rather obscure. The initial conditions for the protostellar collapse are likely to be determined at the end of this phase. Furthermore, the lack of consistent observational evidence concerning the intermediate stages of the protostellar collapse renders the problem of star formation even more difficult. Notable theoretical efforts have been made in order to fill the observational gap existing between interstellar clouds and star-like objects. Most of this work has been mainly focussed on the classical problem of angular momentum redistribution during the collapse, which is crucial for understanding the sequence of events in the process of star formation.

Realistic calculations of protostellar collapse should involve the solution of the equations of hydrodynamics in two or three space dimensions for the case of a self-gravitating

fluid, including the effects of gas pressure, rotation, magnetic fields, turbulent viscosity, and molecular viscosity. The solution of these equations must be coupled to a simultaneous calculation of the equation of state of the gas. Also, a full treatment of radiation transfer, as well as possibly convective transfer, is necessary in order to account for the dependence of the collapse itself upon the rate at which compressional heat is being liberated from the system. The process of formation, growth, and destruction of dust grains must also be considered. Dust grains are expected to interact with the gas molecules providing firstly an efficient cooling mechanism, which operates through the isothermal phase, and secondly the most important source of opacity to the infra-red radiation later in the near-isothermal and non-isothermal regimes. The above considerations give a rough idea of how complex a realistic treatment of protostellar collapse would be. This high degree of complexity gives rise to a number of inevitable restrictions which obviously limit the class of problems which can be successfully solved. Even when the physics is simplified to include only the dominant dynamical effects, the structure of the resulting equations is still so complicated that they can be only solved by means of suitable numerical methods. Experience shows that explicit numerical methods are especially suitable for the initial dynamical collapse stages. However, these methods are not applied to describe the complete evolution towards a star-like object. Due to the non-homologous nature of the gravitational collapse, both time and length scales vary by several orders of magnitude during the evolution of a protostellar cloud. At the end of the relevant dynamical stages when a considerable density enhancement has formed in the inner regions of the collapsing system, the main difficulties are in getting reasonable spatial resolution and accuracy at acceptable computational cost and in physically and consistently describing the overall flow pattern inside the col-

lapsing cloud. The flow pattern can basically be divided into two parts, a supersonic region (comprising the infalling outer envelope) and a quasi-hydrostatic part (comprising the pre-stellar nucleus), which are separated by a strong shock region (the accretion shock). This shock front is then of great importance for determining the structure of the protostar because the kinetic energy of the infalling matter in the envelope (ahead of the shock), is transformed in the shock region into outgoing radiation (i.e. giving rise to luminosity). Furthermore, the shock plays an important role in determining the structure (entropy distribution) of the outer layers of the pre-stellar core.

In this thesis, we describe the construction of an explicit hydrodynamic numerical code in order to follow theoretically the early isothermal collapse of spherically symmetric (1-dimensional code), axisymmetric (2-dimensional code), and non-axisymmetric (3-dimensional code) protostellar clouds. The hydrodynamical equations are solved on a moving spherical grid with only the effects of gravity, rotation and gas pressure being included and, with the gas being taken as ideal and at constant temperature. The Poisson equation for the gravitational potential is solved, on the same computational grid used for the hydrodynamics, by using a spherical harmonic expansion in order to allow a separation of variables. This gives rise to a radial linear differential equation which can be accurately solved by means of a tridiagonal matrix algorithm. The equations of continuity and momentum transfer are discretized and set in finite-difference form using an explicit time integration and a constant-volume boundary condition. The hydrodynamical transport through the grid is performed using the donor cell method. The use of this method besides guaranteeing the transportive fluid property, ensures the global conservation of the advected quantities. However, it is formally only first-order accurate and hence introduces a spurious diffusion of the variables within the grid, i.e.

local conservation is not necessarily ensured. However, local conservation of angular momentum has been substantially improved by using a partially centred scheme for the specific angular momentum rather than advecting it by the standard donor cell method. The codes use a one-step solution procedure with the time increment for advancing the system being constrained by the Courant-Friedrichs-Lewy condition. Reasonable accuracy and good stability and convergence properties are guaranteed by the resulting set of finite-difference equations.

The 1-dimensional code was tested against the well-known analytical solutions for the spherically symmetric collapse of a pressureless sphere. In this case, the numerically obtained density plateau matched the analytic one quite well. The same test was then used to determine the best choice of numerical treatment for the further runs. Indirect comparisons with numerical results obtained by other workers, have shown that the spherically symmetric code is able to reproduce well, situations which one expects to be encountered during the isothermal collapse phase. A further test made in order to check the sensitivity of the scheme to the onset of gravitational instability for uniform density isothermal clouds, has demonstrated its ability to reproduce the Jeans's criterion with a surprisingly good accuracy.

The 2-dimensional version of the code has been used to observe the response of the numerical scheme to the process of ring formation. For all of the runs carried out, the solutions obtained compared well qualitatively with those previously reported by other investigators. In many cases, ring formation is observed at the end of the calculations, with the collapse being initially characterized by an overall flattening of the cloud followed by a bounce of the material in the central zones and subsequent shock formation. The axisymmetric code is able to locally conserve the angular momentum

and to recognize a spherically symmetric configuration in the absence of rotation.

The 3-dimensional code was only tested superficially due to the strong computational restrictions. Since all of the calculations were performed on a Gould computer, comparisons with the runs of other workers on a CDC 7600 machine in single precision (60 bits) were only possible using the double precision accuracy of the Gould machine (64 bits). Under these circumstances, a 3-dimensional run required a very large amount of CPU time even to follow an evolution for only one free-fall time. Thus, a full isothermal run could not be completed. However, when the calculation was carried in single precision accuracy with large initial fractions of the Courant time step, an evolution was completed after roughly 25 hours of CPU time. Even though fragmentation has been observed, this run cannot be considered as a production run due to the inaccuracy implicit in the use of the single precision on the Gould computer. More consistent solutions with the present non-axisymmetric code require a faster computer whose single precision accuracy is at least comparable with that of a CDC 7600 machine.

The main goal of this investigation was that of developing suitable two- and three-dimensional computer codes, which would remain open to the possibility of including additional physics and more powerful methods for consistently tackling the problem of protostellar collapse and fragmentation into multiple stellar systems. In Chapter 2, we discuss the relevant physical situations presumably encountered during the early star formation phase. A discussion is also given of the central problem regarding angular momentum transfer during the protostellar collapse. In Chapter 3, we comment on the physical assumptions made and present the basic differential equations as well as the initial and boundary conditions necessary for obtaining numerical solutions of these equations. The description of the computational grid is given in Chapter 4. The

Poisson solver is together with tests of its accuracy fully described in Chapter 5. Chapter 6 is entirely devoted to the hydrodynamical approximation and the development of the codes. In Chapter 7, we discuss the results obtained for spherically symmetric collapse and, in Chapter 8, we describe the phenomenon of ring formation as it has been observed with the 2-dimensional axisymmetric code. Finally, Chapter 9 contains brief comments on further lines of work. Three appendices have also been included. Appendix A gives details of the Poisson solver implemented for the 2-dimensional calculations. In Appendix B, we illustrate a root-finding algorithm for the zeros of the Legendre polynomials of odd degree, which are used in determining the structure of the grid along the θ -direction. In Appendix C, we conclude by giving the basic forms of the finite-difference replacements used in the discretization of the Poisson equation and the equations of motion.

Chapter 2

The Physical Problem

In the course of the last twenty years considerable theoretical and observational efforts have been addressed in the spirit of solving the longstanding problem of star formation. Although these attempts have undoubtedly introduced significant progress in the field, we may ascertain that we are still far from achieving that aim.

Well-known standard troubles such as, for instance, the circumstantial and scarce observational evidence on the very early stages of stellar evolution, the rather poorly understood physical processes behind such stages, and the inevitable mathematical complexity which arises from handling consistent and complete physics, have converted the problem in a harder one, and hence any attempt toward a satisfactory solution is quite difficult and uncertain.

In the next sections, we shall try to depict the more relevant physical situations, which are presumably encountered during the early phases of star formation, and mention some important observational background supporting the scenario and defining both the initial and final stages of the protostellar collapse period, which is the main subject of the present investigation.

2.1 The Early Stellar Evolution Period

It has been long believed and formally accepted that the starting point of star formation is provided by the existence of very diffuse, low-density ($\sim 10^{-23} gcm^{-3}$), low-temperature ($\sim 75K$), large-sized ($\sim 2 \times 10^{19} cm$) configurations predominantly composed of neutral hydrogen and dust, which are present in the interstellar medium [10]. With this basic hypothesis, the overall evolution leading to solar-type stars ($\rho \sim 1 gcm^{-3}$) should go throughout a density range involving 23-22 magnitude increase.

On theoretical grounds, the early stellar evolution (or star formation process) may be subdivided into three main phases [10], namely: (a) the low-density star-formation phase; (b) the protostellar collapse phase; and (c) the slow-contraction phase, each of them being characterized by distinct physical events.

The first phase is the most obscure and probably the least understood. However, it is believed to start when the very diffuse, neutral hydrogen, interstellar matter is initially compressed to higher densities by an externally induced pressure. The need of some pressure-inducing mechanism in order to start the gravitational collapse of these primeval configurations is theoretically evidenced by their unbound nature. In the framework of the up-to-date theory of star formation, the existence of very massive ($\sim 10^4 - 10^5 M_{\odot}$), dense ($\sim 10^{-19} - 10^{-21} gcm^{-3}$), cool molecular clouds, as confirmed by radio observations of the molecular spectral lines, may be explained during this early stage.

It has been hypothesized that by the time the density has increased to roughly $10^{-22} gcm^{-3}$, the generated compressional heat has been efficiently radiated away from the cloud due to its very low opacity, while nearly all of the initial neutral hydro-

gen has been converted into molecular form. The final effect is then a decrease of the initial mean temperature to about 10K [7,10,61] followed by an increase of the mean density to the point where self-gravitation takes over. Because of the expected non-homogeneous structure of these configurations, probably due to internal turbulent motion and viscosity effects, it is quite possible that they evolve to even higher densities ($\sim 10^{-19} - 10^{-20} \text{gcm}^{-3}$) in certain portions, favoring in this way a low-density fragmentation process leading to protostellar blobs with a wide spectrum of masses [109]. Unfortunately, the way in which such a low-density fragmentation occurs is not clear due to the lack of available observational evidence of this stage.

Reddish [97] and Ibáñez [55] suggested that molecular chemistry could certainly influence the dynamic collapse and subsequent break-up into protostellar fragments especially if a dominant species is involved, as is the case when atomic hydrogen makes the transition to predominantly molecular form. On the other hand, the hydrodynamic effects of turbulence and viscosity remain somewhat controversial and uncertain because of the difficulty of simulating their physics in detail. The role played by magnetic fields and rotation will be considered separately in a following section.

The time-scale for molecular cloud formation is estimated to be about 10^7 years, afterward the evolution should run through the independent collapse of the protostellar fragments, with only little influence of the parental massive cloud [61]. In this view, the low-density star formation phase is crucial for our understanding of the subsequent evolution, since its outcome provides the initial conditions for protostellar collapse.

So far, the first main hypothesis that has been made is that stars originate from interstellar matter. Observational evidence encouraging this point of view and suggesting the tendency of stars to appear in clusters or associations, have been circumstantially

reported in the literature.

T-Tauri stars together with Herbig Ae and Be stars constitute good examples of star-like objects, which are evolving towards the main sequence while surrounded by their placental dense interstellar cloud complexes [105,106]. Similarly, observations in the infra-red region of the spectrum [107] have shown Herbig-Haro objects which are interpreted as reflection nebulae [117], whose illuminating stars are extremely young objects (with age $\sim 10^5$ years) located within dark cloud material.

The O- and B-star associations and the young cluster NGC 2264 are, on the other hand, examples of newly born stars formed in associations and clusters from the interstellar matter. Miller and Scalo [77] from a survey of open clusters, OB-, T-, and R-associations, concluded that at least 65% of all stars more massive than $\sim 2 - 5 M_{\odot}$ presently being formed appear in associations, while about 10% of all field stars are contained in galactic clusters. However, the possibility of encountering completely isolated forming stars out of an individual cloud cannot be excluded, as suggested by the presence of Wolf-Rayet stars [92]. Aveni and Hunter [2] identified several young isolated stars whose birthsite cannot be known clusters or associations.

Observations directed to study the overall molecular cloud properties are of primary importance in connection with the protostellar collapse problem. Such background information is expected to ease the difficult problem of setting adequate initial conditions for theoretical collapse simulations.

Interstellar clouds have been observed with densities of a few H atoms cm^{-3} up to densities of $\sim 10^4 - 10^5$ H_2 molecules cm^{-3} and masses ranging from a few M_{\odot} to $\sim 10^5 M_{\odot}$. Equilibrium temperatures in typical interstellar conditions have been calculated by Spitzer and Tomasko [103], who found that at these densities the gas

temperature should be 10K-20K, with negligible dependence of the temperature on the cosmic-ray intensity. Since under these conditions it is expected that molecular clouds will be cooled to $\sim 10K$ [48,61] due to the dominant cooling processes involving collisional transfer of energy from gas molecules to dust grains and subsequent infra-red emission by dust grains, the slightly higher temperatures exhibited by dense molecular clouds may be attributed to heating from stars forming within them.

Indirect evidence for the existence of large amounts of H_2 in dust clouds is given by Heiles [50] from observations in the OH line for a sample of four clouds. Observations of different systems by other workers have also revealed the same conclusion.

The second main hypothesis made by the theory of star formation consists of assuming some mechanism as being responsible for the formation of the observed molecular clouds. Four mechanisms have been proposed as the major candidates [10], each of them being different ways of subjecting a cloud to an external shock pressure. Such mechanisms are: (a) cloud-cloud collisions; (b) nearby supernova explosions; (c) expanding regions of ionized hydrogen (H_{II}) that form around newly born, hot stars embedded in dark material; and (d) shock waves coming from the spiral-structure density wave in the Galaxy. Observational background evidence exists for all of these shock sources.

The clouds NGC 1333 [69] and LkH α 198 [71] may constitute good examples of cloud-cloud collisions. Both clouds were observed to contain infra-red stars within a gravitationally bound region at the collision interface probably produced by two separate clouds. Observations in the CO line suggest a state of non-homologous collapse ($v \sim r^{-1/2}$) for the bound region in NGC 1333 and LkH α 198.

The R-association CMa R1 containing two classical Herbig emission stars is observed to lie at the edge of a large-scale ring interpreted as a supernova remnant and coincident

with an expanding H_I shell [51], which is in agreement with theoretical expectations of supernova-explosion events. The close correspondence between the age of the Herbig emission stars ($\sim 10^5$ and $\sim 10^6$ years) and that of the supernova remnant ($\sim 5 \times 10^5$ years) together with the presence of a runaway star "HD 54662" in CMa OB1, suggests for this case a scenario of supernova-induced compression with subsequent star formation.

Loren and Wootten [72] give evidence of star formation in the IC 1848 A bright-rimmed dust cloud as probably being induced by the expansion of the H_{II} region formed around the OB stars in the central regions of the molecular cloud IC 1848. The increased external pressure of the expanding H_{II} regions is thought to be responsible for the rapid emerging of a B star detected in IC 1848 A at the perimeter of the H_{II} region. Other evidence for star formation initiated by the compression of an external H_{II} region is provided by the molecular cloud $BD + 40^\circ 4124$ [69].

As postulated by the density wave theory of spiral structure [67], the matter in the Galaxy can maintain a density wave through gravitational interaction in the presence of the differential rotation of the various parts of the disk. This density wave provides a spiral gravitational field which underlies the observable concentration of young stars and gas. In this way, an observable spiral pattern can be maintained over the whole galactic disk.

Roberts [99] suggested that some of the large clouds and cloud complexes may be on the verge of gravitational collapse before reaching the galactic shock due to H_{II} regions that form around newly born O and B stars. A sudden compression of these clouds in the spiral shock could trigger the collapse of some of the largest clouds, which in turn may induce the subsequent compression and collapse of the individual sub-cloud

components. Each sub-cloud may then form a star which lies in association with the stars emerging from all the other sub-clouds inside the large cloud. That this could be the case is suggested by the fact that the amount of compression necessary for initiating the collapse of a gas concentration varies as M^{-2} . Therefore, it is much easier to induce the collapse of a large cloud rather than a sub-cloud. Furthermore, it has been inferred that sub-clouds can form stars only if they are contained in large clouds or in large cloud complexes.

Milman's [79] observation of the dust globule B361, interpreted as a small cloud with estimated mass $M \geq 125M_{\odot}$ and core density $n \geq 10^4 H_2 cm^{-3}$, may well represent an example of an isolated sub-cloud which does not seem to have any stars nearby or embedded in it. The observed widths of the CO lines suggest a radial collapse at $v \sim 1 km s^{-1}$, however, they may be also due to turbulent motion inside the cloud.

Ideas about the beginning of the protostellar collapse phase are connected with the hypothesis that favourable conditions for gravitational collapse to occur are likely to be achieved at the end of the low-density phase. This hypothesis is expressed quantitatively in terms of the Jeans criterion [10,11,61]

$$E_{grav} > \sum_i E_i \quad , \quad (2.1)$$

where E_{grav} denotes the gravitational potential energy of the cloud and the sum extends to all possible sources of energy present in the cloud.

In the idealized case in which only thermal and gravitational energies are important, equation (2.1) takes the standard form [10]

$$M_J = M_{min} \propto \left(\frac{T}{\mu} \right)^{\frac{3}{2}} \rho^{-\frac{1}{2}} \quad , \quad (2.2)$$

where the Jeans mass M_J is defined as the minimum mass required for the gravitational

collapse of a cloud at (ρ, T) . For a typical diffuse cloud at $T = 75K$ to collapse and overcome its thermal pressure, its mass must exceed about $10^4 M_\odot$, thus a solar mass cloud will only collapse if its density is several orders of magnitude higher than $\sim 10 H cm^{-3}$ for such clouds. The above suggests that in the presence of an externally induced pressure capable of enhancing the cloud density over its initial value, the Jeans mass required for collapse will decrease.

On the other hand, if the density of a large massive molecular cloud increases as long as its temperature is kept nearly constant, the minimum mass for collapse will progressively decrease suggesting a continuous disruption of the cloud into smaller and smaller mass-sized pieces. Such a fragmentation sequence may only stop when the last formed pieces become optically thick to their own radiation. In this way, their temperature may well increase up to the point where the critical Jeans mass exceeds their actual masses. Theoretical predictions give a lower limit of $0.01 M_\odot$ [102] at which further fragmentation is inhibited. This value agrees with the mass spectrum of the observed lower main-sequence stars.

Bodenheimer [10] has summarized the main stages encountered during the protostellar collapse phase. Most of the details about this period have basically come from spherically symmetric collapse simulations of a $1 M_\odot$ spherical protostar [61,85,118].

From densities of about $10^{-19} g cm^{-3}$ up to $\sim 10^{-13} g cm^{-3}$, the collapse proceeds isothermally with $T \sim 10K$, as determined by the point at which the heating and cooling rates balance [48,61]. However, more recent calculations including radiation transfer in the Eddington approximation [18] have shown that in the diffusion approximation the temperature in regions of intermediate optical depth are underestimated. This implies that the temperature is likely to rise at much lower densities and thereby,

the initial infall will proceed with the temperature increasing slowly rather than in a rigorous isothermal manner.

The evolution in the innermost higher density regions takes place faster than in the outer parts of the cloud, since the free-fall time is proportional to $\rho^{-1/2}$. The cloud then experiences a non-homologous contraction with the density varying as r^{-2} in the outer envelope [61].

Gerola and Sofia [44] obtained from a simplified analysis of CO and HCN observations, a number density distribution for molecular hydrogen $n = Ar^{-2} \text{cm}^{-3}$ with $A = 2 \times 10^{41}$, for the Orion A cloud. Brandshaft et al [20] indicated a dust density distribution proportional to r^{-n} with $n \sim 2$ around the centre of the same cloud from observations of the far infra-red emission.

Evidence for collapsing clouds shows that some clouds with embedded young stars have CO line widths which vary as $v \sim r^{-1/2}$, as expected for non-homologous collapse [70,72]. Moreover, theoretical calculations predict maximum infall velocities of $\sim 2 - 3 \text{km s}^{-1}$, which are in good agreement with those observed of $\sim 2 - 10 \text{km s}^{-1}$ for large-scale motions in molecular clouds.

When the central density exceeds $10^{-13} \text{g cm}^{-3}$, about 1% of the total cloud mass in the innermost portions approaches a non-isothermal regime. As the density increases in these regions, the free-fall time [$t_{ff} = (3\pi/32G\rho)^{1/2}$] rapidly becomes shorter than the time needed for the radiation to escape and diffuse outwards from the collapsing material. The matter then becomes opaque and the trapped compressional heat results in a setting up of a temperature gradient between the innermost zones and the outer isothermal regions. The resulting increasing thermal pressure eventually impedes further collapse and favours the formation of a small region in hydrostatic equilibrium at

$T \sim 170K$ and central density $\rho_c \sim 2 \times 10^{-10} gcm^{-3}$. An external shock develops and allows the hydrostatic core to accrete more and more material until $T \sim 1800K$ and $\rho_c \sim 10^{-7} gcm^{-3}$ are reached.

At temperatures of 1800K-2000K, the molecular hydrogen in the core begins to dissociate and a further collapse takes over on a very short time-scale (~ 1 year). By the time that all of the molecular hydrogen has been dissociated, heating and rapid pressure increase again result in the formation of a second small core of about $10^{-3} M_\odot$ in hydrostatic equilibrium at $T \sim 2 \times 10^4 K$ and $\rho_c \sim 10^{-2} gcm^{-3}$. This core will then define the nucleus of the equilibrium star, with the subsequent evolution being mainly dominated by an accretion phase in which the material ahead the newly formed shock accretes onto the stellar core. A maximum mass for a newly formed core is set by the action of the radiation, which it produces, in reversing the infall of outer material [62].

The time-scale of the whole protostellar collapse phase is estimated to be about 10^6 years [10]. It has been shown that the properties of the resulting stellar nucleus are generally independent of the initial conditions, being rather weakly dependent on the total cloud mass.

2.2 The Angular Momentum Problem

Considerations of the effects of rotation and magnetic fields are of great importance in understanding the problem of star formation.

Observational evidence suggests that we may expect interstellar clouds to be rotating at least with the galactic rate ($\omega \sim 10^{-15} s^{-1}$) for a cloud at the sun's distance from the centre of the Galaxy. Therefore, a perfectly spherical, uniformly rotating, interstellar cloud of mass $M \sim 10^4 M_\odot$ and uniform density $\rho = 10^{-23} gcm^{-3}$ would have

a spin angular momentum J of $\sim 5 \times 10^{61} \text{ g cm}^2 \text{ s}^{-1}$, corresponding to a specific angular momentum J/M of roughly $10^{24} \text{ cm}^2 \text{ s}^{-1}$. This value appears to be about nine orders of magnitude higher than the present value inferred for the sun ($J/M \sim 10^{15} \text{ cm}^2 \text{ s}^{-1}$) and six to seven orders of magnitude higher than those observed for the most rapidly rotating stars ($J/M \sim 10^{17} \text{ cm}^2 \text{ s}^{-1}$) on the upper main sequence [7,13].

However, the assumption that the angular momentum of interstellar clouds, and hence the angular momentum of the observed stars, originates from the galactic rotation alone is rather controversial [109]. If this were the case, the stellar rotation axes and binary axes should exhibit a preferentially perpendicular orientation with respect to the galactic plane, instead of being randomly oriented as they are actually observed to be. This randomness suggests that the turbulent motions, which take place in the interstellar medium, could also contribute to the final angular momentum of equilibrium stars. In this case, a protostellar cloud will have nearly comparable rotational and translational kinetic energies yielding a J/M for such cloud even higher than that inferred from pure galactic rotation.

This situation indicates that rotational effects must become significantly important well before reaching stellar conditions, and that angular momentum must be redistributed during the collapse in order to explain the several orders of magnitude difference in J/M between interstellar clouds and main-sequence stars.

The galactic magnetic field, estimated to be of $\sim 3 \mu\text{G}$ [21], is expected to thread the interstellar matter present in the Galaxy. Therefore, interstellar clouds should be magnetically coupled with the surrounding intercloud medium. Although the effects of such a magnetic field upon the collapse of cool interstellar clouds have not yet been modeled in detail, observational evidence and theoretical arguments strongly suggest

that they are likely to play a role during the low-density phase.

Mestel and Spitzer [76] showed that as long as the galactic magnetic field is frozen into a collapsing cloud, the magnetic pressure sets a lower limit for the mass that can remain gravitationally bound. If we consider in equation (2.1) only the magnetic term, we find that a typical interstellar cloud of $10^4 M_\odot$ at $n \sim 10 \text{ H cm}^{-3}$ is able to contract provided that the magnetic field strength drops below $\sim 1.6 \mu\text{G}$. A cloud of solar mass will require a much smaller magnetic field ($\sim 0.08 \mu\text{G}$).

Since in a very low-density regime, we expect the collapse to occur rather isotropically, with the field varying as $\rho^{2/3}$ and the magnetic flux (BR^2) remaining constant, the critical mass for gravitational instability will be independent of the density, and the molecular stage will be then reached with conditions which are not favourable for fragmentation. It is therefore expected that at typical molecular densities, the field diffuses allowing anisotropic collapse and subsequent fragmentation into protostars.

Observational evidence for initial isotropic contraction is provided by the fact that the galactic field runs longitudinally along the spiral arms of the Galaxy [41]. This implies that the rotational axis of interstellar clouds should be aligned roughly perpendicular to the galactic field lines.

It is known that in the presence of the galactic magnetic field, an interstellar cloud is forced to contract with an approximately uniform rotation rate rather than with uniform angular momentum [41], because the magnetic energy density $B^2/8\pi$ will always be greater than the turbulent kinetic energy $\rho u^2/2$. The interior field of the cloud is expected to distort due to the compression of the cloud relative to the galactic background. As the cloud attempts to rotate more quickly, the field lines become more distorted and hydromagnetic waves are generated, which then travel along the twisted

magnetic field lines transporting angular momentum away from the cloud [45,76,82]. The transfer of angular momentum will be efficient as long as the magnetic field remains essentially frozen into the cloud.

In dense interstellar clouds, incoming cosmic radiation partially ionizes the hydrogen. The compressed magnetic field then exerts a Lorentz force acting on the ions and electrons immersed in the plasma. As the cloud reaches higher densities, the cosmic-ray flux is eventually screened via magnetic scattering. At this point, the ionization rate of hydrogen is drastically reduced, and hence the ion density will decrease. Thereafter, the magnetic field, which is anchored to the ions, will start decoupling as the remaining ions leave by ambipolar diffusion. As the magnetic field detaches from the cloud, the magnetic torques necessary in order to brake the cloud become less effective, and angular momentum is no longer transferred to the intercloud medium. Further collapse should then proceed with local conservation of angular momentum.

In this way, the initial angular momentum of a protostar will be established at the decoupling epoch, which is the time at which the interstellar cloud is expected to fragment. The time-scale for angular momentum transfer, on the other hand, is determined by the ambipolar diffusion time t_D . So as long as, $t_D > t_{ff}$, the field remains essentially coupled, and the cloud is able to lose angular momentum. When $t_D \sim t_{ff}$, decoupling of the magnetic field should occur.

Observations of the Zeeman splitting of OH emission lines in two dust clouds [29] imply an upper limit of $\sim 50\mu G$ for magnetic field strengths. This result is important because it suggests that magnetic fields have already separated from interstellar matter in dust clouds. Theoretically, interstellar material with an initial $n \sim 10H\,cm^{-3}$ and $B \sim 3\mu G$ would have fields of several hundred μG if the field were frozen into the gas

during the collapse to $n \sim 10^3 - 10^4 H_2 cm^{-3}$.

Nakano and Tademaru [83] argued that if cosmic rays were absent or strongly screened at low density, the decoupling of the magnetic field would occur at much lower densities. This could explain the absence of very high fields in some dense clouds. Moreover, that magnetic field must diffuse out of the cloud as the collapse proceeds, is shown observationally by the very weak field strength exhibited by most stars.

The crucial question is at which critical density magnetic braking diffuses out so that fragmentation can take over in a contracting interstellar cloud. For clouds of $10^4 M_\odot$ rotating at the galactic rate, Nakano and Tademaru [83] suggested a critical density $n_H \geq 2 \times 10^9 cm^{-3}$ for the ambipolar diffusion time to become comparable with the free-fall time. Mouschovias [82], however, suggested a critical density range of $2.2 \times 10^6 cm^{-3} \geq n \geq 7.5 \times 10^3 cm^{-3}$ at which the magnetic flux must break down if the observed periods of binary stars are to be accounted for. He argued that decoupling is likely to occur only in the denser cores of collapsing interstellar clouds, the collapse of the outlying portions being halted by the tension of the field lines which do not detach from those of the galactic background.

Scalo [100], on the other hand, showed that the observed low cloud temperatures cannot be accounted for, unless the magnetic field varies as $n_H^{0.55}$ rather than at the $n_H^{2/3}$ rate that applies for isotropic collapse. Otherwise, the heating produced by the friction associated with ambipolar diffusion would yield clouds hotter than those actually observed. It was suggested that this slightly weaker dependence may be due to a violation of the frozen-in approximation at $n_H > 10^4 cm^{-3}$.

Other workers have predicted critical densities lying in the range $10^5 cm^{-3} < n < 10^7 cm^{-3}$. It is clear that no strict agreement exists between different theoretical pre-

dictions. So once more, we must turn to observations of molecular clouds in order to estimate roughly how much angular momentum has been lost by magnetic braking. The observed densities of such clouds also give an estimate of the critical densities at which the effects of the galactic magnetic field become less important.

Observations in the CO line of the Orion A molecular cloud [68] indicated an angular velocity of $\sim 2 - 4 \times 10^{-14} s^{-1}$ at a density of $\sim 2 \times 10^3 H_2 cm^{-3}$. Phillips et al [94] interpreted the Orion structure as a disk-like model undergoing collapse perpendicular to the disk plane while rotating about its axis of symmetry. The dust globule B361 has been observed to spin with $\omega \sim 10^{-13} s^{-1}$ [79]. Similarly, CO observations of the Monoceros R2 cloud [70] indicated $\omega \sim 1.4 \times 10^{-14} s^{-1}$ and $n \sim 10^4 H_2 cm^{-3}$, while Kutner and Tucker [58] inferred $\omega \geq 7.4 \times 10^{-14} s^{-1}$ for the same cloud in the CS molecule. Other observations reported in the literature have indicated dust clouds with angular velocities up to $9 \times 10^{-14} s^{-1}$ [7].

Taking $10^{-13} s^{-1}$ to $10^{-14} s^{-1}$ as typical angular velocities, a solar-mass sized protostellar spherical cloud with $n \sim 10^4 H_2 cm^{-3}$ will have specific angular momenta J/M ranging from $\sim 1.5 \times 10^{21} cm^2 s^{-1}$ to $\sim 1.5 \times 10^{22} cm^2 s^{-1}$. In comparison, a large cloud with typical interstellar conditions will have $J/M \sim 10^{24} cm^2 s^{-1}$. This result indicates that during the low-density phase leading to protostellar formation, the specific angular momentum may well be reduced by 2-3 orders of magnitude.

The 6-7 orders of magnitude difference in J/M between molecular clouds and solar-type stars may be further reduced by considering the observed difference in rotational velocities between pre-main and main sequence stars. Boss [13] inferred a $J/M \sim 10^{17} cm^2 s^{-1}$ as a plausible value for pre-main sequence stars (of the late type), which are expected to approach the lower main-sequence as the present sun did. A gap of

roughly 4-5 orders of magnitude in J/M is then found between observed molecular clouds ($J/M \sim 10^{22} - 10^{21} \text{cm}^2 \text{s}^{-1}$) and pre-main sequence stars ($J/M \sim 10^{17} \text{cm}^2 \text{s}^{-1}$).

In order to explain this gap in J/M a second important mechanism has been introduced, which includes conversion of spin angular momentum into orbital motion by fragmentation of a collapsing cloud. In this picture, when a cloud collapses and eventually fragments into two parts, most of the original spin angular momentum of the cloud will supply the orbital motion of the emerging binary system, while only a small fraction will go into spin of the single fragments. Break-up into a binary system, as well as being a common occurrence in nature, represents the simplest possibility and the lowest order deviation from axial symmetry [63].

Bodenheimer [7] proposed a hierarchical fragmentation sequence to explain the formation of multiple star systems. He showed that a rotating interstellar cloud can collapse and form final fragments in the observed stellar range, if transfer of spin angular momentum into orbital angular momentum is assumed at each fragmentation stage. However, star formation, in this scenario, is an inefficient process because very high initial masses are needed to produce small stellar systems, which only contain from 0.4% to 3% of the total available mass. A further mechanism which may be important involves the transfer of angular momentum, within the cloud by means of eddies or spiral density waves [66].

2.3 The Ratio a/m

The ratio a/m between the specific angular momentum a and the total mass m , where both quantities are defined in units of length, is a rotational parameter given by the

relation

$$\frac{a}{m} = \frac{cJ}{GM^2} \quad , \quad (2.3)$$

J being the total angular momentum of a particular collapsing object of mass M , c the speed of light and G the gravitational constant.

The ratio a/m provides information about the distribution of the specific angular momentum with respect to the total mass of the bodies existing in the Universe. The physical relevance of this parameter comes from relativistic theoretical predictions concerning black holes. According to the General Theory of Relativity, a stationary black hole state is completely characterized by the total mass M , the total angular momentum J , and the total electric charge Q , such that the following condition holds

$$m^2 \geq a^2 + q^2 \quad , \quad (2.4)$$

where $m = GM/c^2$, $a = J/cM$, and $q = G^{1/2}Q/c^2$. If we solve eq.(2.4) for a/m , we find that

$$\frac{a}{m} = \frac{cJ}{GM^2} \leq \left[1 - \left(\frac{q}{m} \right)^2 \right]^{\frac{1}{2}} \quad , \quad (2.5)$$

where $\{1 - (\frac{q}{m})^2\}$ is a positive number less than unity. Without loss of generality, we may simplify condition (2.5) by stating that $a/m < 1$ is a necessary condition for a black hole to exist. In this picture, the ratio a/m should play a crucial role in deciding whether or not an evolved object will approach a black hole state.

De Felice and Yu Yunqiang [36] estimated the ratio a/m of typical main-sequence stars to be in the range $6 < a/m < 122$. They found that the ratio a/m generally increases for increasing values of the mass, radius, and equatorial rotational velocity. Of greater interest were the calculations of the ratio a/m for main-sequence stellar cores. Such calculations provide an estimate of the ratio a/m which a core would have prior to

undergoing further collapse. Estimates for a rigidly rotating $1M_{\odot}$ core of a $10M_{\odot}$ star yielded a/m -values from 10 to 50. For differentially rotating cores, this range extended to include values up to $\sim 10^2$. Furthermore, calculations of the ratio a/m during post-main-sequence evolution indicated that as the cores contract to higher densities ($\rho \sim 10^7 - 10^8 \text{ g cm}^{-3}$), the angular momentum is redistributed so that the ratio a/m decreases by only a very small factor. However, there is no direct observational evidence of collapsed objects with $a/m > 1$. This point was also illustrated by de Felice and Yu Yunqiang [36], who estimated the ratio a/m of the rotating neutron star associated with the Crab pulsar. This is observed to rotate with a period $P \sim 33 \times 10^{-3} \text{ s}$, which is much larger than the theoretically predicted period ($P = 0.57 \times 10^{-3} \text{ s}$) which would be necessary to yield a ratio a/m slightly larger than one.

It is believed that most of the a/m is diffused out from the neutron star after its formation, owing to the effects of two different processes which convert rotational energy into translational energy. Harrison and Tademaru (1975) suggested the first of these processes which may act during the formation stage of a pulsar. At this stage, a considerable amount of the kinetic rotational energy of the pulsar goes into translational energy of the forming neutron star because of an inherent anisotropy in the supernova explosion, which then leads to the emission of asymmetric electromagnetic radiation. The second process operates after pulsar formation, and it is of minor importance in reducing the ratio a/m . In this process, diffusion of angular momentum occurs through a mechanism involving continued emission of radiation due to the presence of an off-centered dipolar magnetic field.

Calculations of the ratio a/m for the Crab pulsar [36] confirmed the above considerations. At the beginning of its acceleration process, the pulsar was found to be rotating

with a period nearly equal to that giving $a/m \sim 1$, while at the end of the acceleration process, a/m was strongly reduced. Hence, a newly formed neutron star is likely to have $a/m \sim 1$, in agreement with classical predictions.

Although the mechanisms responsible for the a/m -reduction from expected main-sequence values ($a/m > 1$) to observed neutron stars ($a/m \sim 10^{-1} - 10^{-3}$) are nearly understood, those which act reducing the ratio a/m for collapsing cores ending up as black holes are rather unknown. Miller and de Felice [78] and de Felice et al [38] suggested two different mechanisms, in which transfer of angular momentum away from the core occurs by mass shedding and by gravitational radiation, as good candidates for the a/m transfer. It was found that mass shedding can be efficient in reducing the ratio a/m , but only if the initial a/m of the evolved object is < 2.5 can it be reduced to order unity in a single collapse phase. Furthermore, the gravitational radiation mechanism is effective in decreasing the ratio a/m to unity, only when the gravitational collapse is sufficiently slow.

In a more recent paper, de Felice and Yu Yunqiang [39] showed that formation of a surrounding ring, disk, or any other diffuse configuration is not sufficient to ensure an appreciable decrease of the ratio a/m to values less than one, unless angular momentum significantly redistributes from the central core. It was then argued that probably a simultaneous combination of the above mechanisms can drastically reduce the ratio a/m of collapsing cores ending in black holes [38,39].

So far, we have briefly discussed the physical relevance of the ratio a/m at very advanced stages of stellar evolution, and have also indicated why it has to be considered as an essential parameter in any collapse simulation explaining either neutron star or black hole formation.

In what follows, we shall examine the importance of the ratio a/m during the early phases of the stellar evolution. As far as we know, no work has been done considering this quantity in the classical scenario of star formation, partly because of the role played by the parameter J/M , and partly because of its rather obscure meaning. However, we must emphasize here that the ratio J/M only gives information on the specific angular momentum and not on its distribution with respect to the mass, which is provided by the ratio a/m .

In Table 1, we report calculations of the ratio a/m for a sample of 31 observed close detached binaries [40]. For each of these systems, we know the mass and the size of the component stars as well as the orbital period of the system. If we then assume that each system is close enough to be in a complete phase locking state, in which the single components are in synchronous rotation with their orbital motion, we may compute the ratio a/m of the individual stars. This situation is likely to occur in close binaries, since in most cases the observed spin periods are nearly equal to the orbital period of the system. Furthermore, taking each component as a rigidly rotating spherical body and defining $M = M_1 + M_2$ as the total mass of the system, we have

$$\left(\frac{a}{m}\right)_i = \frac{2}{5} \frac{c r_i^2}{(2\pi G)^{\frac{1}{3}}} \frac{M^{\frac{2}{3}}}{M_i} P^{\frac{1}{3}} \quad (i = 1, 2), \quad (2.6)$$

where the subscript i refers to a particular component, r_i denotes its radius in units of the semi-major axis of the rotating system, and P is the orbital period.

The total a/m of the system is given by

$$\left(\frac{a}{m}\right)_T = \sum_{i=1}^2 \left(\frac{a}{m}\right)_i \mu_i^2 + \left(\frac{a}{m}\right)_{orb}, \quad (2.7)$$

where $\mu_i = M_i/M$ is the ratio between the i th mass component and the total mass of the binary system, and $(\frac{a}{m})_{orb}$ is the orbital contribution to $(\frac{a}{m})_T$, which is defined by

TABLE 1

SYSTEM	P(days)	r_1	r_2	M_0/M_\odot	M_1/M_\odot	M_2/M_\odot	$\left(\frac{a}{m}\right)_1$	$\left(\frac{a}{m}\right)_2$	$\left(\frac{a}{m}\right)_{orb}$
V805 Aq	2.4082377	0.199	0.147	3.74	2.11	1.63	34.19	24.34	429.3
σ Aq	1.95026	0.279	0.201	12.20	6.81	5.39	42.68	30.67	270.6
V 539 Ara	3.169129	0.217	0.154	11.32	6.10	5.22	32.23	18.83	328.7
HW Aur	2.525019	0.162	0.150	3.76	1.97	1.79	24.74	23.14	441.7
AR Aur	4.134672	0.100	0.098	4.93	2.60	2.33	10.08	10.80	475.3
ZZ Boo	4.991744	0.125	0.115	3.41	1.71	1.70	19.95	17.05	573.9
SV Cam	0.59306995	0.352	0.244	1.69	1.00	0.69	83.30	57.94	345.0
AS Cam	3.4309714	0.146	0.128	5.80	3.30	2.50	17.74	18.03	416.3
CW Cep	2.72914	0.234	0.203	22.89	11.80	11.09	29.48	23.53	248.5
TV Cet	9.1032884	0.0587	0.0502	2.66	1.39	1.27	5.605	4.47	760.2
XY Cet	2.780712	0.172	0.143	3.38	1.75	1.63	30.19	22.37	473.06
RS Cha	1.66987	0.23	0.26	3.68	1.86	1.82	45.36	59.93	388.4
MY Cyg	2.002593	0.144	0.133	3.59	1.81	1.78	19.09	16.50	416.1
V453 Cyg	3.8898128	0.294	0.177	25.67	14.45	11.22	46.18	21.41	265.2
V1143 Cyg	7.640754	0.061	0.053	2.62	1.33	1.29	5.90	4.59	722.05
BS Dra	3.364012	0.109	0.106	2.74	1.37	1.37	14.35	13.63	541.3
CW Eri	2.7283737	0.182	0.132	2.80	1.52	1.28	34.12	21.47	497.4
YY Gem	0.81428254	0.170	0.149	1.19	0.62	0.57	27.57	23.09	444.7
RX Her	1.17785724	0.230	0.174	5.00	2.70	2.30	39.15	26.20	355.9
TX Her	2.05981	0.163	0.148	3.07	1.62	1.45	24.86	22.77	441.2
HS Hya	1.568024	0.171	0.154	2.63	1.34	1.29	27.24	22.92	425.3
CM Lac	1.6046916	0.181	0.174	3.36	1.88	1.48	25.30	30.16	389.5
UV Leo	0.60008516	0.280	0.296	1.91	0.99	0.92	57.99	69.26	343.2
UX Meu	4.1811	0.092	0.087	2.34	1.17	1.17	11.58	10.31	613.4
U Oph	1.677346	0.268	0.234	9.71	5.11	4.60	42.95	36.18	280.8
WZ Oph	4.183511	0.096	0.093	5.20	2.80	2.40	8.37	9.85	467.4
V451 Oph	2.1965988	0.0210	0.170	2.24	1.13	1.11	48.98	32.91	502.2
EE Peg	2.628208	0.173	0.108	3.30	2.01	1.29	25.69	15.61	446.3
AG Per	2.0287293	0.220	0.162	8.72	4.56	4.16	32.10	19.0	310.2
CD Tau	3.435137	0.129	0.122	2.71	1.40	1.31	19.56	18.70	546.5
CV Vel	6.892	0.117	0.113	12.08	6.10	5.98	12.68	12.02	419.2

the relation

$$\left(\frac{a}{m}\right)_{orb} = \left(\frac{P}{2\pi}\right)^{\frac{1}{3}} \frac{cM_1M_2}{(GM^2)^{\frac{1}{3}}}, \quad (2.8)$$

Results from the applications of equations (2.6) and (2.8) are shown in the last three columns of Table 1. It is observed that the a/m -values of the individual components $(\frac{a}{m})_1$ and $(\frac{a}{m})_2$, respectively, are all ranged between ~ 5 and ~ 80 , in good agreement with the de Felice and Yu Yunqiang [36] estimates for main-sequence stars. The more massive components ($i = 1$) have ratios a/m slightly larger than their less massive companions ($i = 2$), while most of the total a/m is contained in the form of orbital motion. In fact, the $(\frac{a}{m})_{orb}$ is significantly larger than the (a/m) 's of the single stars by about 1-2 orders of magnitude. This situation is consistent with the assumption that

these binaries are produced by a fragmentation sequence, in which most of the specific angular momentum of the placental configuration goes into orbital angular momentum of the resulting fragments.

It is observed that single component stars have a/m -values larger than one in the range found by de Felice and Yu Yunqiang [36] for main-sequence stars. Furthermore, Table 1 indicates that any process of fragmentation in a rotating interstellar cloud must move most of the original a/m into orbital motion, and lead to final fragments with a/m of the same order as those observed, since it is likely that any subsequent evolution towards the main sequence is not in general accompanied by drastic reductions of the ratio a/m .

The observed values in Table 1, can be compared with those deduced from theoretical models of star formation. A direct comparison is possible in the case of Bodenheimer [7]. His successive fragmentation sequence in pairs of spinning blobs with equal masses, produces final fragments in the normal stellar range. In Table 2, we report calculations of the ratio a/m of these final fragments, of the resulting binary systems, and finally of the placental interstellar cloud, for five different fragmentation sequences. The a/m entries in the second column have been obtained by setting the spin period of each fragment equal to the period of the orbital system to which it belongs. Both the spin and the orbital a/m -values are in good agreement with those in Table 1. This suggests that a successive transfer of spin into orbital angular momentum, at each fragmentation stage, proves to be an efficient mechanism for reducing the a/m ratio from $\sim 10^4 - 10^5$ (interstellar clouds) to $\sim 10 - 10^2$ (stellar fragments).

From the above considerations, the ratio a/m could also represent an indicator of the physical plausibility of any protostellar collapse model, since a decrease of ~ 3

TABLE 2

SEQUENCE	$\left(\frac{a}{m}\right)$ spin last fragments	$\left(\frac{a}{m}\right)$ orb. last pair	$\left(\frac{a}{m}\right)$ spin initial cloud
III	59.20	411.2	3.965×10^4
IV	56.86	409.6	3.965×10^4
V	77.57	539.6	3.965×10^4
VI	16.24	1175.2	3.965×10^4
VII	82.08	591.9	1.123×10^5

orders of magnitude in a/m is needed to explain star formation.

Calculations of the ratio a/m of fragments obtained from 3-D simulations by Boss [15] and Norman and Wilson [87], are shown in Tables 3 and 4, respectively. In these cases, a direct comparison with Table 1 is not possible, since these simulations refer to low-density stages of the evolution (isothermal collapse).

As shown in Table 3, an initial cloud may fragment into a binary system, or form a ring surrounding a centrally condensed blob, or even contract into a single blob. It is observed that the ratio a/m of the isothermal fragments does not decrease with respect to the initial a/m ($\sim 10^5$) of the cloud. On the contrary, the a/m ratio has increased over its initial value, in disagreement with the one order of magnitude decrease predicted by the Bodenheimer [7] sequences during the isothermal fragmentation stage. A similar situation is found in Table 4, where the large values of a/m for the fragments indicate, as for the Boss case, that either they will fragment or will necessary face very efficient dissipative processes which allow reduction of their a/m .

TABLE 3

MODELS	$\frac{M_1}{M_0}$	$\frac{M_2}{M_0}$	$\left(\frac{a}{m}\right)$ spin fragments		$\left(\frac{a}{m}\right)_{\text{orb}}$	$\left(\frac{a}{m}\right)_{\text{initial cloud}}$
			$(a/m)_1$	$(a/m)_2$		
Model I (Binary system)	0.15	0.15	2.61×10^5	2.61×10^5	3.27×10^5	1.45×10^5
Model II (Binary System)	0.07	0.06	1.52×10^6	2.20×10^6	8.84×10^5	1.45×10^5
Model IV (Binary System)	0.16	0.16	2.92×10^5	2.92×10^5	7.30×10^5	2.062×10^5
Model VI (well defined single blob)	$\left(\frac{M}{M_0}\right)_{\text{blob}} = 0.11$		$\left(\frac{a}{m}\right)_{\text{spin blob}} = 4.68 \times 10^6$		--	1.24×10^5
Model VII (single blob and a ring)	$\left(\frac{M}{M_0}\right)_{\text{blob}} = 0.03$		$\left(\frac{a}{m}\right)_{\text{spin blob}} = 1.76 \times 10^7$		--	1.35×10^5

De Felice [37] examined the behaviour of the ratio a/m during the adiabatic collapse of $1M_{\odot}$ protostellar clouds as calculated by Boss [16]. The ratio a/m of the initial cloud was estimated to be $\sim 10^4$, while the ratio a/m of the resulting fragments decreased only for the initially more rapidly rotating cloud ($\beta = 0.3$). For initially slow rotators ($\beta \sim 0.1$), the ratio a/m of the final fragments was slightly larger than the initial value. De Felice [37] argued that some correlation seems to exist between the initial amount of rotational energy in the collapsing cloud and the degree of reduction of the ratio a/m .

Three-dimensional calculations indicate that J/M is efficiently reduced by conversion of spin angular momentum into orbital angular momentum, while the same mechanism is apparently inefficient in reducing the ratio a/m . The important question will then regard mechanisms which might contribute greatly to reduction of the ratio a/m , and their effects on the gravitational collapse of interstellar clouds.

A definitive answer to the above question would require the inclusion of complete physics in the theoretical analysis of star formation. It is likely that the effects of

TABLE 4

$\left(\frac{a}{m}\right)_{\text{initial cloud}} = 1.626 \times 10^5$			
BLOBS	$M(\times 10^{12} \text{gr})$	$J_{\text{spin}}(\times 10^{52} \text{gem}^2 \text{sec}^{-1})$	$\left(\frac{a}{m}\right)_{\text{spin blob}}$
RUN 1	1	0.8	2.12×10^5
	2	0.7	1.39×10^5
	3	0.2	8.99×10^4
	4	0.7	1.02×10^5
RUN 2	1	1.3	1.32×10^5
	2	1.5	9.25×10^4
RUN 3	1	1.6	1.06×10^5
	2	1.6	9.17×10^4
RUN 4	1	1.5	1.86×10^5
	2	0.85	8.66×10^4
	3	2.0	1.7×10^5
RUN 5	1	0.6	1.37×10^5
	2	1.4	1.57×10^5
	3	1.3	1.10×10^5

viscosity, turbulent motion, and magnetic fields, become of paramount importance in determining the behaviour of the ratio a/m during the early evolution of stars.

Chapter 3

The Mathematical Problem

A two or three dimensional description of the evolution of initially low-density interstellar gas clouds, leading to star formation, would introduce an extremely complicated mathematical problem, owing to the richness of macroscopic and microscopic physical events occurring during the evolutionary process [10]. It is well-known that the mathematics involved is standard but nonlinear, and therefore, analytically difficult.

Experience shows that, even with the use of sophisticated numerical methods, when more and more physics is added to the problem, the complexity of the resulting equations increases, imposing a severe hindrance on the calculation of realistic models, even in the simplest case when the calculation is confined to one-space dimension. Therefore, we are constrained to model only particular main stages of the whole evolution process, with the aid of simplifying physical assumptions and mathematical conditions. That is, the dominant effects are isolated and adequate boundary and symmetry conditions are imposed.

In the present work, we are concerned with the calculation of theoretical models of protostellar collapse and fragmentation, in order to address some of the physical problems discussed in Chapter 2. We shall start by summarizing the relevant physical

assumptions and then, we shall give the resulting basic equations to be solved, as well as the initial and boundary conditions which allow for numerical solutions of those equations.

3.1 Physical Assumptions

The following standard assumptions are made:

(a) An initial protostellar cloud is represented as a gas configuration of predominantly molecular hydrogen. The gas is assumed to be ideal, with a typical composition $X = 0.653$, $Y = 0.323$, and $Z = 0.024$, where X is the mass fraction of hydrogen, Y is that of helium, and Z is that of all heavier elements.

(b) The collapse is assumed to proceed isothermally over the density range $10^{-19} < \rho < 3 \times 10^{-13} \text{gcm}^{-3}$, with typical gas temperatures oscillating about 10K [48,61]. Therefore, a pressure-law of the form $p \propto \rho$ will be sufficient for our purposes.

(c) The calculations are carried beyond the isothermal regime, into the density range $3 \times 10^{-13} < \rho < 10^{-11} \text{gcm}^{-3}$, by simply approximating the effects of radiation transfer with a hypothetical pressure-law of the form

$$p = p_{lim} \left(\frac{\rho}{\rho_{lim}} \right)^{7/5}, \quad (3.1)$$

where $\rho_{lim} = 3 \times 10^{-13} \text{gcm}^{-3}$ and $p_{lim} \propto \rho_{lim}$. Equation (3.1) was suggested by Boss [13] as representing a good approximation for the near-isothermal effects. It is also the equation governing the adiabatic behaviour of a gas of purely molecular hydrogen.

(d) The effects of the galactic magnetic field are neglected, so we are considering the collapse of clouds denser than $n \sim 10^4 \text{H}_2 \text{cm}^{-3}$. Above this critical density, the magnetic field is substantially decoupled and hence it has little effect on the further collapse.

(e) The effects of molecular viscosity and turbulence are also neglected. This assumption rests on the fact that molecular viscosity is quite small during the initial stages of the collapse of interstellar clouds. Even a turbulent viscosity would have little effect on these early phases [59]; however, it may become important if substantial turbulence is present in the later phases of the non-isothermal evolution.

3.2 Basic Equations

The gravitational isothermal collapse of an inviscid, non-heat-conducting, compressible, rotating gas cloud is completely described by the following equations

$$\frac{\partial \rho}{\partial t} + \nabla \cdot (\rho \mathbf{v}) = 0 \quad , \quad (3.2)$$

$$\rho \frac{\partial \mathbf{v}}{\partial t} + (\mathbf{v} \cdot \nabla) \mathbf{v} = -\nabla p - \rho \nabla \Phi \quad , \quad (3.3)$$

$$\nabla^2 \Phi = 4\pi G \rho \quad , \quad (3.4)$$

$$p = \text{const} \cdot \rho \quad , \quad (3.5)$$

where $\rho = \rho(\mathbf{x}, t)$ denotes the mass-density, $\mathbf{v} = \mathbf{v}(\mathbf{x}, t)$ the fluid velocity, $\Phi = \Phi(\mathbf{x}, t)$ the gravitational potential, and $p = p(\mathbf{x}, t)$ the gas pressure.

Equation (3.2) is the equation of continuity expressing mass conservation and represents the time rate of change of mass. Equation (3.3) is the Euler equation describing the motion of the self-gravitating fluid. This equation represents the time rate of change of momentum. Equation (3.4) is the Poisson equation for the gravitational potential, and equation (3.5) is the equation of state for an ideal gas. Generally, we take $\text{const} = R_g T / \mu$ or $\text{const} = (X/2 + Y/4 + Z/A_M) k T / m_p$, where R_g is the gas constant, T the temperature, μ the mean molecular weight, k the Boltzmann constant, m_p the

mass of the proton, and A_M an averaged atomic number, obtained from the detailed cosmic abundances of the heavy elements, which is usually taken equal to 16.78.

Equation (3.5) defines a simple pressure-density relation. It is adequate for calculations of the isothermal phase of protostellar collapse [61]. However, when the density exceeds the value $3 \times 10^{-13} \text{ g cm}^{-3}$, the radiation transfer effects become important, and the collapse of the densest regions proceeds non-isothermally. At this point the physics becomes more complicated, and further calculations require the inclusion of an extra differential equation, for the rate of change of the specific internal energy, coupled with the radiation transfer equation, the equation of state of the gas and the opacity function. However, we can account in a first approximation for the non-isothermal effects by replacing equation (3.5) by an adiabatic pressure-law of the form

$$p = K \rho^\gamma \quad , \quad (3.6)$$

where γ is the adiabatic exponent related to the polytropic index n by $\gamma = 1 + 1/n$, and K is a constant determined from the initial conditions [16].

The hydrodynamic equations (3.2) and (3.3) are hyperbolic in form and describe the time evolution of the primary variables ρ and \mathbf{v} , while the Poisson equation (3.4) is a typical elliptic partial differential equation. These equations together with the pressure-law (3.5), or (3.6), form a consistent set of equations sufficient to determine the problem for given initial and boundary conditions.

3.3 The Concept of Grid Motion

One of the problems usually encountered in numerical calculations of protostellar collapse models, is the lack of appropriate spatial resolution. The difficulty arises when high density concentrations with scale-lengths smaller than or comparable to the mesh-

size develop in the central portions of the collapsing cloud. Once this situation occurs, the further evolution of these small features cannot be followed with reasonable accuracy. An apparently logical way of avoiding this sort of deficiency, is to adopt a grid with a small spacing everywhere. However, if the calculation is carried out in two- or three-space dimensions, the storage and computational time required would render the calculation prohibitive and this imposes a limit on the number of mesh-points to be used.

Many authors [3,13,89,115] have in part circumvented this general difficulty by implementing an automatic grid rezoning technique. Here by grid rezoning we mean a gradual contraction of the grid, in which the spacings are continuously varied from a coarse mesh structure covering most of the flow field to a fine grid resolving the inner high density concentrations [90]. In other words, we define a coordinate system co-moving with the fluid, on which we shall solve the relevant equations.

The motion of the grid is not handled in a strict Lagrangian sense in order to avoid strong distortions of the mesh, which would lead to additional computational difficulties. Hence, the best way of introducing a moving grid is by assuming the grid velocity to be nearly equal to the local fluid velocity.

In this way, denoting by \mathbf{v}_g the grid velocity with respect to a fixed Eulerian observer and by $\mathbf{U} = \mathbf{v} - \mathbf{v}_g$ the relative fluid velocity, the continuity equation (3.2) modified to include the grid motion effects, becomes [3]

$$\frac{\partial \rho}{\partial t} + \nabla \cdot (\rho \mathbf{U}) = -\rho \nabla \cdot \mathbf{v}_g \quad , \quad (3.7)$$

where the additional term $\rho \nabla \cdot \mathbf{v}_g$ represents the contribution to the net change of density due to changes in the grid zones. In equation (3.7), we have set $\mathbf{v}_g \cdot \nabla \rho = 0$. This means that the grid is not allowed to drag material as it moves. Otherwise,

convergence to physical solutions cannot be guaranteed. Similar modifications are also implemented for the Euler equation (3.3).

The divergence of the grid velocity satisfies the identity

$$\nabla \cdot \mathbf{v}_g = \frac{d}{dt} (\ln dV) \quad , \quad (3.8)$$

where dV denotes the element of volume of a particular moving grid zone.

Equation (3.7), expressed in the co-moving frame with the fluid, is physically equivalent to equation (3.2) defined in the inertial frame of an Eulerian observer. Then, setting $\mathbf{v}_g = 0$, we recover equation (3.2). The hydrodynamic equations modified for grid motion will determine the physical problem, together with eqs.(3.4) and (3.5), once \mathbf{v}_g is specified.

In what follows, we give the equations as they are actually used in the 1-, 2-, and 3-dimensional calculations. The structural form of these equations is obtained by writing them in spherical polar coordinates (r, θ, ϕ) .

3.4 Spherically Symmetric Flows: The 1-D Problem

The differential equations used have their simplest structural form when each particle of fluid is constrained to move with only one degree of freedom, i.e. when the material in the cloud is allowed to contract only in the radial direction. The collapse of such a configuration is commonly referred to as spherically symmetric collapse, since all variables will only be explicit functions of the radial coordinate and of time ($\partial/\partial\theta=\partial/\partial\phi=0$). In this case, the velocity vector of the fluid with respect to the moving coordinate system is defined by

$$\mathbf{U} = \mathbf{r}(v_r - v_g) = \mathbf{r} \left(v_r - \frac{dr}{dt} \right) \quad , \quad (3.9)$$

where v_r is the local fluid velocity with respect to the inertial frame of reference.

Then, the relevant equations will have the form

$$\frac{\partial \rho}{\partial t} + \frac{1}{r^2} \frac{\partial}{\partial r} (r^2 \rho U) = -\rho \frac{1}{r^2} \frac{\partial}{\partial r} (r^2 v_g) \quad , \quad (3.10)$$

$$\frac{\partial(\rho v_r)}{\partial t} + \frac{1}{r^2} \frac{\partial}{\partial r} (r^2 \rho v_r U) = -\rho v_r \frac{1}{r^2} \frac{\partial}{\partial r} (r^2 v_g) - \frac{\partial \Phi}{\partial r} - \frac{\partial p}{\partial r} \quad , \quad (3.11)$$

$$\frac{1}{r^2} \frac{\partial}{\partial r} \left(r^2 \frac{\partial \Phi}{\partial r} \right) = 4\pi G \rho \quad . \quad (3.12)$$

The second terms in the left-hand sides of equations (3.10) and (3.11) are referred to as the advective parts, and represent the net changes of mass and radial momentum, respectively, due to the mechanical transport of fluid particles from place to place.

3.5 Axisymmetric Flows: The 2-D Problem

In collapsing clouds, to allow for the effects of rotation, an extra dimension has to be added. In the axisymmetric case we can assume, in principle, that each particle of fluid in the cloud rotates about the axis of symmetry. Moreover, the motion will be confined to the (r, θ) -plane, and the assumption made that all variables are explicit functions of time and of the r - and θ -coordinates, so that $\partial/\partial\phi=0$. In other words, we study the influence of rotation on the way the material is being transported in both the r - and θ -directions.

If the grid is allowed to move only radially such that $\mathbf{v}_g = (v_g, 0)$, the poloidal fluid velocity relative to the contracting grid will be

$$\mathbf{v} = \mathbf{r}U + \theta v_\theta = \mathbf{r} \left(v_r - \frac{dr}{dt} \right) + \theta v_\theta \quad , \quad (3.13)$$

where $v_r = v_r(r, \theta)$, $v_\theta = v_\theta(r, \theta)$, and $v_g = v_g(r)$. If rotation is included in the calculation each fluid particle will move with a velocity

$$\mathbf{v} = \mathbf{r} \left(v_r - \frac{dr}{dt} \right) + \theta v_\theta + \phi v_\phi \quad , \quad (3.14)$$

where $v_\phi = v_\phi(r, \theta)$.

For axisymmetric rotating flows equation (3.7) takes the form

$$\frac{\partial \rho}{\partial t} + \frac{1}{r^2} \frac{\partial}{\partial r} (r^2 \rho U) + \frac{1}{r \sin \theta} \frac{\partial}{\partial \theta} (\sin \theta \rho v_\theta) = -\rho \frac{1}{r^2} \frac{\partial}{\partial r} (r^2 v_g) \quad , \quad (3.15)$$

while the motion equation (3.3) splits up into three equations, namely

$$\begin{aligned} \frac{\partial(\rho v_r)}{\partial t} + \frac{1}{r^2} \frac{\partial}{\partial r} (r^2 \rho v_r U) + \frac{1}{r \sin \theta} \frac{\partial}{\partial \theta} (\sin \theta \rho v_r v_\theta) = -\rho v_r \frac{1}{r^2} \frac{\partial}{\partial r} (r^2 v_g) - \\ - \rho \frac{\partial \Phi}{\partial r} - \frac{\partial p}{\partial r} + \frac{\rho}{r} (v_\theta^2 + v_\phi^2) \quad , \end{aligned} \quad (3.16)$$

describing momentum transfer in the r -direction,

$$\begin{aligned} \frac{\partial(\rho v_\theta)}{\partial t} + \frac{1}{r^2} \frac{\partial}{\partial r} (r^2 \rho v_\theta U) + \frac{1}{r \sin \theta} \frac{\partial}{\partial \theta} (\sin \theta \rho v_\theta v_\theta) = -\rho v_\theta \frac{1}{r^2} \frac{\partial}{\partial r} (r^2 v_g) - \\ - \rho \frac{1}{r} \frac{\partial \Phi}{\partial \theta} - \frac{1}{r} \frac{\partial p}{\partial \theta} - \frac{\rho}{r} (v_r v_\theta - v_\phi^2 \cot \theta) \quad , \end{aligned} \quad (3.17)$$

describing the momentum transfer in the θ -direction, and

$$\frac{\partial(\rho A)}{\partial t} + \frac{1}{r^2} \frac{\partial}{\partial r} (r^2 \rho A U) + \frac{1}{r \sin \theta} \frac{\partial}{\partial \theta} (\sin \theta \rho A v_\theta) = -\rho A \frac{1}{r^2} \frac{\partial}{\partial r} (r^2 v_g) \quad , \quad (3.18)$$

for the specific angular momentum transfer. Equation (3.18) has been written in terms of the variable A ($= r \sin \theta v_\phi$) which is the specific angular momentum of each particle of fluid. Nevertheless, the ϕ -velocity component v_ϕ is also regarded as a primary variable because it enters in the undifferentiated terms of equations (3.16) and (3.17), respectively.

The Poisson equation (3.4) becomes

$$\frac{1}{r^2} \frac{\partial}{\partial r} \left(r^2 \frac{\partial \Phi}{\partial r} \right) + \frac{1}{r^2 \sin \theta} \frac{\partial}{\partial \theta} \left(\sin \theta \frac{\partial \Phi}{\partial \theta} \right) = 4\pi G \rho \quad , \quad (3.19)$$

with $\Phi = \Phi(r, \theta)$ and $\rho = \rho(r, \theta)$.

3.6 Non-Axisymmetric Flows: The 3-D Problem

A more realistic description of protostellar collapse may be given by solving equations (3.2), (3.3), and (3.4) in the full three-dimensional space. In this case, no restrictions will be imposed on the motion of the fluid and all variables will be explicit functions of time and of the coordinates r , θ , and ϕ .

For a radially contracting grid with velocity $\mathbf{v}_g = (v_g, 0, 0)$, the fluid velocity relative to the grid is given by

$$\mathbf{v} = \mathbf{r} \left(v_r - \frac{dr}{dt} \right) + \theta v_\theta + \phi v_\phi \quad , \quad (3.20)$$

where $v_r = v_r(r, \theta, \phi)$, $v_\theta = v_\theta(r, \theta, \phi)$, and $v_\phi = v_\phi(r, \theta, \phi)$, respectively. Then, the 3-dimensional equations describing the non-axisymmetric collapse of initially rotating configurations are

$$\begin{aligned} \frac{\partial \rho}{\partial t} + \frac{1}{r^2} \frac{\partial}{\partial r} (r^2 \rho U) + \frac{1}{r \sin \theta} \frac{\partial}{\partial \theta} (\sin \theta \rho v_\theta) + \frac{1}{r \sin \theta} \frac{\partial}{\partial \phi} (\rho v_\phi) = \\ = -\rho \frac{1}{r^2} \frac{\partial}{\partial r} (r^2 v_g) \quad , \end{aligned} \quad (3.21)$$

the continuity equation; and

$$\begin{aligned} \frac{\partial(\rho v_r)}{\partial t} + \frac{1}{r^2} \frac{\partial}{\partial r} (r^2 \rho v_r U) + \frac{1}{r \sin \theta} \frac{\partial}{\partial \theta} (\sin \theta \rho v_r v_\theta) + \frac{1}{r \sin \theta} \frac{\partial}{\partial \phi} (\rho v_r v_\phi) = \\ = -\rho v_r \frac{1}{r^2} \frac{\partial}{\partial r} (r^2 v_g) - \rho \frac{\partial \Phi}{\partial r} - \frac{\partial p}{\partial r} + \frac{\rho}{r} (v_\theta^2 + v_\phi^2) \quad , \end{aligned} \quad (3.22)$$

$$\begin{aligned} \frac{\partial(\rho v_\theta)}{\partial t} + \frac{1}{r^2} \frac{\partial}{\partial r} (r^2 \rho v_\theta U) + \frac{1}{r \sin \theta} \frac{\partial}{\partial \theta} (\sin \theta \rho v_\theta v_\theta) + \frac{1}{r \sin \theta} \frac{\partial}{\partial \phi} (\rho v_\theta v_\phi) = \\ = -\rho v_\theta \frac{1}{r^2} \frac{\partial}{\partial r} (r^2 v_g) - \rho \frac{1}{r} \frac{\partial \Phi}{\partial \theta} - \frac{1}{r} \frac{\partial p}{\partial \theta} - \frac{\rho}{r} (v_r v_\theta - v_\phi^2 \cot \theta) \quad , \end{aligned} \quad (3.23)$$

$$\frac{\partial(\rho A)}{\partial t} + \frac{1}{r^2} \frac{\partial}{\partial r} (r^2 \rho A U) + \frac{1}{r \sin \theta} \frac{\partial}{\partial \theta} (\sin \theta \rho A v_\theta) + \frac{1}{r \sin \theta} \frac{\partial}{\partial \phi} (\rho A v_\phi) =$$

$$= -\rho A \frac{1}{r^2} \frac{\partial}{\partial r} (r^2 v_g) - \rho \frac{\partial \Phi}{\partial \phi} - \frac{\partial p}{\partial \phi} \quad , \quad (3.24)$$

the r -, θ -, and angular momentum transfer equations, respectively.

The Poisson equation becomes

$$\frac{1}{r^2} \frac{\partial}{\partial r} \left(r^2 \frac{\partial \Phi}{\partial r} \right) + \frac{1}{r^2 \sin \theta} \frac{\partial}{\partial \theta} \left(\sin \theta \frac{\partial \Phi}{\partial \theta} \right) + \frac{1}{r^2 \sin^2 \theta} \frac{\partial^2 \Phi}{\partial \phi^2} = 4\pi G \rho \quad , \quad (3.25)$$

where $\Phi = \Phi(r, \theta, \phi)$ and $\rho = \rho(r, \theta, \phi)$.

Here after, we shall refer to the second, third, and fourth terms on the left-hand side of equations (3.21)-(3.24) as the r -, θ -, and ϕ -advective terms, respectively, and to the first term on the right-hand side as the grid contraction term.

3.7 Initial and Boundary Conditions

To allow for numerical solutions of the foregoing sets of partial differential equations, it is necessary to specify suitable initial conditions and boundary conditions.

The problem of setting consistent initial conditions, for protostellar collapse calculations, is physically difficult due to the obscure processes that characterize the earlier low-density star formation period. However, under our physical assumptions, the most important hypothesis is to consider the Jeans limit for a spherical cloud as the starting point of any collapse calculation.

A particular initial model will be defined by the following parameters: the total cloud mass M , the density distribution ρ , the velocity field \mathbf{v} , and the size of the configuration R_0 , which is calculated as a secondary parameter from the initially known mass M and density distribution ρ . If the grid is allowed to move approximately with the fluid flow, we must also specify the grid velocity \mathbf{v}_g at $t = 0$.

For pure isothermal calculations, the set of initial conditions will be completed by choosing a constant temperature T (usually taken to be 10K) and the mean molecular

weight μ of the predominant chemical composition. These two parameters are needed for defining the initial gas pressure [eq.(3.5)]. For adiabatic calculations, the initial conditions are completed by specifying the adiabatic exponent γ and the initial pressure p , as required by equation (3.5) in order to determine the value of the constant K .

In practice, for most of our models, we take a perfectly spherical $1M_{\odot}$ cloud initially at rest, with uniform density and angular velocity distributions. So, for spherically symmetric collapse calculations, we set at $t = 0$

$$\left\{ \begin{array}{l} \rho_i(r) = \rho_0 = \text{constant}, \\ v_{r_i}(r) = v_{g_i}(r) = 0 \Rightarrow U_i(r) = 0, \\ M = 1M_{\odot}, T = \text{const.}, \mu = \text{const.}, \quad \text{for isothermal collapse,} \\ M = 1M_{\odot}, p_i(r) = p_0, \gamma = \text{const.}, \quad \text{for adiabatic collapse.} \end{array} \right.$$

For multi-dimensional calculations, the initial state of the collapsing configuration will be one of pure rotation, i.e. with the only non-zero velocity component being v_{ϕ} .

Then at $t = 0$, we have

$$\left\{ \begin{array}{l} \rho_i = \rho_0 = \text{constant}, \\ v_{r_i} = v_{\theta_i} = v_{g_i} = 0 \Rightarrow U_i = 0, \\ \omega_i = \omega_0 = \text{constant}, \\ M = 1M_{\odot}, T = \text{const.}, \mu = \text{const.}, \quad \text{for isothermal collapse,} \\ M = 1M_{\odot}, p_i = p_0, \gamma = \text{const.}, \quad \text{for adiabatic collapse,} \end{array} \right.$$

where all of the initial variables may be functions of either (r, θ) (axisymmetric case) or (r, θ, ϕ) (non-axisymmetric case).

Initially non-uniform density distributions of the form

$$\rho_i = \rho_0 \left(1 - \frac{r}{nR_0} \right) \quad \text{with } n \geq 1, \quad (3.26)$$

for centrally condensed configurations, and

$$\rho_i = \rho_0 (1 + a \cos m\phi) \quad \text{with } a \text{ real and } m \text{ integer,} \quad (3.27)$$

for ϕ -perturbed density distributions, may be also tried for multi-dimensional calculations.

The existence of scaling laws for similar flows of the isothermal and adiabatic equations of motion [7,15] reduces the number of parameters necessary for describing the initial state of a particular rotating protostar. If we define the absolute value of the ratio of thermal to gravitational energy

$$\alpha_0 = |E_T|/|E_G| = \frac{5}{2} \frac{R_g R_0 T}{G M \mu} \quad , \quad (3.28)$$

and the ratio of rotational to gravitational energy

$$\beta_0 = |E_R|/|E_G| = \frac{1}{3} \frac{\omega_0^3 R_0^3}{G M} \quad , \quad (3.29)$$

the initial state of a perfectly spherical, rotating cloud at rest, may then be fully described by the parameters α_0 and β_0 , instead of specifying as above ρ_i , ω_i , R_0 , μ , and T . Results for any configuration with different values of M , T , and μ , can then be obtained from the isothermal scaling laws. In the adiabatic case, we need an additional parameter and the initial conditions are then completely specified by setting α_0 , β_0 , and γ , instead of giving ρ_i , ω_i , p_i , R_0 , and γ . Using the adiabatic scaling laws we may then again infer results for the collapse of any cloud with different values of M and K .

The hydrodynamical boundary conditions are specified in such a way as to avoid over-specification of the problem. In our case, over-specification may occur if each of the primary variables ρ , v_r , v_θ , and A (or v_ϕ), is independently assigned on the boundaries of the computational domain, due to the hyperbolic character of the relevant differential equations. Here, a consistent formulation is obtained by determining some of the boundary variables from the equations themselves. In practice, all boundary densities are determined from the continuity equation, while only those velocity components, which are either normal to any of the boundaries or required to simplify the calculations, will be specified independently.

For 2- and 3-dimensional calculations, we define four geometrical boundaries: the critical centre ($r = 0$), the rotational axis ($\theta = 0$), the equatorial plane ($\theta = \pi/2$), and an external spherical surface ($r = R_0$) (as discussed below). Only the centre and the rotational axis represent singularities for the hydrodynamic equations. The conditions on the velocity field for each of these locations are as follows:

- (a) At the centre, the flow is constrained by setting

$$v_r = v_\theta = v_\phi \equiv 0 \quad \text{for } t \geq 0,$$

so that there is no mass crossing the centre.

- (b) Along the rotational axis we impose the conditions

$$v_\theta = v_\phi \equiv 0 \quad \text{for } t \geq 0,$$

which is physically consistent with the fact that the mass on the rotational axis can only flow radially.

- (c) Reflection symmetry about the equatorial plane is assumed by constraining the flow to have

$$v_\theta \equiv 0 \quad \text{at } \theta = \pi/2 \text{ for } t \geq 0.$$

The use of this symmetry condition means that we only need to calculate part of the flow. The saving of time produced in this way is particularly important when the scheme is extended to three-space dimensions.

- (d) A constant-volume boundary condition [$R_0(t) = \text{const}$] is applied at the external spherical surface by assuming that

$$v_r = v_\theta \equiv 0 \quad \text{at } r = R_0 \text{ for } t \geq 0,$$

which means that no mass is allowed to flow across the surface of the spherical volume enclosing the protostellar cloud. This type of boundary condition has been widely implemented in many collapse calculations [13,61,63,74]. It is physically justified on the grounds that, only small changes would take place in the flow near to this boundary and hence, the original equilibrium conditions would be nearly maintained [74]. Therefore, it is expected that the gas in the neighbourhood of the boundary surface R_0 does not move by a significant amount. The physical assumption, which is made by using such condition, is that the pressure on the spherical edge varies with time in such a way as to keep the volume fixed.

The boundary conditions for the solution of the Poisson equation are discussed in Chapter 5, Section 5.1.

Chapter 4

The Computational Grid

4.1 Description

In order to obtain numerical solutions of equations (3.2)-(3.5), we must start by dividing the spherical volume containing the fluid into a discrete number of cells. The set of these cells defines the computational grid and introduces the concept of control-volume. In dealing with multi-dimensional calculations, the introduction of control-volumes turns out to be of great help in finding the correct finite-difference form of the relevant differential equations.

In our specific case, the Poisson equation and the Eulerian equations of hydrodynamics are discretized on a spherical coordinate grid [See Figures 4.1(a) and 4.1(b)]. Figure 4.1(a) is an (r, θ) -slice perpendicular to the equatorial plane ($\theta = \pi/2$), and Figure 4.1(b) is a representation of an (r, ϕ) -plane perpendicular to the rotational axis ($\theta = 0$). The 3-dimensional grid is composed of a single spherical cell centered at the origin ($r = 0$) of the coordinate system, a cone of N_r cells along the rotational axis, and $(N_r \times N_\theta \times N_\phi)$ cells filling the rest of the top hemisphere of the spherical configuration. Here N_r , N_θ , and N_ϕ denote the maximum number of cells in the r , θ , and ϕ directions, respectively.

The points in Figure 4.1 represent the geometrical centres of the 3-dimensional cells, where all of the physical variables which characterize the fluid, are defined. The centre-point of a typical main grid-cell is labeled by the integer indices (i, j, k) denoting a particular value of the coordinates (r, θ, ϕ) . The i index increases with increasing r , the j index with increasing θ , and the k index with increasing ϕ . A general variable $X = X(r, \theta, \phi)$ evaluated at the cell centre ijk is denoted by X_{ijk} such that X_{ijk} represents a mean value for cell (i, j, k) .

The zones along $j = N_\theta + 1$, in Figure 4.1(a), are used to apply the reflection symmetry condition about the equatorial plane at $j = N_\theta$, while the true boundary of the problem is defined by zones with $i = N_r$ for any j and k . The axial cells are only labeled by the index i and the central cell by the subscript c . As shown in Figure 4.1(b) a periodic boundary condition for the ϕ -coordinate is enforced by carrying two extra angular zones, labeled $k = N_\phi + 1$ and $k = N_\phi + 2$, which coincide with zones $k = 1$ and $k = 2$, respectively.

In order to get appropriate spatial resolution with a discrete number of cells and, hence, acceptable accuracy in the central regions of the cloud, the grid is allowed to contract radially during the calculations [See Section 4.3]. This is done by means of an automatic rezoning which is activated during the main infall stages of the evolution. The motion of the grid is handled so that the centre (at $r = 0$) and the boundary (at $r = R_0$) are held fixed in space and time. The interior points are able to follow, roughly, the motion of the fluid. After a time $t \gg 0$, the radial grid-structure becomes strongly non-uniform, with the r -spacings being successively smaller towards the centre of the collapsing cloud. On the other hand, the θ - and ϕ -grid positions are not allowed to move, with the ϕ -grid spacing being exactly uniform. The θ -grid is fairly uniform

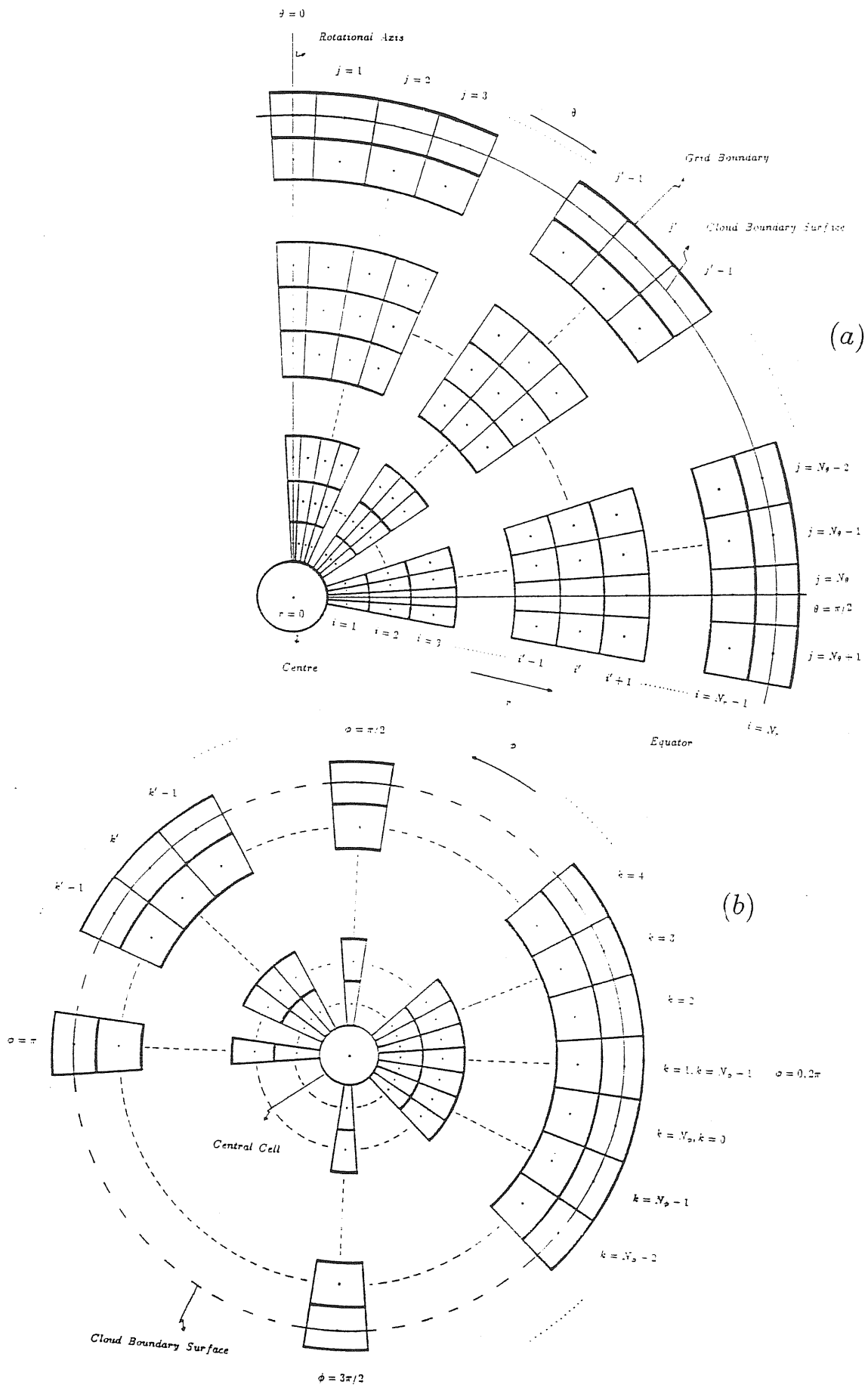


Figure 4.1: (a). (r, θ) -meridional plane, and (b) (r, ϕ) -equatorial plane of the 3-dimensional grid.

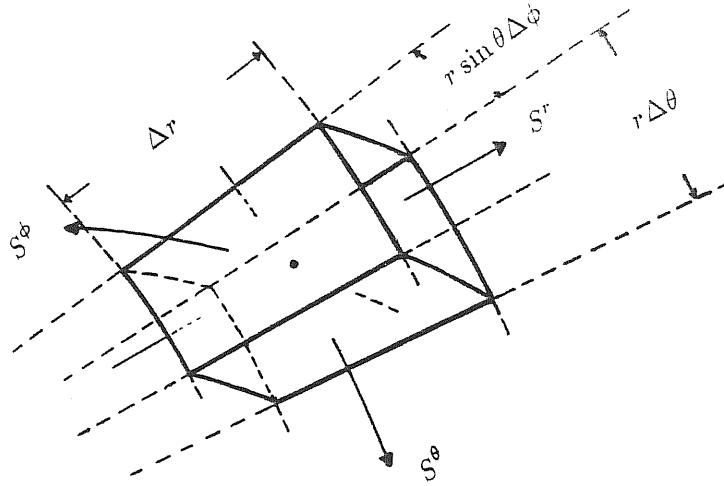


Figure 4.2: Three-dimensional picture of a typical computational cell

except for the axial cells, which have θ -spacings smaller than those of the corresponding main grid-cells. This is due to the fact that the θ -grid positions are determined by the roots of the Legendre polynomials P_l [See Chapter 5, Section 5.2]. Thus, for any value of r , the angular distance between the axis and the nearest point ilk is smaller than the theta inter-point distances of the main grid.

Generally, in most calculations we adopt $N_r = 20$, $N_\theta = 11$, and $N_\phi = 16$. However, for specific tests, these numbers may be varied. Because of the assumption of reflection symmetry about the equatorial plane, the calculations are carried out for only the top half of the spherical volume ($0 \leq \theta \leq \pi/2$), but they include the full 2π radians in the azimuthal direction. In the more restricted axisymmetric case ($N_\phi = 1$), the calculations are carried out for only one-quarter of a meridional plane (r, θ) , [See Figure 4.1(a)].

4.2 Geometrical Grid Properties

Consider an element of volume in spherical coordinates [as shown in Figure 4.2]. A typical main grid-cell will exhibit exactly the same geometrical form.

In Figure 4.2, S^r , S^θ , and S^ϕ are the surface areas of the cell-volume open to the flow in the r -, θ -, and ϕ -directions, respectively. They are defined by

$$\begin{aligned} S^r &= r^2 \sin \theta \Delta \theta \Delta \phi, \\ S^\theta &= r \sin \theta \Delta r \Delta \phi, \\ S^\phi &= r \Delta r \Delta \theta, \end{aligned} \tag{4.1}$$

while the volume occupied by the cell is given by

$$\Delta V = r^2 \sin \theta \Delta r \Delta \theta \Delta \phi. \tag{4.2}$$

Using these well-known relations, we can define the geometrical properties of a typical cell (i, j, k) . Since its geometrical centre is located at the point ijk , we shall denote by $S_{i\pm 1/2, jk}^r$ the areas of contact surfaces between the cell (i, j, k) and the cells $(i \pm 1, j, k)$, open to the r -direction flow; by $S_{i, j\pm 1/2, k}^\theta$ those between the cell (i, j, k) and the cells $(i, j \pm 1, k)$, open to the θ -direction flow; and finally by $S_{ij, k\pm 1/2}^\phi$ the areas of the contact surfaces between the cell (i, j, k) and the cells $(i, j, k \pm 1)$, open to the ϕ -direction flow. According to relations (4.1), we set

$$\begin{aligned} S_{i\pm 1/2, jk}^r &= r_{i\pm 1/2}^2 \sin \theta_j \Delta \theta_{j+1/2} \Delta \phi_{k+1/2}, \\ S_{i, j\pm 1/2, k}^\theta &= r_i \sin \theta_{j\pm 1/2} \Delta r_{i+1/2} \Delta \phi_{k+1/2}, \\ S_{ij, k\pm 1/2}^\phi &= r_i \Delta r_{i+1/2} \Delta \theta_{j+1/2}, \end{aligned} \tag{4.3}$$

and from (4.2), the volume of the cell, denoted by V_{ijk} , will be

$$V_{ijk} = r_i^2 \sin \theta_j \Delta r_{i+1/2} \Delta \theta_{j+1/2} \Delta \phi_{k+1/2}. \tag{4.4}$$

In the above relations, $r_{i\pm 1/2}$ and $\theta_{j\pm 1/2}$ define interface positions, which are calculated as simple averages

$$r_{i\pm 1/2} = \frac{1}{2} (r_i + r_{i\pm 1}),$$

$$\theta_{j\pm 1/2} = \frac{1}{2}(\theta_j + \theta_{j\pm 1}), \quad (4.5)$$

while the r -, θ -, and ϕ -spacings are given by

$$\begin{aligned} \Delta r_{i+1/2} &= \frac{1}{2}(\Delta r_i + \Delta r_{i+1}), \\ \Delta \theta_{j+1/2} &= \frac{1}{2}(\Delta \theta_j + \Delta \theta_{j+1}), \\ \Delta \phi_{k+1/2} &= \frac{1}{2}(\Delta \phi_k + \Delta \phi_{k+1}), \end{aligned} \quad (4.6)$$

where

$$\begin{aligned} \Delta r_i &= r_i - r_{i-1} & \text{and} & & \Delta r_{i+1} &= r_{i+1} - r_i, \\ \Delta \theta_j &= \theta_j - \theta_{j-1} & \text{and} & & \Delta \theta_{j+1} &= \theta_{j+1} - \theta_j, \\ \Delta \phi_k &= \phi_k - \phi_{k-1} & \text{and} & & \Delta \phi_{k+1} &= \phi_{k+1} - \phi_k. \end{aligned} \quad (4.7)$$

Since the ϕ -grid is always perfectly uniform, we have that $\Delta \phi_{k+1} = \Delta \phi_k$ for any k and hence, in expressions (4.3) and (4.4), we may set $\Delta \phi_{k+1/2} = \Delta \tilde{\phi}$.

It is important to remark that all of the above relations define the properties of the grid used in the non-axisymmetric calculations. In particular, in the spherically symmetric problem the role of a “cell” is played by concentric spherical shells, while in the axisymmetric case a computational cell is represented by a toroidal annulus around the symmetry axis. For these restricted symmetries the grid structure is a simplification of that used for the general non-axisymmetric calculations. Hence, the corresponding geometrical properties are directly recovered from relations (4.3) and (4.4).

In Tables 5 and 6, we summarize the relevant properties of the computational grid to be used in the 1- and 2-dimensional calculations, respectively. All quantities appearing in the relations are defined as in (4.5), (4.6), and (4.7).

TABLE 5

*Geometrical Properties of Mesh Shells for the
Spherically Symmetric Case*

<i>Property</i>		
<i>Volume</i>	V_i	$4\pi r_i^2 \Delta r_{i+1/2}$
<i>Interfaces</i>	$S_{i\pm 1/2}^r$	$4\pi r_{i\pm 1/2}^2$

TABLE 6

*Geometrical Properties of Mesh Cells for the
Axisymmetric Case*

<i>Property</i>		
<i>Volume</i>	V_{ij}	$2\pi r_i^2 \sin \theta_j \Delta r_{i+1/2} \Delta \theta_{j+1/2}$
<i>r - Interfaces</i>	$S_{i\pm 1/2, j}^r$	$2\pi r_{i\pm 1/2}^2 \sin \theta_j \Delta \theta_{j+1/2}$
<i>θ - Interfaces</i>	$S_{i, j\pm 1/2}^\theta$	$2\pi r_i \sin \theta_{j\pm 1/2} \Delta r_{i+1/2}$

4.3 Grid Motion Routine

The grid is initially allowed to follow the radial motion of the fluid by automatically rezoning all mesh-points at each computational cycle. The grid rezoning has been made dependent on the development of the internal hydrodynamic solution. Since the continuous increase of density in the central portions is the most significant feature of the gravitational collapse of protostellar clouds, the evolution of the central density may be taken as a suitable criterion for grid rezoning.

In Appendix C, Section C.1, we have derived finite-difference replacements, for a radially non-uniform grid, which approximate the radial portions of the Laplacian in equation (3.4) to second order accuracy if the following condition holds [90]

$$\Delta r_{i+1} = \xi \Delta r_i \quad (i = 1, 2, \dots, N_r), \quad (4.8)$$

where the stretch parameter ξ must always be of order unity for smooth variations of the radial spacings. The use of eq.(4.8) will give the desired new radial positions when the stretch parameter is specified.

In order to get an inward grid motion, ξ must be slightly greater than unity. Furthermore, the progressive contraction of the radial grid requires a gradual increase of ξ . In other words, if at some particular step n , $\xi^{(n)}$ decreases with respect to its earlier value $\xi^{(n-1)}$ at step $n-1$, then the grid will expand back and the accuracy of the entire hydrodynamical approximation will deteriorate. This effect may be observed from the leading truncation errors in sequences (6.32) and (6.33). If the grid velocity changes sign and inverts its direction with respect to the local fluid velocity, we obtain that $|U_{ijk}| > |v_{r_{ijk}}|$, so that the magnitudes of those truncation errors which are proportional to U_{ijk} , will inevitably increase. This technical difficulty, however, may easily

be avoided by delaying the motion of the grid by one step ($\xi^{(n)} = \xi^{(n-1)}$) whenever $\xi^{(n)} < \xi^{(n-1)}$.

For 1-dimensional calculations, a feasible way of computing the stretch parameter is to follow the increase of the central density ρ_c at each cycle. This is done by defining at a particular step n

$$\xi^{(n)} = \rho_c^n / \rho_c^{n-1}. \quad (4.9)$$

This relation ensures a progressive increase of ξ during the main infall phases of collapse. Since the variation per step of the central cell density is usually small for small Δt , ξ will be always of order of unity. However, experience with 2-dimensional calculations indicates that the use of prescription (4.9), is not sufficient to guarantee a satisfactory contraction of the grid. For this reason, we have adopted a version of the method originally implemented by Larson [61] and Black and Bodenheimer [3], and used by Boss [13].

For convenience in solving the Poisson equation [see Chapter 5, Section 5.3], the radial grid is chosen such that Δr_1 is always equal to Δr_2 . Consequently, equation (4.8) must be re-defined as

$$\begin{aligned} \Delta r_2 &= \Delta r_1, \\ \Delta r_{i+1} &= \xi \Delta r_i \quad (i = 2, 3, \dots, N_{r-1}). \end{aligned} \quad (4.10)$$

Straightforward algebra then yields

$$\begin{aligned} r_2 &= 2r_1, \\ r_3 &= (2 + \xi)r_1, \\ r_4 &= (2 + \xi + \xi^2)r_1, \\ &\vdots \end{aligned}$$

$$\begin{aligned}
& \vdots \\
& \vdots \\
r_{N_r} &= (2 + \xi + \xi^2 + \xi^3 + \xi^4 + \dots + \xi^{N_r-2})r_1,
\end{aligned} \tag{4.11}$$

where all radial grid positions are defined in terms of the distance r_1 between the centre ($r = 0$) and the first radial mesh-point. The use of the constant-volume boundary condition imposes $r_{N_r} = R_0$, in the last relation of (4.11). Furthermore, if we define $\tilde{r}_1 = r_1/R_0$, this relation can be manipulated to give

$$\left[1 + \left\{ 1 + \xi + \xi^2 + \xi^3 + \xi^4 + \dots + \xi^{N_r-2} \right\} \right] \tilde{r}_1 = 1, \tag{4.12}$$

which is equivalent to

$$\left[1 + \left(\frac{1 - \xi^{N_r-1}}{1 - \xi} \right) \right] \tilde{r}_1 = 1. \tag{4.13}$$

Since $\xi > 1$, we may write $\xi = 1 + \eta$, where η is generally a small number in the range $0 \leq \eta < 1$. So equation (4.13) becomes

$$\tilde{r}_1(1 + \eta)^{N_r-1} - \eta(1 - \tilde{r}_1) - \tilde{r}_1 = 0. \tag{4.14}$$

This non-linear equation, for known values of N_r and \tilde{r}_1 , is efficiently solved for η by means of a rapidly convergent, fifth-order Newton iteration scheme [30,43]. The use of such a high order scheme is necessary because of the rather poor convergence exhibited by the non-linear equation (4.14). The value of \tilde{r}_1 for the solution of this equation, is easily determined at each time step by constraining the innermost grid-points to follow the fluid motion as closely as possible. In spherically symmetric flows, this may be done by requiring that the mesh-point r_1 should move in a strictly Lagrangian sense. Thus, at step $n + 1$, we have

$$r_1^{n+1} = r_1^n + \Delta t v_{r_1}^n, \tag{4.15}$$

where $v_{r_1}^n$ is the local fluid velocity at $r = r_1$ and step n .

For 2- and 3-dimensional calculations, eq.(4.15) is no longer valid. In these cases, the collapse of the inner regions will not necessarily proceed in a spherically symmetric manner. In order to avoid a progressive distortion of the grid, equation (4.15) for non-axisymmetric flows is modified as

$$r_{1jk}^{n+1} = r_{1jk}^n + \Delta t \langle v_{r_1} \rangle^n, \quad (4.16)$$

where $\langle v_{r_1} \rangle^n$ is an arithmetic average of the local fluid velocities $v_{r_{1jk}}^n$ in the innermost cells, i.e.

$$\langle v_{r_1} \rangle^n = \frac{\left(v_{r_1}^n + \sum_{k=1}^{N_\phi} \sum_{j=1}^{N_\theta} v_{r_{1jk}}^n \right)}{1 + N_\theta N_\phi}, \quad (4.17)$$

$v_{r_1}^n$ being the axial fluid velocity at $r = r_1$. For axisymmetric flows, the counterpart of equation (4.16) is obtained by removing the index k and by averaging only in the θ -direction.

In this manner, the motion of the grid is fully determined from ξ and r_1^{n+1} by using the relations (4.11) for the new positions r_i^{n+1} .

4.4 Grid Velocity

The grid velocity $\mathbf{v}_g = (v_g, 0, 0)$ is computed from the old and new positions. It is interpreted as the time rate of change of the radial grid-points. A suitable approximation for the grid velocity $v_{g,i}$, is obtained by expanding r_i at the new time level $(n+1)$ in a Taylor series about its corresponding value at the old time level (n) , that is

$$r_i^{n+1} = r_i^n + \left(\frac{\partial r}{\partial t} \right)_i^n \Delta t + \frac{1}{2} \left(\frac{\partial^2 r}{\partial t^2} \right)_i^n \Delta t^2 + \dots$$

Then, defining $v_{g_i} = (\partial r / \partial t)_i$ and neglecting all terms of order higher than one, we obtain

$$v_{g_i}^n \approx \frac{r_i^{n+1} - r_i^n}{\Delta t} + O\{\Delta t\} \quad (i = 1, 2, \dots, N_r - 1). \quad (4.18)$$

From equation (4.18) it follows that $v_g = 0$ for $i = 0$ (centre) and for $i = N_r$ (external boundary). The grid interface velocities $v_{g_{i \pm 1/2, jk}} = v_{g_{i \pm 1/2}}$ are calculated as simple averages, i.e.

$$v_{g_{i \pm 1/2}} = \frac{1}{2} (v_{g_{i \pm 1}} + v_{g_i}) \quad , \quad (4.19)$$

so that, the velocity of the innermost interfaces $(1 - 1/2, jk)$ is given by $v_{g_{1-1/2}} = \frac{1}{2} v_{g_1}$, and similarly, that of the outermost interfaces $(N_r - 1/2, jk)$ is given by $v_{g_{N_r-1/2}} = \frac{1}{2} v_{g_{N_r-1}}$.

Chapter 5

Poisson Solver

This chapter is devoted to describing the numerical algorithm used for solving the Poisson equation (3.4). Since the procedure used to solve this equation in 1- or 2-space dimensions, is a particular case of the full 3-dimensional treatment, we shall refer here only to the latter. However, due to its usefulness in many interesting situations, we give details of the 2-dimensional Poisson solver in Appendix A.

5.1 Solution Method

The Poisson equation (3.25) in 3-space dimensions is solved by separation of variables. This is done by expanding the gravitational potential Φ and the density ρ in terms of the spherical harmonics $Y_{lm}(\theta, \phi)$

$$\begin{aligned}\Phi(r, \theta, \phi) &= \sum_{l=0}^{\infty} \sum_{m=-l}^l \Phi_{lm}(r) Y_{lm}(\theta, \phi), \\ \rho(r, \theta, \phi) &= \sum_{l=0}^{\infty} \sum_{m=-l}^l \rho_{lm}(r) Y_{lm}(\theta, \phi).\end{aligned}\tag{5.1}$$

Substitution of the spherical harmonic expansions (5.1) into eq.(3.25) leads to the form

$$\begin{aligned}& \frac{1}{\Phi_{lm}(r)} \frac{\partial}{\partial r} \left(r^2 \frac{\partial \Phi_{lm}(r)}{\partial r} \right) + \frac{1}{Y_{lm}(\theta, \phi)} \times \\ & \times \left\{ \frac{1}{\sin \theta} \frac{\partial}{\partial \theta} \left(\sin \theta \frac{\partial}{\partial \theta} \right) + \frac{1}{\sin^2 \theta} \frac{\partial^2}{\partial \phi^2} \right\} Y_{lm}(\theta, \phi) = 4\pi G \frac{r^2 \rho_{lm}(r)}{\Phi_{lm}(r)},\end{aligned}\tag{5.2}$$

which holds for any permitted values of the pair (l, m) . The angular operator acting on $Y_{lm}(\theta, \phi)$, on the left-hand side of equation (5.2), is the well-known Legendre operator \mathbf{L}^2 , which satisfies the eigenvalue equation

$$\mathbf{L}^2 Y_{lm}(\theta, \phi) = l(l+1) Y_{lm}(\theta, \phi), \quad (5.3)$$

for integer values of l . Hence, using equation (5.3) in eq.(5.2), we finally obtain the simplified form

$$\frac{d^2 \Phi_{lm}(r)}{dr^2} + \frac{2}{r} \frac{d\Phi_{lm}(r)}{dr} - \frac{l(l+1)}{r^2} \Phi_{lm}(r) = 4\pi G \rho_{lm}(r). \quad (5.4)$$

Equation (5.4) is a linear, second-order, ordinary differential equation defining the potential coefficients needed in the spherical harmonic expansion for $\Phi(r, \theta, \phi)$. Hence, the 3-dimensional Poisson problem reduces to solving, for any permitted combination of the integers l and m , a set of equations similar to the one-dimensional equation (5.4).

The density coefficients $\rho_{lm}(r)$ are calculated by using the orthogonality condition for the spherical harmonics, and can be expressed in the form

$$\rho_{lm}(r) = \int_0^{2\pi} d\phi \int_0^\pi \rho(r, \theta, \phi) Y_{lm}^*(\theta, \phi) \sin \theta d\theta, \quad (5.5)$$

where, according to the conventional definition of the spherical harmonics

$$Y_{lm}^*(\theta, \phi) = \sqrt{\frac{2l+1}{4\pi} \frac{(l-m)!}{(l+m)!}} P_l^m(\cos \theta) e^{-im\phi}, \quad (5.6)$$

$P_l^m(\cos \theta)$ being the associated Legendre functions. Defining the constants

$$C_l^m = \sqrt{\frac{2l+1}{4\pi} \frac{(l-m)!}{(l+m)!}}, \quad (5.7)$$

equation (5.5) may be re-written in the more explicit form

$$\rho_{lm}(r) = C_l^m \int_0^{2\pi} e^{-im\phi} d\phi \int_0^\pi \rho(r, \theta, \phi) P_l^m(\cos \theta) \sin \theta d\theta, \quad (5.8)$$

for any integers $l \geq 0$ and $-l \leq m \leq +l$.

To solve equation (5.4) one needs to specify boundary conditions for the gravitational potential. Since we are mainly interested in the collapse of completely isolated protostellar clouds so that there is no hydrodynamical transport of mass across the external boundary surface, the obvious assumption to make is that there are no masses outside the fixed volume enclosing the collapsing system which contribute to the gravitational potential. Therefore, for any $r > R_0$, we set $\rho(r, \theta, \phi) = 0$, or equivalently, from equation (5.5), $\rho_{lm}(r) = 0$. This constraint together with the requirement that the gravitational potential $\Phi(r, \theta, \phi)$, as well as its first derivatives, remains finite as $r \rightarrow \infty$, constitute outer boundary conditions on $\Phi_{lm}(r)$. If we then put $\rho_{lm}(r) = 0$ in equation (5.4) and solve for $\Phi_{lm}(r)$, we obtain only one solution for all coefficients, with $l \neq 0$ and $m \neq 0$, which remains finite as $r \rightarrow \infty$:

$$\Phi_{lm}(r) \propto r^{-(l+1)}, \quad (5.9)$$

for any $r \geq R_0$. Differentiating (5.9) once, we may write at the external surface $r = R_0$

$$\left[\frac{d\Phi_{lm}(r)}{dr} \right]_{r=R_0} + \left[\frac{(l+1)}{r} \Phi_{lm}(r) \right]_{r=R_0} = 0. \quad (5.10)$$

Equation (5.10) defines a mixed boundary condition on $\Phi_{lm}(r)$ at the surface of the spherical cloud. However, the level of Φ is arbitrary in the sense that equation (5.10) holds for any exterior point and hence, it could be expressed at any radius completely outside the physical cloud configuration.

At the centre of the collapsing protostar, the gravitational potential and its first derivatives must be continuous functions. This is the only requirement that is necessary in order to specify the inner boundary condition. On the other hand, the addition of a boundary condition expressing reflection symmetry about the equatorial plane

simplifies the calculations, since only the $l+m$ even terms will be needed in the spherical harmonic expansions (5.1). This fact implies that the number of differential equations, of the form of eq.(5.4) for the $\Phi_{lm}(r)$, is consequently reduced.

In the 3-dimensional problem, it is also necessary to enforce a periodic boundary condition for the ϕ variable. Its specification is superfluous, since it is implicit in the expansions (5.1) for $\Phi(r, \theta, \phi)$ and $\rho(r, \theta, \phi)$.

The foregoing standard analytical procedure has reduced the problem of solving the complicated partial differential equation (3.25) to a classical ordinary-value problem involving a derivative boundary condition.

The first step in our numerical approach to equation (5.4), is to approximate the double integral in equation (5.8) with the help of appropriate mechanical quadratures.

5.2 Determination of the Density Coefficients

Equation (5.8) can be written as

$$\rho_{lm}(r) = C_l^m \int_0^{2\pi} e^{-im\phi} d\phi \int_{-1}^{+1} \rho(r, x, \phi) P_l^m(x) dx, \quad (5.11)$$

where the limits of integration $(0, 2\pi)$ have been normalized to $(-1, +1)$ by effecting the change of variable $x = \cos \theta$. The integral

$$\int_{-1}^{+1} \rho(r, x, \phi) P_l^m(x) dx \quad (5.12)$$

may be regarded as the inner product of two functions over the interval $[-1, +1]$ with respect to a weight function $\omega(x) = 1$. If we then take this product as a single function, the integral (5.12) can be conveniently evaluated with a Gauss integration rule [57], which consists of replacing (5.12) with a weighted sum of discrete values of the product

$\rho(r, a_j, \phi)P_l^m(a_j)$, namely

$$\int_{-1}^{+1} \rho(r, x, \phi)P_l^m(x)dx = \sum_{j=1}^N H_j \rho(r, a_j, \phi)P_l^m(a_j), \quad (5.13)$$

where the abscissae a_j must be suitably distributed between the limits of integration. The full determination of the N-point Gauss quadrature (5.13) will consist of finding the set of discrete abscissae a_j and their corresponding weight coefficients H_j , which make eq.(5.13) exact provided that the degree of the polynomial approximating the function $F(x) = \rho(r, x, \phi)P_l^m(x)$, does not exceed $2N - 1$.

In our case, the abscissae a_j are chosen as the roots of the Legendre polynomial $P_N(x)$. This is justified because the Legendre polynomials form a family of orthogonal functions with respect to the weight $\omega(x) = 1$ within the interval $[-1, +1]$, and satisfy the orthogonality condition

$$\int_{-1}^{+1} P_l(x)P_{l'}(x)dx = \frac{2}{2l+1}\delta_{ll'}, \quad (5.14)$$

where $\delta_{ll'} = 1$ if $l \neq l'$ and 0 otherwise. In this way, the abscissae a_j will be distinct, real, and located in the interior of the interval $[-1, +1]$, as required for a Gaussian quadrature. Also, these properties will guarantee the positivity of the weight coefficients H_j , which is crucial in keeping down round-off errors.

When the product $F(x) = \rho(r, x, \phi)P_l^m(x)$ is not a polynomial of degree less than $2N$, the use of approximation (5.13) introduces an error. Following Kopal [57], this error is given by

$$\varepsilon_N = \frac{2^{2N+1}(N!)^4}{(2N+1)[(2N)!]^3} F^{(2N)}(\xi) \quad -1 < \xi < 1. \quad (5.15)$$

The magnitude of ε_N becomes smaller, the smaller the value of $F^{(2N)}(\xi)$ and the larger the value of N . However, a precise estimate of ε_N is made difficult by the usual uncertainty in evaluating $F^{(2N)}(\xi)$.

Denoting the zeros of the Legendre polynomial of degree N , $P_N(x)$, by a_1, a_2, \dots, a_N , the N weight coefficients H_j may be expressed as explicit functions of the roots by the relation [30]

$$H_j = \frac{2}{(1 - a_j^2)[P'_N(a_j)]^2} \quad \text{for } j = 1, 2, \dots, N, \quad (5.16)$$

where $P'_N(a_j)$ denotes the first derivative of $P_N(a_j)$. Inserting (5.16) into eq.(5.13), we get

$$\int_{-1}^{+1} \rho(r, x, \phi) P_l^m(x) dx \simeq 2 \sum_{j=1}^N \frac{\rho(r, a_j, \phi) P_l^m(a_j)}{(1 - a_j^2)[P'_N(a_j)]^2}, \quad (5.17)$$

which defines an N -point Gauss-Legendre quadrature formula for the definite integral (5.12).

It can be seen, from equation (5.11), that the approximation (5.17) implies that the density of the axial cells will not influence the coefficients $\rho_{lm}(r)$ and hence the gravitational potential of the main grid-cells. This is due to the fact that the Gauss-Legendre quadrature (5.17) is of the open type, i.e. its marginal abscissae a_1 and a_N do not coincide with the limits of integration. Therefore, the axial points $\theta = 0$ ($x = +1$) and $\theta = \pi$ ($x = -1$) are excluded from the summation. The polar location of the main grid-points [See Figure 4.1(a)] will be determined by the relation $a_j = \cos \theta_j$.

Owing to the symmetry of the Legendre polynomials about $\theta = \pi/2$ ($x = 0$), their non-zero roots will occur in pairs $\pm a_j$, and their weight coefficients will obey the symmetry relation $H_j = H_{N-j+1}$. In this way, the zero abscissa denoting the equator will have $j = (N + 1)/2$, for a particular odd value of N . The number $(N + 1)/2$ gives exactly the number of cells N_θ (along the θ -direction) filling the top hemisphere of the spherical volume. From the above considerations and from the condition of reflection symmetry about the equatorial plane (which implies that $\rho(r, a_j, \phi) = \rho(r, -a_j, \phi)$ for

any j) the calculation of the summation in eq.(5.17) is simplified by setting

$$\int_{-1}^{+1} \rho(r, x, \phi) P_l^m(x) dx \simeq \sum_{j=1}^{(N+1)/2} H'_j \rho(r, a_j, \phi) P_l^m(a_j), \quad (5.18)$$

for $a_j \geq 0$ since $P_l^m(a_j) = P_l^m(-a_j)$ when $l + m$ is even. The new weights H'_j are related to the old ones (defined in (5.16)) by

$$\begin{aligned} H'_j &= 2H_j & \text{for } j = 1, 2, \dots, (N-1)/2, \\ H'_j &= H_j & \text{for } j = (N+1)/2 \end{aligned} \quad (5.19)$$

so that

$$\sum_{j=1}^N H_j = \sum_{j=1}^{(N+1)/2} H'_j = 2. \quad (5.20)$$

Here we are interested in solving equation (5.18) for $N_\theta = (N+1)/2 = 11$. We have adopted the method given by Davis and Rabinowitz [30] (based on a Newton-Raphson iteration scheme) for computing the roots of the Legendre polynomial $P_{21}(x)$, due to the almost complete lack of tabulated values for this case. In Appendix B, we give the root-finding algorithm implemented, as well as the results for the non-negative abscissae and the corresponding weights of the 21-point Gauss-Legendre quadrature formula.

Substitution of eq.(5.18) into eq.(5.11) leads to the semi-analytical expression

$$\rho_{lm}(r) \simeq C_l^m \sum_{j=1}^{N_\theta} H'_j P_l^m(a_j) \int_0^{2\pi} e^{-im\phi} \rho(r, a_j, \phi) d\phi, \quad (5.21)$$

which may be separated into its real and imaginary parts

$$\Re[\rho_{lm}(r)] = C_l^m \sum_{j=1}^{N_\theta} H'_j P_l^m(a_j) \int_0^{2\pi} \rho(r, a_j, \phi) \cos(m\phi) d\phi, \quad (5.22)$$

$$\Im[\rho_{lm}(r)] = -C_l^m \sum_{j=1}^{N_\theta} H'_j P_l^m(a_j) \int_0^{2\pi} \rho(r, a_j, \phi) \sin(m\phi) d\phi. \quad (5.23)$$

The integrals in equations (5.22) and (5.23) are of the form of the finite integrals involved in the calculation of Fourier cosine and sine transforms. They can be approximated using Filon's method for finite Fourier integrals [30,57], provided that the values of the integer m are small. Otherwise, the rapid oscillations of the periodic functions $\cos(m\phi)$ and $\sin(m\phi)$ will affect the accuracy of the approximation, unless the interval of integration is subdivided into very small steps which, however, would render the calculation prohibitive.

Following Davis and Rabinowitz [30] and Kopal [57], if we divide the ϕ -grid into an even number (say, $2n$) of discrete, equally spaced intervals $\Delta\tilde{\phi}$, we have that

$$\int_0^{2\pi} \rho(r, a_j, \phi) \cos(m\phi) d\phi \approx \Delta\tilde{\phi} \{ \beta(\lambda) C_{2n} + \gamma(\lambda) C_{2n-1} \}, \quad (5.24)$$

and

$$\int_0^{2\pi} \rho(r, a_j, \phi) \sin(m\phi) d\phi \approx \Delta\tilde{\phi} \{ \beta(\lambda) S_{2n} + \gamma(\lambda) S_{2n-1} \}, \quad (5.25)$$

respectively, where $N_\phi = 2n$, $\Delta\tilde{\phi} = 2\pi/N_\phi$, and $\lambda = m\Delta\tilde{\phi}$. The functions β and γ are the Filon coefficients given by

$$\begin{aligned} \beta(\lambda) &= 2\{\lambda(1 + \cos^2 \lambda) - 2 \sin \lambda \cos \lambda\} / \lambda^3, \\ \gamma(\lambda) &= 4\{\sin \lambda - \lambda \cos \lambda\} / \lambda^3. \end{aligned} \quad (5.26)$$

The quantities C_{2n} and C_{2n-1} are sums formed from $\rho(r, a_j, \phi) \cos(m\phi)$ and defined as

$$\begin{aligned} C_{2n} &= -\frac{1}{2}[\rho(r, a_j, 0) + \rho(r, a_j, 2\pi)] + \sum_{k=0}^n \rho(r, a_j, 2\Delta\tilde{\phi}k) \cos(2m\Delta\tilde{\phi}k), \\ C_{2n-1} &= \sum_{k=1}^n \rho(r, a_j, 2\Delta\tilde{\phi}k - \Delta\tilde{\phi}) \cos(2m\Delta\tilde{\phi}k - m\Delta\tilde{\phi}), \end{aligned} \quad (5.27)$$

while S_{2n} and S_{2n-1} are sums formed from the terms $\rho(r, a_j, \phi) \sin(m\phi)$ and given by

$$S_{2n} = \sum_{k=0}^n \rho(r, a_j, 2\Delta\tilde{\phi}k) \sin(2m\Delta\tilde{\phi}k),$$

$$S_{2n-1} = \sum_{k=1}^n \rho(r, a_j, 2\Delta\tilde{\phi}k - \Delta\tilde{\phi}) \sin(2m\Delta\tilde{\phi}k - m\Delta\tilde{\phi}). \quad (5.28)$$

It can be seen that for $m = 0$, the Filon coefficients (5.26) become indeterminate. In this case, the problem of evaluating these coefficients at the singularity $\lambda = 0$ is solved by expanding (5.26) in a Taylor series [57]. The following expansions are obtained

$$\begin{aligned} \beta(\lambda) &\approx \frac{2}{3} + \frac{2}{15}\lambda^2 - \frac{4}{105}\lambda^4 + \frac{2}{567}\lambda^6 + \dots, \\ \gamma(\lambda) &\approx \frac{4}{3} - \frac{2}{15}\lambda^2 + \frac{1}{210}\lambda^4 - \frac{1}{11340}\lambda^6 + \dots, \end{aligned} \quad (5.29)$$

so that $\beta(0) = 2/3$ and $\gamma(0) = 4/3$. The forms (5.29) are also suitable for small values of $\lambda (\leq 1/6 \sim 0.1666\dots)$ [30].

In contrast to the Gauss-Legendre quadratures, Filon's formulae are of the closed type, that is, the limits of integration are included in the evaluation of the integrands. The abscissae, on the other hand, are all pre-assigned with the requirement that they must be uniformly distributed along the integration range. Following Kopal [57], the error introduced by using the approximations (5.24) and (5.25) is shown to be of the order

$$\varepsilon_F \sim \frac{2\pi}{12} \Delta\tilde{\phi}^3 \left\{ 1 - \frac{1}{16} \sec\left(\frac{\lambda}{4}\right) \right\} \sin\left(\frac{\lambda}{2}\right) \rho^{IV}(r, a_j, \xi), \quad (5.30)$$

for $0 \leq \xi \leq 2\pi$. It is generally recommended that one should keep the parameter λ smaller than unity. Then, taking $N_\phi = 16$ for the full 2π radians, we have a uniform angular spacing of $\Delta\tilde{\phi} = \pi/8$ rad. This resolution leads to $\lambda < 1$ when $m \leq 2$. However, in order to accurately evaluate the gravitational potential, it is necessary to include terms in the spherical harmonic expansions at least with $l \leq 6$, so that $-6 \leq m \leq 6$. Hence, values of $m > 2$ (leading to $\lambda > 1$) will occur in the Filon quadrature formulae (5.24) and (5.25). The use of eq.(5.30) with $N_\phi = 16$ gives errors of $\sim 10^{-2} \rho^{IV}(r, a_j, \xi)$ for values of the integer m as high as $m = 6$. A crude estimate

of $\rho^{IV}(r, a_j, \xi)$ can be made by taking for each radius r , an average of $\rho(r, a_j, \phi_k)$ over θ and ϕ . By considering such estimates, we have satisfied ourselves that $\rho^{IV}(r, a_j, \xi)$ will always be small enough to keep reasonable accuracy, even when high values of m are included.

Inserting the approximations (5.24) and (5.25) into equations (5.22) and (5.23), respectively, the density coefficients are finally determined by

$$\begin{aligned} \rho_{lm}(r) \approx & C_l^m \sum_{j=1}^{N_\theta} H_j' P_l^m(a_j) \left\{ \Delta\tilde{\phi} [\beta(\lambda)C_{2n} + \gamma(\lambda)C_{2n-1}] \right\} - \\ & - iC_l^m \sum_{j=1}^{N_\theta} H_j' P_l^m(a_j) \left\{ \Delta\tilde{\phi} [\beta(\lambda)S_{2n} + \gamma(\lambda)S_{2n-1}] \right\}. \end{aligned} \quad (5.31)$$

By virtue of equation (5.31), the gravitational potential coefficients will also be complex functions of the form

$$\Phi_{lm}(r) = \Re[\Phi_{lm}(r)] + i\Im[\Phi_{lm}(r)]. \quad (5.32)$$

Consequently, equation (5.4) splits into two linear second-order differential equations for the real and imaginary parts of the potential coefficients.

5.3 Calculation of the Potential Coefficients

The potential coefficients $\Phi_{lm}(r)$ are numerically computed by replacing the exact differential equation (5.4) by a set of approximate finite-difference equations. In order to do so we first consider, for particular values of θ and ϕ , a radial distribution of cells as shown in Figure 3.1.

The radial grid-points are labeled $i = 1, 2, \dots, N_{r-1}, N_r$, and the value of r at the i th point is denoted by r_i . The intervals between the radial points, denoted by Δr_i and Δr_{i+1} , as well as the grid spacings $\Delta r_{i+1/2}$, are defined in Chapter 4, Section 4.2. The

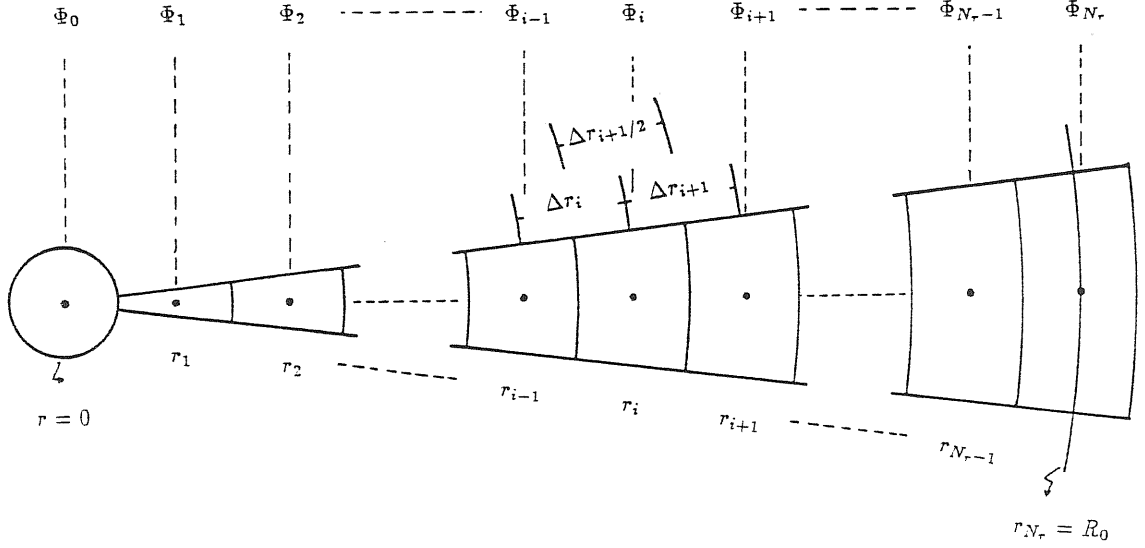


Figure 5.1: Radial distribution of main grid-cells for discretization of the simplified Poisson equation.

first step in our discretization procedure consists of evaluating equation (5.4) at each point r_i in the computational domain $r_1 \leq r \leq r_{N_r} = R_0$. We write, in index notation,

$$\left\{ \frac{d^2 \Phi^{R,I}}{dr^2} \right\}_i + \frac{2}{r_i} \left\{ \frac{d\Phi^{R,I}}{dr} \right\}_i - \frac{l(l+1)}{r_i^2} \Phi_i^{R,I} = 4\pi G \rho_i^{R,I}, \quad (5.33)$$

for $(i = 1, 2, \dots, N_r)$. The superscripts R and I will be used to denote the real and imaginary parts of the potential and density coefficients. Furthermore, in equation (5.33), we have adopted the following definitions

$$\Phi_{lm}(r_i) = \Phi_i, \quad \rho_{lm}(r_i) = \rho_i,$$

for the functions evaluated at a particular point r_i . The subscripts l and m have been omitted for simplicity, although it is implicit that the density and potential coefficients are always characterized by the triplet (l, m, i) .

Secondly, we evaluate the first and second derivatives in equation (5.33) by using appropriate finite-differences. As we have commented in Chapter 4, the radial grid structure varies with time, becoming more and more stretched as the calculation proceeds. This means that after an evolutionary time \tilde{t} , the radial points are no longer centred as they were at the beginning of the calculation, when the grid was perfectly uniform. This apparent disadvantage is greatly compensated by the fact that a progressive reduction of the grid size (in the inner regions), decreases the amount of computer memory and time required to obtain improved solutions (over the same regions), as compared with the case of using a small mesh size everywhere.

In Appendix C, Section C.1, we have deduced three-point finite-difference formulae, which are particularly suitable for problems dealing with a variable grid structure. Such formulae are usually referred to as partially centered replacements. They may be written as

$$\left\{ \frac{d\Phi}{dr} \right\}_i \approx \frac{1}{2\Delta r_{i+1/2}} \left[\frac{\Delta r_i}{\Delta r_{i+1}} (\Phi_{i+1} - \Phi_i) + \frac{\Delta r_{i+1}}{\Delta r_i} (\Phi_i - \Phi_{i-1}) \right] + O\{(\Delta r_i)^2\}, \quad (5.34)$$

$$\left\{ \frac{d^2\Phi}{dr^2} \right\}_i \approx \frac{1}{\Delta r_{i+1/2}} \left[\frac{(\Phi_{i+1} - \Phi_i)}{\Delta r_{i+1}} - \frac{(\Phi_i - \Phi_{i-1})}{\Delta r_i} \right] + O\{(\Delta r_i)\}, \quad (5.35)$$

according to our notation. If the radial grid varies smoothly, it is always possible to match the truncation error of the replacement (5.34), for the first derivative, with that of (5.35), for the second derivative, in order to approximate the left-hand side of eq.(5.35) to second-order accuracy [See Appendix C, Section C.1]. Consequently, the discretization of equation (5.33) based upon approximations (5.34) and (5.35), is nearly second-order accurate.

Inserting the replacements (5.34) and (5.35) into equation (5.33) and grouping similar terms, we obtain the finite-difference form (at a particular point r_i) of the exact

differential equation (5.4)

$$\begin{aligned}
& \frac{1}{\Delta r_{i+1/2} \Delta r_i} \left(1 - \frac{\Delta r_{i+1}}{r_i} \right) \Phi_{i-1}^{R,I} - \\
& - \left\{ \frac{1}{\Delta r_{i+1/2} \Delta r_i} \left(1 - \frac{\Delta r_{i+1}}{r_i} \right) + \frac{1}{\Delta r_{i+1/2} \Delta r_{i+1}} \left(1 + \frac{\Delta r_i}{r_i} \right) + \frac{l(l+1)}{r_i^2} \right\} \Phi_i^{R,I} + \\
& + \frac{1}{\Delta r_{i+1/2} \Delta r_{i+1}} \left(1 + \frac{\Delta r_i}{r_i} \right) \Phi_{i+1}^{R,I} = 4\pi G \rho_i^{R,I}. \tag{5.36}
\end{aligned}$$

Equation (5.36) can be written in the more convenient form

$$C_{i1} \Phi_{i-1}^{R,I} + C_{i2} \Phi_i^{R,I} + C_{i3} \Phi_{i+1}^{R,I} = C_{i4}^{R,I}, \tag{5.37}$$

where

$$\begin{aligned}
C_{i1} &= \left(1 - \frac{\Delta r_{i+1}}{r_i} \right) / \Delta r_{i+1/2} \Delta r_i, \\
C_{i3} &= \left(1 + \frac{\Delta r_i}{r_i} \right) / \Delta r_{i+1/2} \Delta r_{i+1}, \\
C_{i2} &= -C_{i1} - C_{i3} - \frac{l(l+1)}{r_i^2}, \\
C_{i4}^{R,I} &= 4\pi G \rho_i^{R,I}. \tag{5.38}
\end{aligned}$$

The coefficients C_{i1} , C_{i2} , and C_{i3} are known constants for any interior point of the computational domain, while $C_{i4}^{R,I}$ is determined by the local values of the density coefficients. Equation (5.37), for $i = 1, 2, \dots, N_r - 1$, defines two sets of $N_r - 1$ linear algebraic equations, which have to be solved simultaneously for the $2N_r - 2$ unknowns Φ_i^R and Φ_i^I . Special care must be taken when extreme values of the index i are assigned in equation (5.37). For $i = 1$, we have

$$C_{11} \Phi_0^{R,I} + C_{12} \Phi_1^{R,I} + C_{13} \Phi_2^{R,I} = C_{14}^{R,I},$$

where $\Phi_0 = \Phi_0^R + i\Phi_0^I$ denotes the value of the potential coefficient at the centre of the cloud [See Figure 3.1]. An explicit boundary condition for the centre is completely unnecessary and the effort of evaluating $\Phi_0^{R,I}$ may easily be avoided. Without introducing

any approximation, if we choose the non-uniform radial grid such that Δr_1 is always equal to Δr_2 , then the coefficient C_{11} vanishes and the above sets of linear equations become independent of the central potential. Hence, for $i = 1$, we may write

$$C_{12}\Phi_1^{R,I} + C_{13}\Phi_2^{R,I} = C_{14}^{R,I}, \quad (5.39)$$

where the relation between $\Phi_1^{R,I}$ and $\Phi_2^{R,I}$ serves as an inner boundary condition [104].

On the other hand, when $i = N_r - 1$, we get

$$C_{N_r-1,1}\Phi_{N_r-2}^{R,I} + C_{N_r-1,2}\Phi_{N_r-1}^{R,I} + C_{N_r-1,3}\Phi_{N_r}^{R,I} = C_{N_r-1,4}^{R,I},$$

where we need to specify the boundary potential coefficients in order to close the system. This is done by using the external boundary equation (5.10), which may be set in the finite-difference form

$$\begin{aligned} \frac{1}{2\Delta r_{N_r+1/2}} \left[\frac{\Delta r_{N_r}}{\Delta r_{N_r-1}} (\Phi_{N_r+1}^{R,I} - \Phi_{N_r}^{R,I}) + \frac{\Delta r_{N_r+1}}{\Delta r_{N_r}} (\Phi_{N_r}^{R,I} - \Phi_{N_r-1}^{R,I}) \right] + \\ + \frac{(l+1)}{r_{N_r}} \Phi_{N_r}^{R,I} = 0, \end{aligned} \quad (5.40)$$

by again using the replacement (5.34). Due to the three-point approximation nature of the partially centered formulae, the evaluation of the first derivative at the cloud boundary introduces information about the fictitious point r_{N_r+1} , which is outside the computational domain. However, we can eliminate $\Phi_{N_r+1}^{R,I}$ by simply combining equation (5.40) with equation (5.36) evaluated at the boundary ($r = r_{N_r}$). After some rather cumbersome algebra, we finally obtain the relation

$$\Phi_{N_r}^{R,I} = \frac{\Phi_{N_r-1}^{R,I} - 2\pi G \Delta r_{N_r}^2 \rho_{N_r}^{R,I}}{\left\{ 1 + \frac{(l+1)\Delta r_{N_r} \left[r_{N_r} + \frac{1}{2}(l+2)\Delta r_{N_r} \right]}{r_{N_r}^2} \right\}}, \quad (5.41)$$

which is, however, free of any dependence on the fictitious coordinate r_{N_r+1} . The use of this relation in equation (5.37), for $i = N_r - 1$, leads to the following equation

$$C_{N_r-1,1}\Phi_{N_r-2}^{R,I} + \tilde{C}_{N_r-1,2}\Phi_{N_r-1}^{R,I} = \tilde{C}_{N_r-1}^{R,I}, \quad (5.42)$$

where

$$\begin{aligned}
\tilde{C}_{N_r-1,2} &= C_{N_r-1,2} + \left\{ 1 + \frac{(l+1)\Delta r_{N_r} \left[r_{N_r} + \frac{1}{2}(l+2)\Delta r_{N_r} \right]}{r_{N_r}^2} \right\}^{-1} C_{N_r-1,3}, \\
\tilde{C}_{N_r-1,4}^{R,I} &= C_{N_r-1,4}^{R,I} + \\
&+ 2\pi G \Delta r_{N_r}^2 \rho_{N_r}^{R,I} \left\{ 1 + \frac{(l+1)\Delta r_{N_r} \left[r_{N_r} + \frac{1}{2}(l+2)\Delta r_{N_r} \right]}{r_{N_r}^2} \right\}^{-1} C_{N_r-1,3}. \quad (5.43)
\end{aligned}$$

The set of equations (5.39), (5.42), and (5.37) for the remaining $N_r - 3$ points, are $2N_r - 2$ simultaneous linear equations for the $2N_r - 2$ unknowns Φ_i^R and Φ_i^I . This set of equations can be consistently solved by applying the tridiagonal matrix algorithm method [See, for example, C. Chuen-Yen [25]].

Since we are concerned with protostellar configurations with radii of the order of $10^{17} - 10^{18} \text{cm}$, for a discrete number of radial points, we are compelled to work with relatively large Δr . From the definitions (5.38), the coefficients C_{i1} , C_{i2} , and C_{i3} (being proportional to Δr^{-2}) will generally be very small for large values of Δr . Such small values will introduce underflow computing problems in the tridiagonal operating routine. This is because the tridiagonal elimination scheme involves an increasing number of products of these small coefficients, which then yield prohibitively small numbers as the calculation proceeds. In order to circumvent this difficulty, we normalize all of the coefficients, in each equation, by dividing through by the first one appearing in the equation. In this way the set of linear equations (5.39), (5.42), and (5.37) may be written in the more convenient form

$$\begin{aligned}
\Phi_1^{R,I} + S_{13}\Phi_2^{R,I} &= S_{14}^{R,I} & (i=1), \\
\Phi_{i-1}^{R,I} + S_{i2}\Phi_i^{R,I} + S_{i3}\Phi_{i+1}^{R,I} &= S_{i4}^{R,I} & (i=2, 3, \dots, N_r-2), \\
\Phi_{N_r-2}^{R,I} + S_{N_r-1,2}\Phi_{N_r-1}^{R,I} &= S_{N_r-1,4}^{R,I} & (i=N_r-1),
\end{aligned} \quad (5.44)$$

where $S_{13} = C_{13}/C_{12}$, $S_{14}^{R,I} = C_{14}^{R,I}/C_{12}$. The other normalized coefficients are all of the form $S_{ix} = C_{ix}/C_{i1}$.

Expressed in matrix notation, equations (5.44) become

$$\begin{pmatrix} 1 & S_{13} & 0 & 0 & 0 & \dots & 0 & 0 & 0 \\ 1 & S_{22} & S_{23} & 0 & 0 & \dots & 0 & 0 & 0 \\ 0 & 1 & S_{32} & S_{33} & 0 & \dots & 0 & 0 & 0 \\ 0 & 0 & 1 & S_{42} & S_{43} & \dots & 0 & 0 & 0 \\ \vdots & \vdots & \vdots & \vdots & \vdots & \ddots & \vdots & \vdots & \vdots \\ \vdots & \vdots & \vdots & \vdots & \vdots & \ddots & \vdots & \vdots & \vdots \\ 0 & 0 & 0 & 0 & 0 & \dots & 1 & S_{N_r-2,2} & S_{N_r-2,3} \\ 0 & 0 & 0 & 0 & 0 & \dots & 0 & 1 & S_{N_r-1,2} \end{pmatrix} \begin{pmatrix} \Phi_1^{R,I} \\ \Phi_2^{R,I} \\ \Phi_3^{R,I} \\ \Phi_4^{R,I} \\ \vdots \\ \vdots \\ \vdots \\ \Phi_{N_r-2}^{R,I} \\ \Phi_{N_r-1}^{R,I} \end{pmatrix} = \begin{pmatrix} S_{14}^{R,I} \\ S_{24}^{R,I} \\ S_{34}^{R,I} \\ S_{44}^{R,I} \\ \vdots \\ \vdots \\ \vdots \\ S_{N_r-2,4}^{R,I} \\ S_{N_r-1,4}^{R,I} \end{pmatrix}. \quad (5.45)$$

The coefficient matrix on the left-hand side of equation (5.45) is a tridiagonal matrix, whose non-vanishing elements form a band three elements wide along the diagonal. It is well-known that this set of equations can be solved very efficiently by using the Gaussian elimination method [25]. Our case is a particular one, since the appearance of unitary coefficients in the lower diagonal band simplifies the elimination scheme. This elimination process is accompanied by a successive re-naming of the coefficients according to the rule

$$\begin{aligned} S_{i2} &\leftrightarrow (S_{i2}S_{i-1,2} - S_{i-1,3}), \\ S_{i3} &\leftrightarrow (S_{i3}S_{i-1,2}), \\ S_{i4}^{R,I} &\leftrightarrow (S_{i4}^{R,I}S_{i-1,2} - S_{i-1,4}^{R,I}), \end{aligned} \quad (5.46)$$

for $i = 2, 3, \dots, N_r - 2$. At the end of the elimination scheme, all of the algebraic equations in (5.44) are in the simple form of having only two terms on the left-hand side. From the last two of the resulting equations (for $i = N_r - 2$ and $i = N_r - 1$,

respectively), we then obtain that

$$\Phi_{N_r-1}^{R,I} = \frac{S_{N_r-2,2}S_{N_r-1,4}^{R,I} - S_{N_r-2,4}^{R,I}}{S_{N_r-2,2}S_{N_r-1,2} - S_{N_r-2,3}}. \quad (5.47)$$

The remaining unknowns are then computed using a backward substitution scheme. In this way, the potential coefficients are first calculated for the outermost grid-points according to the recurrence formula

$$\Phi_i^{R,I} = \frac{S_{i4}^{R,I} - S_{i3}\Phi_{i+1}^{R,I}}{S_{i2}} \quad (i = N_r - 2, N_r - 3, \dots, 2, 1). \quad (5.48)$$

Finally, the boundary potential coefficients are calculated using equation (5.41) once the $\Phi_{N_r-1}^{R,I}$ have been determined via equation (5.47).

In practice, if we consider terms up to and including $l = 6$ such that only those with $l + m$ even are effectively included in the summation (5.1) for $\Phi(r, \theta, \phi)$, we shall have 28 equations for the $\Re[\Phi_{lm}(r)]$'s and 28 more for the $\Im[\Phi_{lm}(r)]$'s of the form of equation (5.4). Hence, the potential coefficients needed to evaluate $\Phi(r_i, \theta, \phi)$ are obtained after applying the tridiagonal solution method 56 times.

5.4 Gravitational Potential for the Main Grid-Cells

For a particular grid-point (r, θ, ϕ) , with $r \neq 0$ and $\theta \neq 0$, the gravitational potential is then computed using the expansion (5.1). From the definition of the spherical harmonics (5.6) and relation (5.32), the gravitational potential may be expressed in complex notation as

$$\Phi(r, \theta, \phi) = \Re[\Phi(r, \theta, \phi)] + i\Im[\Phi(r, \theta, \phi)], \quad (5.49)$$

where

$$\Re[\Phi(r, \theta, \phi)] = \sum_{l=0}^{\infty} \sum_{m=-l}^l C_l^m P_l^m(\cos \theta) \{ \Re[\Phi_{lm}(r)] \cos(m\phi) - \Im[\Phi_{lm}(r)] \sin(m\phi) \}, \quad (5.50)$$

and

$$\Im[\Phi(r, \theta, \phi)] = \sum_{l=0}^{\infty} \sum_{m=-l}^l C_l^m P_l^m(\cos \theta) \{ \Re[\Phi_{lm}(r)] \sin(m\phi) + \Im[\Phi_{lm}(r)] \cos(m\phi) \}. \quad (5.51)$$

In order to get acceptable physical solutions, the imaginary part (5.51) must be identically zero. That is, for any l and m , the following relation must hold

$$\tan(m\phi) = -\frac{\Im[\Phi_{lm}(r)]}{\Re[\Phi_{lm}(r)]}. \quad (5.52)$$

The accuracy of the numerically obtained potential is discussed in Section 5.7 for a few test cases.

5.5 Gravitational Potential for the Axial Cells

For the axial cells, the gravitational potential is easily determined by setting $\theta = 0$ in the expansion (5.1). Then, from the definition of the spherical harmonics (5.6), we may write explicitly

$$\Phi(r, 0, \phi) = \sum_{l=0}^{\infty} \sum_{m=-l}^l C_l^m P_l^m(1) \Phi_{lm}(r) e^{im\phi}, \quad (5.53)$$

where $P_l^m(1) = 1$ only when $m = 0$, and is identically zero otherwise. Hence, the only non-vanishing terms in the summation (5.53) are those having $m = 0$. Setting $m = 0$, equation (5.53) reduces to

$$\Phi(r, 0) = \sum_{l=0}^{\infty} C_l^0 \Phi_{l0}(r), \quad (5.54)$$

where the expansion includes only terms with l even, due to the reflection symmetry about the equatorial plane. Finally, evaluating C_l^0 from relation (5.7) and denoting the axial potential by $\Phi'(r)$, we have

$$\Phi'(r) = \frac{1}{2\sqrt{\pi}} \sum_{l=0}^{\infty} \sqrt{2l+1} \Phi_{l0}(r). \quad (5.55)$$

The potential coefficients $\Phi_{l0}(r)$ are real functions. This may be verified directly from equation (5.8) by setting $m = 0$. The factor $e^{im\phi}$ disappears from the integrand, and the imaginary part of the density coefficients $\rho_{l0}(r)$ vanishes.

5.6 Gravitational Potential at the Centre

The gravitational potential at the cloud centre ($r = 0$), denoted by Φ_c , is obtained by following a procedure similar to that used by Stoeckly [104] for the same problem but in 2-space dimensions. Let us consider the 3-dimensional Poisson equation (3.25), evaluate it at $r = 0$ and integrate each term over θ and ϕ . The limiting form is found to be

$$\int_0^{2\pi} d\phi \int_{-1}^{+1} \left[\frac{\partial^2}{\partial r^2} \Phi(r, x, \phi) \right]_{r=0} dx = \frac{4\pi G}{3} \int_0^{2\pi} d\phi \int_{-1}^{+1} \rho(0, x, \phi) dx, \quad (5.56)$$

where for convenience we have performed the change of variable $\cos \theta \rightarrow x$. Before evaluating the integrals, equation (5.56) must be put in finite-difference form. This is done by expanding the function $\Phi(r_1, x, \phi)$ in a Taylor series about $r = 0$

$$\begin{aligned} \Phi(r_1, x, \phi) = & \Phi(0, x, \phi) + \left[\frac{\partial \Phi(r, x, \phi)}{\partial r} \right]_{r=0} r_1 + \\ & + \frac{1}{2} \left[\frac{\partial^2 \Phi(r, x, \phi)}{\partial r^2} \right]_{r=0} r_1^2 + \frac{1}{6} \left[\frac{\partial^3 \Phi(r, x, \phi)}{\partial r^3} \right]_{r=0} r_1^3 + \dots, \end{aligned} \quad (5.57)$$

where r_1 is the radius of the first shell of cells surrounding the central spherical cell [See Figure 4.1(a)]. By applying the condition $[\partial \Phi(r, \theta, \phi) / \partial r]_{r=0} = 0$ and neglecting derivatives higher than the second in equation (5.57), we get

$$\left[\frac{\partial^2 \Phi(r, x, \phi)}{\partial r^2} \right]_{r=0} \approx \frac{2[\Phi(r_1, x, \phi) - \Phi(0, x, \phi)]}{r_1^2} + O\{(\Delta r_1)\}, \quad (5.58)$$

which defines a forward finite-difference approximation for the second derivative at $r = 0$. Inserting (5.58) into equation (5.56), we finally obtain

$$\int_0^{2\pi} d\phi \int_{-1}^{+1} \Phi(0, x, \phi) dx \simeq \int_0^{2\pi} d\phi \int_{-1}^{+1} \Phi(r_1, x, \phi) dx - \frac{2}{3} \pi G r_1^2 \int_0^{2\pi} d\phi \int_{-1}^{+1} \rho(0, x, \phi) dx. \quad (5.59)$$

The integrals in equation (5.59) are calculated by means of a Gauss-Legendre quadrature for the x integration and with a Filon quadrature for the ϕ integration. Following the considerations of Section 5.2, equation (5.59) may be then written in the semi-numerical form

$$\sum_{j=1}^{N_\theta} H'_j \int_0^{2\pi} \Phi(0, a_j, \phi) d\phi \approx \sum_{j=1}^{N_\theta} H'_j \left\{ \int_0^{2\pi} \Phi(r_1, a_j, \phi) d\phi - \frac{2}{3} \pi G r_1^2 \int_0^{2\pi} \rho(0, a_j, \phi) d\phi \right\}. \quad (5.60)$$

The ϕ integrals are of the form of eq.(5.24) with $m = 0$. Then, taking the Filon coefficients $\beta(\lambda) = 2/3$ and $\gamma(\lambda) = 4/3$, as appropriate for $\lambda = 0$, and using the summations (5.27), we obtain that

$$\begin{aligned} \int_0^{2\pi} \Phi(0, a_j, \phi) d\phi &\approx \frac{2}{3} \Delta \tilde{\phi} \sum_{k=1}^n [\Phi(0, a_j, 2\Delta \tilde{\phi} k) + 2\Phi(0, a_j, 2\Delta \tilde{\phi} k - \Delta \tilde{\phi})] \equiv \\ &\equiv 2n \Delta \tilde{\phi} \Phi^\dagger(0, a_j), \\ \int_0^{2\pi} \Phi(r_1, a_j, \phi) d\phi &\approx \frac{2}{3} \Delta \tilde{\phi} \sum_{k=1}^n [\Phi(r_1, a_j, 2\Delta \tilde{\phi} k) + 2\Phi(r_1, a_j, 2\Delta \tilde{\phi} k - \Delta \tilde{\phi})], \quad (5.61) \\ \int_0^{2\pi} \rho(0, a_j, \phi) d\phi &\approx \frac{2}{3} \Delta \tilde{\phi} \sum_{k=1}^n [\rho(0, a_j, 2\Delta \tilde{\phi} k) + 2\rho(0, a_j, 2\Delta \tilde{\phi} k - \Delta \tilde{\phi})] \equiv \\ &\equiv 2n \Delta \tilde{\phi} \rho^\dagger(0, a_j). \end{aligned}$$

In the above approximations, we have used the fact that $X(r, \theta, 0) = X(r, \theta, 2\pi)$ at the periodic boundary. Furthermore, from the property (5.20), we have that

$$\sum_{j=1}^{N_\theta} H'_j \Phi^\dagger(0, a_j) \equiv 2\Phi_c, \quad (5.62)$$

and

$$\sum_{j=1}^{N_\theta} H'_j \rho^{\dagger}(0, a_j) \equiv 2\rho_c, \quad (5.63)$$

where Φ_c and ρ_c denote, respectively, the potential and density at the centre. By virtue of the approximations (5.61) and the relations (5.62) and (5.63), equation (5.60) becomes

$$\Phi_c \approx \frac{1}{2} \sum_{j=1}^{N_\theta} H'_j \left\{ \frac{1}{n} \sum_{k=1}^n \frac{1}{3} [\Phi(r_1, a_j, 2\Delta\tilde{\phi}k) + 2\Phi(r_1, a_j, 2\Delta\tilde{\phi}k - \Delta\tilde{\phi})] \right\} - \frac{2}{3} \pi G r_1^2 \rho_c, \quad (5.64)$$

which defines the central potential in terms of the potential of the neighbouring main grid-cells. Equation (5.64) is only an approximate formula for Φ_c . However, it has been found to give accurate results. The limit of the summation for the index k is related to the number of cells in the ϕ -direction by $N_\phi = 2n$.

Note that the neighbouring axial cell does not contribute to the determination of Φ_c .

5.7 Accuracy and Tests

The accuracy of the Poisson solver has been checked by comparing the numerically obtained potential and its radial gradient with a few available analytical solutions. The tests were mainly aimed at checking the tridiagonal matrix algorithm and finding the effects of the limited number of terms allowed in the spherical harmonic (5.1) and Legendre polynomial (A.1) [See Appendix A] expansions. All calculations were carried out on a Gould computer in double precision (always keeping 14 significant figures). This is slightly better than working in single precision on a CDC 7600 machine.

The first analytical solutions which we used for the gravitational potential were for

the case of a spherically symmetric configuration with a uniform-density distribution

$$\Phi(r) = \frac{2}{3}\pi G\rho_0 \left(r^2 - 3R_0^2\right). \quad (5.65)$$

Although this test will only estimate the accuracy of the potential coefficients $\Phi_{lm}(r)$, for $l = 0$ and $m = 0$, it is suitable for establishing the accuracy of the initial potential gradients for clouds collapsing from uniform-density conditions, as is the case for most of the multi-dimensional calculations. When the 2-dimensional Poisson solver is run (with the radial grid being uniform), the numerically obtained potential matched the analytic profile (5.65) with a relative error of $\sim 10^{-14}\%$ towards the centre and of $\sim 10^{-13}\%$ towards the outermost zones, while the radial gradients were accurate to $\sim 10^{-12}\%$ throughout the computational grid. Furthermore, the θ -gradients were exactly zero, except for a few external zones near to the rotational axis (with $j = 1$ and $j = 2$) where $\partial\Phi/\partial\theta \sim 10^{-20}$. For the same test, the 3-dimensional Poisson solver produced values of Φ accurate to $\sim 10^{-13}\%$ in the central zones and to $\sim 10^{-12}\%$ towards the spherical boundary, and radial gradients accurate to $\sim 10^{-11}\%$ throughout the grid. This high accuracy shows that the tridiagonal matrix algorithm is extremely efficient in calculating the gravitational potential for uniform-density spheres, and that even with a coarse mesh (241 cells for the 2-D run and 3541 cells for the 3-D run) the multi-dimensional Poisson solvers are able to recognize a spherically symmetric configuration.

It was noticed that with a first version of the 3-D Poisson solver, the analytical profile (5.65) was reproduced exactly until the twelfth digit out of the fourteen carried, with substantial variations in the 13th and 14th digits for different values of θ and ϕ . A similar situation was also reported by Boss [13]. Such variations introduce initial gravitational instabilities for the non-axisymmetric collapse models, even when the simulations are constrained to start from uniform-density conditions. This effect

will have implications on the global conservation of angular momentum [See equation (3.24)], and will certainly prejudice results from the 3-dimensional code because any unexpected growth of this artificial perturbation could eventually induce a purely numerical fragmentation of the collapsing cloud. Four main sources of error in the calculation of $\Phi(r, \theta, \phi)$, are likely to be responsible for this instability. The first error is introduced by evaluating the oscillatory factors $e^{-im\phi}$ in the Filon integration for the density coefficients. Similarly, a second error may come from evaluating the factors $e^{im\phi}$ in the spherical harmonic expansions (5.1). A third error is implicit in the way the density is being weighted by the Filon quadratures (5.24) and (5.25). The Filon integration method basically uses a parabolic interpolation of the non-oscillatory part of the integrand over each double interval [See summations (5.27) and (5.28)], in order to allow for an explicit integration by parts of the Fourier transforms. In this way, the density at odd values of the index k is weighted at twice the weight of the even numbered ϕ -points and hence, a tendency towards gravitational instability could arise between particular ϕ -points. The fourth error is certainly coming from the finite number of terms retained in the spherical harmonic expansions ($l \leq 6$ and $-6 \leq m \leq 6$). These numerical difficulties have here been circumvented in a way different from that used by Boss [13]. In our case, the 3-D Poisson solver was equipped with a special subroutine, which acts on the computer's internal representation of the numbers (values of the Φ_{ijk}) by zeroing the last two bits without modifying the corresponding decimal representation. In other words, any numerical fluctuation introduced in the decimal conversion of the gravitational potential is artificially smoothed. In this way, $\Phi(r, \theta, \phi)$ is made ignorant of any preferred directions and the background gravitational instability is essentially removed. In order to check this subroutine, we have computed the

ϕ -gradients by carrying 15 significant figures, and found that $\partial\Phi/\partial\phi$ was exactly zero, except for a very small number of grid-points where $\partial\Phi/\partial\phi \sim 10^{-18}$. When the same calculation was repeated with the grid refined ($\xi = 1.5$), the ϕ -gradients were exactly zero everywhere. These results then leave us confident that any artificial perturbation in the initial conditions is automatically damped. Furthermore, the imaginary part of the gravitational potential [See equation (5.51)] was numerically found to be $\sim 10^{-20}$ for all grid-points, which corresponded to $\sim 10^{-31} - 10^{-33}$ times the real part. These numbers, on the other hand, give an estimate of the rounding error introduced by the machine in evaluating the oscillatory terms $\cos(m\phi)$ and $\sin(m\phi)$ in the summation (5.51) since the imaginary parts of the coefficients $\rho_{00}(r)$ and $\Phi_{00}(r)$ were numerically zero. By way of comparison, for the uniform-density test Boss [13] obtained an accuracy of $10^{-12}\%$ in Φ and $10^{-9}\%$ in $\partial\Phi/\partial r$ in single precision on a CDC 7600 machine, while Black and Bodenheimer [3] with a finer 2-D grid (of 40×40 cylindrical coordinate points) obtained Φ accurate to $5 \times 10^{-4}\%$ and the gradients to 0.01% on the same machine. Our better accuracy, with respect to the Boss [13] case, may be attributed to a slight advantage implicit in the double precision accuracy of the Gould machine (64 bits) with respect to the single precision of a CDC 7600 computer (60 bits).

The multi-dimensional Poisson solvers were also tested for a spherically symmetric, centrally condensed density distribution of the form

$$\rho(r) = \rho_0 \left(1 - \frac{r}{nR_0}\right)^5, \quad (5.66)$$

which admits the analytical potential

$$\Phi(r) = \frac{2}{3}\pi G\rho_0 r^2 \left\{ 1 - \frac{r}{nR_0} \left[\frac{5}{2} - \frac{r}{nR_0} \left(3 - \frac{r}{nR_0} \left(2 - \frac{r}{nR_0} \left(\frac{5}{7} - \frac{3}{28} \frac{r}{nR_0} \right) \right) \right) \right] \right\} + \Phi_0, \quad (5.67)$$

with $\Phi_0 = \Phi(r = 0)$ being

$$\Phi_0 = -\frac{2}{3}\pi G\rho_0 R_0^2 \left\{ 3 - \frac{1}{n} \left[10 - \frac{1}{n} \left(15 - \frac{1}{n} \left(12 - \frac{1}{n} \left(5 - \frac{6}{7n} \right) \right) \right) \right] \right\}.$$

The non-linear profile (5.66) comes closer to mimicing the radial density gradients encountered during the early protostellar collapse, and hence should give a better estimate of the Poisson solver. To reproduce the analytical profile (5.66) more accurately, we took a stretched $N_r = 20$ radial grid, with the innermost spacing Δr_1 being a fraction $f \sim 0.1$ of the uniform Δr . Then, setting $n = 1.010101\dots$, we defined a centrally condensed configuration with the central density $\rho_c \sim 10^{10}$ times the boundary density. For this model, the 3-D Poisson solver reproduced the potential accurate to $\sim 0.2\%$ in the central regions and $\sim 1\%$ towards the external boundary, the gradients being substantially more accurate than the Φ representation, with relative errors of $\sim 2 \times 10^{-3}\%$ in the inner portions and of $\sim 0.8\%$ in the outermost zones. When the resolution was increased in the centre ($\Delta r_1 \sim 0.01\Delta r_{uniform}$), the potential was accurate to $\sim 0.1\%$ and the gradient to $\sim 3 \times 10^{-5}\%$. It was noticed that the accuracy of the potential was not strongly sensitive to a particular choice of the computational grid. When the same test was run with a uniform radial grid, the potential was accurate to $\sim 0.4 - 0.3\%$ throughout the grid, while the accuracy of the gradient deteriorated to $\sim 0.3\%$ in the centre. For similar tests, Black and Bodenheimer [3] calculated Φ accurate to $10^{-2}\%$ and the gradients accurate to $10^{-3}\%$ throughout most of the grid, for a sphere with mean density $\bar{\rho} = (1/61)\rho_0$, while Boss [13], using $\bar{\rho} = (1/56)\rho_0$, calculated the potential accurate to $5 \times 10^{-5}\%$ in the inner regions and 1% near the boundary and the gradient accurate to $2 \times 10^{-3}\%$ in the centre and 1% towards the boundary. The important conclusion from this test is that for typical stretch parameters encountered at the end of the calculations ($\xi \sim 1.2 - 1.5$), the Poisson solver is seen to be sensitive with respect

to the large radial gradients expected to occur in the inner regions of collapsing clouds.

A further analytical test was considered in order to estimate the accuracy of the potential coefficients $\Phi_{lm}(r)$ with $l \neq 0$ and $m \neq 0$. For this case, we took a uniform-density oblate spheroid, symmetric with respect to the x -axis and embedded in the spherical grid volume. In spherical coordinates, the surface of this oblate spheroid obeys the equation

$$\frac{1}{r^2} = \frac{1}{R_0^2} + \cos^2 \phi \sin^2 \theta \left(\frac{1}{b^2} - \frac{1}{R_0^2} \right) \quad \text{for } b < R_0,$$

where we have chosen the semi-major axes of the spheroid to coincide with the radius of the spherical grid. The components of the gravitational attraction at any point inside the spheroid are given by [109]

$$\begin{aligned} \frac{\partial \Phi(r, \theta, \phi)}{\partial r} &= 2\pi G \rho_0 r \left\{ \gamma + (\beta - \gamma) \sin^2 \theta \cos^2 \phi \right\}, \\ \frac{\partial \Phi(r, \theta, \phi)}{\partial \theta} &= \pi G \rho_0 r^2 (\beta - \gamma) \sin 2\theta \cos^2 \phi, \\ \frac{\partial \Phi(r, \theta, \phi)}{\partial \phi} &= -\pi G \rho_0 r^2 (\beta - \gamma) \sin 2\phi \sin^2 \theta, \end{aligned} \tag{5.68}$$

where γ and β are expressed in terms of the eccentricity $e = (1 - b^2/R_0^2)^{1/2}$ by means of the following relations

$$\begin{aligned} \gamma &= \frac{(1 - e^2)^{1/2}}{e^3} \sin^{-1} e - \frac{(1 - e^2)}{e^2}, \\ \beta &= \frac{2}{e^2} - \frac{2(1 - e^2)^{1/2}}{e^3} \sin^{-1} e. \end{aligned}$$

In order to make direct comparison with the results obtained by Boss [13], we have taken the density of the homogeneous spheroid to be ten times that of the background spherical medium, and the axis ratio b/R_0 to be 1/5. The 3-D Poisson solver gave radial gradients accurate to $\sim 3\%$ and ϕ - and θ -gradients accurate to ~ 6 and $\sim 5\%$, respectively. For the same orientation of the spheroid, Boss [13] obtained all gradients

accurate to 4% inside the spheroid. This test shows the difficulty which the present Poisson solver has in recognizing a discontinuous density distribution. However, its interest may be regarded as purely academic since we do not expect to find this type of distribution during the early stages of protostellar collapse. Also, the presence of a discontinuous jump between two adjacent grid-points penalizes the present method. As argued by Boss [13], the difficulty results from the inability of the quadrature formulae (used to solve the ϕ -integrals in the expression for the density coefficients) to detect exactly where the jump in density has occurred.

In summary, from the high accuracy of the spherically symmetric tests, we may assert in a first approximation that the tridiagonal solution method is not providing the main source of error in the calculating the gravitational potential, even when strong radial variations of the density are involved. On the contrary, the accuracy of the Poisson solver drops when discontinuities in θ and ϕ are present in the computational grid. This means that the major sources of error are implicit in the quadrature formulae used to determine the coefficients $\rho_{lm}(r)$, and in the finite spherical harmonic expansion. As previously noted, situations in which sudden discontinuities occur between adjacent mesh-points, are not suitable for testing the accuracy of the solver for early protostellar collapse simulations. A better estimate should be obtained by considering density distributions that vary rather continuously in θ and ϕ . Although, in these cases analytical solutions for the potential cannot be obtained (at least not consistently with our boundary conditions), we may try to test the effects of the errors for more realistic density distributions by simply reassembling the original density ρ from the numerically obtained coefficients, via equation (5.1). This possibility was suggested by Boss [13] on the grounds that errors in the reassembled density are likely to provide an upper limit

to the errors of the potential gradients, at least in those zones of the grid where the density is smallest.

For the spherically symmetric tests, the reassembled density $\tilde{\rho}$ was calculated with a relative error of $\sim 10^{-12}\%$ throughout the grid. In the case of the oblate spheroid, $\tilde{\rho}$ was accurate to $\sim 5 \times 10^{-2} - 3 \times 10^{-4}\%$ inside the spheroid and to $80 - 112\%$ outside. For the same test, Boss [13] obtained $\tilde{\rho}$ accurate to $\sim 2 \times 10^{-3}\%$ inside and 100% outside, with the representation of the gradients being more accurate (to 10%) for exterior points. Although, we have not estimated the accuracy of the gradients outside the spheroid, from the good agreement with the estimates made by Boss [13], we may expect the exterior gradients to be accurate at least to $\sim 10\%$.

We have also tested the accuracy of the reassembled density for a distribution of the form

$$\rho(r, \theta) = \rho_0 \left(1 - \frac{r}{nR_0}\right)^5 e^{-\alpha\theta} \quad \text{with } \alpha = \frac{\ln 100}{\pi} \text{ and } n = 1.0101..., \quad (5.69)$$

which defines a centrally condensed configuration falling off in θ , with the central density being $\sim 10^{10}$ times the boundary density (for any θ) and with the equatorial density being 10 times the density at the pole (for any r). Such a density distribution should give a better idea of the accuracy of the quadrature formulae and of the finite spherical harmonic expansion, in protostellar collapse calculations. For this case, $\tilde{\rho}$ was accurate to $\sim 6\%$ (relative error) near the axis and $\sim 2\%$ towards the equatorial plane. The 6% relative error in the zones of lower density corresponds to an absolute error of $\sim 0.8\%$ (compared with the maximum density in the innermost equatorial cell). When terms up to and including $l = 16$ were retained in the spherical harmonic expansions, the accuracy did not improve appreciably. Since, the Poisson solver tends to be more accurate for the higher density regions, the absolute error of the reassembled density

should provide the best estimate of the error to be expected for the potential gradients. We may then conclude that the present Poisson solver is able to calculate potential gradients accurate to at least 1%, for the density gradients expected during the collapse of protostellar configurations.

Chapter 6

Hydrodynamics

In this chapter we shall introduce and describe the basic algorithm which has been implemented for the solution of the set of hydrodynamic equations. Roughly speaking, the numerical solution method is based on a finite-difference technique, which consists of discretizing the continuity and the momentum transfer equations on the same computational grid as used for the solution of the Poisson equation. The discretization is carried out by simply replacing the partial derivative terms of the exact differential equations by appropriate difference formulae. The basic form of these replacements and also the associated truncation errors, are described in Appendix C.

6.1 General Method

Each of our fundamental equations [See Chapter 3] is composed of three main parts, namely: (a) a time derivative part, (b) a transport part, and (c) a source or acceleration part. Thus, for a generalized density X , where X may be ρ , ρv_r , ρv_θ , or ρA , we can symbolically split the time derivative of each equation into the sum of two independent terms

$$\frac{\partial X}{\partial t} = \left(\frac{\partial X}{\partial t} \right)_{TRANSPORT} + \left(\frac{\partial X}{\partial t} \right)_{SOURCE} . \quad (6.1)$$

Setting $(\partial X/\partial t)_{SOURCE} = 0$, we recover the correct symbolic representation of the continuity equation. It can also be seen that the form of the angular momentum transfer equation (3.18), used for the axisymmetric calculations, is similar to that of the continuity equation.

The source part of eq.(6.1) is represented by the acceleration gradients plus some additional undifferentiated terms (appearing in the r - and θ -momentum equations), which contain combinations of the fluid velocity components. Once the gravitational potential Φ and the gas pressure p have been determined at each point of the computational domain, the contribution of the acceleration gradients is numerically evaluated by using the finite-difference replacements (C.14), (C.16), and (C.17) [See Appendix C, Section C.2], for the r -, θ -, and ϕ -gradients, respectively. The advantage of using three-point differences, such as (C.14) and (C.16), is that they formally approximate the r - and θ -gradients to second-order accuracy even for a variable non-uniform grid. Moreover, they automatically reduce to central differences of the form of (C.17) for a uniform grid spacing. This could be the situation encountered for the θ -grid, which starts with a non-uniform structure in the regions near to the rotational axis and then, progressively, becomes fairly uniform towards the equatorial plane. The contribution of the undifferentiated terms will be free of discretization errors, and they are computed simply by evaluating their exact expressions at each grid-point.

The numerical treatment of the transport part needs some more comments. In the general 3-dimensional case, the transport part will be composed of three terms dealing with advection in the r -, θ -, and ϕ - directions, plus a fourth term accounting for the compressional effects of the radially moving grid. In terms of the generalized density

X , for any of the 3-dimensional equations, we shall have

$$\begin{aligned} \left(\frac{\partial X}{\partial t} \right)_{TRANSPORT} = & -\frac{1}{r^2} \frac{\partial}{\partial r} (r^2 X U) - \frac{1}{r \sin \theta} \frac{\partial}{\partial \theta} (\sin \theta X v_\theta) - \frac{1}{r \sin \theta} \frac{\partial}{\partial \phi} (X v_\phi) - \\ & - X \frac{1}{r^2} \frac{\partial}{\partial r} (r^2 v_g), \end{aligned} \quad (6.2)$$

where the first three terms on the right-hand side are set in difference form by means of the replacements (C.20), (C.21), and (C.22), respectively. As discussed in Appendix C, the basic form (C.20) becomes only a first-order accurate replacement for the first term on the right-hand side of equation (6.2), if the radial grid becomes strongly non-uniform, while (C.21) approximates the θ -advective term nearly to second-order accuracy due to the fairly uniform structure of the θ -grid. Only (C.22) will be exactly accurate to second-order since only the ϕ -grid is exactly uniform. However, the direct application of the approximations (C.20), (C.21), and (C.22) involves a proper centering of the fluxes at the cell interfaces. In other words, to correctly simulate the transport of the fluid through the computational mesh, it is necessary to make an adequate evaluation of the terms $(r^2 X U)_{i\pm 1/2, jk}$, $(\sin \theta X v_\theta)_{i, j\pm 1/2, k}$, and $(X v_\phi)_{ij, k\pm 1/2}$ at the numerically discontinuous advecting fluid interfaces. In the calculations, these terms are written in the more convenient form

$$\begin{aligned} (r^2 X U)_{i\pm 1/2, jk} &= r_{i\pm 1/2}^2 \langle X \rangle_{i\pm 1/2, jk} U_{i\pm 1/2, jk}, \\ (\sin \theta X v_\theta)_{i, j\pm 1/2, k} &= \sin \theta_{j\pm 1/2} \langle X \rangle_{i, j\pm 1/2, k} v_{\theta, i, j\pm 1/2, k}, \\ (X v_\phi)_{ij, k\pm 1/2} &= \langle X \rangle_{ij, k\pm 1/2} v_{\phi, ij, k\pm 1/2}, \end{aligned} \quad (6.3)$$

where the interface positions $r_{i\pm 1/2}$ and $\theta_{j\pm 1/2}$ are defined by relations (4.5). The velocity components $U_{i\pm 1/2, jk}$, $v_{\theta, i, j\pm 1/2, k}$, and $v_{\phi, ij, k\pm 1/2}$ are the so-called advective velocities. Physically, they represent the velocities at which the quantity X per unit volume, is

being fluxed across the cell interfaces with respect to the moving grid, in the r -, θ -, and ϕ -directions, respectively. These velocities are computed as the boundary cell averages of the relative fluid velocity components

$$\begin{aligned} U_{i\pm 1/2,jk} &= \frac{1}{2}(U_{i\pm 1,jk} + U_{ijk}), \\ v_{\theta_{i,j\pm 1/2,k}} &= \frac{1}{2}(v_{\theta_{i,j\pm 1,k}} + v_{\theta_{ijk}}), \\ v_{\phi_{ij,k\pm 1/2}} &= \frac{1}{2}(v_{\phi_{ij,k\pm 1}} + v_{\phi_{ijk}}), \end{aligned} \tag{6.4}$$

with $U_{ijk} = v_{r_{ijk}} - v_{g_i}$ denoting the radial fluid velocity relative to the grid-mesh.

However, we must be careful in calculating the quantities $\langle X \rangle$. In principle, it would be desirable to centre the $\langle X \rangle$ at the cell boundaries, as we have done for the advective velocities in (6.4). However, experience indicates that the use of the interface cell averages of X in the replacements (C.20), (C.21), and (C.22) could lead to a set of finite-difference equations exhibiting very poor stability properties. Furthermore, with such a straightforward scheme, it is quite possible to generate unphysical results in the course of the calculation such as, for example, negative cell mass-densities.

In order to avoid numerical trouble and hence, obtain reasonable physical solutions, it is mandatory to choose an advection method leading to a stable set of finite-difference equations. Following this ideal, we have adopted a variant of the Fluid-in-Cell technique originally proposed by Gentry, Martin, and Daly [42]. Their method basically works by using a two-step solution procedure to solve equation (6.1). The first step consists of solving finite-difference approximations to the “source part equations”

$$\frac{\partial X}{\partial t} = \left(\frac{\partial X}{\partial t} \right)_{SOURCE}.$$

In this way, the acceleration effects are evaluated separately and intermediate fluid velocities are obtained extrapolating forward in time by means of an explicit integration

scheme such as the one given by the replacement (C.24) [See Appendix C, Section C.4]. Setting $X = \rho v_\nu$ and defining the time increment by $\Delta t = t^{n+1} - t^n$, the ν component of the intermediate fluid velocity \tilde{v} at the new time level $(n+1)$ is then computed in terms of quantities at the old time level (n) according to the finite-difference equation

$$\tilde{v}_{\nu_{ijk}}^{(n+1)} = v_{\nu_{ijk}}^{(n)} - \frac{\Delta t}{\rho_{ijk}^{(n)}} \left\{ \frac{Acceleration}{gradients} + \frac{Undifferentiated}{terms} \right\}_{ijk}^{(n)}. \quad (6.5)$$

In writing equation (6.5), we have taken $X^{(n+1)} = \rho^{(n)} \tilde{v}_\nu^{(n+1)}$.

In the second step, the hydrodynamical advection is performed by solving finite-difference approximations to the "transport part equations"

$$\frac{\partial X}{\partial t} = \left(\frac{\partial X}{\partial t} \right)_{TRANSPORT}$$

Then, setting $X = \rho$, the transport of mass is calculated by assuming that the mass flow crossing the cell interfaces carries advective velocities corresponding to the updated intermediate values as determined from equation (6.5). Similarly, the flow of the momentum components is computed by assuming that the mass flowing across the cell boundaries carries momentum corresponding to the updated intermediate velocities, that is, instead of using $\langle X \rangle = \langle \rho v_\nu \rangle$ in the relations (6.3), we set $\langle X \rangle = \langle \rho \tilde{v}_\nu \rangle$. The advective intermediate velocities are, in both cases, obtained using average relations similar to (6.4). To calculate the $\langle X \rangle$ at the cell borders, a flow differencing technique, commonly known as the donor cell method, is applied. With this method, the cell boundary densities $\langle \rho \rangle$ are determined by assuming that the mass which flows from cell to cell is directly proportional to the density ρ of the cell from which the fluid is coming. The transport of the momentum components is computed by assuming that the mass which crosses the cell borders carries the velocity of the adjoining donor cells.

This method has been extensively applied by many authors [3,13,52,111] to a wide

number of physical situations involving the solution of the Euler equations of hydrodynamics for inviscid compressible flows. It has been found to be computationally stable and easy to implement. In complicated problems where, in practice, there are no available analytical solutions, a stable finite-difference scheme is of primary importance because only such schemes could guarantee that the numerically obtained solutions converge to the true ones, as the time and space intervals are reduced. On the other hand, the possibility that a cell could develop a negative density (which may occur as a result of improper centering of the $\langle X \rangle$ at the cell borders) is effectively minimized with the donor cell method in zones of severe mass depletion, and even eliminated by choosing a small enough Δt . A further important advantage of the donor-cell advection is that it is conservative and, hence, is especially convenient in cases where the exact differential equations are discretized in conservation form. That is, when the numerical integration is extended over the whole computational grid, the donor cell treatment of the advecting fluid interfaces will ensure strict global conservation of the advected quantities. In this way, the globally conserved mass and momentum components will be free of discretization errors. This feature is always desirable because it enhances the accuracy of the obtained solutions. However, the donor cell method is only accurate to first-order and introduces a large numerical diffusion of the hydrodynamical variables within the grid.

6.2 One-Step Solution Procedure

By a variant of the original Fluid-in-Cell method, we mean that the hydrodynamics is solved by implementing a single step procedure rather than the two-step solution method described above.

Although, as argued by Norman and Winkler [89], a multi-step solution procedure generally turns out to be more accurate than a straightforward one-step solution, this will certainly depend on the formal accuracy of the advection method. We have made several tests with the 1-dimensional code version in order to clarify this point. We concluded that if the donor cell differencing technique is implemented, only negligible additional accuracy could be gained by using two-step hydrodynamics. This is probably due to the formal first-order accuracy of the donor cell method [See Section 6.6]. In view of this it will be sufficient, for our immediate purposes, to calculate the hydrodynamics with a simple one-step solution procedure.

Taking our model equation (6.1) and approximating the time-derivative, on its left-hand side, with the forward time differencing (C.24), we enforce an explicit time integration for the equations of hydrodynamics, which is only first-order accurate. In this manner, for a typical main grid-cell, the generalized variable X_{ijk} is advanced to the new time $(t + \Delta t)$ by using only information at the old time t , which enters as input data in the difference equation

$$X_{ijk}^{n+1} = X_{ijk}^n - \Delta t \left\{ \frac{Transport}{part} + \frac{source}{part} \right\}_{ijk}^n, \quad (6.6)$$

where the superscripts are again used to denote the time level. From the truncation error carried by the time finite-difference (C.24), the time extrapolation implied by equation (6.6) will contribute to the total discretization error of X_{ijk}^{n+1} , with an error of the order of $O\{(\Delta t)^2\}$ at each time step.

The basic approximation made by using equation (6.6), is that both the transport and the source parts are evaluated simultaneously, without the extra calculation of intermediate fluid velocities.

6.3 Compact Radial Quotients

Improvements to enhance the accuracy of the numerical solutions have been introduced by writing the differential equations in compact form. Following Tscharnutter and Winkler [115], the radial part of the divergences $[\nabla \cdot (X\mathbf{U})]_r$ and $[\nabla \cdot \mathbf{v}_g]_r$ may be written using the differential quotients

$$\frac{1}{r^2} \frac{\partial}{\partial r} (r^2 X U) \longrightarrow 3 \frac{\partial}{\partial(r^3)} (r^2 X U), \quad (6.7)$$

$$\frac{1}{r^2} \frac{\partial}{\partial r} (r^2 v_g) \longrightarrow 3 \frac{\partial}{\partial(r^3)} (r^2 v_g), \quad (6.8)$$

which should lead to more accurate difference representations for the r -advective and grid compression terms [See Appendix C, Section C.3]. This can easily be observed by comparing the truncation errors carried by the form (C.19) with those of its counterpart (C.20). The difference between these two formulae lies in the denominator

$$\frac{\left\{ 3 \frac{\partial}{\partial(r^3)} (r^2 X U) \right\}_{ijk}}{\left\{ \frac{1}{r^2} \frac{\partial}{\partial r} (r^2 X U) \right\}_{ijk}} = \frac{r_i^2 \Delta r_{i+1/2}}{\frac{1}{3} (r_{i+1/2}^3 - r_{i-1/2}^3)} < 1. \quad (6.9)$$

The radial factor of the volume of a particular cell, is exactly computed by using the replacement (C.20), while it is underestimated if we use the difference approximation (C.19). Furthermore, the difference approximation (C.19) deteriorates in the limit $r \rightarrow 0$, due to the presence of the factor r_i^2 in the denominator.

The use of the compact radial quotients will introduce slight modifications to the geometrical grid properties, defined in Chapter 4, Section 4.2. That is, the areas of the contact surfaces (4.3) between a particular cell (ijk) and the adjoining cells in the r -, θ -, and ϕ -directions, become

$$S_{i\pm 1/2}^r = r_{i\pm 1/2}^2 \sin \theta_j \Delta \theta_{j+1/2} \Delta \phi_{k+1/2},$$

$$\begin{aligned}
S_{i,j\pm 1/2,k}^\theta &= \frac{1}{2} \left(r_{i+1/2}^2 - r_{i-1/2}^2 \right) \sin \theta_{j\pm 1/2} \Delta \phi_{k+1/2}, \\
S_{ij,k\pm 1/2}^\phi &= \frac{1}{2} \left(r_{i+1/2}^2 - r_{i-1/2}^2 \right) \Delta \theta_{j+1/2},
\end{aligned} \tag{6.10}$$

and the volume (4.4) of a cell is now given by

$$V_{ijk} = \frac{1}{3} \left(r_{i+1/2}^3 - r_{i-1/2}^3 \right) \sin \theta_j \Delta \theta_{j+1/2} \Delta \phi_{k+1/2}. \tag{6.11}$$

Similar modifications are also made in Tables 5 and 6, for the 1- and 2-dimensional meshes.

6.4 Donor Cell Assignments

The finite-difference replacements used in the calculations to approximate the right-hand side of equation (6.2), are

$$\left\{ 3 \frac{\partial(r^2 X U)}{\partial(r^3)} \right\}_{ijk} \approx \frac{[r_{i+1/2}^2 \langle X \rangle_{i+1/2,jk} U_{i+1/2,jk} - r_{i-1/2}^2 \langle X \rangle_{i-1/2,jk} U_{i-1/2,jk}]}{\frac{1}{3} (r_{i+1/2}^3 - r_{i-1/2}^3)}, \tag{6.12}$$

$$\begin{aligned}
&\left\{ \frac{1}{r \sin \theta} \frac{\partial(\sin \theta X v_\theta)}{\partial \theta} \right\}_{ijk} \approx \\
&\approx \frac{[\sin \theta_{j+1/2} \langle X \rangle_{i,j+1/2,k} v_{\theta_{i,j+1/2,k}} - \sin \theta_{j-1/2} \langle X \rangle_{i,j-1/2,k} v_{\theta_{i,j-1/2,k}}]}{\langle r_i \rangle \sin \theta_j \Delta \theta_{j+1/2}},
\end{aligned} \tag{6.13}$$

$$\left\{ \frac{1}{r \sin \theta} \frac{\partial(X v_\phi)}{\partial \phi} \right\}_{ijk} \approx \frac{[\langle X \rangle_{ij,k+1/2} v_{\phi_{ij,k+1/2}} - \langle X \rangle_{ij,k-1/2} v_{\phi_{ij,k-1/2}}]}{\langle r_i \rangle \sin \theta_j \Delta \phi_{k+1/2}}, \tag{6.14}$$

where

$$\langle r_i \rangle = \frac{2}{3} \frac{(r_{i+1/2}^2 + r_{i+1/2} r_{i-1/2} + r_{i-1/2}^2)}{(r_{i+1/2} + r_{i-1/2})}, \tag{6.15}$$

consistently with definitions (6.10) and (6.11).

The finite-difference replacements (6.12)-(6.14) follow from (C.20), (C.21), and (C.22) by substituting the relations (6.3). All quantities are evaluated at the time level (n), according to equation (6.6). The superscript is omitted here for simplicity.

In the donor cell scheme, the replacement for the $\langle X \rangle$ is chosen by taking into account the sign of the fluid velocity at the cell interfaces. This means that the flow entering a cell is proportional to the density of the donor cell and therefore, the possibility of getting negative cell densities drops when $\Delta t \rightarrow 0$. Moreover, this method guarantees the fluid transportive property, since any disturbances in the flow are only advected in the direction of the fluid velocity [42].

As commented in Section 6.1, strict global conservation of the advected quantities is also ensured by the donor cell transport. If we multiply for each cell the advective terms (6.12), (6.13), and (6.14) by the volume of the cell (6.11), and then sum over the whole grid, the fluxes at the cell interfaces will cancel out in pairs, so that only the contributions across the exterior boundaries will remain. In this way, the time rate of change of the numerically conserved quantities (mass and angular momentum) will only depend on the flux at these boundaries.

In Figures 6.1, 6.2, and 6.3, we show control volumes for the donor cell transport of the hydrodynamical variables in the r -, θ -, and ϕ -directions respectively.

(a) Radial Advection.

$$\langle X \rangle_{i+1/2,jk} = \begin{cases} X_{ijk} & \text{if } U_{i+1/2,jk} \geq 0 \\ X_{i+1,jk} & \text{if } U_{i+1/2,jk} < 0 \end{cases} \quad (6.16)$$

$$\langle X \rangle_{i-1/2,jk} = \begin{cases} X_{i-1,jk} & \text{if } U_{i-1/2,jk} \geq 0 \\ X_{ijk} & \text{if } U_{i-1/2,jk} < 0 \end{cases}$$

where the radial relative velocity U is taken to be positive towards the cloud boundary and negative towards the centre.

(b) θ -Advection.

$$\langle X \rangle_{i,j+1/2,k} = \begin{cases} X_{ijk} & \text{if } v_{\theta,i,j+1/2,k} \geq 0 \\ X_{i,j+1,k} & \text{if } v_{\theta,i,j+1/2,k} < 0 \end{cases}$$

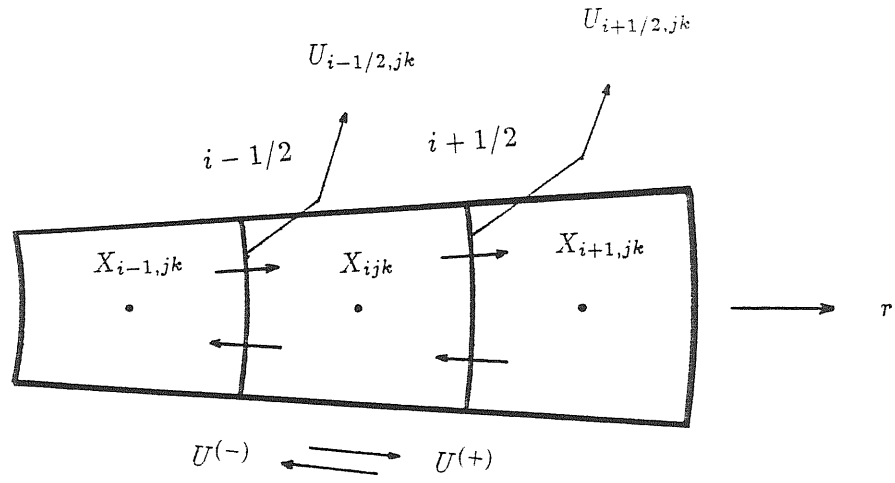


Figure 6.1: Control volume for radial advection.

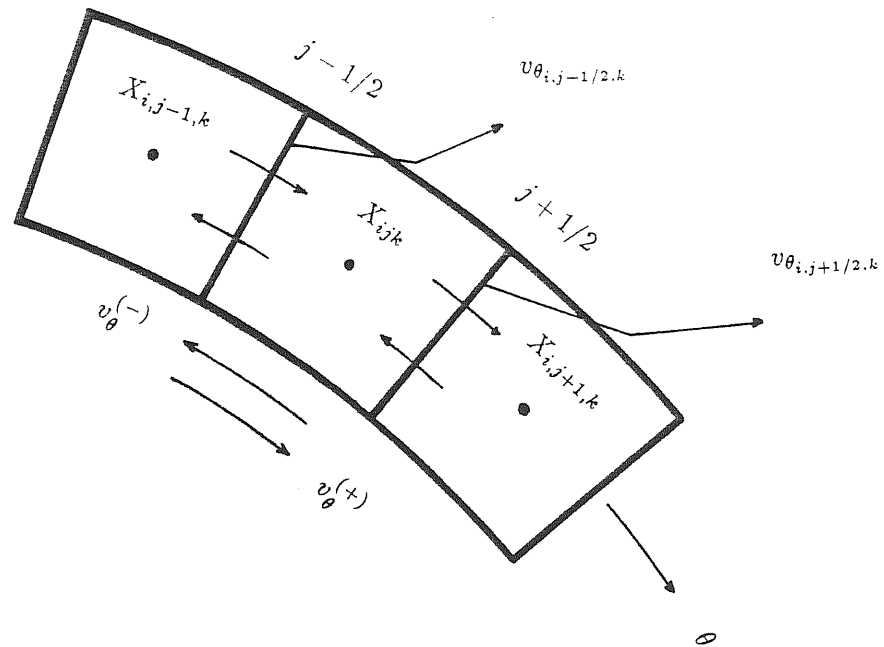


Figure 6.2: Control volume for θ -advection.

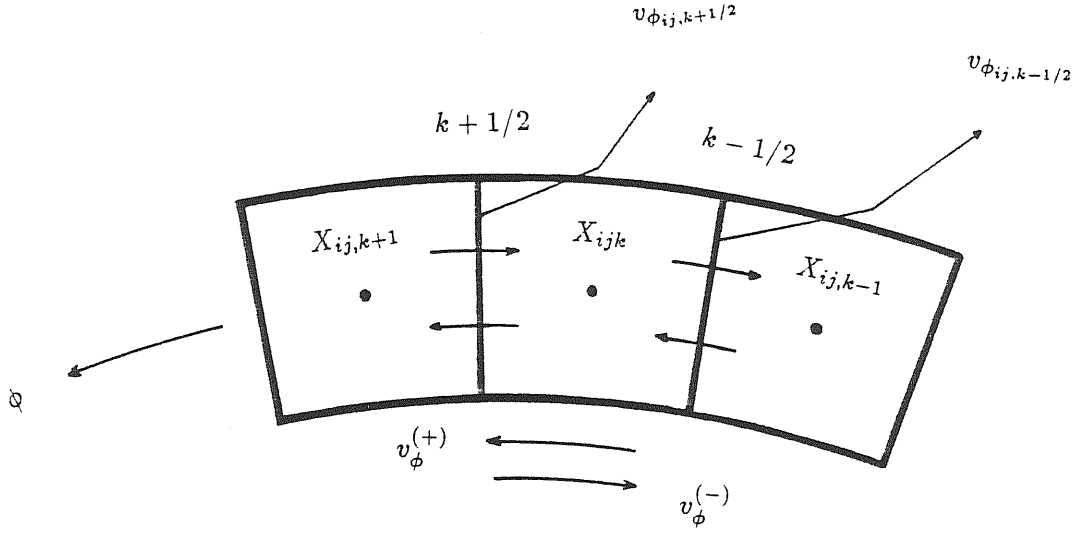


Figure 6.3: Control volume for ϕ -advection.

(6.17)

$$\langle X \rangle_{i,j-1/2,k} = \begin{cases} X_{i,j-1,k} & \text{if } v_{\theta,i,j-1/2,k} \geq 0 \\ X_{ijk} & \text{if } v_{\theta,i,j-1/2,k} < 0 \end{cases}$$

where the θ -velocity is taken positive in the direction towards the equatorial plane and negative towards the pole.

(c) ϕ -Advection.

$$\langle X \rangle_{ij,k+1/2} = \begin{cases} X_{ijk} & \text{if } v_{\phi,ij,k+1/2} \geq 0 \\ X_{ij,k+1} & \text{if } v_{\phi,ij,k+1/2} < 0 \end{cases}$$

(6.18)

$$\langle X \rangle_{ij,k-1/2} = \begin{cases} X_{ij,k-1} & \text{if } v_{\phi,ij,k-1/2} \geq 0 \\ X_{ijk} & \text{if } v_{\phi,ij,k-1/2} < 0 \end{cases}$$

The ϕ -velocity component is taken positive in the counterclockwise direction and negative otherwise.

6.5 Grid Contraction Effects

The contribution to the net change of the generalized density X due to changes in the cell volumes, is given by the last term on the right-hand side of equation (6.2). So, if

we neglect the transport effects, in the complete absence of source forces, we may write

$$\left(\frac{\partial X}{\partial t}\right) = -3X \frac{\partial(r^2 v_g)}{\partial(r^3)}, \quad (6.19)$$

where we have used the compact form (6.8)

As previously noted in Chapter 3, Section 3.3, this term has been added in the equations of motion in such a way as to leave unaltered the hydrodynamical solutions expected in the inertial frame of the Eulerian observer. The same purpose can be achieved numerically if the grid motion does not affect the global conservation of the advected quantities or enhance the local spurious diffusion of the donor cell scheme. A suitable finite-difference form of equation (6.19) is then obtained by demanding conservation of mass and momentum within the mesh (locally). Defining \tilde{X} as the density X multiplied by the volume of the cell, where \tilde{X} may be M , Mv_r , Mv_θ , or MA , using the volume (6.11), and imposing that $\tilde{X}_{ijk}^{n+1} = \tilde{X}_{ijk}^n$ for a typical cell, we find that

$$X_{ijk}^{n+1} = X_{ijk}^n \frac{(r_{i+1/2}^3 - r_{i-1/2}^3)^n}{(r_{i+1/2}^3 - r_{i-1/2}^3)^{n+1}}, \quad (6.20)$$

where the superscripts refer to the time level. Furthermore, if we write equation (6.19) in the explicitly time integrated form of equation (6.6), and then combine with equation (6.20) to eliminate X_{ijk}^{n+1} , we obtain

$$\left\{ 3X \frac{\partial(r^2 v_g)}{\partial(r^3)} \right\}_{ijk}^n \approx X_{ijk}^n \frac{1}{\Delta t} \left\{ \frac{(r_{i+1/2}^3 - r_{i-1/2}^3)^{(n+1)} - (r_{i+1/2}^3 - r_{i-1/2}^3)^{(n)}}{(r_{i+1/2}^3 - r_{i-1/2}^3)^{(n+1)}} \right\}. \quad (6.21)$$

The finite-difference replacement (6.21) is consistent with the identity (3.8). In other words, if we calculate the time derivative of the volume (6.11), we find that the size of a typical zone will change at the rate

$$\left(\frac{dV_{ijk}}{dt}\right)^n = \sin \theta_j \Delta \theta_{j+1/2} \Delta \phi_{k+1/2} \left[r_{i+1/2}^2 v_{g_{i+1/2}} - r_{i-1/2}^2 v_{g_{i-1/2}} \right]^n. \quad (6.22)$$

If we integrate the above equation (by using the forward time differencing (C.24)), we then recover the identity (3.8) in difference form

$$\frac{\left[r_{i+1/2}^2 v_{g_{i+1/2}} - r_{i-1/2}^2 v_{g_{i-1/2}} \right]^n}{\frac{1}{3} \left(r_{i+1/2}^3 - r_{i-1/2}^3 \right)^{n+1}} = \frac{\left[\left(r_{i+1/2}^3 - r_{i-1/2}^3 \right)^{(n+1)} - \left(r_{i+1/2}^3 - r_{i-1/2}^3 \right)^{(n)} \right]}{\Delta t \left(r_{i+1/2}^3 - r_{i-1/2}^3 \right)^{(n+1)}}. \quad (6.23)$$

The finite-difference replacement (6.21) will ensure the global conservation of the advected quantities at the new time level $(n + 1)$, provided that the radial factors in the replacements (6.12)-(6.14) are evaluated at the new level $(n + 1)$.

6.6 Numerical Stability and Accuracy

A finite-difference scheme is considered to be particularly convenient or not depending on its stability properties. Whenever a finite-difference set of equations gives rise to rapidly growing and oscillating solutions, which in no way resemble those expected from the exact differential equations, we say that the numerical scheme is computationally unstable. This deficiency is generally detected when a “saw-tooth” behaviour occurs in the distribution of the physical variables [60,80,90]. A similar effect is also observed when strong shock fronts are generated within the field of solution. These structures will appear as strong discontinuities in the hydrodynamical approximation. Due to the large gradients associated with them, accurate numerical solutions will generally be extremely difficult to obtain. However, in this situation the computational instability which arises may be minimized or even eliminated by introducing an artificial diffusion. In practice, this is done with an artificial viscosity technique, which consists in broadening the forming shock structure over a few grid-cells by adding a viscous pressure force in the equations of motion before differencing [See Section 6.10]. The Fluid-in-Cell method [42], originally included an artificial viscosity term to improve the stability of the donor-

cell advection in regions of the mesh where the fluid velocity is much smaller than the local sound speed.

When we deal with linear difference equations with constant coefficients, it is possible to make a full stability analysis and hence any computational difficulty can be avoided, if we use the Fourier stability method introduced by von Neuman [52,60,80,98]. However, for non-linear coupled systems of partial differential equations with non-constant coefficients, such as those which we are trying to solve here, a global linearized Fourier analysis is not sufficient to predict the required stability conditions. Hirt [52] proposed a heuristic-empirical technique based on study of the truncation errors, for detecting the origin of non-linear instabilities. He treated the Euler equations of motion for inviscid fluids with a number of advection methods, all of which appeared to be stable according to a linearized Fourier analysis, but all of them turned out to be actually unstable because of non-linear effects, with the single exception of the donor cell method. In spite of the non-linear nature of our relevant differential equations, we may expect to predict in a first approximation, with a local linearized Fourier analysis, the necessary conditions for the stability of the resulting difference equations. By a local Fourier analysis, we mean that the linearization is to be applied for an individual computational cell, where we can neglect the non-linearity of the relevant equations. As a model equation, we take the equation of continuity (3.20). Then, for a typical main grid-cell, this equation may be written in finite-difference form by using the replacements (6.12)-(6.14) in equation (6.6) with $X_{ijk} = \rho_{ijk}$. For reasons of simplicity, we shall consider the grid fixed and the radial term (6.12) in its less compact form (C.19). The Fourier method will then consist in assuming for ρ_{ijk}^n an exponentially

growing solution of the form

$$\rho_{ijk}^n = \hat{\xi}^n e^{\check{i}\tilde{k}_1 i \Delta r_{i+1/2}} e^{\check{i}\tilde{k}_2 j \Delta \theta_{j+1/2}} e^{\check{i}\tilde{k}_3 k \Delta \phi_{k+1/2}}, \quad (6.24)$$

where $\hat{\xi}$ is the amplification factor of the propagating wave and \tilde{k}_1 , \tilde{k}_2 , and \tilde{k}_3 are the spatial frequencies or wave numbers associated with the r -, θ -, and ϕ -spacings, respectively. In expression (6.24), we have used \check{i} to differentiate the imaginary number from the radial index i .

If we define the Courant numbers in spherical coordinates as

$$\begin{aligned} \Gamma &= \frac{\Delta t v_{r_{ijk}}}{\Delta r_{i+1/2}}, \\ \Lambda &= \frac{\Delta t v_{\theta_{ijk}}}{r_i \Delta \theta_{j+1/2}}, \\ \Upsilon &= \frac{\Delta t v_{\phi_{ijk}}}{r_i \sin \theta_j \Delta \phi_{k+1/2}}, \end{aligned} \quad (6.25)$$

the equation of continuity (3.20) in difference form will read

$$\begin{aligned} \rho_{ijk}^{n+1} = & \rho_{ijk}^n - \Gamma \left(\frac{r_{i+1/2}^2}{r_i^2} \langle \rho \rangle_{i+1/2,jk}^n - \frac{r_{i-1/2}^2}{r_i^2} \langle \rho \rangle_{i-1/2,jk}^n \right) - \\ & - \Lambda \left(\frac{\sin \theta_{j+1/2}}{\sin \theta_j} \langle \rho \rangle_{i,j+1/2,k}^n - \frac{\sin \theta_{j-1/2}}{\sin \theta_j} \langle \rho \rangle_{i,j-1/2,k}^n \right) - \\ & - \Upsilon \left(\langle \rho \rangle_{ij,k+1/2}^n - \langle \rho \rangle_{ij,k-1/2}^n \right). \end{aligned} \quad (6.26)$$

In writing equation (6.26), we have approximated the cell-interface velocities as being constant and equal to the velocities at the cell centre. Now using the donor cell assignments (6.16)-(6.18) for the mass-density ρ and substituting the Fourier component (6.24) into equation (6.26), we solve for the amplification factor. If $\hat{\xi}$ has a magnitude greater than unity for any value of \tilde{k}_1 , \tilde{k}_2 , and \tilde{k}_3 , the finite-difference equation (6.26) will be unstable because the Fourier component (6.24) will grow exponentially with

time through the term $\hat{\xi}^n$. Therefore, for stability we must always have $|\hat{\xi}| \leq 1$. After some tedious algebra, we found that this condition is satisfied only if

$$\begin{aligned}
|\Gamma| &\leq C_{r_i} & \text{or} & & \Delta t_{r_{ijk}} &\leq C_{r_i} \frac{\Delta r_{i+1/2}}{|v_{r_{ijk}}|}, \\
|\Lambda| &\leq C_{\theta_j} & \text{or} & & \Delta t_{\theta_{ijk}} &\leq C_{\theta_j} \frac{r_i \Delta \theta_{j+1/2}}{|v_{\theta_{ijk}}|}, \\
|\Upsilon| &\leq 1 & \text{or} & & \Delta t_{\phi_{ijk}} &\leq \frac{r_i \sin \theta_j \Delta \phi_{k+1/2}}{|v_{\phi_{ijk}}|},
\end{aligned} \tag{6.27}$$

where C_{r_i} and C_{θ_j} are numbers of the order of unity and are defined as combinations of the interface and cell centre coordinates. From an inspection of equation (6.26), we may note that conditions (6.27) are actually conditions for non-negative cell-densities. In order that our donor cell scheme will be able to propagate a disturbance moving as fast as the sound speed relative to the fluid, conditions (6.27) need to be slightly modified. That is, we must define new Courant numbers in terms of the local sound speed $C_{ss_{ijk}}$

$$\begin{aligned}
\Gamma' &= \frac{\Delta t C_{ss_{ijk}}}{\Delta r_{i+1/2}}, \\
\Lambda' &= \frac{\Delta t C_{ss_{ijk}}}{r_i \Delta \theta_{j+1/2}}, \\
\Upsilon' &= \frac{\Delta t C_{ss_{ijk}}}{r_i \sin \theta_j \Delta \phi_{k+1/2}}.
\end{aligned} \tag{6.28}$$

Then, setting $\Gamma \rightarrow \Gamma + \Gamma'$, $\Lambda \rightarrow \Lambda + \Lambda'$, and $\Upsilon \rightarrow \Upsilon + \Upsilon'$ in equation (6.26), with Γ , Λ , and Υ as defined by (6.25), we obtain the following stability conditions

$$\begin{aligned}
\Delta t_{r_{ijk}} &\leq \frac{\Delta r_{i+1/2}}{|v_{r_{ijk}}| + C_{ss_{ijk}}}, \\
\Delta t_{\theta_{ijk}} &\leq \frac{r_i \Delta \theta_{j+1/2}}{|v_{\theta_{ijk}}| + C_{ss_{ijk}}}, \\
\Delta t_{\phi_{ijk}} &\leq \frac{r_i \sin \theta_j \Delta \phi_{k+1/2}}{|v_{\phi_{ijk}}| + C_{ss_{ijk}}},
\end{aligned} \tag{6.29}$$

associated with the r -, θ -, and ϕ -flows, respectively. Since the geometrical factors C_r , and C_θ , are generally greater than unity, they can be removed from the stability conditions for the r - and θ -flows. Inequalities (6.29) are usually referred to as the Courant-Friedrichs-Lewy (CFL) conditions for explicit hydrodynamics. They are used in the calculations to determine the optimum stable Δt required to advance the hydrodynamical system from a particular old time level (n) to a new level ($n + 1$).

The time steps Δt_r , Δt_θ , and Δt_ϕ are calculated independently for each computational cell, so that the CFL-time is defined by the minimum time step over the whole grid

$$\Delta t_{CFL} = \min \left\{ \Delta t_{r_{ijk}}, \Delta t_{\theta_{ijk}}, \Delta t_{\phi_{ijk}} \right\}. \quad (6.30)$$

The CFL-time is then established by those zones with very small spacings and large fluid velocities. Special restrictions may come from the inner shells where the cell volumes are the smallest [See Figure 4.1(a)]. Formally, for dynamic flows the accuracy of the numerical solutions should increase when smaller and smaller Δt 's are chosen. For this reason, the effective time step Δt is defined as an arbitrary fraction ($f \leq 9$) of the optimum Δt_{CFL} .

As we have commented earlier, the donor cell transport leads only to a first-order accurate numerical scheme. In fact, it introduces first-order truncation errors, which contribute to an artificial diffusion of mass and momentum within the computational grid. This implies that mass and momentum cannot be conserved locally with the donor cell method. On the other hand, these diffusion errors can become dominant in regions where there are large gradients, as would be the case for a shock.

The exact form of the truncation errors is easily obtained by expanding each term of our finite-difference equations in Taylor series. For reasons of simplicity, we shall

suppose that the radial grid is uniform and fixed, and that the r -advective term is written in its less compact form as in (C.19). Then using the donor cell replacements (6.16)-(6.18) and neglecting the acceleration gradients, the generalized finite-difference equation (6.6) will introduce the following dominant truncation errors

$$\begin{aligned}
& -\frac{1}{2} \left[\frac{\partial^2 X}{\partial t^2} \right]_{ijk} \Delta t - \dots \\
& \dots + \frac{1}{2} \left[|v_r| \frac{\partial^2 X}{\partial r^2} \right]_{ijk} \Delta r_i \pm \frac{1}{2} \left[\frac{1}{r^2} \frac{\partial X}{\partial r} \frac{\partial(r^2 v_r)}{\partial r} \right]_{ijk} \Delta r_i - \\
& -\frac{1}{6} \left[v_r \frac{\partial^3 X}{\partial r^3} \right]_{ijk} \Delta r_i^2 - \frac{1}{4} \left[\frac{1}{r^2} \frac{\partial^2 X}{\partial r^2} \frac{\partial(r^2 v_r)}{\partial r} \right]_{ijk} \Delta r_i^2 - \frac{1}{8} \left[\frac{1}{r^2} \frac{\partial X}{\partial r} \frac{\partial^2(r^2 v_r)}{\partial r^2} \right]_{ijk} \Delta r_i^2 - \\
& -\frac{1}{24} \left[X \frac{1}{r^2} \frac{\partial^3(r^2 v_r)}{\partial r^3} \right]_{ijk} \Delta r_i^2 \pm O\{(\Delta r_i)^3\} - \dots \\
& \dots + \frac{1}{2} \left[|v_\theta| \frac{1}{r} \frac{\partial^2 X}{\partial \theta^2} \right]_{ijk} \Delta \theta_j \pm \frac{1}{2} \left[\frac{1}{r \sin \theta} \frac{\partial(\sin \theta v_\theta)}{\partial \theta} \frac{\partial X}{\partial \theta} \right]_{ijk} \Delta \theta_j - \\
& -\frac{1}{6} \left[v_\theta \frac{1}{r} \frac{\partial^3 X}{\partial \theta^3} \right]_{ijk} \Delta \theta_j^2 - \frac{1}{4} \left[\frac{1}{r \sin \theta} \frac{\partial(\sin \theta v_\theta)}{\partial \theta} \frac{\partial^2 X}{\partial \theta^2} \right]_{ijk} \Delta \theta_j^2 - \\
& -\frac{1}{8} \left[\frac{1}{r \sin \theta} \frac{\partial^2(\sin \theta v_\theta)}{\partial \theta^2} \frac{\partial X}{\partial \theta} \right]_{ijk} \Delta \theta_j^2 - \frac{1}{24} \left[X \frac{1}{r \sin \theta} \frac{\partial^3(\sin \theta v_\theta)}{\partial \theta^3} \right]_{ijk} \Delta \theta_j^2 \pm \\
& \pm O\{(\Delta \theta_j)^3\} - \dots \\
& \dots + \frac{1}{2} \left[|v_\phi| \frac{1}{r \sin \theta} \frac{\partial^2 X}{\partial \phi^2} \right]_{ijk} \Delta \phi_k \pm \frac{1}{2} \left[\frac{1}{r \sin \theta} \frac{\partial v_\phi}{\partial \phi} \frac{\partial X}{\partial \phi} \right]_{ijk} \Delta \phi_k - \\
& -\frac{1}{6} \left[v_\phi \frac{1}{r \sin \theta} \frac{\partial^3 X}{\partial \phi^3} \right]_{ijk} \Delta \phi_k^2 - \frac{1}{4} \left[\frac{1}{r \sin \theta} \frac{\partial v_\phi}{\partial \phi} \frac{\partial^2 X}{\partial \phi^2} \right]_{ijk} \Delta \phi_k^2 -
\end{aligned}$$

$$\begin{aligned}
& -\frac{1}{8} \left[\frac{1}{r \sin \theta} \frac{\partial^2 v_\phi}{\partial \phi^2} \frac{\partial X}{\partial \phi} \right]_{ijk} \Delta \phi_k^2 - \frac{1}{24} \left[X \frac{1}{r \sin \theta} \frac{\partial^3 v_\phi}{\partial \phi^3} \right]_{ijk} \Delta \phi_k^2 \pm \\
& \pm O\{(\Delta \phi_k)^3\} - \dots, \tag{6.31}
\end{aligned}$$

where we have retained effective diffusion coefficients through terms of order Δt , Δr^2 , $\Delta \theta^2$, and $\Delta \phi^2$. The first error term in (6.31) is not a dominant one because the relative change per step of the cell densities is generally small. On the other hand, the truncation errors related to the finite spatial width of the cells, such as the leading terms in the second, fifth, and ninth rows of (6.31), are more likely to be dominant since limitations of machine storage and running time constrain us to work with a rather coarse mesh for two- and three-dimensions.

According to Hirt [52], those truncation errors involving a second space derivative of the density X in (6.31) would contribute more to the local diffusion of mass and momentum. However, in regions where strong shocks develop, the spurious diffusion of the hydrodynamical variables could be very well governed by those terms containing first space derivatives of the velocity and density.

For a radially moving, non-uniform grid, the form of the leading diffusion errors in the second row of (6.31) is slightly modified and extra terms appear. From the donor cell prescriptions (6.16), if $U_{i+1/2,jk} \geq 0$ and $U_{i-1/2,jk} \geq 0$, we have

$$\begin{aligned}
& \dots - \left[U \frac{\partial X}{\partial r} \right]_{ijk} \left\{ \frac{1 - \nu_{i+1}}{1 + \nu_{i+1}} \right\} + \\
& + \left[U \frac{\partial^2 X}{\partial r^2} \right]_{ijk} \frac{\Delta r_i}{(1 + \nu_{i+1})} + \left[\frac{1}{r^2} \frac{\partial X}{\partial r} \frac{\partial(r^2 U)}{\partial r} \right]_{ijk} \frac{\Delta r_i}{(1 + \nu_{i+1})} + \\
& + \frac{1}{4} \left[X \frac{1}{r^2} \frac{\partial^2(r^2 U)}{\partial r^2} \right]_{ijk} \Delta r_i (1 - \nu_{i+1}) - \dots, \tag{6.32}
\end{aligned}$$

where $\nu_{i+1} = \Delta r_{i+1}/\Delta r_i$. On the other hand, if $U_{i+1/2,jk} < 0$ and $U_{i-1/2,jk} < 0$, we then obtain

$$\begin{aligned} & \dots - \left[U \frac{\partial X}{\partial r} \right]_{ijk} \left\{ \frac{\nu_{i+1} - 1}{\nu_{i+1} + 1} \right\} - \\ & - \left[U \frac{\partial^2 X}{\partial r^2} \right]_{ijk} \frac{\nu_{i+1}^2 \Delta r_i}{(1 + \nu_{i+1})} - \left[\frac{1}{r^2} \frac{\partial X}{\partial r} \frac{\partial(r^2 U)}{\partial r} \right]_{ijk} \frac{\nu_{i+1}^2 \Delta r_i}{(1 + \nu_{i+1})} - \\ & - \frac{1}{4} \left[X \frac{1}{r^2} \frac{\partial^2(r^2 U)}{\partial r^2} \right]_{ijk} \Delta r_i (\nu_{i+1} - 1) + \dots \end{aligned} \quad (6.33)$$

In (6.32) and (6.33), we have neglected all terms beyond those of first order.

The errors in the first and third rows, have been introduced by the non-uniform nature of the grid. That is, if at some step, we freeze out the computational grid by setting $v_{g_i} = 0$, these terms will survive and only the errors carried by the grid-contraction difference will disappear. From a direct comparison of (6.32) and (6.33) with the leading radial terms in (6.31), we may note that a non-uniform grid provides a lower accuracy due to the presence of a zero-order truncation error, which does not arise when differencing on a uniform grid. However, the influence of this error can be circumvented if the computational grid moves approximately with the radial flow. Then, for $v_{r_{ijk}} \sim v_{g_i}$ and $\nu_{i+1} = O\{1\}$, the effective contribution of this error is largely compensated by the fact that the magnitudes of the leading truncation errors, in the second and third rows of (6.32) and (6.33), will be always much smaller than those of (6.31) for a fixed uniform grid, since generally $|U_{ijk}| \ll |v_{r_{ijk}}|$.

On the other hand, at some advanced time in the collapse, we will be interested in having much greater spatial resolution in the inner regions than in the outermost regions. At that time, if the grid has become stretched enough, we may freeze it out and carry on the calculation with the grid fixed. In this case, since ν_{i+1} will increase

towards the external boundary, the accuracy is formally poor in the outer regions where the Δr_i are larger. However, in the innermost regions where the radial zones will be even smaller than the θ and ϕ spacings, the ν_{i+1} are nearly unity. Hence, the zero-order term in (6.32) and (6.33) will usually be small. In any case, the leading diffusion errors in the second row become much smaller than they would be for a uniform coarse grid, since typically the stretched Δr_i correspond to very small fractions of the initially uniform Δr_i .

6.7 Finite-Difference Hydrodynamic Equations

In the previous sections, we have presented the basic numerical method and have introduced the various technical tools necessary for the construction of the 1-, 2-, and 3-dimensional versions of the code. Here, we shall display the equations in finite-difference form as they are actually used in the calculations. Since the 1- and 2-dimensional versions of the code are restricted cases of the full 3-dimensional code, in this section we shall only write the finite-difference equations for 3-space dimensions.

We first consider the continuity equation and then the r - and θ -components of the momentum transfer equation, for of all those computational cells which do not coincide with any of the boundaries of the system. The formal treatment of the hydrodynamical boundaries is developed in Section 6.9

(A) CONTINUITY EQUATION.

The exact differential equation (3.21) is written in difference form by using equation (6.6) with the replacements (6.12)-(6.14), for the advective terms, and (6.21), for the grid contraction term. Then, setting $X = \rho$, we obtain

$$\rho_{ijk}^{n+1} = \rho_{ijk}^n - \Delta t \left\{ \frac{[r_{i+1/2}^2 \langle \rho \rangle_{i+1/2,jk} U_{i+1/2,jk} - r_{i-1/2}^2 \langle \rho \rangle_{i-1/2,jk} U_{i-1/2,jk}]}{\frac{1}{3}(r_{i+1/2}^3 - r_{i-1/2}^3)} + \right.$$

$$\begin{aligned}
& + \frac{[\sin \theta_{j+1/2} \langle \rho \rangle_{i,j+1/2,k} v_{\theta_{i,j+1/2,k}} - \sin \theta_{j-1/2} \langle \rho \rangle_{i,j-1/2,k} v_{\theta_{i,j-1/2,k}}]}{\langle r_i \rangle \sin \theta_j \Delta \theta_{j+1/2}} + \\
& + \frac{[\langle \rho \rangle_{ij,k+1/2} v_{\phi_{ij,k+1/2}} - \langle \rho \rangle_{ij,k-1/2} v_{\phi_{ij,k-1/2}}]}{\langle r_i \rangle \sin \theta_j \Delta \phi_{k+1/2}} \Big\}^n - \\
& - \rho_{ijk}^n \frac{[(r_{i+1/2}^3 - r_{i-1/2}^3)^{n+1} - (r_{i+1/2}^3 - r_{i-1/2}^3)^n]}{(r_{i+1/2}^3 - r_{i-1/2}^3)^{n+1}}, \tag{6.34}
\end{aligned}$$

where the cell interface densities $\langle \rho \rangle$ are given by the donor-cell prescriptions (6.16)-(6.18). Equation (6.34) as it stands, is then used to compute the mass-density at the new step $n+1$, for all main grid-cells with indices $i = 1, 2, \dots, N_r - 1$; $j = 1, 2, \dots, N_\theta - 1$; and $k = 1, 2, \dots, N_\phi - 1$.

(B) RADIAL MOMENTUM TRANSFER EQUATION.

In a similar manner, equation (3.22) is expressed in difference form by again using the same replacements as above, for the transport part in equation (6.6), and the three-point approximation (C.14), for the acceleration gradients. Then, setting $X = \rho v_r$, we have for a typical cell

$$\begin{aligned}
& (\rho v_r)_{ijk}^{n+1} = (\rho v_r)_{ijk}^n - \\
& - \Delta t \left\{ \frac{[r_{i+1/2}^2 \langle \rho v_r \rangle_{i+1/2,jk} U_{i+1/2,jk} - r_{i-1/2}^2 \langle \rho v_r \rangle_{i-1/2,jk} U_{i-1/2,jk}]}{\frac{1}{3}(r_{i+1/2}^3 - r_{i-1/2}^3)} + \right. \\
& + \frac{[\sin \theta_{j+1/2} \langle \rho v_r \rangle_{i,j+1/2,k} v_{\theta_{i,j+1/2,k}} - \sin \theta_{j-1/2} \langle \rho v_r \rangle_{i,j-1/2,k} v_{\theta_{i,j-1/2,k}}]}{\langle r_i \rangle \sin \theta_j \Delta \theta_{j+1/2}} + \\
& + \frac{[\langle \rho v_r \rangle_{ij,k+1/2} v_{\phi_{ij,k+1/2}} - \langle \rho v_r \rangle_{ij,k-1/2} v_{\phi_{ij,k-1/2}}]}{\langle r_i \rangle \sin \theta_j \Delta \phi_{k+1/2}} \Big\}^n - \\
& - (\rho v_r)_{ijk}^n \frac{[(r_{i+1/2}^3 - r_{i-1/2}^3)^{n+1} - (r_{i+1/2}^3 - r_{i-1/2}^3)^n]}{(r_{i+1/2}^3 - r_{i-1/2}^3)^{n+1}} -
\end{aligned}$$

$$\begin{aligned}
& -\Delta t \left\{ \rho_{ijk} \frac{1}{2\Delta r_{i+1/2}} \left[\frac{\Delta r_i}{\Delta r_{i+1}} (\Phi_{i+1,jk} - \Phi_{ijk}) + \frac{\Delta r_{i+1}}{\Delta r_i} (\Phi_{ijk} - \Phi_{i-1,jk}) \right] + \right. \\
& + \frac{1}{2\Delta r_{i+1/2}} \left[\frac{\Delta r_i}{\Delta r_{i+1}} (p_{i+1,jk} - p_{ijk}) + \frac{\Delta r_{i+1}}{\Delta r_i} (p_{ijk} - p_{i-1,jk}) \right] - \\
& \left. - \rho_{ijk} \frac{1}{r_i} (v_{\theta_{ijk}}^2 + v_{\phi_{ijk}}^2) \right\}^n, \tag{6.35}
\end{aligned}$$

where the cell-boundary quantities $\langle \rho v_r \rangle$ are treated in the same manner as the mass-density by using prescriptions (6.16)-(6.18). Equation (6.35) then gives the r -momentum density at the new time level $n+1$, for all of the main grid-cells with $i = 1, 2, \dots, N_r - 1$; $j = 1, 2, \dots, N_\theta - 1$; and $k = 1, 2, \dots, N_\phi - 1$. The new radial velocities are computed, using the updated densities, from

$$v_{r_{ijk}}^{n+1} = \frac{\rho_{ijk}^n v_{r_{ijk}}^n}{\rho_{ijk}^{n+1}} - \Delta t \frac{1}{\rho_{ijk}^{n+1}} \{ \dots \}_{ijk}^n. \tag{6.36}$$

(C) θ -MOMENTUM TRANSFER EQUATION.

Following exactly the same procedure as before but now using the replacement (C.16) for the acceleration gradients, equation (3.23) becomes

$$\begin{aligned}
& (\rho v_\theta)_{ijk}^{n+1} = (\rho v_\theta)_{ijk}^n - \\
& - \Delta t \left\{ \frac{[r_{i+1/2}^2 \langle \rho v_\theta \rangle_{i+1/2,jk} U_{i+1/2,jk} - r_{i-1/2}^2 \langle \rho v_\theta \rangle_{i-1/2,jk} U_{i-1/2,jk}]}{\frac{1}{3}(r_{i+1/2}^3 - r_{i-1/2}^3)} + \right. \\
& + \frac{[\sin \theta_{j+1/2} \langle \rho v_\theta \rangle_{i,j+1/2,k} v_{\theta_{i,j+1/2,k}} - \sin \theta_{j-1/2} \langle \rho v_\theta \rangle_{i,j-1/2,k} v_{\theta_{i,j-1/2,k}}]}{\langle r_i \rangle \sin \theta_j \Delta \theta_{j+1/2}} + \\
& + \frac{[\langle \rho v_\theta \rangle_{ij,k+1/2} v_{\phi_{ij,k+1/2}} - \langle \rho v_\theta \rangle_{ij,k-1/2} v_{\phi_{ij,k-1/2}}]}{\langle r_i \rangle \sin \theta \Delta \phi_{k+1/2}} \Big\}^n - \\
& - (\rho v_\theta)_{ijk}^n \frac{[(r_{i+1/2}^3 - r_{i-1/2}^3)^{n+1} - (r_{i+1/2}^3 - r_{i-1/2}^3)^n]}{(r_{i+1/2}^3 - r_{i-1/2}^3)^{n+1}} -
\end{aligned}$$

$$\begin{aligned}
& -\Delta t \left\{ \rho_{ijk} \frac{1}{r_i} \frac{1}{2\Delta\theta_{j+1/2}} \left[\frac{\Delta\theta_j}{\Delta\theta_{j+1}} (\Phi_{i,j+1,k} - \Phi_{ijk}) + \frac{\Delta\theta_{j+1}}{\Delta\theta_j} (\Phi_{ijk} - \Phi_{i,j-1,k}) \right] + \right. \\
& + \frac{1}{r_i} \frac{1}{2\Delta\theta_{j+1/2}} \left[\frac{\Delta\theta_j}{\Delta\theta_{j+1}} (p_{i,j+1,k} - p_{ijk}) + \frac{\Delta\theta_{j+1}}{\Delta\theta_j} (p_{ijk} - p_{i,j-1,k}) \right] + \\
& \left. + \rho_{ijk} \frac{1}{r_i} (v_{r_{ijk}} v_{\theta_{ijk}} - v_{\phi_{ijk}}^2 \cos \theta_j / \sin \theta_j) \right\}^n, \tag{6.37}
\end{aligned}$$

where the θ -momentum is again advected by using the donor-cell prescriptions (6.16)-(6.18)

In analogy with equation (6.36), the θ -velocity is then computed as a primary variable from equation (6.37) by setting

$$v_{\theta_{ijk}}^{n+1} = \frac{\rho_{ijk}^n v_{\theta_{ijk}}^n}{\rho_{ijk}^{n+1}} - \Delta t \frac{1}{\rho_{ijk}^{n+1}} \{ \dots \}_{ijk}^n, \tag{6.38}$$

for all cells with $i = 1, 2, \dots, N_r - 1$; $j = 1, 2, \dots, N_\theta - 1$; and $k = 1, 2, \dots, N_\phi - 1$.

6.8 The Angular Momentum Transport

The ϕ -component of the momentum transfer equation [See eqs.(3.18) and (3.24)], has been expressed in terms of the specific angular momentum $A = r \sin \theta v_\phi$, which is physically a more relevant quantity than the simple ϕ -velocity for rotating protostar collapse calculations.

The physical importance of this variable lies in the fact that for axisymmetric flows, it is exactly conserved along a fluid streamline if the dissipative effects caused by viscosity or magnetic fields are neglected [115]. This means that under such ideal conditions the specific angular momentum A is locally conserved in the axially symmetric collapse of protostellar configurations. However, as discussed in Section 6.6, strict local conservation of the angular momentum, or of any other hydrodynamical variable, cannot be achieved numerically with the donor cell scheme. If we set $X = \rho A$, we note

from (6.31) that the donor-cell advection introduces first-order errors, whose effect is to strongly diffuse angular momentum between advected fluid elements (cells) which should theoretically locally conserve specific angular momentum.

Numerical efforts addressed to minimizing the effects of diffusion errors on the local conservation of angular momentum in protostellar collapse calculations, have led to the concept of consistent advection. This notion was first introduced by Norman, Wilson, and Barton [88], and successively applied with good results by Boss [13] and by Norman and Wilson [87] in their calculations. Basically, by a consistent advection of the angular momentum, we mean that instead of fluxing the quantity $\langle \rho A \rangle$ as a single variable, we flux the product $\langle \rho \rangle \langle A \rangle$ in such a way as to transport the angular momentum consistently with the mass through the computational grid. In this manner, the numerical diffusion of angular momentum within the grid can be effectively minimized by advecting $\langle A \rangle$ with a more accurate method.

We shall implement here a technique intensively tested by Boss [13], which consists of calculating the cell boundary values of the specific angular momentum A as the square root of the product between the specific angular momenta of the gaining and losing cells, while $\langle \rho \rangle$ is determined by the density of the adjoining cell from which the fluid is coming (donor cell). By applying this method, we partially centre A at the cell interfaces and hence, improve the local conservation of angular momentum without compromising the stability of the donor cell scheme.

With the above considerations in mind, we then write equation (3.24) in finite-difference form by again using equation (6.6) (with $X = \rho A$) together with the replacements (6.12)-(6.14) and (6.21), for the transport part, and (C.17) for the acceleration

gradients. So, defining for a typical main grid-cell

$$A_{ijk} = r_i \sin \theta_j v_{\phi_{ijk}}, \quad (6.39)$$

we have that

$$\begin{aligned} (\rho A)_{ijk}^{n+1} &= (\rho A)_{ijk}^n - \\ &- \Delta t \left\{ \frac{[r_{i+1/2}^2 (\langle \rho \rangle \langle A \rangle)_{i+1/2,jk} U_{i+1/2,jk} - r_{i-1/2}^2 (\langle \rho \rangle \langle A \rangle)_{i-1/2,jk} U_{i-1/2,jk}]}{\frac{1}{3}(r_{i+1/2}^3 - r_{i-1/2}^3)} + \right. \\ &+ \frac{[\sin \theta_{j+1/2} (\langle \rho \rangle \langle A \rangle)_{i,j+1/2,k} v_{\theta_{i,j+1/2,k}} - \sin \theta_{j-1/2} (\langle \rho \rangle \langle A \rangle)_{i,j-1/2,k} v_{\theta_{i,j-1/2,k}}]}{\langle r_i \rangle \sin \theta_j \Delta \theta_{j+1/2}} + \\ &+ \left. \frac{[(\langle \rho \rangle \langle A \rangle)_{ij,k+1/2} v_{\phi_{ij,k+1/2}} - (\langle \rho \rangle \langle A \rangle)_{ij,k-1/2} v_{\phi_{ij,k-1/2}}]}{\langle r_i \rangle \sin \theta_j \Delta \phi_{k+1/2}} \right\}^n - \\ &- (\rho A)_{ijk}^n \frac{[(r_{i+1/2}^3 - r_{i-1/2}^3)^{n+1} - (r_{i+1/2}^3 - r_{i-1/2}^3)^n]}{(r_{i+1/2}^3 - r_{i-1/2}^3)^{n+1}} - \\ &- \left\{ \rho_{ijk} \frac{[\Phi_{ij,k+1} - \Phi_{ij,k-1}]}{2\Delta \phi_k} + \frac{[p_{ij,k+1} - p_{ij,k-1}]}{2\Delta \phi_k} \right\}^n, \quad (6.40) \end{aligned}$$

where for the radial advection, we define

$$\langle A \rangle_{i\pm 1/2,jk} = \begin{cases} +\sqrt{A_{ijk} A_{i\pm 1,jk}} & \text{if } A_{ijk} > 0 \\ -\sqrt{A_{ijk} A_{i\pm 1,jk}} & \text{if } A_{ijk} < 0 \end{cases} \quad (6.41)$$

for $A_{ijk} A_{i\pm 1,jk} \geq 0$, while the $\langle \rho \rangle$ are given by the donor-cell prescriptions (6.16). If $A_{ijk} A_{i\pm 1,jk} < 0$, we set $\langle \rho \rangle_{i\pm 1/2,jk} \langle A \rangle_{i\pm 1/2,jk} = \langle \rho A \rangle_{i\pm 1/2,jk}$ in equation (6.40) and perform the advection according to the usual donor-cell replacements.

Similarly, for the θ -advection, we have

$$\langle A \rangle_{i,j\pm 1/2,k} = \begin{cases} +\sqrt{A_{ijk} A_{i,j\pm 1,k}} & \text{if } A_{ijk} > 0 \\ -\sqrt{A_{ijk} A_{i,j\pm 1,k}} & \text{if } A_{ijk} < 0 \end{cases}$$

(6.42)

for $A_{ijk}A_{i,j\pm 1,k} \geq 0$. The transport of mass along the θ -direction is performed according to the replacements (6.17). If $A_{ijk}A_{i,j\pm 1,k} < 0$, we set as before $\langle \rho \rangle_{i,j\pm 1/2,k} \langle A \rangle_{i,j\pm 1/2,k} = \langle \rho A \rangle_{i,j\pm 1/2,k}$ and use the donor cell advection.

Finally, for the ϕ -advection, we define

$$\langle A \rangle_{ij,k\pm 1/2} = \begin{cases} +\sqrt{A_{ijk}A_{ij,k\pm 1}} & \text{if } A_{ijk} > 0 \\ -\sqrt{A_{ijk}A_{ij,k\pm 1}} & \text{if } A_{ijk} < 0 \end{cases} \quad (6.43)$$

for $A_{ijk}A_{ij,k\pm 1} \geq 0$, while the $\langle \rho \rangle$ are as defined by (6.18). If $A_{ijk}A_{ij,k\pm 1} < 0$, we again make recourse to the donor cell transport.

Equation (6.40) is then used in the calculations to compute the specific angular momentum at the new time level $n + 1$ by setting

$$A_{ijk}^{n+1} = \frac{\rho_{ijk}^n A_{ijk}^n}{\rho_{ijk}^{n+1}} - \Delta t \frac{1}{\rho_{ijk}^{n+1}} \{ \dots \}_{ijk}^n, \quad (6.44)$$

for all computational cells with indices $i = 1, 2, \dots, N_r - 1$; $j = 1, 2, \dots, N_\theta - 1$; and $k = 1, 2, \dots, N_\phi - 1$. It is interesting to note that although the specific angular momentum is regarded as a primary variable, the ϕ -velocity component would be equally important from a computational point of view, since it is always needed in equations (6.34), (6.35), (6.37), and (6.40), to perform mass and momentum transport along the ϕ -direction. The ϕ -velocities are easily computed from the updated angular momentum distribution by using relation (6.39). Similarly, the updated angular velocities ω_{ijk} are obtained as functions of the ϕ -velocities and positions in the grid by means of the relation $\omega = v_\phi / r \sin \theta$.

That the partially centred scheme above is effectively superior to the pure donor cell differencing, can be observed by comparing resulting truncation errors associated

with the advective part of equation (6.40), for the two methods. Retaining only first-order terms, we find from (6.31) that the donor cell formalism introduces the following dominant errors

$$\begin{aligned}
& -\frac{1}{2} \left[\frac{\partial^2(\rho A)}{\partial t^2} \right]_{ijk} \Delta t - \dots \\
& \dots + \frac{1}{2} \left[|v_r| \frac{\partial^2(\rho A)}{\partial r^2} \right]_{ijk} \Delta r_i \pm \frac{1}{2} \left[\frac{1}{r^2} \frac{\partial(\rho A)}{\partial r} \frac{\partial(r^2 v_r)}{\partial r} \right]_{ijk} \Delta r_i - \dots \\
& \dots + \frac{1}{2} \left[|v_\theta| \frac{1}{r} \frac{\partial^2(\rho A)}{\partial \theta^2} \right]_{ijk} \Delta \theta_j \pm \frac{1}{2} \left[\frac{1}{r \sin \theta} \frac{\partial(\sin \theta v_\theta)}{\partial \theta} \frac{\partial(\rho A)}{\partial \theta} \right]_{ijk} \Delta \theta_j - \dots \\
& \dots + \frac{1}{2} \left[|v_\phi| \frac{1}{r \sin \theta} \frac{\partial^2(\rho A)}{\partial \phi^2} \right]_{ijk} \Delta \phi_k \pm \frac{1}{2} \left[\frac{1}{r \sin \theta} \frac{\partial v_\phi}{\partial \phi} \frac{\partial(\rho A)}{\partial \phi} \right]_{ijk} \Delta \phi_k - \dots, \quad (6.45)
\end{aligned}$$

where for simplicity it has been assumed that $v_{g_i} = 0$ and that the grid is uniform. Expanding equation (6.40) in a Taylor series, with the same simplifying considerations used for deducing the donor cell errors (6.31), we find for the partially centered prescriptions (6.41)-(6.43), the following dominant truncation errors

$$\begin{aligned}
& -\frac{1}{2} \left[\frac{\partial^2(\rho A)}{\partial t^2} \right]_{ijk} \Delta t - \dots \\
& \dots + \frac{1}{2} \left[|v_r| \left(\frac{\partial \rho}{\partial r} \frac{\partial A}{\partial r} + A \frac{\partial^2 \rho}{\partial r^2} \right) \right]_{ijk} \Delta r_i \pm \frac{1}{2} \left[A \frac{1}{r^2} \frac{\partial \rho}{\partial r} \frac{\partial(r^2 v_r)}{\partial r} \right]_{ijk} \Delta r_i - \dots \\
& \dots + \frac{1}{2} \left[|v_\theta| \frac{1}{r} \left(\frac{\partial \rho}{\partial \theta} \frac{\partial A}{\partial \theta} + A \frac{\partial^2 \rho}{\partial \theta^2} \right) \right]_{ijk} \Delta \theta_j \pm \frac{1}{2} \left[A \frac{1}{r \sin \theta} \frac{\partial \rho}{\partial \theta} \frac{\partial(\sin \theta v_\theta)}{\partial \theta} \right]_{ijk} \Delta \theta_j - \dots \\
& \dots + \frac{1}{2} \left[|v_\phi| \frac{1}{r \sin \theta} \left(\frac{\partial \rho}{\partial \phi} \frac{\partial A}{\partial \phi} + A \frac{\partial^2 \rho}{\partial \phi^2} \right) \right]_{ijk} \Delta \phi_k \pm \frac{1}{2} \left[A \frac{1}{r \sin \theta} \frac{\partial \rho}{\partial \phi} \frac{\partial v_\phi}{\partial \phi} \right]_{ijk} \Delta \phi_k - \dots, \quad (6.46)
\end{aligned}$$

where again only first-order terms have been retained. Developing the spatial derivatives involved in the diffusion terms (6.45) and then comparing with (6.51), we find that the dominant donor-cell errors

$$\begin{aligned}
& \frac{1}{2} \left[|v_r| \rho \frac{\partial^2 A}{\partial r^2} \right]_{ijk} \Delta r_i; \quad \frac{1}{2} \left[|v_\theta| \frac{\rho}{r} \frac{\partial^2 A}{\partial \theta^2} \right]_{ijk} \Delta \theta_j; \quad \frac{1}{2} \left[|v_\phi| \frac{\rho}{r \sin \theta} \frac{\partial^2 A}{\partial \phi^2} \right]_{ijk} \Delta \phi_k; \\
& \frac{1}{2} \left[|v_r| \frac{\partial A}{\partial r} \frac{\partial \rho}{\partial r} \right]_{ijk} \Delta r_i; \quad \frac{1}{2} \left[\frac{|v_\theta|}{r} \frac{\partial A}{\partial \theta} \frac{\partial \rho}{\partial \theta} \right]_{ijk} \Delta \theta_j; \quad \frac{1}{2} \left[\frac{|v_\phi|}{r \sin \theta} \frac{\partial A}{\partial \phi} \frac{\partial \rho}{\partial \phi} \right]_{ijk} \Delta \phi_k; \quad (6.47) \\
& \pm \frac{1}{2} \left[\frac{\rho}{r^2} \frac{\partial A}{\partial r} \frac{\partial(r^2 v_r)}{\partial r} \right]_{ijk}; \quad \pm \frac{1}{2} \left[\frac{\rho}{r \sin \theta} \frac{\partial A}{\partial \theta} \frac{\partial(\sin \theta v_\theta)}{\partial \theta} \right]_{ijk} \Delta \theta_j; \\
& \pm \frac{1}{2} \left[\frac{\rho}{r \sin \theta} \frac{\partial A}{\partial \phi} \frac{\partial v_\phi}{\partial \phi} \right]_{ijk} \Delta \phi_k
\end{aligned}$$

effectively disappear if angular momentum is advected with the partially centered scheme. Highly diffusive terms containing second space derivatives of the mass-density survive in (6.46) because the mass is still being fluxed according to the donor cell method, while similar terms containing the specific angular momentum (the first row in (6.47)) are not present due to the partial centring at cell borders. Therefore, the spurious diffusion of the specific angular momentum is minimized and its local conservation is improved to nearly second-order accuracy.

6.9 Hydrodynamical Boundary Conditions

The finite-difference equations (6.34), (6.35), (6.37), and (6.40) can be used for any interior cell which is not adjacent to or coinciding with any of the boundaries of the computational grid. For 2- or 3-dimensional calculations, our numerical domain consists of three main critical regions where the flow is constrained, i.e. the centre ($r = 0$), the rotational axis ($\theta = 0$), and the bounding spherical surface ($r = R_0$). Also, a

reflective boundary condition for the θ -directed flow, is applied about the equatorial plane ($\theta = \pi/2$) to reduce the computational cost and run time. Furthermore, in 3-space dimensions, the differencing along the azimuthal direction is carried out by enforcing a periodic boundary condition, which is applied for those zones which are adjacent to the cells centered at the coinciding points $\phi = 0$ and $\phi = 2\pi$.

Each of these critical boundaries is handled in such a way as to numerically ensure the global conservation of the advected quantities. In the following, we shall describe and implement the modifications to our set of finite-difference equations.

(A) THE ROTATIONAL AXIS.

The rotational axis is numerically represented by a conical family of cells whose geometrical centres coincide with the rotation axis [See Figure 4.1(a)]. The axial boundary conditions are then specified at each step by setting $v_\theta = v_\phi = 0$ at the cell centres “i0k”, so that the axial cells will always represent a dump for both the theta momentum and the angular momentum. Hereafter, the axial variables will be denoted by X'_i , (i.e. X'_i will be the replacement for X_{i0k}).

Although the theta and angular momenta are not axially advected, some simple modifications are however required in equations (6.37) and (6.40) at the interfaces between the axial ($\theta = 0$) and the main grid-cells ($j = 1$). Since each $j = 1$ cell can lose θ -momentum into the axial cells at the rate

$$-\frac{\sin \theta_{1-1/2} \langle \rho v_\theta \rangle_{i,1-1/2,k} v_{\theta_{i,1-1/2,k}}}{\langle r_i \rangle \sin \theta_1 \Delta \theta_{1+1/2}},$$

the donor-cell fluxing across the interfaces $(i, 1 - 1/2, k)$ is modified by setting

$$\langle \rho v_\theta \rangle_{i,1-1/2,k} = \begin{cases} 0 & \text{if } v_{\theta_{i,1-1/2,k}} \geq 0 \\ \rho_{i1k} v_{\theta_{i1k}} & \text{if } v_{\theta_{i,1-1/2,k}} < 0 \end{cases} \quad (6.48)$$

where $v_{\theta,i,1-1/2,k} = \frac{1}{2}v_{\theta,i1k}$. Furthermore, the θ -gradients in equation (6.37) for the $j = 1$ cells are evaluated using the axial values of the pressure and gravitational potential, p'_i and Φ'_i , respectively.

On the other hand, the angular momentum is not fluxed into the axial cells, as is the θ -momentum, because $A_{i0k} \rightarrow A'_i = 0$ along the axis and hence, from (6.42) it follows that $\langle A \rangle_{i,1-1/2,k} = 0$ at any step. Thus, the modification for the θ -advective terms in equation (6.40), when $j = 1$, is automatic. On the other hand, if the angular momentum is advected with the donor cell scheme, the loss into the axial cells should be computed as in (6.48).

Only mass and radial momentum may be interchanged between the axial and main grid-cells at $j = 1$, (ρ'_i , v'_{r_i} , and U'_i will now be the replacements for “ ρ_{i0k} ”, “ $v_{r_{i0k}}$ ”, and “ U_{i0k} ”). This fact can also be analytically observed from the limiting forms of equations (3.21) and (3.22) at the singularity $\theta = 0$. Integrating these equations over ϕ and taking the limit when $\theta \rightarrow 0$, we obtain the axial equations

$$\frac{\partial \rho'}{\partial t} + 3 \frac{\partial(r^2 \rho' U')}{\partial(r^3)} - \frac{1}{r} \int_0^{2\pi} \frac{\partial(\sin \theta \rho v_\theta)}{\partial(\cos \theta)} \Big|_{\theta=0} d\phi = -3\rho' \frac{\partial(r^2 v_g)}{\partial(r^3)}, \quad (6.49)$$

$$\begin{aligned} \frac{\partial(\rho' v'_r)}{\partial t} + 3 \frac{\partial(r^2 \rho' v'_r U')}{\partial(r^3)} - \frac{1}{r} \int_0^{2\pi} \frac{\partial(\sin \theta \rho v_r v_\theta)}{\partial(\cos \theta)} \Big|_{\theta=0} d\phi &= -3\rho' v'_r \frac{\partial(r^2 v_g)}{\partial(r^3)} - \\ &- \rho' \frac{\partial \Phi'}{\partial r} - \frac{\partial p'}{\partial r}, \end{aligned} \quad (6.50)$$

where the primed variables are functions only of r and time. The structure of these equations reveals that any axial cell can experience r - and θ -advection but never ϕ -advection. Their finite-difference form is similar to that exhibited by equations (6.34) and (6.35) for the main grid-cells, except for the θ -advective terms. The correct differences for such terms can easily be obtained by keeping track of how much mass, or r -momentum, enters or leaves the axial cells, i.e. by just enforcing mass and r -momentum

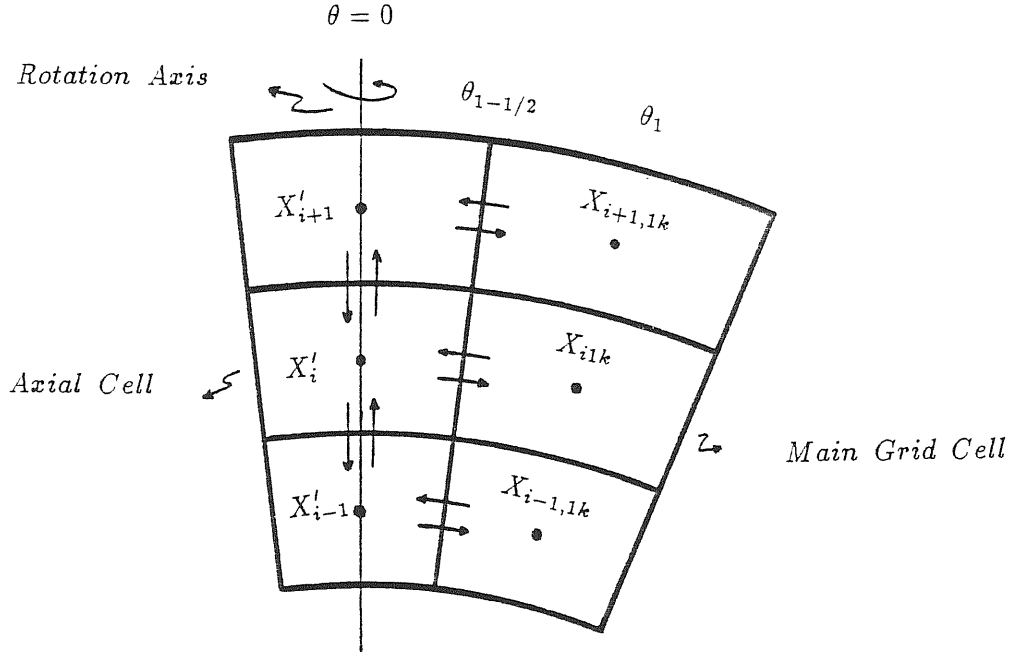


Figure 6.4: Portion of an (r, θ) -slice representing control volumes for axial advection

conservation across the interfaces $(i, 1 - 1/2, k)$ [See Figure 6.4]. A particular cell $(i1k)$ losing mass at the rate

$$\frac{\Delta M_{i1k}}{\Delta t} = \left(\frac{\sin \theta_{1-1/2} \langle \rho \rangle_{i,1-1/2,k} v_{\theta_{i,1-1/2,k}}}{\langle r_i \rangle} \right) \left[\frac{1}{3} (r_{i+1/2}^3 - r_{i-1/2}^3) \Delta \phi_{k+1/2} \right],$$

will contribute to the density of the i th axial cell by

$$\frac{\Delta \rho'_i}{\Delta t} = -\frac{1}{V'_i} \frac{\Delta M_{i1k}}{\Delta t}, \quad (6.51)$$

where V'_i , calculated as

$$V'_i = \frac{2\pi}{3} (r_{i+1/2}^3 - r_{i-1/2}^3) \int_0^{\theta_{1-1/2}} \sin \theta d\theta = \frac{2\pi}{3} (r_{i+1/2}^3 - r_{i-1/2}^3) (1 - \cos \theta_{1-1/2}), \quad (6.52)$$

corresponds to the volume of the i th axial cell occupied by the mass which is coming from the main grid. The net change in the axial density ρ'_i (due to advection in θ) is, therefore, computed by summing the N_ϕ contributions (6.51) of the surrounding $(i1k)$

cells. The finite-difference approximation to the integral term in equation (6.49) may then be written as

$$\left\{ \frac{1}{r} \int_0^{2\pi} \frac{\partial(\sin \theta \rho v_\theta)}{\partial(\cos \theta)} \Big|_{\theta=0} d\phi \right\}_{i1k} \approx - \sum_{k=1}^{N_\phi} \frac{[\sin \theta_{1-1/2} \langle \rho \rangle_{i,1-1/2,k} v_{\theta_{i,1-1/2,k}}] \Delta \phi_{k+1/2}}{2\pi \langle r_i \rangle (1 - \cos \theta_{1-1/2})}. \quad (6.53)$$

An identical form (with $\langle \rho \rangle \rightarrow \langle \rho v_r \rangle$) holds for the θ -advective term in equation (6.50) for the r -momentum transport.

The axial variables are radially advected by using the replacements (6.16) but now with the indices j and k removed. The same is done to represent the radial gradients.

The modifications to the donor-cell replacements (6.17) for advection of mass and r -momentum across the $(i, 1 - 1/2, k)$ interfaces, are obtained by replacing “ ρ_{i0k} ” and “ $\rho_{i0k} v_{r_{i0k}}$ ” by ρ'_i and $\rho'_i v'_{r_i}$, respectively. Similar modifications are also needed in equations (6.34) and (6.35) when $j = 1$.

(B) THE EQUATORIAL PLANE.

At the equator ($\theta = \pi/2$), the flow is constrained to have $v_\theta = 0$ so that there is no mass going from the top to the bottom hemisphere. This boundary condition is then numerically specified by setting $v_{\theta_{iN_\theta k}} = 0$, at any step. In this way, the equatorial cells ($iN_\theta k$) will never be the source of θ -momentum.

In equation (6.37), a trivial modification is needed for the donor-cell transport of θ -momentum when $j = N_\theta - 1$. Since each of the adjoining $(i, N_\theta - 1, k)$ cells can lose θ -momentum into the equatorial cells at the rate

$$\frac{\sin \theta_{N_\theta-1/2} \langle \rho v_\theta \rangle_{i, N_\theta-1/2, k} v_{\theta_{i, N_\theta-1/2, k}}}{\langle r_i \rangle \sin \theta_{N_\theta-1} \Delta \theta_{N_\theta-1/2}},$$

the donor-cell fluxing across the $(i, N_\theta - 1/2, k)$ interfaces is modified by defining

$$\langle \rho v_\theta \rangle_{i, N_\theta-1/2, k} = \begin{cases} \rho_{i, N_\theta-1, k} v_{\theta_{i, N_\theta-1, k}} & \text{if } v_{\theta_{i, N_\theta-1/2, k}} \geq 0 \\ 0 & \text{if } v_{\theta_{i, N_\theta-1/2, k}} < 0 \end{cases}$$

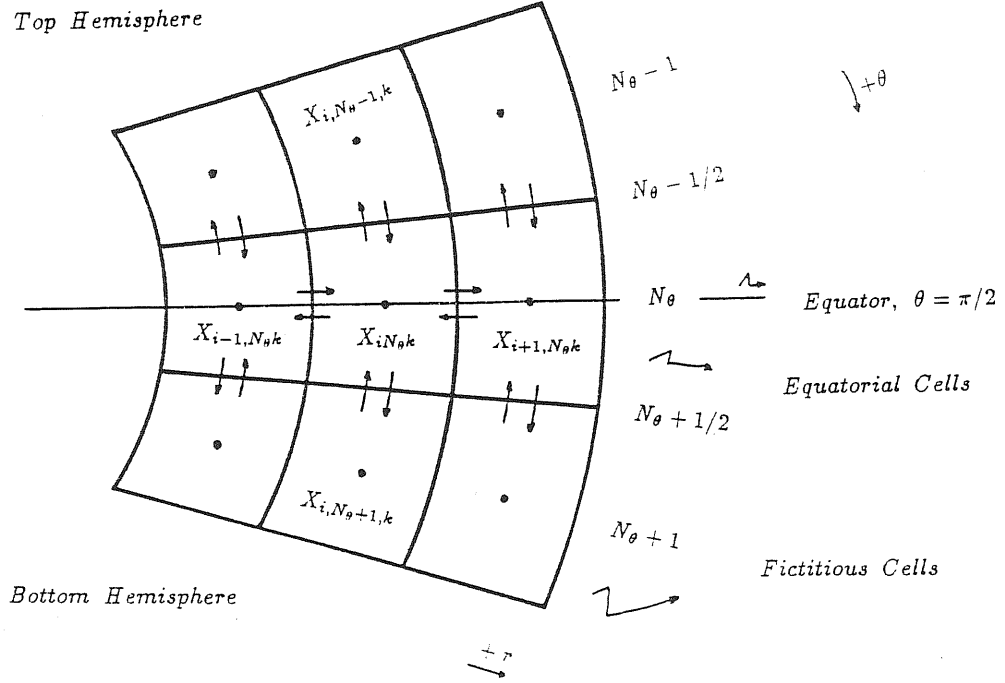


Figure 6.5: Portion of an (r, θ) -slice showing control volumes for equatorial advection

(6.54)

where $v_{\theta, i, N_{\theta}-1/2, k} = \frac{1}{2}v_{\theta, i, N_{\theta}-1, k}$.

On the other hand, due to the assumption of reflection symmetry about the equator, the form of the θ -advective terms in equations (6.34), (6.35), and (6.40) must be modified for the equatorial cells. To numerically apply the condition of reflection symmetry, we define $(N_r \times N_{\phi})$ fictitious cells $(i, N_{\theta} + 1, k)$ (beneath the equatorial cells) whose state at any step is completely defined by the state of the computational $(i, N_{\theta} - 1, k)$ cells at the corresponding time [See Figure 6.5] Then, the prescription for the cells $(i, N_{\theta} + 1, k)$ is that the density, the r -velocity, and the ϕ -velocity must at all times be the same as in cells $(i, N_{\theta} - 1, k)$, and that the normal velocity v_{θ} must be the mirror image of that in cells $(i, N_{\theta} - 1, k)$:

$$\rho_{i, N_{\theta}+1, k}^n = \rho_{i, N_{\theta}-1, k}^n; \quad v_{r, i, N_{\theta}+1, k}^n = v_{r, i, N_{\theta}-1, k}^n; \quad v_{\phi, i, N_{\theta}+1, k}^n = v_{\phi, i, N_{\theta}-1, k}^n,$$

$$v_{\theta_{i,N_{\theta}+1,k}}^n = -v_{\theta_{i,N_{\theta}-1,k}}^n. \quad (6.55)$$

The use of prescriptions (6.55) will ensure that the flow across the $(i, N_{\theta} - 1/2, k)$ interfaces is exactly the same as that across the $(i, N_{\theta} + 1/2, k)$ interfaces in the bottom hemisphere. However, it is important to remark that even if they permit a compact solution of the difference equations (in the sense that the θ -momentum is effectively canceled out for any equatorial cell by the opposite contribution coming from the fictitious cells and, hence, is globally conserved), they cannot be used to replace the actual boundary condition $v_{\theta} = 0$.

Since $\sin \theta_{N_{\theta}+1/2} = \sin \theta_{N_{\theta}-1/2}$, it follows from (6.55) that

$$\left\{ \frac{1}{r \sin \theta} \frac{\partial(\sin \theta X v_{\theta})}{\partial \theta} \right\}_{iN_{\theta}k} \approx - \frac{[\sin \theta_{N_{\theta}-1/2} \langle X \rangle_{i,N_{\theta}-1/2,k} v_{\theta_{i,N_{\theta}-1/2,k}}]}{\langle r_i \rangle \frac{1}{2} \Delta \theta_{N_{\theta}}}, \quad (6.56)$$

where X may be ρ , ρv_r , or ρA .

The use of the form (6.56) in the difference equations (6.34), (6.35), and (6.40), when $j = N_{\theta}$, and the modifications implemented for the θ -advection in the axial difference equations, ensure rigorous global conservation of the θ -advected mass, r -momentum, and angular momentum.

(C) THE CENTRE.

The centre of the protostellar cloud is numerically represented by a single spherical cell [See Figure 4.1], which is centred at the origin ($r = 0$) of the coordinate system. Since, the specification of the inner boundary condition requires that $v_r = v_{\theta} = v_{\phi} = 0$ at $r = 0$, only mass may be freely interchanged between the central and the main grid-cells ($1jk$).

From the limiting form of the continuity equation (3.21) when $r \rightarrow 0$

$$\frac{\partial \rho_c}{\partial t} + 3 \int_0^{2\pi} \int_0^{\pi} \frac{\partial(r^2 \rho U)}{\partial(r^3)} \Big|_{r=0} \sin \theta d\theta d\phi = -3\rho_c \frac{\partial(r^2 v_g)}{\partial(r^3)} \Big|_{r=0}, \quad (6.57)$$

it follows that the central cell will only experience radial advection. The effect upon the central density ρ_c is calculated by enforcing mass conservation across the $(1 - 1/2, jk)$ interfaces. Note that the θ -integration in equation (6.57) includes also the contribution of the innermost neighbouring axial cell ($i = 1$).

Using the volumes (6.11) and (6.52), we have that each main grid-cell $(1jk)$ loses mass to the central cell at the rate

$$\frac{\Delta M_{1jk}}{\Delta t} = \left(r_{1-1/2}^2 \langle \rho \rangle_{1-1/2,jk} U_{1-1/2,jk} \right) \left(\sin \theta_j \Delta \theta_{j+1/2} \Delta \phi_{k+1/2} \right), \quad (6.58)$$

while the corresponding expression for the innermost axial cell is

$$\frac{\Delta M'_1}{\Delta t} = 2\pi \left(r_{1-1/2}^2 \langle \rho' \rangle_{1-1/2} U'_{1-1/2} \right) \left(1 - \cos \theta_{1-1/2} \right). \quad (6.59)$$

The contributions to the central density are then

$$\frac{\Delta \rho_c}{\Delta t} = -\frac{1}{V_c} \frac{\Delta M_{1jk}}{\Delta t}, \quad (6.60)$$

and

$$\frac{\Delta \rho_c}{\Delta t} = -\frac{1}{V_c} \frac{\Delta M'_1}{\Delta t}, \quad (6.61)$$

respectively, where $V_c \left(= \frac{4\pi}{3} r_{1-1/2}^3 \right)$ corresponds to the total volume of the central cell.

The net change in the central density, is obtained by summing the axial contribution (6.61) and the $(N_\theta \times N_\phi)$ main grid-cell contributions (6.60), so that

$$\begin{aligned} 3 \int_0^{2\pi} \int_0^\pi \frac{\partial(r^2 \rho U)}{\partial(r^3)} \Big|_{r=0} \sin \theta d\theta d\phi &\approx \frac{[r_{1-1/2}^2 \langle \rho' \rangle_{1-1/2} U'_{1-1/2}]}{\frac{1}{3} r_{1-1/2}^3} \left(1 - \cos \theta_{1-1/2} \right) + \\ &+ \sum_{j=1}^{N_\theta} \sum_{k=1}^{N_\phi} \frac{\sin \theta_j \Delta \theta_{j+1/2} \Delta \phi_{k+1/2}}{2\pi} \frac{[r_{1-1/2}^2 \langle \rho \rangle_{1-1/2,jk} U_{1-1/2,jk}]}{\frac{1}{3} r_{1-1/2}^3}. \end{aligned} \quad (6.62)$$

This form ensures rigorous global conservation of the radially advected mass.

The modification of the grid contraction term (6.21) is implemented as

$$-3\rho_c \frac{\partial(r^2 v_g)}{\partial(r^3)} \Big|_{r=0} \approx -\rho_c \frac{1}{\Delta t} \left\{ \frac{(r_{1-1/2}^3)^{(n+1)} - (r_{1-1/2}^3)^{(n)}}{(r_{1-1/2}^3)^{(n+1)}} \right\}. \quad (6.63)$$

Substitution of the replacements (6.62) and (6.63) into the exact equation (6.57) provides the counterpart of equation (6.34) for the spherical central cell. The mass is radially advected across the innermost interfaces $(1 - 1/2, jk)$ according to the donor cell prescriptions (6.16), with ρ_c being now the replacement for “ ρ_{0jk} ” (advection from main grid-cells) and “ ρ'_0 ” (advection from the axial cell). Since, r - and θ -momentum may be radially transferred into the central cell, where they are dumped, modifications are also needed in the radial transport terms of equations (6.35) and (6.37) when $i = 1$. These modifications are then implemented by defining

$$\langle \rho v_r \rangle_{1-1/2, jk} = \begin{cases} 0 & \text{if } U_{1-1/2, jk} \geq 0 \\ \rho_{1jk} v_{r_{1jk}} & \text{if } U_{1-1/2, jk} < 0 \end{cases} \quad (6.64)$$

and

$$\langle \rho v_\theta \rangle_{1-1/2, jk} = \begin{cases} 0 & \text{if } U_{1-1/2, jk} \geq 0 \\ \rho_{1jk} v_{\theta_{1jk}} & \text{if } U_{1-1/2, jk} < 0 \end{cases} \quad (6.65)$$

By removing the indices j and k , a similar form to (6.64) is obtained for the radial flow along the rotational axis.

Finally, the global conservation of the r -advected angular momentum is automatically ensured by the partially centred scheme (6.41). The central cell never removes angular momentum from the main grid-cells because since $A_{0jk} \rightarrow A_c \equiv 0$ at the centre, it follows from (6.41) that $\langle A \rangle_{1-1/2, jk} = 0$, at any step.

(D) THE EXTERNAL BOUNDARY SURFACE.

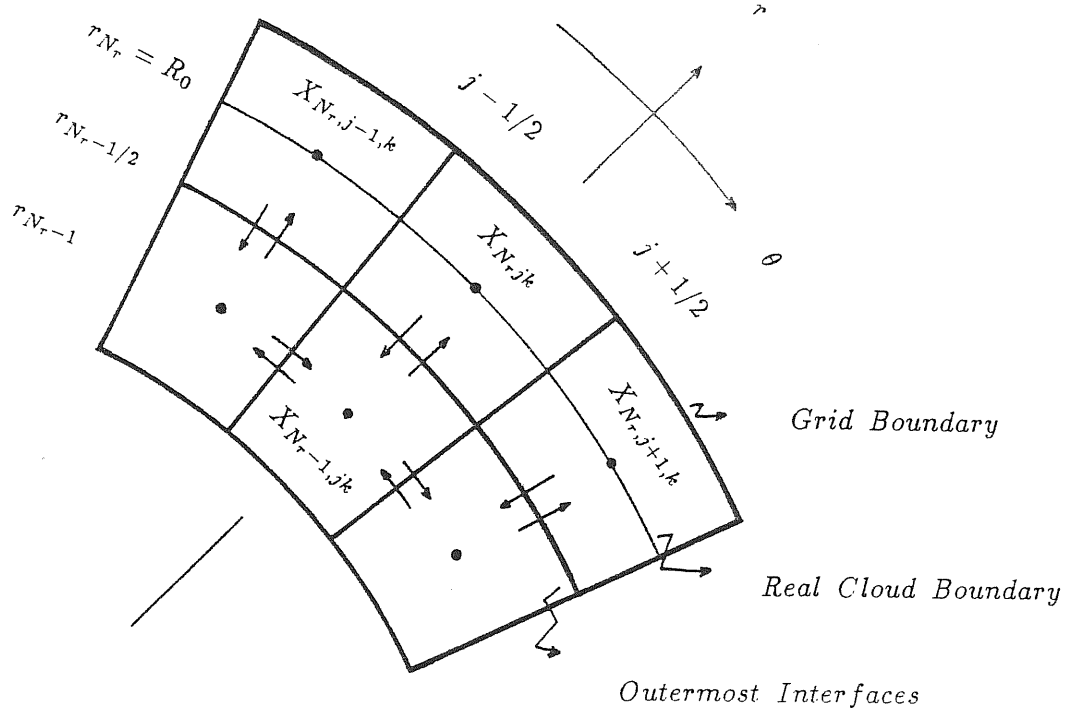


Figure 6.6: Portion of an (r, θ) -slice representing control volumes for the treatment of the external boundary condition

The outer boundary ($r = R_0$) is made to coincide with the outermost grid points “ $N_r j k$ ” and hence, only a half of the external boundary cells will initially contain mass. A constant-volume condition is then numerically specified by setting $v_r = v_\theta = 0$ for the outermost computational points. Hence, the adjoining cells $(N_r - 1, j k)$ can only lose r - and θ -momentum into the boundary cells $(N_r j k)$ across the $(N_r - 1/2, j k)$ interfaces [See Figure 6.6]. The modifications for the radial transport when $i = N_r - 1$ are

$$\langle \rho v_r \rangle_{N_r-1/2, jk} = \begin{cases} \rho_{N_r-1, jk} v_{r, N_r-1, jk} & \text{if } U_{N_r-1/2, jk} \geq 0 \\ 0 & \text{if } U_{N_r-1/2, jk} < 0 \end{cases} \quad (6.66)$$

and

$$\langle \rho v_\theta \rangle_{N_r-1/2, jk} = \begin{cases} \rho_{N_r-1, jk} v_{\theta, N_r-1, jk} & \text{if } U_{N_r-1/2, jk} \geq 0 \\ 0 & \text{if } U_{N_r-1/2, jk} < 0 \end{cases} \quad (6.67)$$

where $U_{N_r-1/2,jk} = \frac{1}{2}U_{N_r-1,jk}$. A form similar to (6.66), with the indices j and k removed, holds for the transport of radial momentum along the axis at the pole of the spherical volume.

Only mass and angular momentum may be freely interchanged between the boundary and the interior $(N_r - 1, jk)$ cells. The external boundary condition for the θ -flow is applied trivially since $v_{\theta_{N_r,j\pm 1/2,k}} \equiv 0$. This means that the boundary cells will not experience θ -advection and, hence, the problem reduces to consistently treating the radial flow across the $(N_r - 1/2, jk)$ interfaces in such a way as to preserve rigorous global conservation of the advected mass and angular momentum. The modification for the r -advective terms (when $i = N_r$) is obtained by expanding the flux $(r^2 X U)_{N_r-1/2,jk}$ in a Taylor series about the boundary points $N_r jk$, so that

$$\left\{ 3 \frac{\partial(r^2 X U)}{\partial(r^3)} \right\}_{N_r jk} \approx - \frac{r_{N_r-1/2}^2 \langle X \rangle_{N_r-1/2,jk} U_{N_r-1/2,jk}}{\frac{1}{3}(r_{N_r}^3 - r_{N_r-1/2}^3)}, \quad (6.68)$$

where $r_{N_r} = R_0$.

The modification for the grid contraction term (6.21) is

$$\left\{ 3X \frac{\partial(r^2 v_g)}{\partial(r^3)} \right\}_{N_r jk} \approx -X_{N_r jk} \frac{\left[(r_{N_r}^3 - r_{N_r-1/2}^3)^{(n+1)} - (r_{N_r}^3 - r_{N_r-1/2}^3)^{(n)} \right]}{(r_{N_r}^3 - r_{N_r-1/2}^3)^{(n+1)}}. \quad (6.69)$$

The replacements (6.68) and (6.69) have been carried out in order to account for the smaller initial dimensions of the partial cells representing the real boundary of the system.

(E) THE PERIODIC BOUNDARY CONDITION.

In order to evaluate the ϕ -advective terms and the ϕ -gradients when $k = 1$ and $k = N_\phi$, we must carry two extra angular zones in the ϕ -direction. As shown in Figure 6.7, a zone labelled “ $ij0$ ” (coinciding with “ ijN_ϕ ”) is carried in the backward direction,

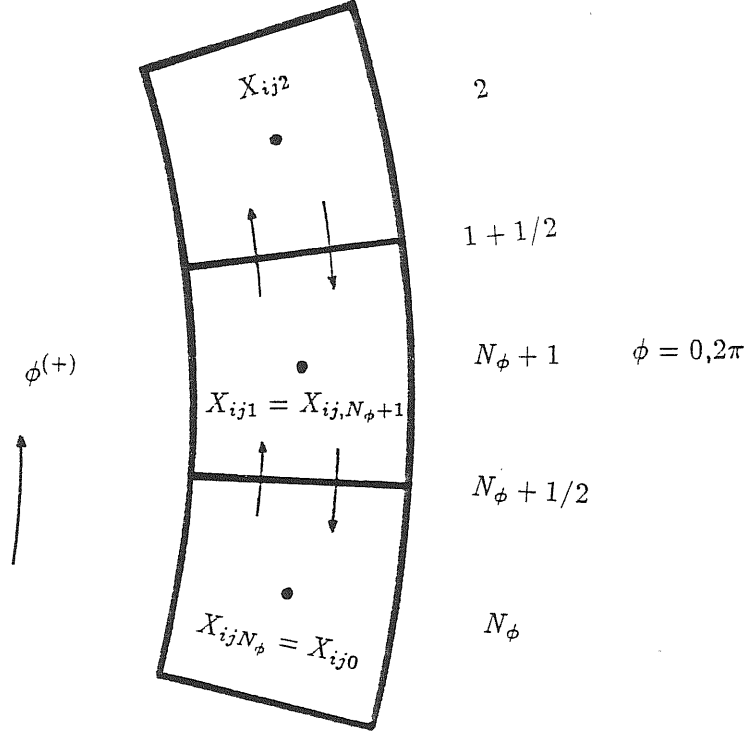


Figure 6.7: Portion of an (r, ϕ) -slice illustrating the periodic boundary condition

and the extra zone “ $ij, N_\phi + 1$ ” (coinciding with “ $ij1$ ”) is carried in the forward direction such that at any step

$$X''_{ij0} = X_{ij N_\phi} \quad \text{for } k = 1, \quad (6.70)$$

and

$$X''_{ij, N_\phi + 1} = X_{ij1} \quad \text{for } k = N_\phi, \quad (6.71)$$

where X may be ρ , ρv_r , ρv_θ , ρA , Φ , or p . The use of the assignments (6.70) and (6.71) in the donor-cell prescriptions (6.18) will ensure global conservation for all of the advected hydrodynamical variables.

6.10 Artificial Viscosity

In forming shock regions where very large gradients start to develop, the accuracy of the numerically obtained solutions progressively deteriorates. This sort of difficulty arises

because of the technical inability of finite-differences to treat those zones of the mesh, where the required assumptions of continuity and differentiability of the flow are no longer valid. Furthermore, shocks are fundamentally inconsistent with the assumption of a perfect fluid. Dissipation is required in order to produce entropy and, failing this, instability will result. This instability is generally detected in the solution field by a well marked saw-tooth behaviour in the distribution of the hydrodynamical variables.

To circumvent this trouble, the general rule is that of enhancing the stability of the difference scheme by numerically mediating the discontinuities in the flow. One efficient way of smoothing out such discontinuities is by adding dissipative-like forces into the equations of motion. These extra terms will enter in the equations as the divergence of a tensor quantity \mathbf{Q} , commonly called artificial viscous stress. It is important to notice that such terms are always added to the "source part" of the momentum transfer equations before writing them in finite-difference form.

A fully correct and suitable definition of artificial viscosity would, in principle, require a tensor formulation. A good example is given by Tscharnuter and Winkler [115], who improved the original von Neumann and Richtmyer (1950) viscosity in connection with simulating accretion flows and explosion processes. In the extreme situations, which they were treating, the presence of strong shock-fronts and simultaneous different flow regimes demand the construction of highly stable schemes equipped with a sophisticated artificial viscosity.

In our case, strong shocks may eventually develop at the end of any calculation, with the intermediate stages of the shock formation being predominantly characterized by a progressive compression of the collapsing material giving rise to a well pronounced density enhancement. At this stage, our calculations are generally stopped either because

large masses are contained in a few hydrodynamical cells (giving loss of resolution in the zones of maximum interest), or because the maximum densities achieved are higher than those for which the near-isothermal approximation is valid, or even because the configuration approaches an apparent equilibrium state, which cannot be followed due to the very small Δt allowed. A simple modified version of von Neumann and Richtmyer (1950) viscosity is, therefore, sufficient for our purposes. Furthermore, the strong diffusion-like nature of the donor-cell differencing generally permits handling of intermediate strength shocks without the need for an additional artificial viscosity. Although the artificial viscosity terms are added into the exact equations, their effect on the difference equations is to enhance the spurious diffusion of the donor-cell advection. Some 1-dimensional collapse tests [See Chapter 7, Section 7.1] made to investigate this point, have confirmed the conclusions arrived at by Boss [13]: when artificial viscosity is introduced from the beginning of the calculations, the hydrodynamical approximation is appreciably affected by the contribution of the artificial viscosity to the local diffusion of the transported variables.

Since we are mainly interested in choosing the artificial viscosity to be sensitive to shocks arising by compression, only the diagonal elements of the tensor artificial viscosity will be retained. The effects of shearing motion (represented by the off-diagonal components) may then be neglected, if the dominant cause of shock formation is the geometrical compression of the inward-directed flow, as is likely to be the case early in the protostellar collapse.

In spherical coordinates, the diagonal components of \mathbf{Q} are denoted by Q_r^r , Q_θ^θ , and Q_ϕ^ϕ , so that the acceleration term $\nabla \cdot \mathbf{Q}$ will enter into the right-hand sides of equations

(3.22), (3.23), and (3.24) as

$$-3 \frac{\partial(r^2 Q_r^r)}{\partial(r^3)}; \quad -\frac{1}{r \sin \theta} \frac{\partial(\sin \theta Q_\theta^\theta)}{\partial \theta}; \quad \text{and} \quad -\frac{\partial Q_\phi^\phi}{\partial \phi}, \quad (6.72)$$

respectively. Note that the radial term has been written in compact form. In the axisymmetric problem ($\partial/\partial\phi = 0$) shock fronts cannot be generated in the ϕ -direction and hence, the last differential term in (6.72) is not needed in the angular momentum equation (3.18).

Following Black and Bodenheimer [3], Boss [13], and Norman and Winkler [89], a form similar to that developed by von Neumann and Richtmyer for problems in slab symmetry, is used here to define the effective diagonal components:

$$Q_r^r = \begin{cases} +\tilde{L}_r^2 \bar{\rho} \left| \frac{\partial v_r}{\partial r} \right| \frac{\partial v_r}{\partial r} & \text{if } \frac{\partial v_r}{\partial r} < 0 \\ 0 & \text{otherwise} \end{cases}$$

$$Q_\theta^\theta = \begin{cases} +\tilde{L}_\theta^2 \bar{\rho} \left| \frac{1}{r} \frac{\partial v_\theta}{\partial \theta} \right| \frac{1}{r} \frac{\partial v_\theta}{\partial \theta} & \text{if } \frac{\partial v_\theta}{\partial \theta} < 0 \\ 0 & \text{otherwise} \end{cases} \quad (6.73)$$

$$Q_\phi^\phi = \begin{cases} +\tilde{L}_\phi^2 \bar{\rho} \left| \frac{1}{r \sin \theta} \frac{\partial v_\phi}{\partial \phi} \right| \frac{1}{r \sin \theta} \frac{\partial v_\phi}{\partial \phi} & \text{if } \frac{\partial v_\phi}{\partial \phi} < 0 \\ 0 & \text{otherwise} \end{cases}$$

where \tilde{L}_r , \tilde{L}_θ , and \tilde{L}_ϕ are spatial quantities related to the spacing of the mesh by the following relations

$$\tilde{L}_r = \bar{C}^{1/2} \Delta r; \quad \tilde{L}_\theta = \bar{C}^{1/2} r \Delta \theta; \quad \tilde{L}_\phi = \bar{C}^{1/2} r \sin \theta \Delta \phi, \quad (6.74)$$

with \bar{C} usually being a constant of order unity.

The definitions (6.73) define a quadratic artificial viscosity, which is slightly different from the form implemented by Gentry, Martin, and Daly [42] for enhancing the stability properties of the original Fluid-in-Cell method.

Finite-difference approximations to the partial derivative terms in (6.72), are constructed by centring the artificial viscosity components at the cell boundaries in such a way as to preserve the global conservation of the advected momentum. So, for cell interfaces open to the radial flow, we set in index notation $Q_{r_{ijk}}^r \rightarrow Q_{r_{i-1/2,jk}}^r$. Similarly, $Q_{\theta_{ijk}}^\theta \rightarrow Q_{\theta_{i,j-1/2,k}}^\theta$, and $Q_{\phi_{ijk}}^\phi \rightarrow Q_{\phi_{ij,k-1/2}}^\phi$, at the cell interfaces open to the θ - and ϕ -flows, respectively. Using the relations (6.74) in the definitions (6.73), we have at the interfaces of a typical main grid-cell

$$\begin{aligned} Q_{r_{i-1/2,jk}}^r &= -\min \left\{ 0; \frac{1}{2} \bar{C}' (\rho_{ijk} + \rho_{i-1,jk}) \left| \Delta v_{r_{ijk}} \right| \Delta v_{r_{ijk}} \right\}, \\ Q_{\theta_{i,j-1/2,k}}^\theta &= -\min \left\{ 0; \frac{1}{2} \bar{C}' (\rho_{ijk} + \rho_{i,j-1,k}) \left| \Delta v_{\theta_{ijk}} \right| \Delta v_{\theta_{ijk}} \right\}, \\ Q_{\phi_{ij,k-1/2}}^\phi &= -\min \left\{ 0; \frac{1}{2} \bar{C}' (\rho_{ijk} + \rho_{ij,k-1}) \left| \Delta v_{\phi_{ijk}} \right| \Delta v_{\phi_{ijk}} \right\}, \end{aligned} \quad (6.75)$$

where the $\bar{\rho}$ are centred at the cell boundaries by taking the average of density between adjacent grid-points, and

$$\begin{aligned} \Delta v_{r_{ijk}} &= v_{r_{ijk}} - v_{r_{i-1,jk}}, \\ \Delta v_{\theta_{ijk}} &= v_{\theta_{ijk}} - v_{\theta_{i,j-1,k}}, \\ \Delta v_{\phi_{ijk}} &= v_{\phi_{ijk}} - v_{\phi_{ij,k-1}}, \end{aligned} \quad (6.76)$$

so that the greater the difference in velocity between two adjacent computational cells, the greater is the magnitude of the viscous pressure. Straightforward modifications are needed in equations (6.75) for those cells having zero velocities. Furthermore, the modification for Q_r^r at the axial cell interfaces ($i - 1/2$), is taken as

$$Q_{r_{i-1/2}}^r = -\min \left\{ 0; \frac{1}{2} \bar{C}' (\rho'_i + \rho'_{i-1}) \left| \Delta v'_{r_i} \right| \Delta v'_{r_i} \right\}, \quad (6.77)$$

with $\Delta v'_{r_i} = v'_{r_i} - v'_{r_{i-1}}$ according to (6.76).

The finite-difference replacements for the divergences (6.72) are obtained in a similar manner as was done for the advective terms. Expanding $(r^2 Q_r^r)_{i\pm 1/2, jk}$ in Taylor series about the common point “ ijk ” at the time step n (the superscript for which is omitted), we obtain that

$$\left\{ 3 \frac{\partial(r^2 Q_r^r)}{\partial(r^3)} \right\}_{ijk} \approx \frac{[r_{i+1/2}^2 Q_{r_{i+1/2, jk}}^r - r_{i-1/2}^2 Q_{r_{i-1/2, jk}}^r]}{\frac{1}{3}(r_{i+1/2}^3 - r_{i-1/2}^3)}, \quad (6.78)$$

with a discretization error

$$\varepsilon_r^r = -\frac{3}{2} (r_{i+1/2}^3 - 2r_i^3 + r_{i-1/2}^3) \left[\frac{\partial^2(r^2 Q_r^r)}{\partial(r^3)^2} \right]_{ijk},$$

which is always better than first-order for a non-uniform grid.

Repeating the same procedure but now for $(\sin \theta Q_\theta^\theta)_{i, j\pm 1/2, k}$, we get

$$\left\{ \frac{1}{r \sin \theta} \frac{\partial(\sin \theta Q_\theta^\theta)}{\partial \theta} \right\}_{ijk} \approx \frac{[\sin \theta_{j+1/2} Q_{\theta_{i, j+1/2, k}}^\theta - \sin \theta_{j-1/2} Q_{\theta_{i, j-1/2, k}}^\theta]}{\langle r_i \rangle \sin \theta_j \Delta \theta_{j+1/2}}, \quad (6.79)$$

with a truncation error

$$\varepsilon_\theta^\theta = -\frac{1}{4} \frac{(\eta_{j+1} - 1) \Delta \theta_j}{\langle r_i \rangle \sin \theta_j} \left[\frac{\partial^2(\sin \theta Q_\theta^\theta)}{\partial \theta^2} \right]_{ijk} - O\{(\Delta \theta_j)^2\},$$

which is nearly second-order ($\eta_{j+1} = \Delta \theta_{j+1} / \Delta \theta_j \sim 1$) for the fairly uniform θ -grid.

Finally, the last term in (6.72) is approximated by using

$$\left\{ \frac{\partial Q_\phi^\phi}{\partial \phi} \right\}_{ijk} \approx \frac{[Q_{\phi_{ij, k+1/2}}^\phi - Q_{\phi_{ij, k-1/2}}^\phi]}{\Delta \phi_{k+1/2}}, \quad (6.80)$$

which is exactly second-order accurate for the uniform ϕ -grid with

$$\varepsilon_\phi^\phi = -\frac{1}{24} (\Delta \phi_k)^2 \left[\frac{\partial^3 Q_\phi^\phi}{\partial \phi^3} \right]_{ijk}.$$

A difference form analogous to (6.78) is used for the axial r -momentum equation, with

$Q_{r_{i\pm 1/2}}^r$ being the replacement for $Q_{r_{i\pm 1/2, jk}}^r$.

Rigorous global conservation of the advected angular momentum is trivially ensured by the form (6.80). When the contributions are summed over the whole ϕ -grid, the terms in the numerator will cancel out in pairs provided that, for $k = 1$ and $k = N_\phi$, we set

$$Q_{\phi_{ij}, N_\phi + 1/2}^\phi = Q_{\phi_{ij}, 1 - 1/2}^\phi,$$

in accordance with the considerations of Section 6.9.

The use of an artificial viscosity imposes a further constraint on the time step condition. Since the effect of the artificial viscosity is to give rise to a diffusion of momentum, for explicit schemes stability requires that [3,89]

$$\Delta t \leq \frac{(\Delta x)^2}{4\nu}, \quad (6.81)$$

where Δx denotes the mesh size in a particular direction, and ν represents the kinematic viscosity. If we now consider the Navier-Stokes equation written in spherical coordinates, the following true viscosity counterparts of the artificial viscosity terms (6.72) are found

$$\begin{aligned} 3 \frac{\partial}{\partial(r^3)} \left(\rho \nu^{rr} r^2 \frac{\partial v_r}{\partial r} \right); \quad & \frac{1}{r^2 \sin \theta} \frac{\partial}{\partial \theta} \left(\rho \nu^{\theta\theta} \sin \theta \frac{\partial v_\theta}{\partial \theta} \right); \\ & \frac{1}{r \sin \theta} \frac{\partial}{\partial \phi} \left(\rho \nu^{\phi\phi} \frac{\partial v_\phi}{\partial \phi} \right). \end{aligned} \quad (6.82)$$

Then, equating each of these terms with the corresponding ones in (6.72), we obtain the following relations between the artificial and kinematic viscosities:

$$Q_r^r = -\rho \nu^{rr} \frac{\partial v_r}{\partial r}; \quad Q_\theta^\theta = -\rho \nu^{\theta\theta} \frac{1}{r} \frac{\partial v_\theta}{\partial \theta}; \quad Q_\phi^\phi = -\rho \nu^{\phi\phi} \frac{1}{r \sin \theta} \frac{\partial v_\phi}{\partial \phi}, \quad (6.83)$$

These relations may be expressed at the borders of a typical main grid-cell by using the artificial viscosity definitions (6.75), so that

$$\nu_{i-1/2, jk}^{rr} = \bar{C} \left| \Delta v_{r_{ijk}} \right| \Delta r_i$$

$$\begin{aligned}
\nu_{i,j-1/2,k}^{\theta\theta} &= \bar{C} \left| \Delta v_{\theta_{ijk}} \right| r_i \Delta \theta_j, \\
\nu_{ij,k-1/2}^{\phi\phi} &= \bar{C} \left| \Delta v_{\phi_{ijk}} \right| r_i \sin \theta_j \Delta \phi_{k+1/2},
\end{aligned} \tag{6.84}$$

where the r -, θ -, and ϕ -spacings are defined as in (4.7). If we now apply the inequality (6.81) for a typical 3-dimensional cell by using the relations (6.84), the following three additional time step constraints are obtained for each zone,

$$\begin{aligned}
\Delta t_{r_{ijk}} &\leq \frac{\Delta r_i}{4\bar{C} |\Delta v_{r_{ijk}}|}, \\
\Delta t_{\theta_{ijk}} &\leq \frac{r_i \Delta \theta_j}{4\bar{C} |\Delta v_{\theta_{ijk}}|}, \\
\Delta t_{\phi_{ijk}} &\leq \frac{r_i \sin \theta_j \Delta \phi_k}{4\bar{C} |\Delta v_{\phi_{ijk}}|},
\end{aligned} \tag{6.85}$$

for non-vanishing values of the Q . The optimum "viscous" time is then computed by taking the minimum step over the entire computational grid

$$\Delta t_{VISCOUS} = \min \left\{ \Delta t_{r_{ijk}}, \Delta t_{\theta_{ijk}}, \Delta t_{\phi_{ijk}} \right\}, \tag{6.86}$$

while the time step needed to advance the hydrodynamical system, is re-defined as a fraction of the minimum of the CFL-time and the "viscous" time

$$\Delta t = f(< 0.9) \times \min \{ \Delta t_{CFL}, \Delta t_{VISCOUS} \}, \tag{6.87}$$

with Δt_{CFL} being calculated using equation (6.30).

Chapter 7

Spherically Symmetric Collapse

Owing to the exploratory nature of the present multi-dimensional numerical code, the construction of an independent 1-dimensional version was mandatory for testing the explicit hydrodynamic approximation method.

Solutions for spherically symmetric collapse were first obtained analytically [54,93] for the ideal case in which a protostellar cloud contracts in free-fall conditions under the action of only its self-gravitation, and then numerically, including the effects of gas pressure in both the isothermal and adiabatic regimes [5,13,61,74], and also the effects of radiation transfer (non-isothermal regime) in the diffusion and Eddington approximations [61,18]. Furthermore, the simplification of considering spherical symmetry has allowed for the inclusion of additional physics [7] and hence, for the extension of the simulations to pre-main sequence stellar densities [48,61]. Such work has been facilitated by the relatively small demands of computational time and memory in comparison with the 2- and 3-dimensional cases, even when the calculations are carried out with a large number of grid points. For any numerical scheme dealing with multi-dimensional calculations of the gravitational collapse of protostellar clouds, the restricted assumption of spherical symmetry provides a good way of testing the sensitivity and accuracy

of the solution method, as well its response to any physical situation.

In following sections, we shall describe the results of the 1-dimensional code for a pressureless collapse test and for a number of isothermal collapse models, in order to allow for comparisons with results previously obtained by other workers for identical models.

7.1 Pressureless Collapse

Hunter [54] demonstrated analytically that a uniform-density, unperturbed, spherically symmetric gas cloud, initially at rest, can condense to higher densities in such a way that the density remains uniform in space at any instant. That is, in this ideal case, the density will be an explicit function only of time. Fixing the origin of time as the instant at which the collapse started ($t_0 = 0$), Hunter's solution reads as follows

$$\begin{aligned} v_r &= -2r \frac{d\beta}{dt} \tan \beta, \\ \rho &= \rho_0 \sec^6 \beta, \\ \beta + \frac{1}{2} \sin 2\beta &= t \sqrt{\frac{1}{3}(8\pi G \rho_0)}, \end{aligned} \tag{7.1}$$

where ρ_0 refers to the initial density.

The solutions (7.1) for the radial velocity and density will be compared here with the numerical solutions of the 1-dimensional code for zero pressure. Furthermore, to allow for comparisons with results from Boss's code [13], we choose a $10M_\odot$ cloud initially at rest, with a uniform density $\rho = 10^{-15} \text{ g cm}^{-3}$. As in the Boss case, for this run the constant-volume boundary condition is replaced by one which mimics the infall of mass exterior to the computational grid. This modification is necessary in order to numerically reproduce the analytical solutions (7.1). Otherwise, owing to the Eulerian character of the hydrodynamical approximation, the presence of a mass discontinuity

at the external boundary of the cloud, will set an initial density gradient, which will then propagate inward destroying the expected density plateau. The infalling mass boundary condition, is constructed consistently with the analytical solutions (7.1) by setting

$$\begin{aligned}\rho_{N_r} &= \rho_{N_r-1}, \\ \frac{v_{r_{N_r}}}{r_{N_r}} &= \frac{v_{r_{N_r-1}}}{r_{N_r-1}},\end{aligned}\tag{7.2}$$

at any time, and by allowing the outermost grid-point r_{N_r} to move with the flow, instead of being held fixed as required by the usual constant-volume boundary condition. This is easily done by modifying prescription (4.11) to include a fictitious point r_{N_r+1} , which must be exterior to the computational domain and initially at an arbitrary distance from r_{N_r} .

In Figures 7.1(a) and 7.1(b), we show plots for the density and radial velocity profiles at $0.5t_{ff}$, as produced by the 1-dimensional pressureless code, while in Figures 7.2(a) and 7.2(b) the corresponding profiles are shown at $0.895t_{ff}$. The calculations were carried out with 20 moving radial grid points and using a small fraction of the CFL-time step ($\Delta t = 0.1\Delta t_{CFL}$).

At $0.5t_{ff}$ in the collapse, the density has not increased much over its initial value, so that the numerical and analytical profiles compare quite well, with relative errors of only $10^{-3}\%$ in the inner parts and $10^{-1} - 10^{-2}\%$ in the outer regions. At $0.895t_{ff}$, the density has increased to about 20 times its initial value. The flatness of the numerical plateau is still in good agreement with that of the uniform density analytical solution. However, the relative errors for the density have increased to $0.1 - 0.2\%$ in the central portions, and those of the radial velocity to $0.3 - 0.4\%$ throughout the grid.

Similar plateaus were obtained by Boss [13] at $0.894t_{ff}$. He argued that after this

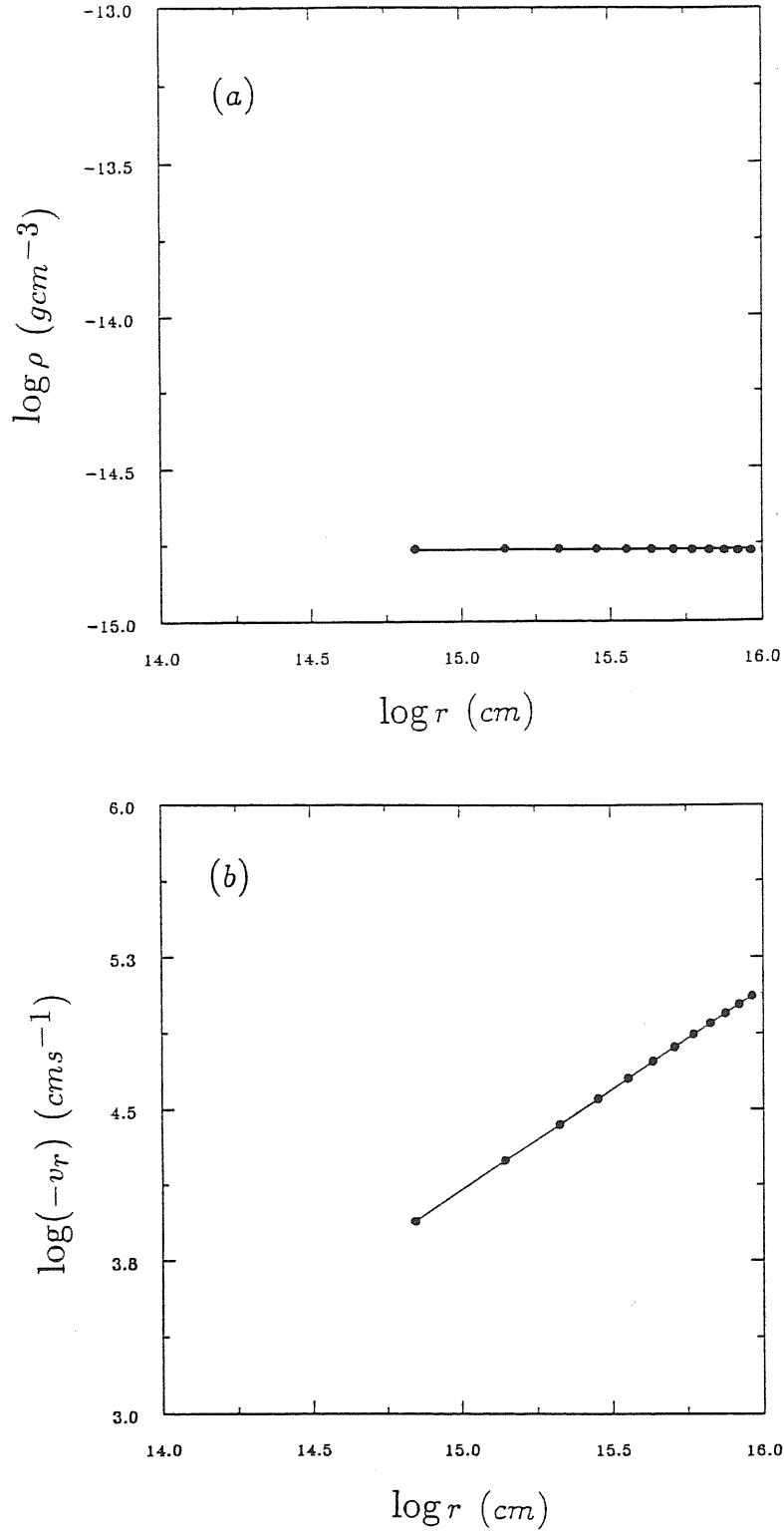


Figure 7.1: (a) Density and (b) velocity profiles as produced by the 1-D code (dots) compared with the analytical solution (solid lines) after $0.5t_{ff}$ in the collapse from $\rho = 10^{-15} gcm^{-3}$ with zero pressure.

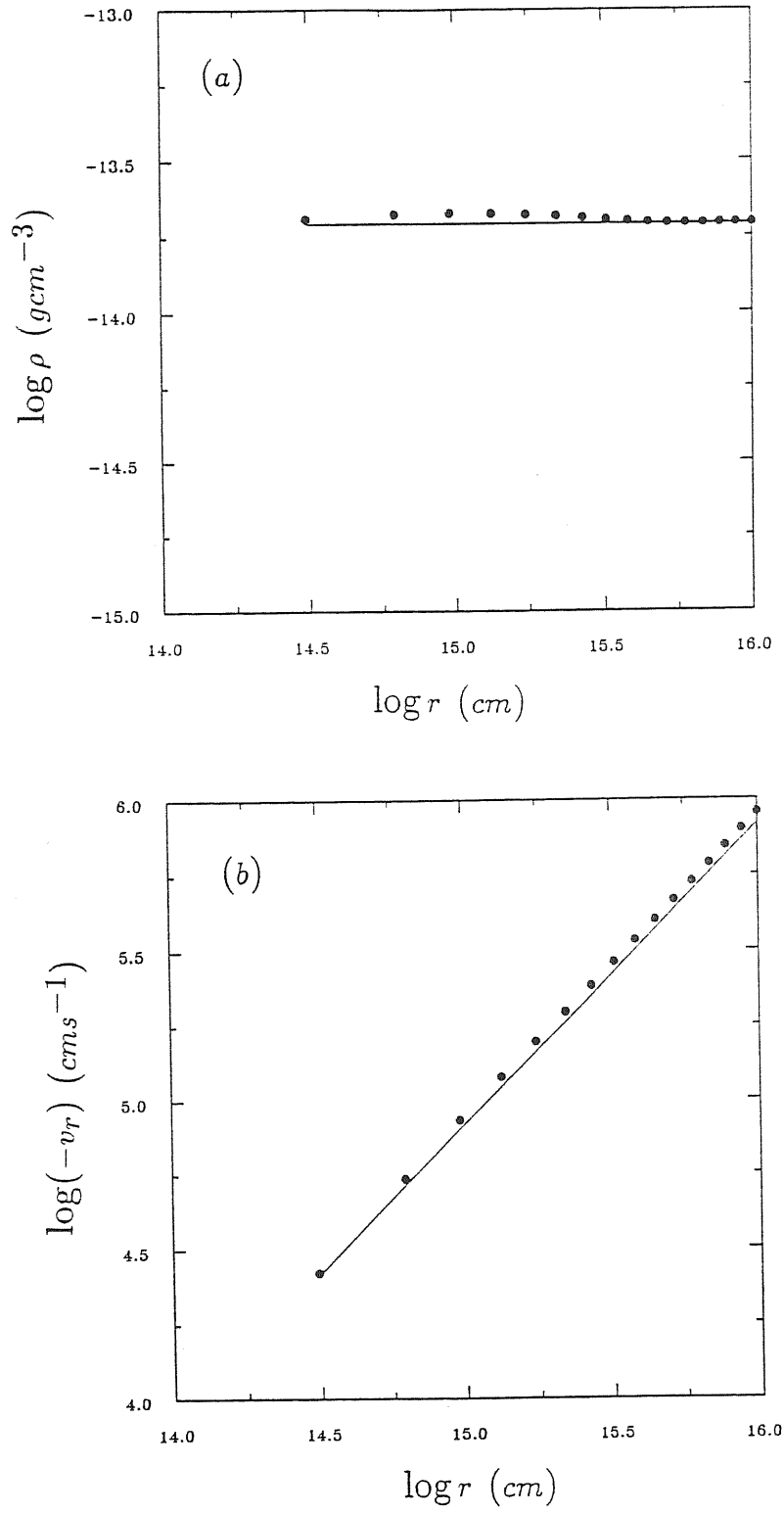


Figure 7.2: (a) Density and (b) velocity profiles for the same model as in Figure 7.1 at $0.895t_{ff}$.

time, the accuracy of the numerical plateau deteriorates due to a systematic error in the donor-cell advection in the inner portions of the cloud. This feature is also observed in Figure 7.2(a), where the computed density is slightly too high in the intermediate regions. We may then expect that the errors will progressively grow due to the shorter free-fall time of the higher density regions. However, in our case significant deterioration occurs after $0.925t_{ff}$. In other words, the present 1-dimensional code is apparently able to maintain a fairly accurate inner plateau (with relative errors of $\sim 0.2 - 0.3\%$) for a longer time than Boss code. This improvement is probably due to the superior finite-difference replacement (6.12) used to represent the radial advective terms in equations (3.10) and (3.11).

The pressureless collapse test has been found to be a good detector of any diffusion errors implicit in the hydrodynamic approximation. Therefore, we may use this test case to infer how the donor-cell transport of mass is affected by different choices of numerical treatment. In order to do so, we shall consider the same initial model as before but now with a larger fraction of the CFL-time ($f = 0.4$). The reason for using this value is that the same fraction was used for most of the 2-dimensional runs.

In Figure 7.3, we then display four different density profiles. Curves (a) and (b) were both obtained with twenty fixed grid-points, but for (a), the artificial viscosity was activated from the beginning whereas no artificial viscosity was used for (b). Curves (c) and (d), on the other hand, were computed with twenty and forty moving grid points, respectively, without including artificial viscosity. All runs were stopped at approximately the same time (after $0.894t_{ff}$). Comparisons between these curves will be discussed in terms of the flatness $\Delta = |\log \rho_{\max} - \log \rho_{\min}|$ of the density profile, so that the greater the accuracy, the smaller Δ should be. From curves (b) and (c),

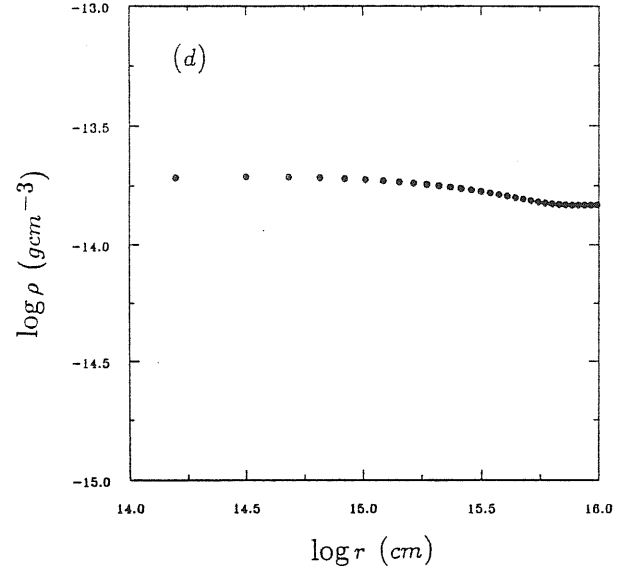
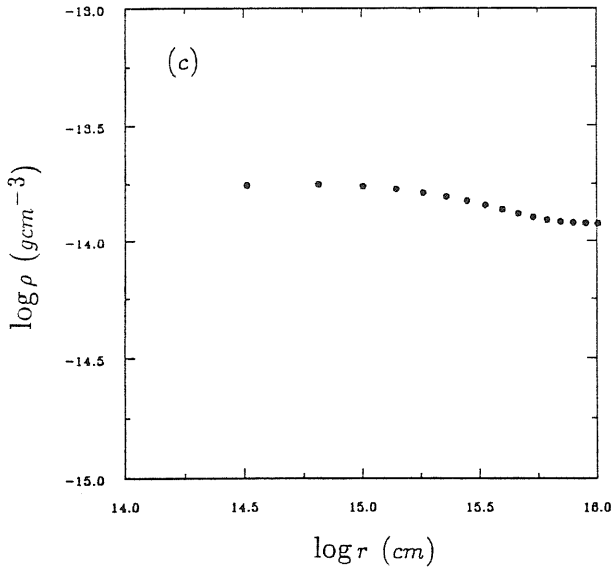
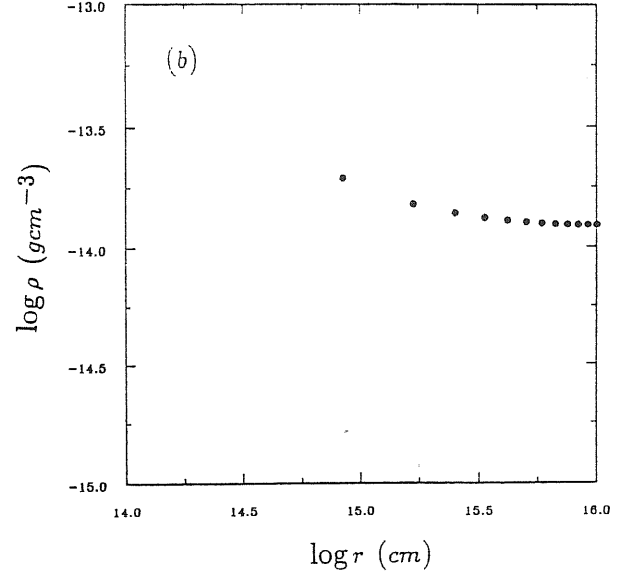
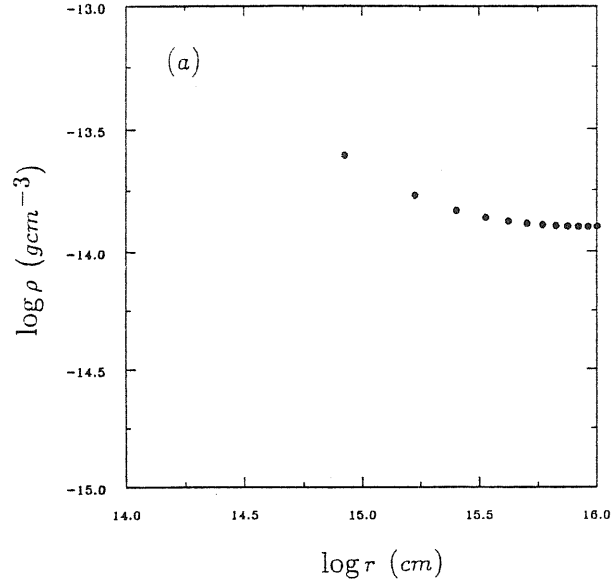


Figure 7.3: Density profiles after $\sim 0.894t_{ff}$ for the pressureless collapse from $\rho = 10^{-15} gcm^{-3}$, for different choices of the numerical treatment: (a) with 20 fixed grid-points and artificial viscosity coefficient $\tilde{C} = 2$, (b) as in (a) but with $\tilde{C} = 0$, (c) with 20 moving points and $\tilde{C} = 0$, (d) with 40 moving points and $\tilde{C} = 0$.

we note that the accuracy is improved when the grid is allowed to move with the fluid. [See Chapter 6, Section 6.6]. In fact, the truncation error produced by the fixed grid has given rise to a stronger deviation from the expected uniform plateau (in the inner regions) than for the moving grid case. The relative errors for curve (b) are of nearly 1%, i.e. two times greater than those obtained for curve (c). Furthermore, by comparing curves (a) and (b) for the same fixed grid, we note that the use of artificial viscosity exacerbates the spurious diffusion of mass in the inner portions of the cloud, with the relative errors for (a) being roughly twice those obtained for (b). Therefore, artificial viscosity must be avoided during the initial dynamical stage of collapse. Curve (c) may be also compared with the density profile in Figure 7.2(a). It is evident that more accuracy is achieved when the time step is set to a smaller fraction the Δt_{CFL} . This is consistent with the fact that numerical solutions should converge to the true ones as $\Delta t \rightarrow 0$. Finally, comparisons between curves (c) and (d) show that the flow is more accurately calculated when a larger number of grid-points is included. The forty-point run has a flatness $\Delta \sim 0.15$ and relative errors in the zones of maximum deviation of roughly 0.4%, while the twenty-point run has $\Delta \sim 0.17$ and corresponding relative errors of about 0.6% in the central regions.

In figure 7.4, we show the final density profile at $1.006t_{ff}$, for the pressureless collapse of an isolated $1M_{\odot}$ cloud initially at rest with a uniform density $\rho = 1.4 \times 10^{-19} gcm^{-3}$. This model is computed to observe the effects of the constant-volume boundary condition on a free-fall collapse. In contrast with the pressureless test for Hunter's analytical solution, here we shall consider the pressureless collapse of the whole configuration. This calculation was carried out with forty moving grid-points and was completed after 239 cycles, with $\Delta t = 0.4\Delta t_{CFL}$. The profile is qualitatively

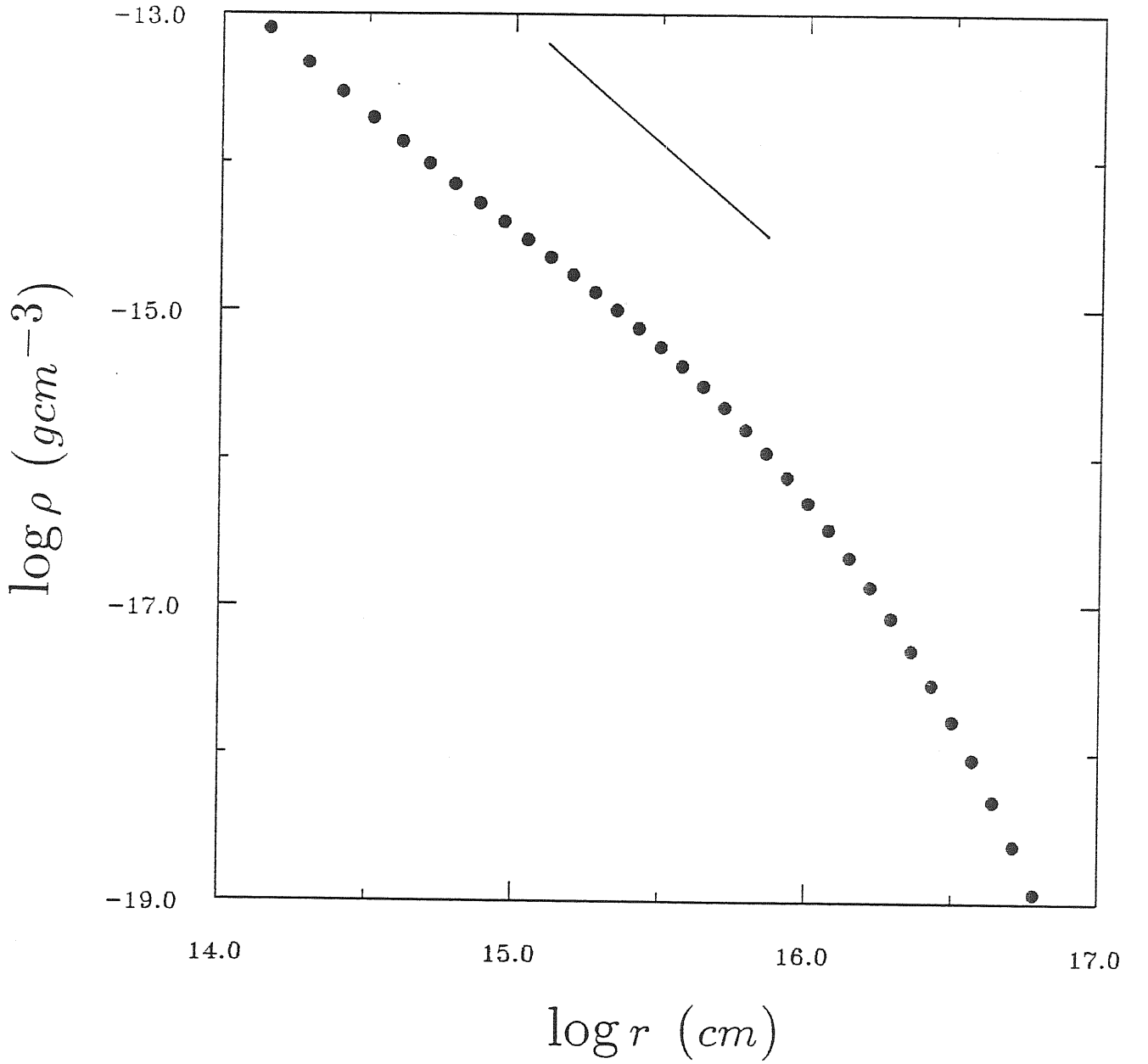


Figure 7.4: Density profile obtained after $1.006t_{ff}$ for the pressureless collapse from $1.4 \times 10^{-19} \text{gcm}^{-3}$ at rest, with a constant-volume boundary condition. The solid line shows the slope of the Penston analytical solution $\rho \propto r^{-12/7}$.

similar to that obtained by Boss [13] at $1.01t_{ff}$ for the same initial model (the only difference being that his run was performed with $\Delta t = 0.5\Delta t_{CFL}$). As in the Boss case, we observe again that the central regions match very well the analytical law $\rho \propto r^{-12/7}$ derived by Penston [93] (in an asymptotic similarity solution for pressureless collapse). Furthermore, it is noted that the numerical density profile diverges from the Penston solution as we go towards the external boundary of the collapsing cloud. This situation inevitably occurs due to the effects of the constant-volume boundary condition used for this run and to the inapplicability of the Penston solution to the outer regions of the cloud. As previously noted, the pressureless collapse is influenced, especially near the boundary, by the initially sharp density gradient at the edge of the configuration.

7.2 Isothermal and Adiabatic Collapse

In this section, we shall describe the response of the 1-dimensional code to the physical situations encountered during the isothermal stage. A calculation with an adiabatic pressure-law is also described.

We start our discussion of the isothermal collapse by referring to Figures 7.5(a) and 7.5(b), which illustrate the density and radial velocity profiles after $0.994t_{ff}$, for the gravitational collapse of a $10M_{\odot}$ cloud composed of atomic hydrogen ($\mu = 1$) and initially at rest with a temperature $T = 100K$ and a uniform density $\rho = 10^{-15}gcm^{-3}$. The same model has previously been calculated at comparable central densities by Bodenheimer and Sweigart [5] after $0.99t_{ff}$ and by Boss [13] after $1.00t_{ff}$. In order to allow for direct comparisons with the Boss profiles, we have again used 20 moving radial grid points. The agreement is qualitatively good, and the persistence of a clear inner density plateau (interpreted as a relic of the uniform density initial conditions)

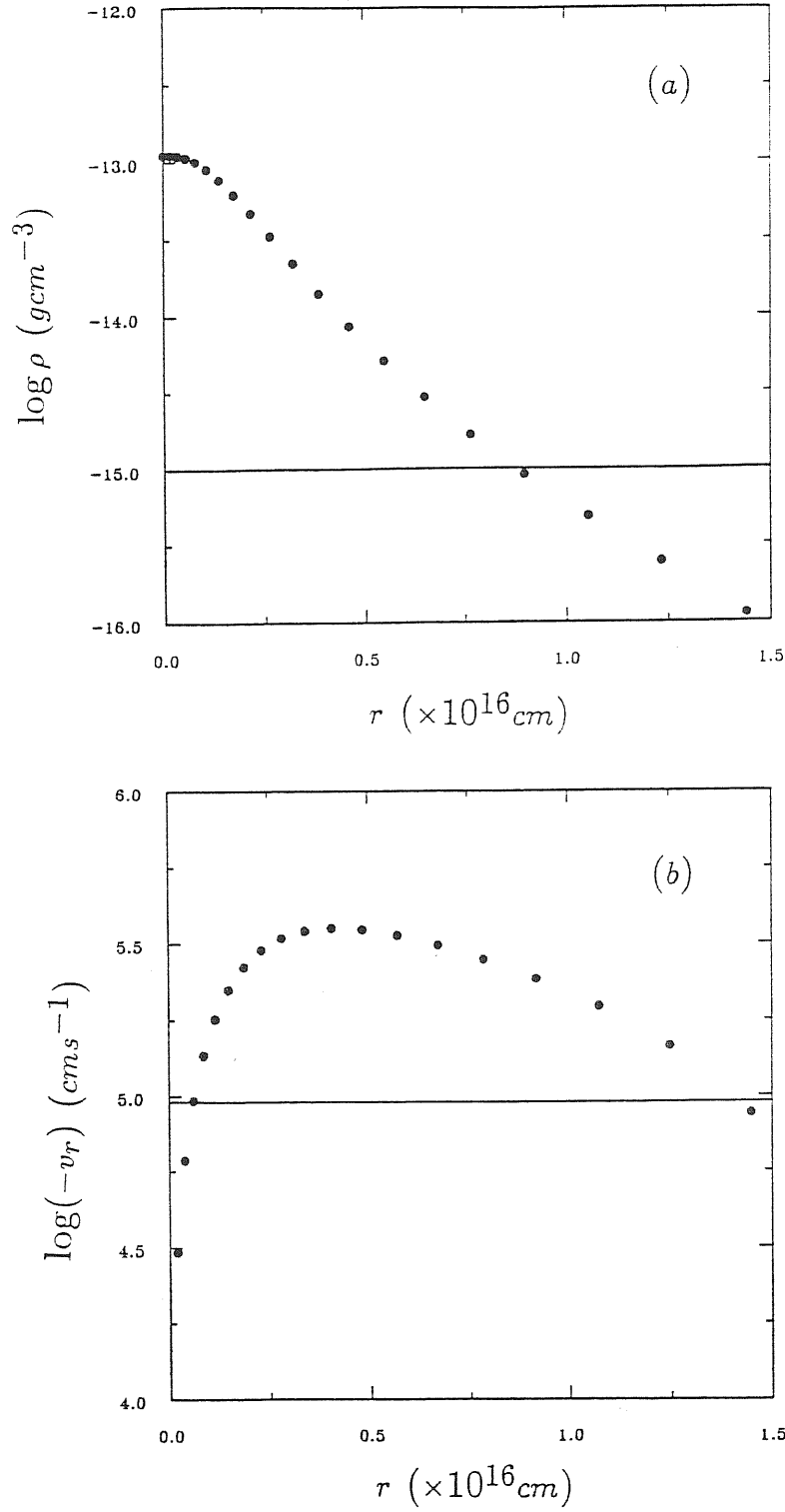


Figure 7.5: (a) Density and (b) radial velocity profiles after $0.994t_{ff}$ for an isothermal collapse from $\rho = 10^{-15} \text{ g cm}^{-3}$. The solid line in (a) shows the initial density distribution and that in (b) shows the isothermal sound speed. These calculations were carried out with 20 moving grid points and $\Delta t = 0.5\Delta t_{CFL}$.

is well confirmed by the calculation. As demonstrated by Bodenheimer and Sweigart [5], the persistence of such a plateau represents a physical situation encountered in the isothermal collapse of clouds for which the “sound-speed time” ($t_{ss} \sim R_0/C_{ss}$) is greater than the free-fall time t_{ff} . The collapse of the interior regions will proceed at uniform density until the rarefaction wave from the boundary (which carries information regarding the surface pressure at the sound speed rate) has reached the centre. Once this occurs, the central plateau will then disappear and further collapse will proceed with a well-marked central density gradient. In our case, $t_{ss} \sim 2.8t_{ff}$ and hence, by $0.994t_{ff}$ the rarefaction wave has not had time to reach the innermost portions of the collapsing cloud, and so there is not yet any coupling between the centre and the external surface. As argued by Boss [13], the Lagrangian scheme implemented by Bodenheimer and Sweigart [5] can resolve better the location of the inner plateau than the Eulerian schemes. However, in our case, the 1-dimensional Eulerian code has produced a central plateau which is slightly more pronounced than that previously obtained by Boss [13], even with the mass being transported according to the donor cell method. Furthermore, from Figure 7.5(b), we observe that the flow is supersonic in most parts of the collapsing cloud, except for a few zones near to the centre and inside the external boundary. This is in perfect agreement with the results obtained by Bodenheimer and Sweigart [5] who also detected a subsonic flow just inside the cloud surface. The position and value of the maximum infall velocity are, on the other hand, in good agreement with the Boss results.

The density profile for a full isothermal collapse run through six orders of magnitude increase in the central density, is plotted in Figure 7.6. The initial model was taken to be a $1M_{\odot}$ protostellar cloud of predominantly molecular hydrogen, with $X = 0.635$,

$Y = 0.323$ and $Z = 0.224$, initially at rest with a constant temperature $T = 10K$ and a uniform density $\rho = 1.4 \times 10^{-19} gcm^{-3}$. The calculation was made with forty moving grid-points, and the density profile shown was obtained at $1.27t_{ff}$ when the central density has increased to roughly $0.92 \times 10^{-13} gcm^{-3}$. At this time in the collapse, the intermediate regions of the cloud as well as those zones near to the centre, are collapsing supersonically with maximum infall velocities of $\sim 1.6C_{ss}$. The density distribution of the envelope varies as $\rho \propto r^{-2.16}$. This law roughly matches the form $\rho \propto r^{-2}$ predicted by Bodenheimer and Sweigart [5] and by Larson [61]. In comparison, Boss [13] for a similar initial model obtained for the envelope $\rho \propto r^{-2.3}$. On the other hand, the density profile shows a tendency to flatten in the very innermost regions of the cloud, as predicted by Shu [101].

In Figure 7.7, we show the evolution of the central density. Note that by $1t_{ff}$ the central density has increased by only two orders of magnitude, with the collapse having proceeded rather slowly due to the resistance of the pressure forces. By about $1.1t_{ff}$, the density of the innermost regions has increased enough to allow the collapse of these regions to proceed on a relatively short time-scale. At this point, the self-gravitation of the central nucleus has become much stronger than the gas pressure, and the central density grows rapidly by 3 orders of magnitude in $\sim 0.17t_{ff}$. The density of the outer regions is nearly constant. This behaviour confirms the non-homologous character of the collapse [61]. The mass of the outer zones does not change by an appreciable amount during the evolution, so that only a small fraction of the total mass is effectively contained within the central high density portions.

In order to test the ability of the present numerical code in maintaining an equilibrium configuration over long time-scales, we have calculated the spherically symmetric

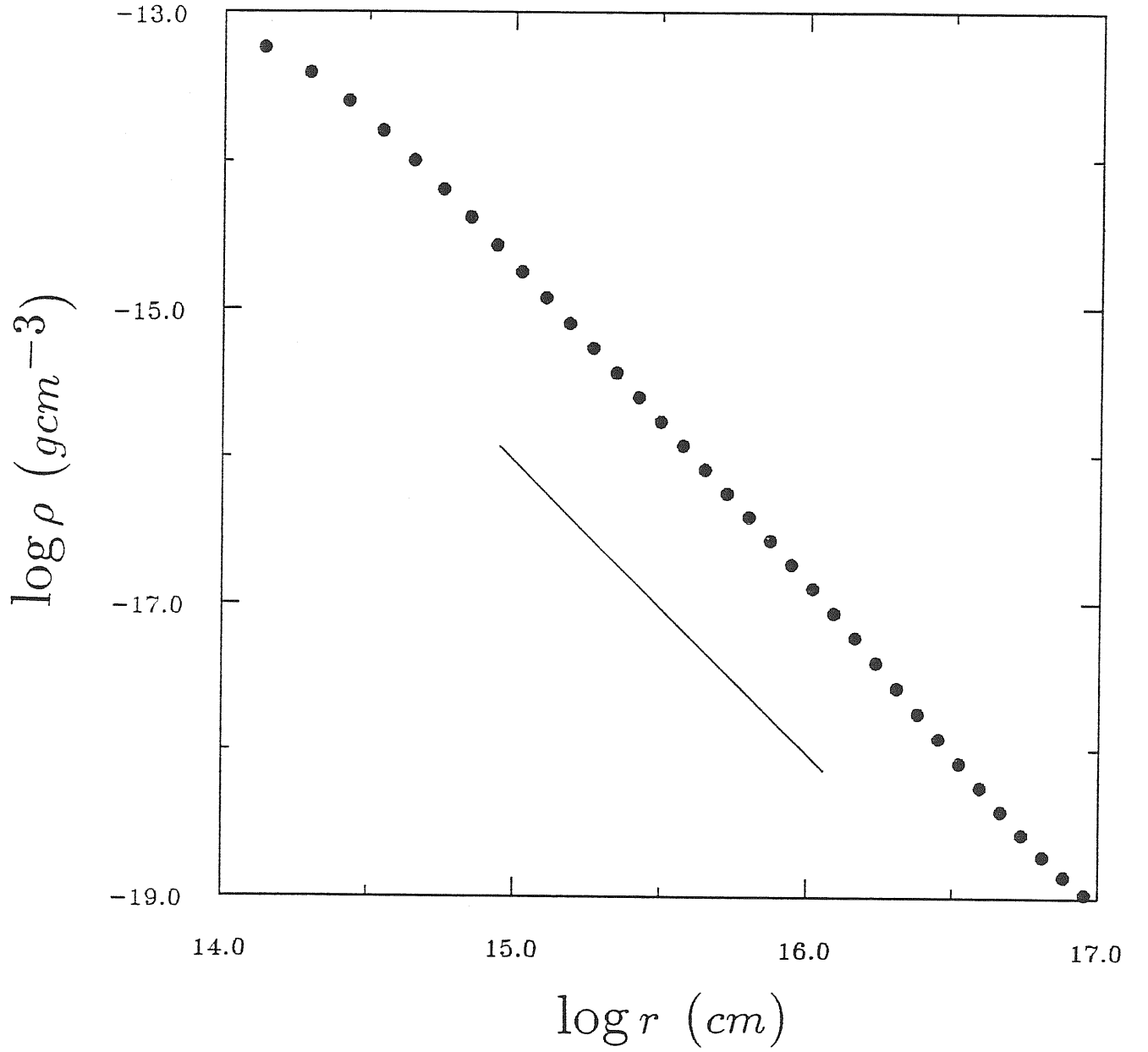


Figure 7.6: Density profile after $1.27t_{ff}$ for the isothermal collapse of a molecular cloud initially at rest with $\rho = 1.4 \times 10^{-19} \text{ g cm}^{-3}$. The calculations were carried out with 40 moving points and $\Delta t = 0.4\Delta t_{CFL}$. The solid line corresponds to the profile $\rho \propto r^{-2}$.

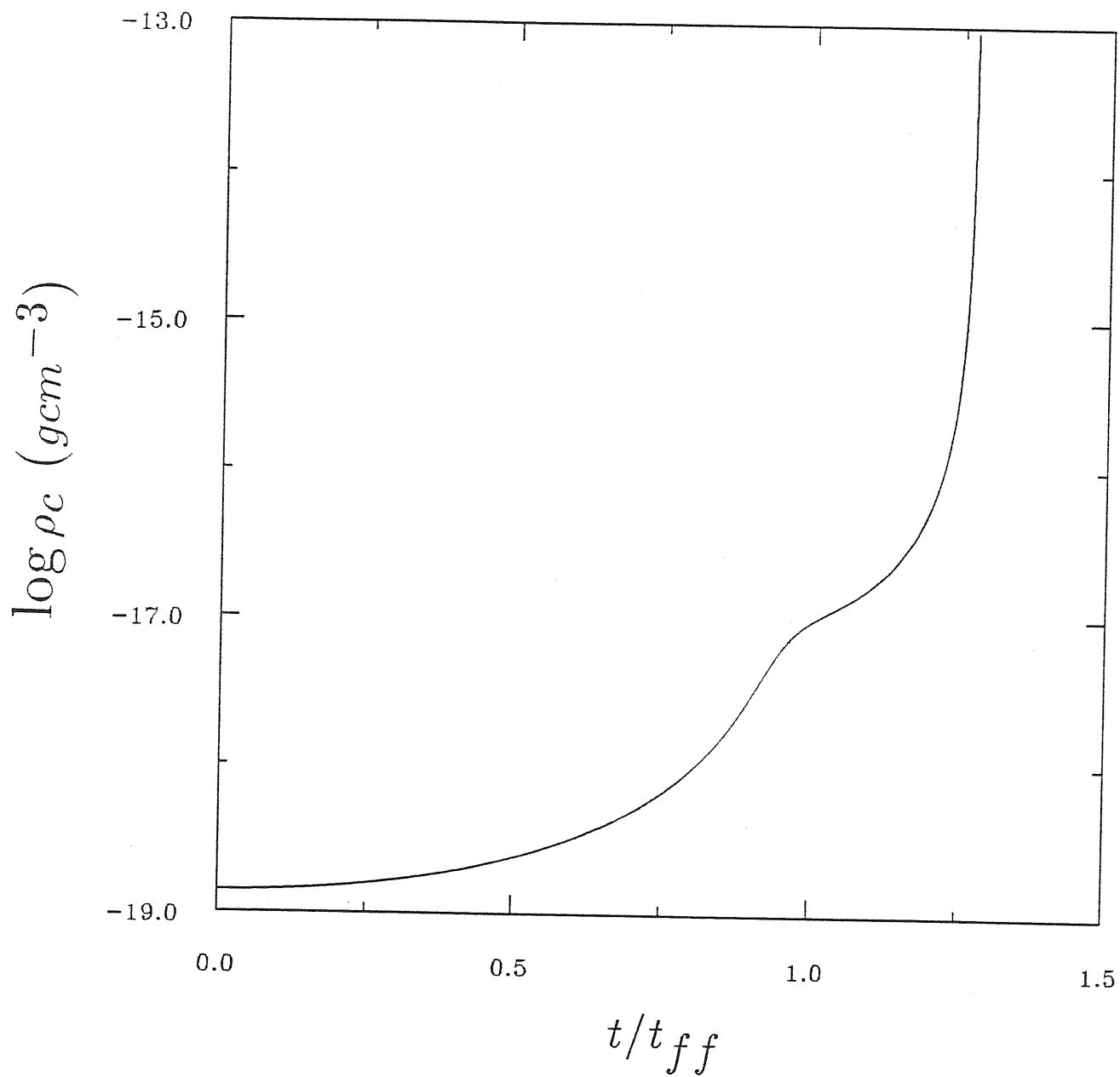


Figure 7.7: Evolution of the central density for the same model of Figure 7.6.

collapse of a $1M_{\odot}$ cloud with an adiabatic pressure-law $p \propto \rho^{7/5}$, which is appropriate for molecular hydrogen. The calculation started from initial static and uniform density ($\rho = 1.38 \times 10^{-18} gcm^{-3}$) conditions, with forty moving grid points and with $\Delta t = 0.4\Delta t_{CFL}$. Boss [13] claimed that the collapse of such a cloud is halted at around $1t_{ff}$, with the further evolution being characterized by rapid oscillations of the central density about a value roughly twice that of the initial configuration. This general situation is confirmed by the present code, as shown in Figure 7.8. In our case, at $\sim 1t_{ff}$ when the collapse is halted, the central density has increased by roughly two orders of magnitude and it then oscillates about a smaller equilibrium configuration. In Figure 7.8 we have plotted the central density as a function of time only until $4t_{ff}$. The further evolution will be similar with the central density oscillating more slowly. At $4t_{ff}$ the infall velocities in most parts of the cloud range from $\sim 0.3C_{ss}$, to $\sim 0.8C_{ss}$, with the flow being supersonic ($\sim 2C_{ss}$) only for a few zones near to the external boundary surface. The physical significance of the present test is in demonstrating how the collapse would be affected by using a pressure-law which is clearly not suitable for describing the protostellar evolution at low densities ($\sim 10^{-18} - 10^{-19} gcm^{-3}$). We may then compare the results of Figure 7.8 with those of Figure 7.7 obtained with an isothermal pressure-law.

Finally, we test the sensitivity of the numerical code to the gravitational instability of isothermal spheres.

The Jeans criterion for the instability of an isothermal spherical mass of gas was first derived by Bonnor [11]. It states that an extended gas cloud with density ρ and constant temperature T , will be gravitationally unstable only if its external radius R_0

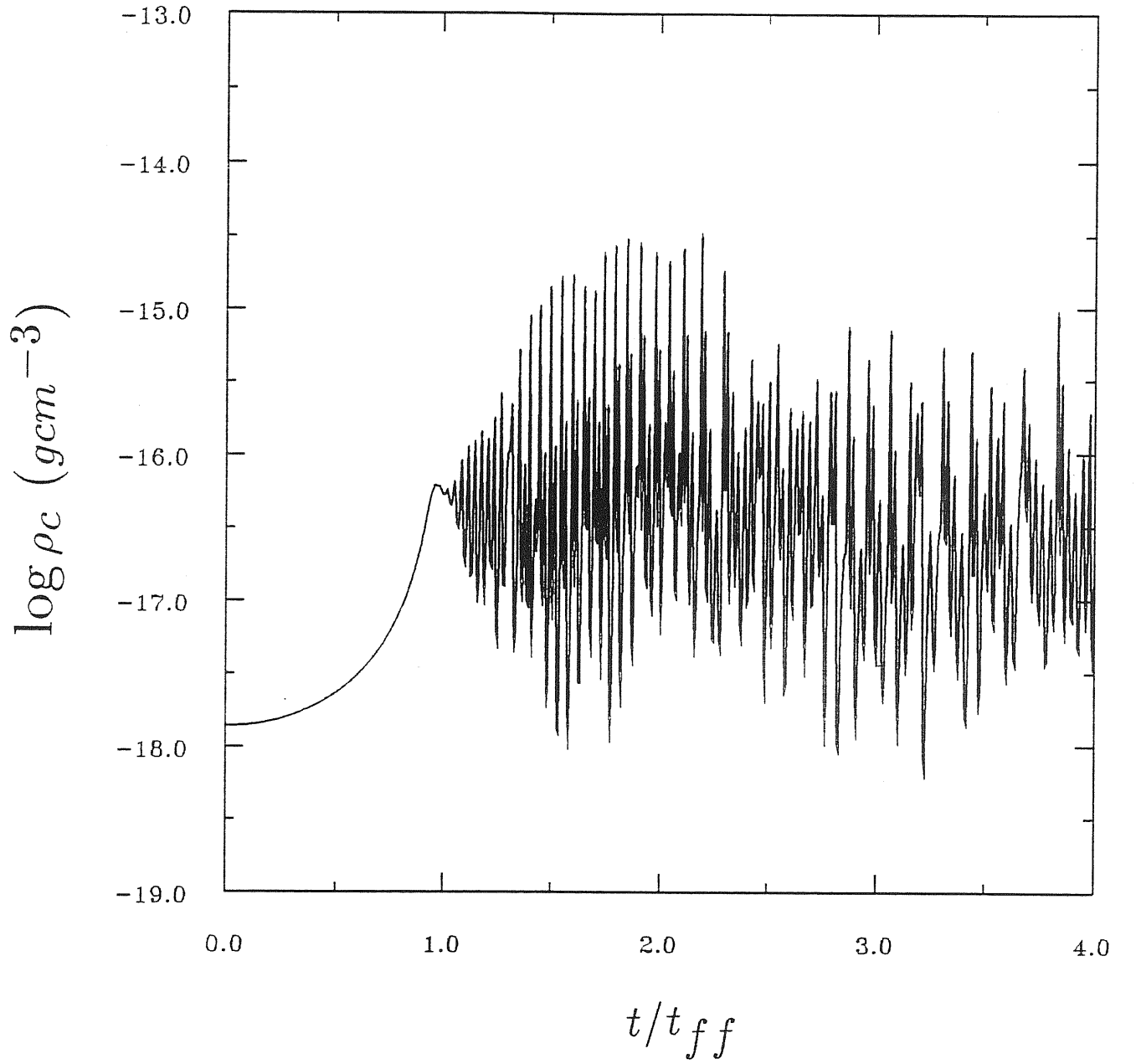


Figure 7.8: Evolution of the central density up to $4t_{ff}$ for the adiabatic collapse of a molecular cloud (with $p \propto \rho^{7/5}$) initially at rest with $\rho = 1.38 \times 10^{-18} \text{g cm}^{-3}$.

exceeds the critical value r_c given by

$$r_c = C_J \left(\frac{kT}{\mu m_p G \rho} \right)^{1/2} \quad \text{with } C_J = 0.89. \quad (7.3)$$

Otherwise, the gas sphere will not completely collapse. For numerically testing this criterion, we assume an initial model identical to that chosen by Larson [61] and Boss [13], i.e. a $1M_\odot$ cloud of molecular hydrogen, initially at rest with a uniform density of $1.1 \times 10^{-19} \text{ g cm}^{-3}$. We may then construct a sequence of initial models by varying the value of the temperature. In other words, we are defining a number of initial protostars with differing thermal energies (by changing T) and the same gravitational energy (by always assuming the same initial ρ). From equation (7.3), it is therefore expected that by progressively decreasing the temperature, r_c will eventually become less than R_0 , and the cloud will then collapse unimpeded without experiencing any bounces. The response of the 1-dimensional code for this test is illustrated in Figure 7.9. The dots indicate the value of the central density at the first bounce for different initial temperatures. The bounce is registered at the instant when the flow in the innermost shell reverses.

As seen in the Boss [13] results, as the temperature is decreased towards the critical value of $7.3K$ [predicted by eq.(7.3)], the cloud experiences a central bounce at progressively higher central densities. For a temperature of $7.549K$, we found that the cloud bounced at a very high central density ($\rho_c \sim 1.2 \times 10^{-13} \text{ g cm}^{-3}$). Only for temperatures less than this value, did we obtain an indefinitely continued collapse. Boss, however, found a numerical critical temperature of $7.7K$ after a sequence of bounces occurring at much lower central densities. Our critical temperature $T = 7.548K$ is surprisingly good, especially if one bears in mind that the calculations were carried out with only twenty radial grid points and $\Delta t = 0.4 \Delta t_{CFL}$.

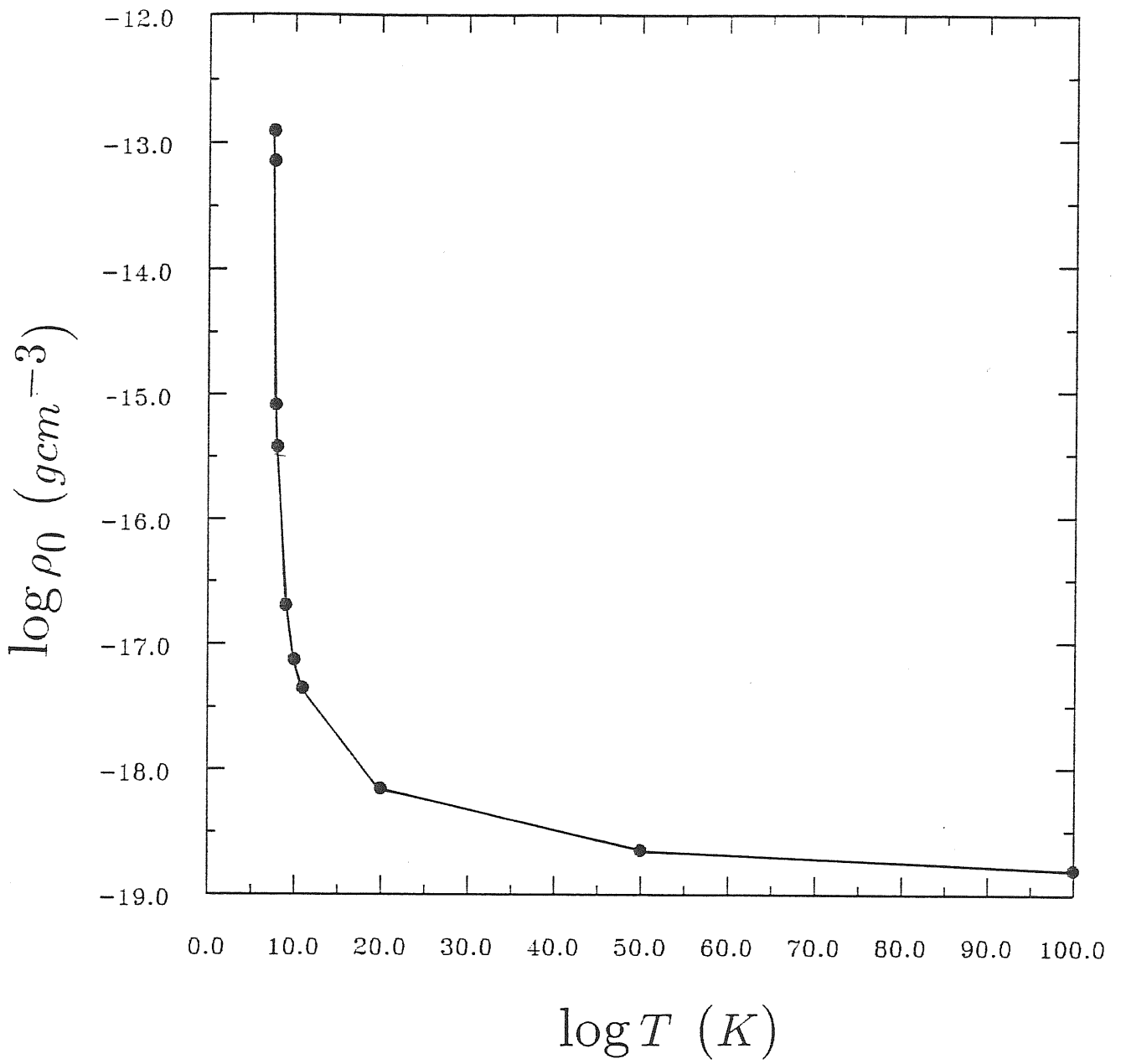


Figure 7.9: Densities at which a central bounce occurs (marked by dots) for isothermal collapse of molecular clouds starting from rest with $\rho = 1.1 \times 10^{-19} \text{ g cm}^{-3}$ and having various temperatures.

If we set $r_c = R_0$ and $T = 7.548K$ in equation (7.3), we then obtain $C_J = 0.875$, which is slightly better than $C_J = 0.87$ obtained by Boss [13]. By comparison, Larson [61] reported $C_J = 0.72$.

7.3 Conclusions

The pressureless collapse tests have tested the accuracy of the present numerical scheme. In agreement with Boss [13], we found that the use of a coarse mesh can lead to reasonably accurate results if: (a) the number of grid points is made as large as possible, (b) the artificial viscosity terms are neglected, (c) the grid is initially allowed to contract with the fluid, (d) a small enough fraction of the CFL-time step is used, and (e) the radial advection terms are written in compact form. Thus, for multi-dimensional calculations, in order to get improved accuracy particular attention should be paid to points (b), (c), and (e), since point (d) is already implicit due to the constraints imposed by the 2- and 3-dimensional meshes. Even for a large fraction ($f = 0.9$) of the CFL-time, the initial optimum Δt will correspond to nearly $1/8$ (2-dimensional case) and to $\sim 1/20$ (3-dimensional case) of the initial Δt allowed by the radial flow in the 1-dimensional case.

The improvements obtained in some of the spherically symmetric runs, with respect to the results of other donor-cell codes, are apparently due to the superior approximation given by the compact representation of the radial advection terms. As previously noted by Durisen et al [33], if the gravitational potential is being sufficiently accurately computed, any improvement further enhancing the accuracy of the Poisson solver, will have negligible effects on the accuracy of the hydrodynamical approximation.

The good response of the 1-dimensional code to the physical situations typically

encountered during the isothermal collapse of protostellar clouds, as well as its high sensitivity with respect to the Jean's criterion, make us guardedly optimistic about the 2- and 3-dimensional schemes.

Chapter 8

Axisymmetric Collapse

More realistic numerical simulations of early protostellar collapse must include at least the effects of magnetic fields and rotation, as is clear from observations of dense interstellar clouds. Such effects are expected to influence gravitational collapse by forcing the cloud to flatten and hence, to substantially deviate from spherical symmetry. These deviations will eventually amplify giving rise to either axisymmetric or non-axisymmetric instabilities. The study of how these perturbations grow during anisotropic protostellar collapse, is of great interest in connection with the theory of star formation. Therefore, a multi-dimensional treatment of the collapse is mandatory if important additional physics is to be gradually incorporated. The extension of the present 1-dimensional version of the code to 2-space dimensions, besides representing the first step in relaxing the idealized assumption of spherical symmetry, allows for dealing with the dynamical growth of axisymmetric perturbations, which may well occur in realistic protostellar evolution.

Most of the implemented 2-dimensional codes have been mainly concerned with studying the effects of rotation only during the isothermal phase of protostellar collapse. The neglect of magnetic fields is physically justified if the calculations are started at

the end of the molecular cloud formation stage ($n > 10^{-4} \text{cm}^{-3}$). At this epoch of the evolution, we may expect the magnetic field in the cloud to be essentially detached from the exterior background medium, so that magnetic torques are no longer able to act so as to transfer angular momentum outwards from the collapsing cloud. Furthermore, the molecular and turbulent viscosities are negligible for the initial collapse phase of interstellar clouds and, hence, we cannot expect appreciable transfer of angular momentum by shear stresses during the isothermal stage. The initial protostellar collapse should therefore proceed dynamically with each element of fluid moving inwards with conserved angular momentum.

That rotation is however a crucial effect was demonstrated by the numerical calculations of Larson [63], who found that initially non-rotating, axisymmetric, isothermal clouds collapse in a similar way to spherically symmetric clouds, even when the initial configurations are assumed to be deformed. This means that in the complete absence of rotation, any tendency of initial deformations to amplify during the gravitational collapse, may very well be impeded by the action of the pressure forces. Only when such clouds were allowed to uniformly rotate, did axisymmetric perturbations grow giving rise to ring-like density enhancement in the inner regions.

Ring formation as first observed by Larson [63], has been successively reported by other workers [4,8,14,17,84,111,115]. This agreement confirmed that the occurrence of ring formation may constitute a natural event in the collapse of axisymmetric isothermal clouds. However, the physical plausibility of this outcome was questioned by the results of a few investigators [31,56,75,85,113], who did not observe ring formation but rather disk formation at the end of their isothermal collapse calculations. This apparent disagreement was attributed in part to deficiencies in numerical techniques, as in the

case of Kamiya [56] (whose Lagrangian code introduced strong distortions of the mesh in the innermost regions of the computational grid), and in part to the inability of some of the schemes to conserve angular momentum locally and globally (as it was the case of Deissler [31] and Tsharnuter [113] codes). Furthermore, semi-analytical [111] and analytical [14] calculations have also shown that the numerically predicted rings may constitute a real phenomenon. Although these calculations were made in the pressureless limit with each particle in the cloud being subjected to a static background potential field, they have provided good physical insight into how rings may develop, in more elaborate numerical simulations. If angular momentum is conserved, the action of the gravitational and centrifugal forces could be sufficient to excite a ring-like density wave. The innermost particles, having collapsed more rapidly than the outermost ones, reach their minimum radii first and start moving outwards away from the rotational axis, while the outer particles, which have not yet reached their minimum radii, are still infalling. In this manner, the outwardly and inwardly directed particles meet each other forming a well pronounced ring-like density enhancement, which then propagates outwards.

The existence of ring solutions is of further importance due to their intrinsic unstable nature with respect to fragmentation when treated in 3-space dimensions [87].

In the following sections, we shall illustrate and discuss a few important tests carried with the 2-dimensional axisymmetric version of the present numerical code. The first crucial test deals with the question of local conservation of angular momentum. The local conservation of the donor-cell advected angular momentum is expected to be improved by the partially centred scheme introduced in Chapter 6. Section 6.8. The 2-dimensional code has also been tested to check the ability of the hydrodynamical

approximation to maintain a spherically symmetric collapse in the absence of rotation. Finally, the sensitivity of the scheme to ring formation is established for three isothermal collapse runs. The initial conditions for such models were chosen to allow for direct comparisons with the results obtained by Black and Bodenheimer [4] and Boss [12,14]. Furthermore, the structure of the numerically obtained rings is compared with the equilibrium structure of the rings predicted analytically by Ostriker [91].

8.1 Consistent Advection of Angular Momentum

As previously noted in Chapter 6, Section 6.8, the first-order accuracy of the donor cell transport introduces a spurious diffusion of angular momentum within the mesh. This anomalous behaviour is corrected here by partially centring the specific angular momentum. In this manner, we improve the local conservation of angular momentum, even though the entire hydrodynamical approximation is still formally first-order accurate due to the donor cell advection of the remaining variables.

To correctly test the sensitivity of the 2-dimensional code with respect to local conservation of angular momentum, we consider the collapse of a uniform-density, uniformly rotating, isothermal cloud, with a small ratio β of rotational to gravitational energy. The collapse of this configuration should initially proceed isotropically, with the density of the inner regions increasing while remaining uniform due to the absence of a central pressure gradient. In these conditions, the fluid in the inner spherical shells, which is still rotating at a uniform rate, will collapse with constant total mass and angular momentum. We may then establish a relation between the density ρ and the angular velocity ω of the central plateau. That is, since $M \propto \rho r^3$ and $J \propto M \omega r^2$ are

constants for some particular shell of radius r , we have that

$$\omega_{\text{plateau}} \propto \rho_{\text{plateau}}^{2/3}, \quad (8.1)$$

if the angular momentum J is locally conserved.

The analytical law (8.1) has been tested numerically for the isothermal collapse of a $1M_{\odot}$ molecular cloud ($\mu = 2$) with a temperature of $10K$ which is initially stationary with $\rho_0 = 1.38 \times 10^{-18} \text{ g cm}^{-3}$ and $\omega_0 = 1.52 \times 10^{-13} \text{ s}^{-1}$. This model corresponds to a protostar with initial ratios of thermal and rotational energy to the gravitational energy of $\alpha = 0.549$ and $\beta = 0.02$, respectively. The calculation was carried out with a radially moving grid ($N_r \times N_{\theta} = 241$ cells) and $\Delta t = 0.4 \Delta t_{ff}$. In figure 8.1, we illustrate the equatorial density and angular velocity profiles at $0.487 t_{ff}$ in the collapse. The central plateau is well confirmed by the calculation, with the density and the angular velocity being uniform for the innermost 11 radial cells. At this time the collapse is roughly spherically symmetric and proceeds rather slowly with maximum infall radial velocities slightly larger ($\sim 0.17 \text{ km s}^{-1}$) along the rotational axis than in the equatorial plane ($\sim 0.16 \text{ km s}^{-1}$).

To find out how well the numerical equatorial profiles (in Figure 8.1) match the analytical law (8.1), we write

$$\log \omega_{\text{plateau}}^{\text{num}} = \lambda \log \rho_{\text{plateau}}^{\text{num}} + \log K, \quad (8.2)$$

where the constant K may readily be obtained from the initial uniform density and angular velocity distributions. Solving for λ in equation (8.2), we obtain that $\omega_{\text{plateau}} \propto \rho_{\text{plateau}}^{2.0022/3}$ for the numerical plateau. This result is surprisingly good and indicates that there is only a very slight amount of remaining inward transfer of angular momentum. When the same run is carried out by advecting the angular momentum with the usual

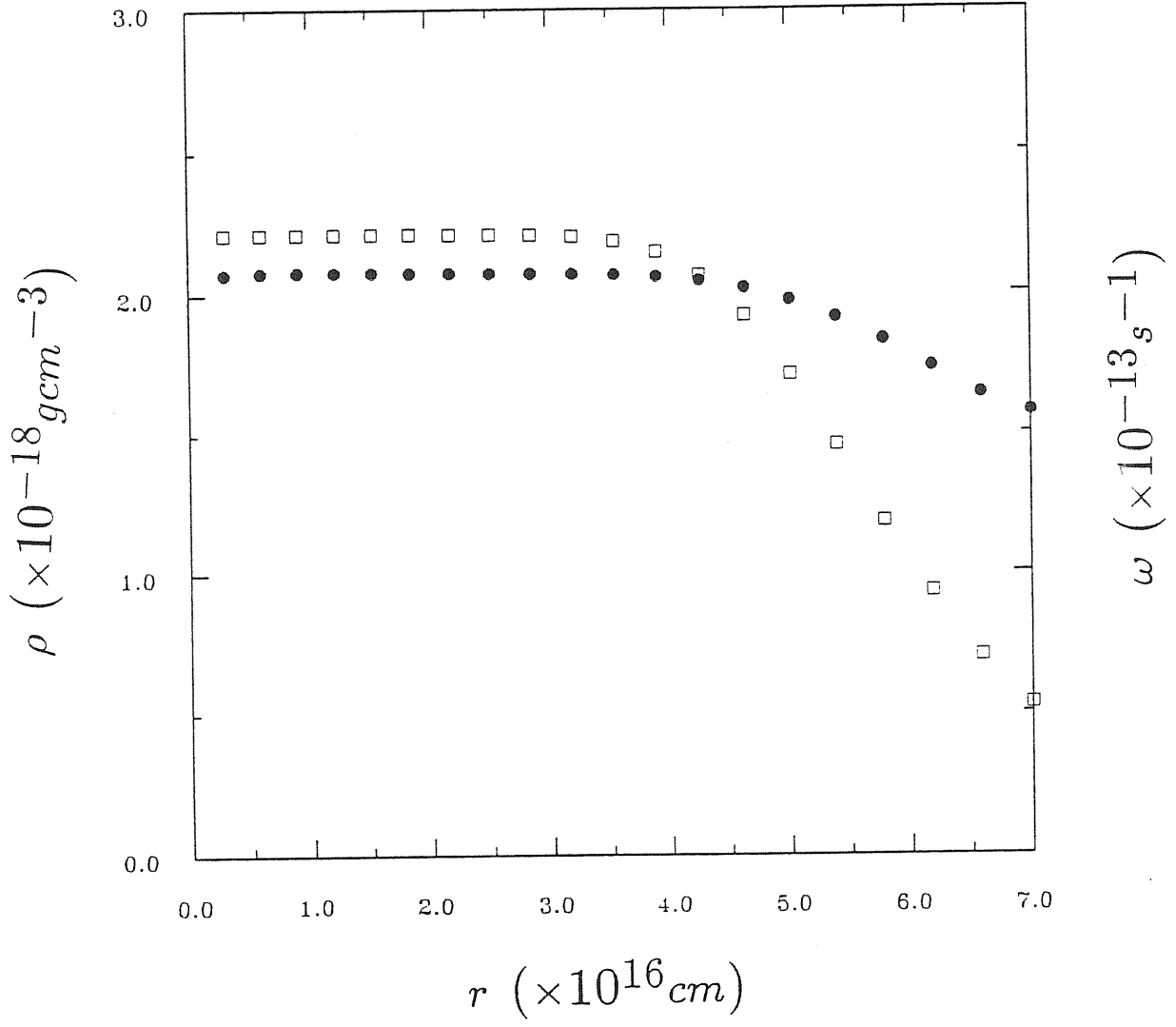


Figure 8.1: Profiles of the equatorial density (blank squares) and angular velocity (dots) at $0.487t_{ff}$ in the collapse. The existence of an extended central plateau is confirmed by the calculation.

donor cell method, the angular velocity of the central plateau varies as $\omega \propto \rho^{2.09/3}$. It is clear that the amount of inward transfer of angular momentum in the inner regions increases due to the rather strong spurious diffusion of the donor-cell advection. This situation confirms the conclusions which were reached in Chapter 6, Section 6.8, by comparing the leading truncation errors for both methods.

For the same initial model Boss [14] obtained the numerical law $\omega \propto \rho^{1.97/3}$ when advecting the angular momentum with the partially centred scheme and $\omega \propto \rho^{2.11/3}$ with the standard donor cell method. In his case, the angular momentum is being slightly transferred outwards rather than inwards. He argued that erring on this side of the analytical law (8.1), ring formation would be inhibited and hence, if rings are numerically detected, they are not being produced by the inward transfer of angular momentum. However, independently of the side on which the numerical exponent is deviating from its analytical value, we may conclude that the present numerical scheme is apparently doing a better job than the Boss code in locally conserving the angular momentum. In our case, the numerical law $\omega \propto \rho^{2.0022/3}$ matches the analytical profile (8.1) with a relative error of 0.001% against the 0.015% relative error obtained by Boss [14]. This improvement may be attributed to the superior difference approximation obtained by the use of the radial compact quotients.

The 2-dimensional code was further tested for an initially non-rotating sphere. The initial conditions were chosen as a $1M_{\odot}$ atomic hydrogen cloud at $T = 100K$ with a uniform density of $10^{-15}gcm^{-3}$. This model is the same one used for testing the 1-dimensional isothermal code [See Figures 7.4(a) and (b) of Chapter 7]. At $0.971t_{ff}$, when the central density reached the value of $\sim 2.2 \times 10^{-13}gcm^{-3}$, the density of the first shell of cells was spherically symmetric up to the ninth significant figure towards the

symmetry axis ($\theta = 0$), and up to the twelfth significant figure towards the equatorial plane ($\theta = \pi/2$), out of fourteen digits carried. The radial velocity, on the other hand, remained spherically symmetric up to the tenth significant figure in the innermost two shells, while for the outer shells both the density and radial velocity were isotropic up to the twelfth digit and, in places, up to the thirteenth digit. This result demonstrates that the 2-dimensional code is able to recognise a spherically symmetric configuration (with good accuracy), confirming the situation found by Larson [63].

8.2 Ring Formation

In this section, we discuss the phenomenon of ring formation in the isothermal collapse of axisymmetric rotating clouds, as it is actually observed with the present 2-dimensional code. We consider three different collapse models initially at rest with uniform density and angular velocity distributions. The first model 2D1 is a $1M_{\odot}$ molecular cloud ($\mu = 2$) at $10K$ with $\rho_0 = 1.38 \times 10^{-18} gcm^{-3}$ and $\omega_0 = 1.52 \times 10^{-13} s^{-1}$, corresponding to initial ratios of thermal and rotational energy to gravitational energy of $\alpha = 0.549$ and $\beta = 0.02$, respectively. This model is the same used in Section 8.1 for testing the local conservation of angular momentum and has been chosen to allow comparisons with results obtained by Black and Bodenheimer [4] (case 1A) and Boss [14] (case I). The second model 2D2 was a $1M_{\odot}$ molecular cloud ($\mu = 2.45$) at $7.5K$ with $\rho_0 = 4.75 \times 10^{-19} gcm^{-3}$, $\omega_0 = 3 \times 10^{-13} s^{-1}$, and initial ratios $\alpha = 0.479$ and $\beta = 0.226$. These initial conditions are nearly the same as those used by Larson [63], with the only difference being that his initial cloud was slightly hotter ($T = 10K$). Model 2D2 has been used to test the consistency of ring formation with the present numerical code. Finally, the third model 2D3 corresponds to a $1M_{\odot}$ molecular hydrogen cloud ($\mu = 2$)

at $10K$ and initially with $\rho_0 = 1.44 \times 10^{-17} gcm^{-3}$, $\omega_0 = 1.56 \times 10^{-12} s^{-1}$, $\alpha = 0.251$, and $\beta = 0.202$. The sets of initial conditions for models 2D2 and 2D3 are the same as those of the Boss [12] cases 2D-II and 2D-IV, respectively.

All runs were performed on a radially moving grid, with either 20 or 30 radial grid points, using a constant-volume boundary condition and usually with $\Delta t = 0.4 \Delta t_{CFL}$. In none of the above cases was additional artificial viscosity needed to mediate the shocks which arose, as the numerical diffusion implicit in the donor-cell advection of the hydrodynamical variables was sufficient to ensure stability. All of the initial models satisfied the instability criterion for gravitational collapse

$$\alpha \leq 1 - 1.43\beta, \quad (8.3)$$

first derived by Larson [63] and then reviewed and expressed in terms of the parameters α and β by Black and Bodenheimer [4]. By neglecting the effects of rotation ($\beta = 0$), inequality (8.3) reduces to the classical Jean's criterion for spherically symmetric collapse.

Model 2D1 is a very slow rotator compared with the other two models. This cloud starts collapsing rather slowly, with the collapse being nearly spherically symmetric until about $0.5t_{ff}$. At this time, the collapse begins to deviate from the initial spherical symmetry, with the material falling down the rotational axis experiencing a slightly more rapid inflow than that near to the equatorial plane. This situation arises because the axially directed flow is not being retarded by the centrifugal forces, which become stronger and stronger towards the equator. There is then a continuous flattening of the cloud in the inner regions due to the non-homologous nature of the collapse. At the end of the flattening phase (by $\sim 1t_{ff}$), the outermost zones are still collapsing approximately in spherical symmetry with infall radial velocities ($\sim 0.2kms^{-1}$) lower

than those experienced by the innermost and intermediate regions. At $1.070t_{ff}$, a well-marked disk-like density distribution forms in the central portions of the cloud, as seen in Figure 8.2.

Figure 8.2 is a meridional contour density plot for the inner nine shells. Due to the assumptions of azimuthal symmetry ($\partial/\partial\phi = 0$) and reflection symmetry about the equator, the calculations are here represented in one-quarter of a full cross-section through the centre of the computational volume [See Figure 4.1(a)]. All contour density plots have been performed with the aid of the CONRAS routine, a “super” version of the CONRAN contour-plotting package. The contour lines are obtained by first triangulating the input data (the logarithms of the cellwise densities) and then by interpolating the triangulated data with a smooth C1 surface interpolation algorithm. The numbers appearing on the contour lines correspond to the logarithm of the density and represent changes by the interval factors given in the captions.

At $1.070t_{ff}$, the material in the inner regions of the cloud is collapsing considerably more quickly along the axis ($v_r \sim 0.8\text{ km s}^{-1}$) than along the equatorial plane ($v_r \sim 0.3\text{ km s}^{-1}$) with the infall radial velocities in the fourth and fifth inner axial and main grid cells being ~ 4 times the isothermal sound speed ($C_{ss} \sim 0.2\text{ km s}^{-1}$). The radial velocities in the innermost three axial and main grid cells ($j \leq 3$) have reversed, so that the material in these regions is now experiencing a bounce. This outwardly directed flow then indicates that a shock front has formed just above the central disk. The shock is strong near the axis and extends up to $\theta \sim 50^\circ$ ($j = 6$), where it diffuses out. The shock has been produced because of the rapid infall of matter in the region of the axis. The effect of this situation is then a continuous piling up of material in the centre, with a consequent abrupt increase of the density to the point where the pressure gradients

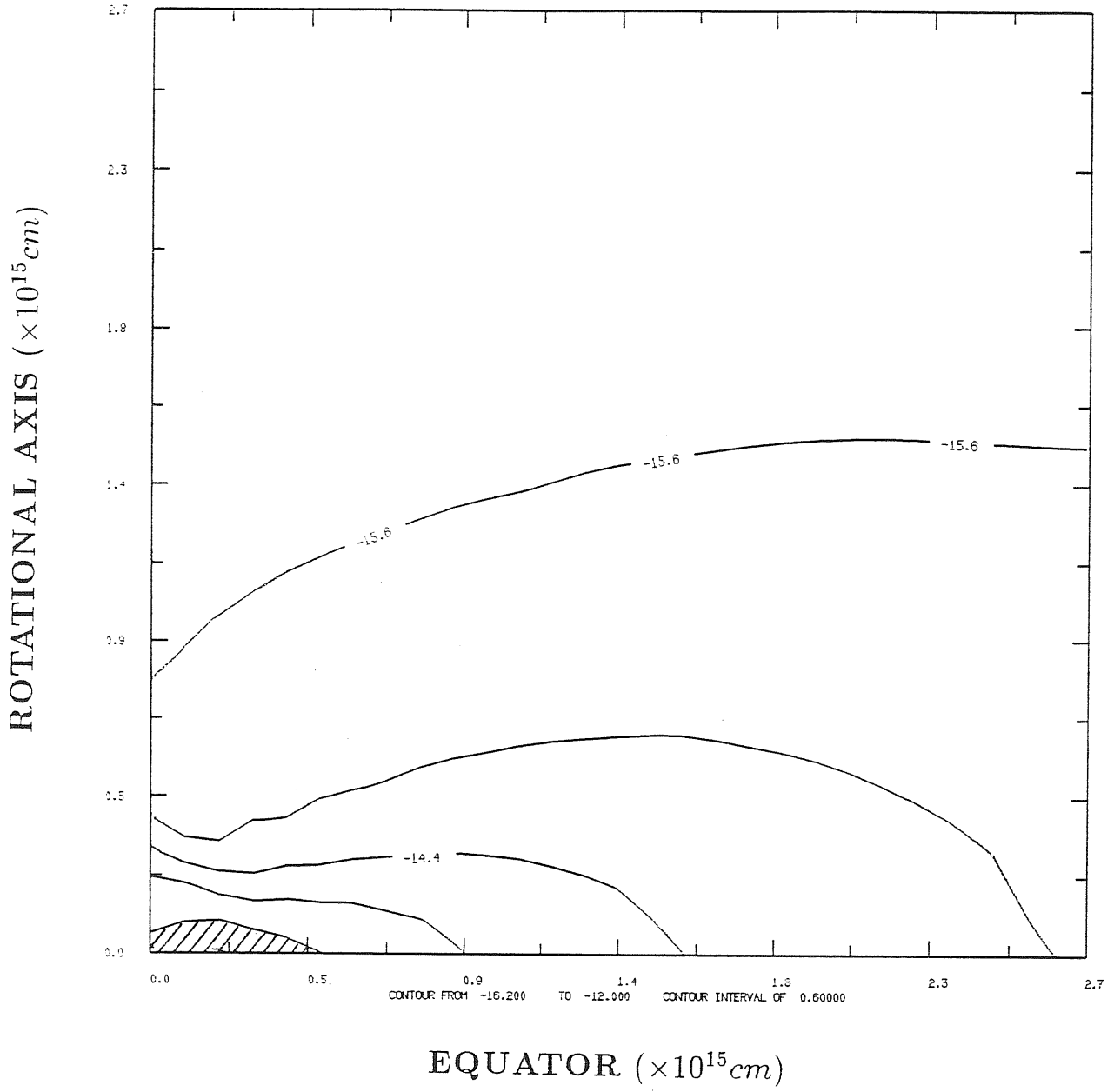


Figure 8.2: Meridional density contour plot for model 2D1 after $1.070t_{ff}$ in the collapse. $\rho_{max} = 4.35 \times 10^{-13} \text{ g cm}^{-3}$. The contour interval factor of 0.6 corresponds to a real factor of 3.98. The cross-hatched region is a region of density maximum.

were first enough to hinder the flow and then to reverse it. The matter in the innermost equatorial zones is still collapsing at a rather slow rate ($v_r \sim 0.1 - 0.2 \text{ km s}^{-1}$) because part of the gravitational force there is supplying the centripetal acceleration of the rotational motion. Note that the maximum central densities of the disk-like core are roughly $4.3 \times 10^{-13} \text{ g cm}^{-3}$, so that by this time a few central zones have exceeded the isothermal limit ($\rho \sim 3 \times 10^{-13} \text{ g cm}^{-3}$). The situation is qualitatively in good agreement with the results obtained by Boss [14] although in his case, the disk formed slightly later (at $\sim 1.079 t_{ff}$) with maximum densities of the order of $1.5 \times 10^{-12} \text{ g cm}^{-3}$, i.e. about three times higher than those reported here. This difference may be explained in terms of the short time-scale governing the events in the central regions of the cloud so that a small shift in time could lead to an appreciable difference in the final maximum densities.

Slightly after $1.070 t_{ff}$, the central density begins to progressively decrease and a new region of maximum density starts forming off-axis in the equatorial plane. This situation arises because the combined effects of the thermal pressure and centrifugal forces are sufficient to produce a slight outflow of mass in the innermost equatorial zones. The maximum off-axis density increases while moving slightly away from the axis on a time-scale of only $0.024 t_{ff}$. The evolution of the central and maximum equatorial densities is shown in Figure 8.3. We note that by $1.09 t_{ff}$, the density at the centre is roughly 2 orders of magnitude smaller than that at the equatorial density peak. In Figure 8.4, we show a contour density plot (including the six inner shells) showing the inner structure of the cloud at $1.094 t_{ff}$. A ring is clearly observed in the equatorial plane. At this time, the shock front has moved down the rotational axis, and is located at $r = 1.98 \times 10^{14} \text{ cm}$, as indicated by the heaping of density contour

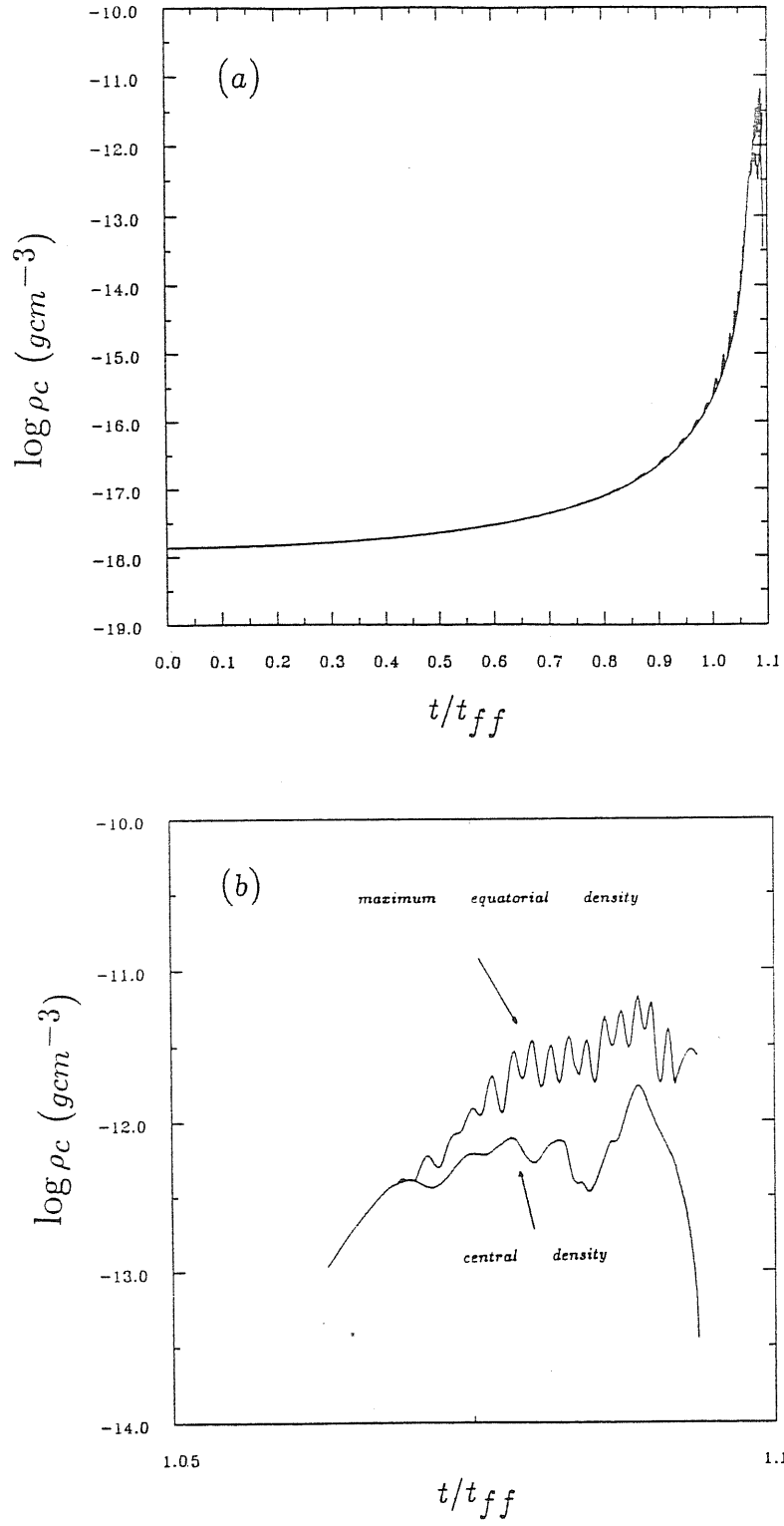


Figure 8.3: (a) Evolution of the central density and maximum equatorial density for model 2D1. (b) Enlargement of (a) showing the increase of the off-axis density maximum.

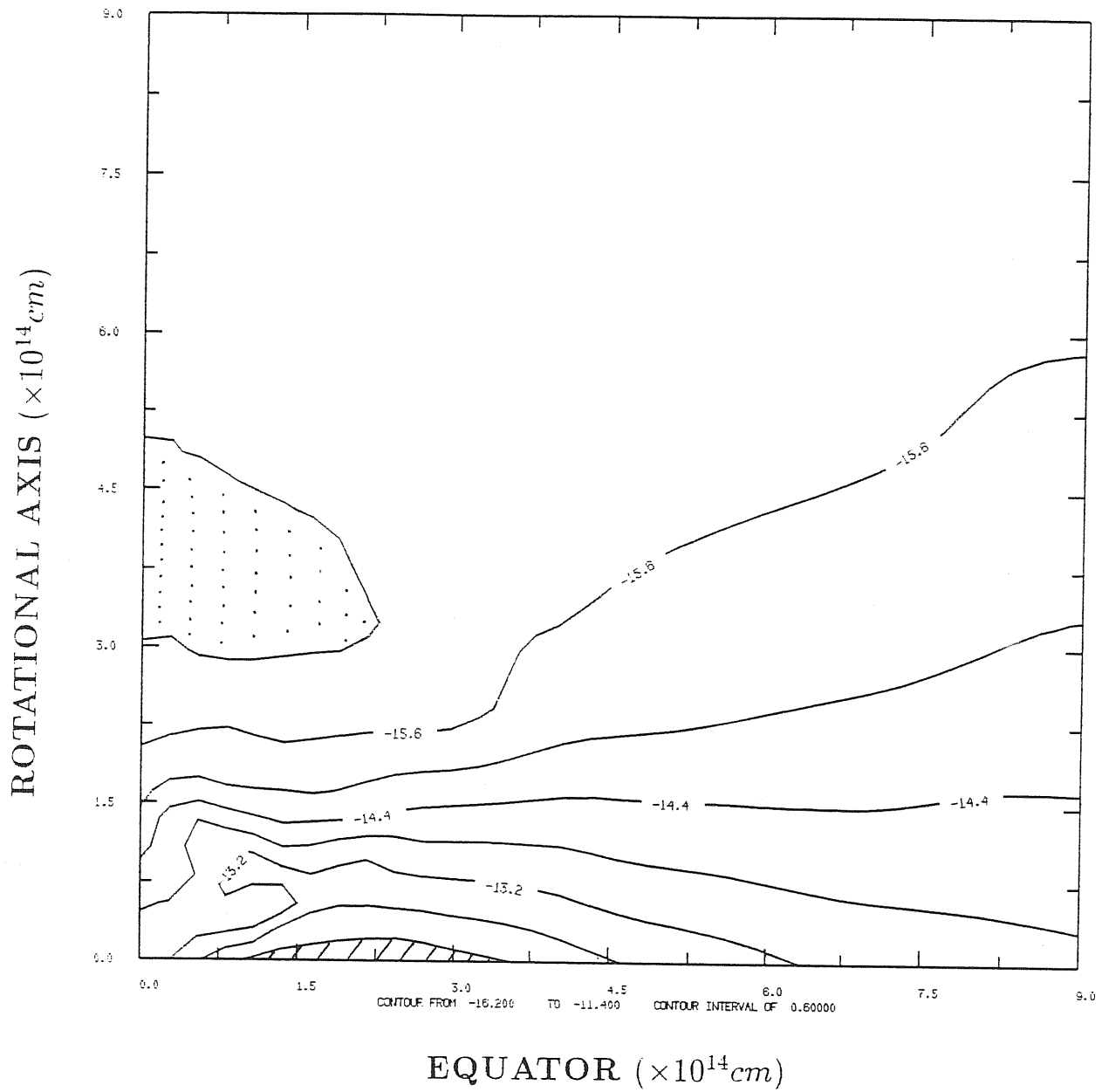


Figure 8.4: Meridional density contour plot at $1.094t_{ff}$ for model 2D1. $\rho_{max} = 2.73 \times 10^{-12} gcm^{-3}$ and $\rho_c = 3.54 \times 10^{-14} gcm^{-3}$. The contour factor of 0.6 corresponds to a real interval of 3.98. The cross-hatched region is a density maximum and the dotted region is a density minimum.

lines near to the axis. The material which is infalling ahead of the shock is eventually diverted away from the cloud centre and is constrained by the shock itself to flow towards the gravitational potential minimum (at the centre of the ring). Meanwhile, the radial velocity field in the innermost equatorial zones is such that the mass from the centre and from the outer regions of the cloud is accreting onto the growing ring. The accretion is observed to be slightly stronger just above the equatorial plane. The maximum radial infall velocities ($\sim 1.36 - 1.37 \text{ km s}^{-1}$) occur in the region of the axis in the range $\sim 3.3 \times 10^{14} \text{ cm} \leq r \leq 5.0 \times 10^{14} \text{ cm}$ (third and fourth axial cells). This is in agreement with the location of the density minimum region in Figure 8.4. The maximum outward r -velocity ($\sim 8.7 \text{ km s}^{-1}$) is observed to occur in the innermost $j = 8$ cell ($\theta \sim 65^\circ$). This high velocity flow is the responsible for the S-shaped density contour line in Figure 8.4. A similar feature was also observed by Boss [14], who argued that this is only a transient feature caused by the rather chaotic nature of the flow pattern in this region of the cloud.

In Figures 8.5, and 8.6, we now show the equatorial density, radial velocity, angular velocity and specific angular momentum profiles at $1.094t_{ff}$. These profiles can be compared with those previously obtained by Black and Bodenheimer [4] (case 1A) and Boss [14] (case I). Qualitatively, the profiles agree quite well although there are some quantitative differences. The ring produced by the present 2-dimensional code is centred at $r = 1.97 \times 10^{14} \text{ cm}$ compared with $3.4 \times 10^{14} \text{ cm}$ for Black and Bodenheimer and $2.7 \times 10^{14} \text{ cm}$ for Boss. Also, the maximum density in the ring is $2.73 \times 10^{-12} \text{ g cm}^{-3}$, in our case, with a central density of $3.54 \times 10^{-14} \text{ g cm}^{-3}$. Black and Bodenheimer obtained a maximum ring density of $1.5 \times 10^{-12} \text{ g cm}^{-3}$ and a central density of $6 \times 10^{-15} \text{ g cm}^{-3}$ at $0.9t_{ff}$, while Boss reported a maximum ring density of $2.5 \times 10^{-12} \text{ g cm}^{-3}$ and a

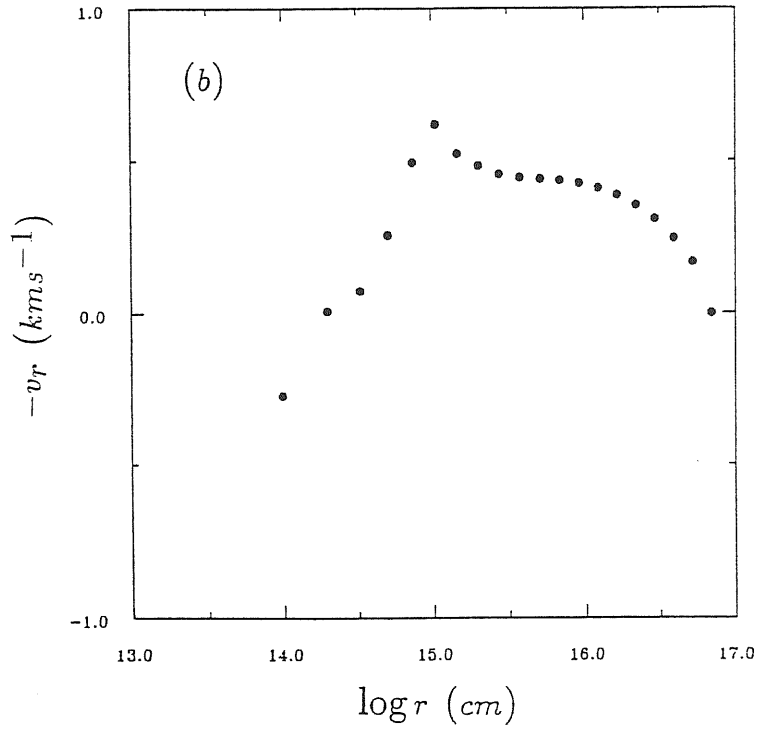
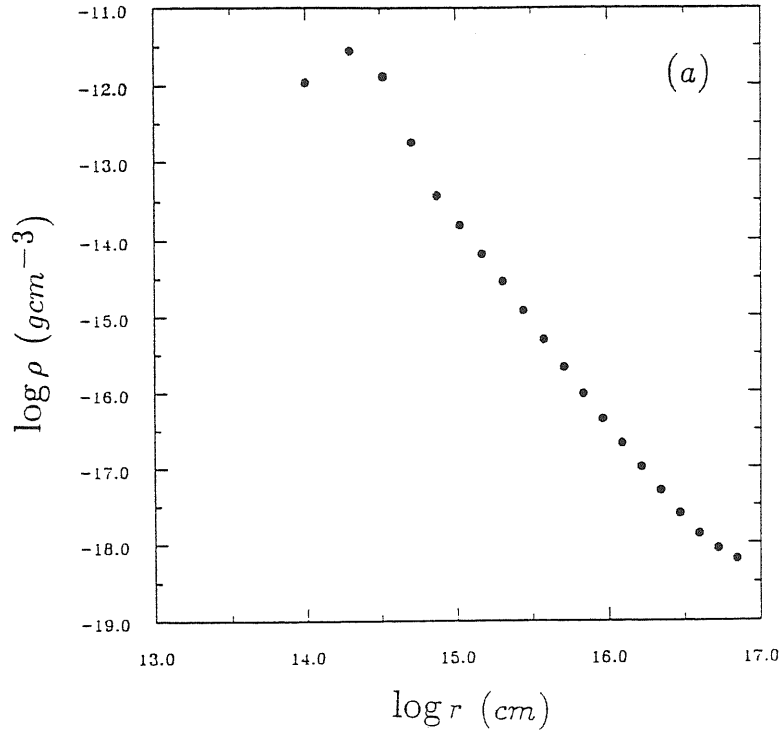


Figure 8.5: (a) Density and (b) radial velocity profiles in the equatorial plane at $1.094t_{ff}$ for model 2D1.

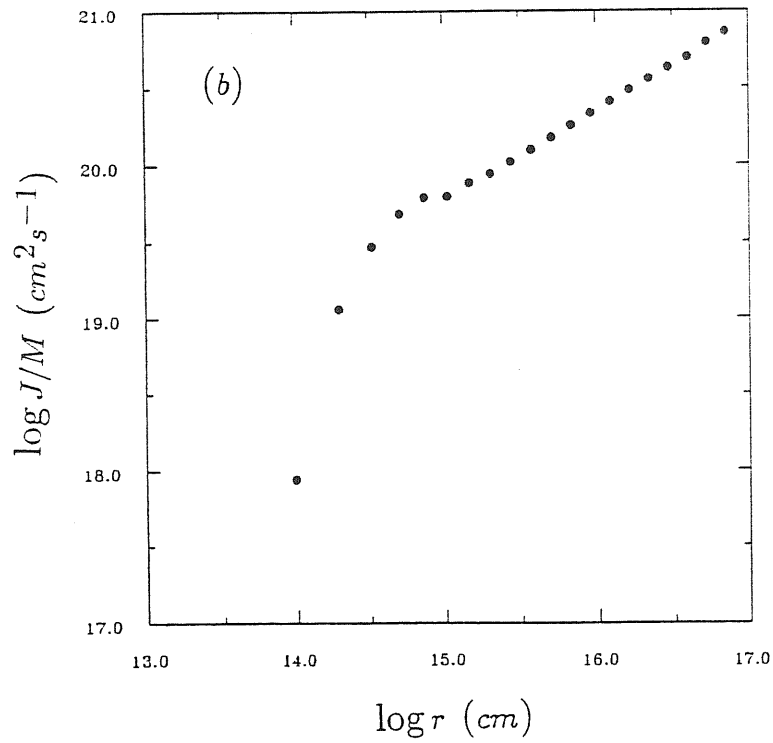
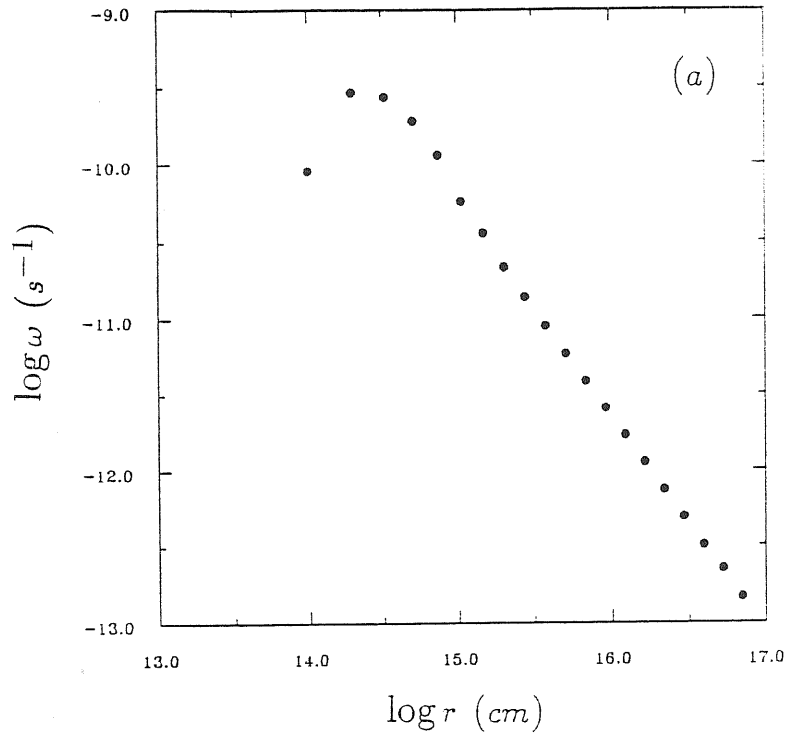


Figure 8.6: (a) Angular velocity and (b) specific angular momentum profiles in the equatorial plane at $1.094t_{ff}$ for model 2D1.

central density of $3.4 \times 10^{-14} \text{ g cm}^{-3}$ at $1.01 t_{ff}$. In all three cases, the numerical rings are consistently formed in the near-isothermal density range. Our results are closer to those given by Boss [14]. In the present case, the ring is slightly more dense than the Boss ring and considerably more dense than Black and Bodenheimer's ring. Boss [14] argued that this difference could be due to the fact that in the Black and Bodenheimer's case the ring is not well in equilibrium. The radial velocity distribution obtained here agrees with that obtained by Boss, with the position of the zero between the outwardly and inwardly directed flows nearly coinciding for the two cases. The value of the maximum infall velocity is also in good agreement. The angular velocity plot confirms that the point of maximum rotation lies at the centre of the growing ring, while the material on either side rotates at a progressively reduced rate as we go further from the region of maximum density. The specific angular momentum profile is in good agreement with the corresponding one obtained by Black and Bodenheimer at $0.9 t_{ff}$. The specific angular momentum decreases monotonically inwards from the outermost portions of the cloud. At $r \sim 1.05 \times 10^{15} \text{ cm}$ (the zone of most rapid equatorial infall), the specific angular momentum shows a weak tendency to increase in the region of minimum mass [See Figure 8.6(b)] and then decreases drastically in the presence of the ring and towards the innermost zone. This behaviour is characteristic in situations where an accreting ring is developing. The mass involved in the inner regions is only a small fraction (~ 0.03) of the total cloud mass.

We now compare the structure of the numerically calculated ring with the equilibrium structure analytically predicted by Ostriker [91], for isothermal, uniformly rotating, self-gravitating rings whose thickness $a_{1/2}$ is small compared with the distance R_r of the ring from the rotational axis. As pointed out by Black and Bodenheimer [4], in

the numerical case the ring is not isolated as in the analytical description, but rather it is embedded in a roughly disk-like mass configuration, which gravitationally influences the ring itself. Also, the numerical rings are not necessarily thin ($a_{1/2} \ll R_r$) or in uniform rotation. It is observed from Figure 8.4, that the numerically obtained ring is highly flattened with an equatorial diameter significantly larger than the diameter perpendicular to the rotational axis. In the following, we shall consider three parameters: (a) the characteristic minor radius of the ring $a_{1/2}$, within which one-half of the ring mass is contained; (b) the mass per unit length of the ring $M_r/L_r = M_r/(2\pi R_r)$, where R_r is the distance of ρ_{max} from the rotation axis; and (c) the specific angular momentum of the ring J_r/M_r . Following Ostriker [91], if the ring is in static equilibrium, we have

$$\frac{M_r}{L_r} = \frac{2kT}{\mu m_p G}, \quad (8.4)$$

$$\frac{J_r}{M_r} = R_r \left(G \frac{M_r}{L_r} \left[\ln \left(\frac{8R_r}{a_{1/2}} \right) - 2 \right] \right)^{1/2}, \quad (8.5)$$

$$a_{1/2} = \left(\frac{M_r}{L_r} \frac{1}{\pi \rho_{max}} \right)^{1/2}. \quad (8.6)$$

A further uncertainty in the comparison of the integral properties, is introduced by the fact that the numerical ring is resolved in only a few grid cells and we are compelled to assign the numerical minor radius $a_{1/2}$ as an average of the values in the directions perpendicular and parallel to the axis [See Boss [12]], with the value of $a_{1/2}$ in each direction being computed as the distance from the point of maximum density to the point where the density has decreased by roughly a factor of 3. The specific angular momentum follows directly from the calculation and is determined by the value at the cell containing the maximum density (of the ring), while the mass per unit length may

be readily obtained from the analytical relation (8.6) by setting

$$\left(\frac{M_r}{L_r}\right)_{num} = \pi \rho_{max} a_{1/2}^2. \quad (8.7)$$

The estimated value of $a_{1/2}$ for the present ring is $4.063 \times 10^{13} cm$ compared with Ostriker's equilibrium value of $a_{1/2} = 3.8 \times 10^{13} cm$. For the mass per unit length and specific angular momentum, we obtain $M_r/L_r = 1.42 \times 10^{16} g cm^{-1}$ and $J_r/M_r = 11.32 \times 10^{18} cm^2 s^{-1}$, respectively, as compared with the Ostriker's values of $M_r/L_r = 1.24 \times 10^{16} g cm^{-1}$ and $J_r/M_r = 7.45 \times 10^{18} cm^2 s^{-1}$. The angular momentum of the ring is within $\sim 34\%$ of the analytical value, while the mass per unit length and the minor radius are only slightly larger than the analytical equilibrium values. We may conclude that the integral properties and structure of the numerically obtained ring roughly agree with those expected for an equilibrium ring as predicted by Ostriker [91]. The discrepancies appear to indicate that the numerical ring is leaving the equilibrium state and entering a phase of self collapse (Phase IV of Black and Bodenheimer [4]). Unfortunately, at this time the calculation is stopped because the ring mass has concentrated into three equatorial cells in radius. This evident lack of resolution would then introduce strong inaccuracies destroying confidence in the physical reality of events in any further evolution. The calculation was completed at $1.094 t_{ff}$ after 993 computational cycles, with the total cloud mass being conserved exactly and the total angular momentum being conserved to $\sim 3 \times 10^{-4}\%$. With the choice of $\Delta t = 0.4 \Delta t_{CFL}$, about one hour of Gould computer time was necessary to carry out the run in double precision accuracy.

The 2-dimensional code was tested further to check the consistency of ring formation with the present scheme. Convergence of the hydrodynamical approximation was tested by varying the number of radial grid-points. For this test, we chose model 2D2, which is

clearly a very fast rotator ($\beta = 0.226$) and hence, we expect ring formation to occur at lower densities than for model 2D1. A first run was carried out with $N_r = 20$ points and a second with $N_r = 30$ points, with $\Delta t = 0.3\Delta t_{CFL}$ in each case. In Figures 8.7 and 8.8, we show the resulting equatorial density profiles. The location of the maximum ring density coincides quite well for the two runs, with the 20 point calculation producing a ring of maximum density $\rho_{max} = 7.6 \times 10^{-15} gcm^{-3}$ and radius $r = 2.27 \times 10^{15} cm$ at $2.034t_{ff}$, and the 30 point run giving a ring with $\rho_{max} = 9.46 \times 10^{-15} gcm^{-3}$ and $r = 2.35 \times 10^{15} cm$ at $1.925t_{ff}$. The 20 point profile has a slightly smaller radius r_1 than the more accurate 30 point case, with the densities there being comparable for the two plots. A similar situation was also found by Boss [12] for similar runs with 20 and 40 radial mesh-points. By way of comparison, the 20 point calculation of Boss [12] produced a ring of radius $r = 2.7 \times 10^{15} cm$ with a maximum density of $7.7 \times 10^{-15} gcm^{-3}$ at $1.968t_{ff}$, while his 40 point run formed a ring at $1.871t_{ff}$ with a maximum density quite comparable to that shown in Figure 8.9 for the present 30 point profile. However, in the Boss case, the rings occurred at the third radial grid point rather than at the second, with the inner points r_1 being at considerable smaller densities. Since the central densities in the present calculations are nearly comparable with those obtained by Boss, this technical discrepancy is not worrying because it is essentially due to the fact that the Boss grid was able to contract slightly more than ours.

The calculations for the plots in Figures 8.7 and 8.8 were stopped at slightly different times corresponding to when a rather strong shock forms on the rotational axis near to the centre of the cloud, which then reduced the time step to a point at which calculation of further evolution would have been prohibitive. Ring formation for this model was

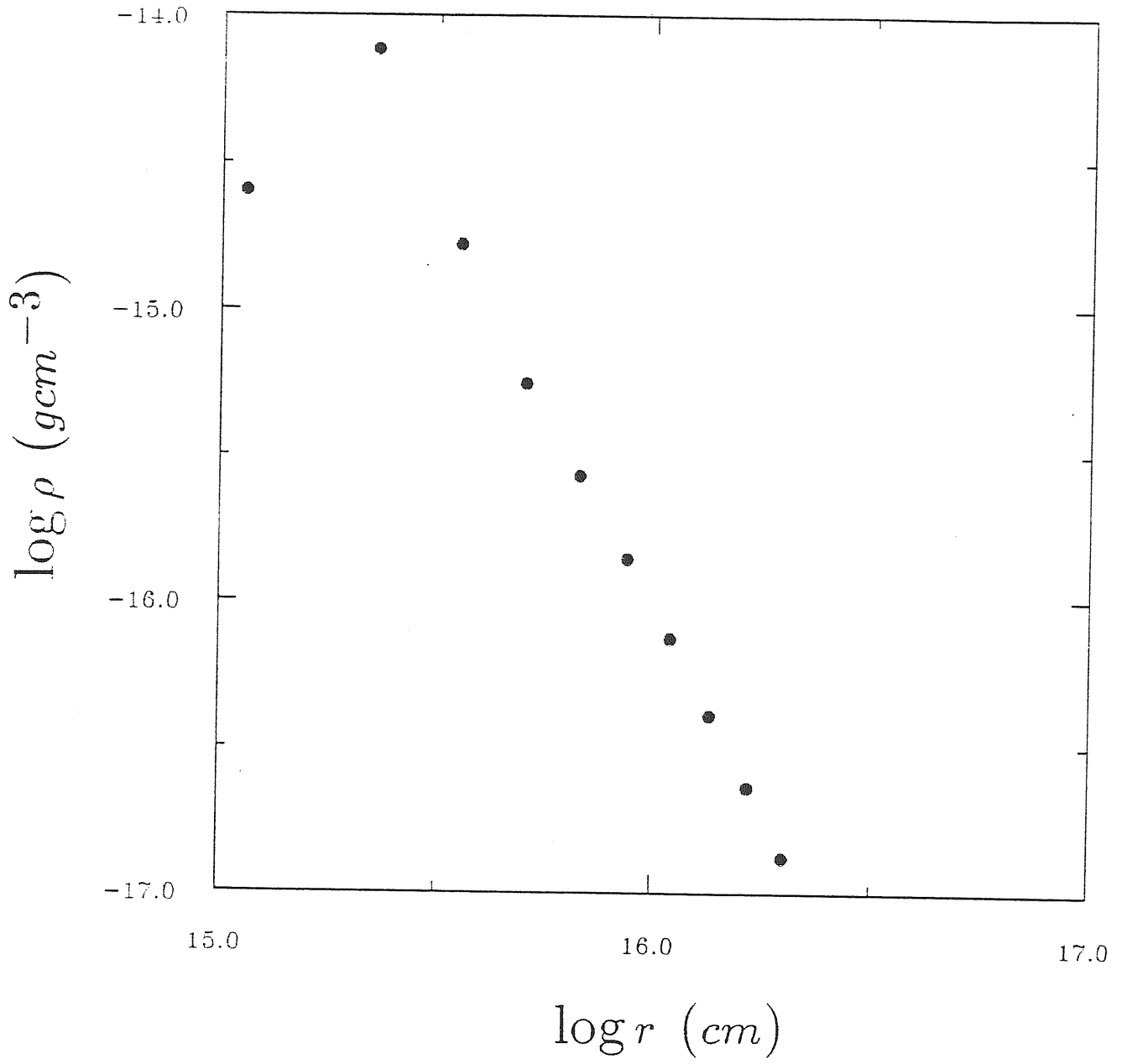


Figure 8.7: Equatorial density profile at $2.034t_{ff}$ showing ring formation for model 2D2. The calculation was carried out with 20 moving radial grid points.

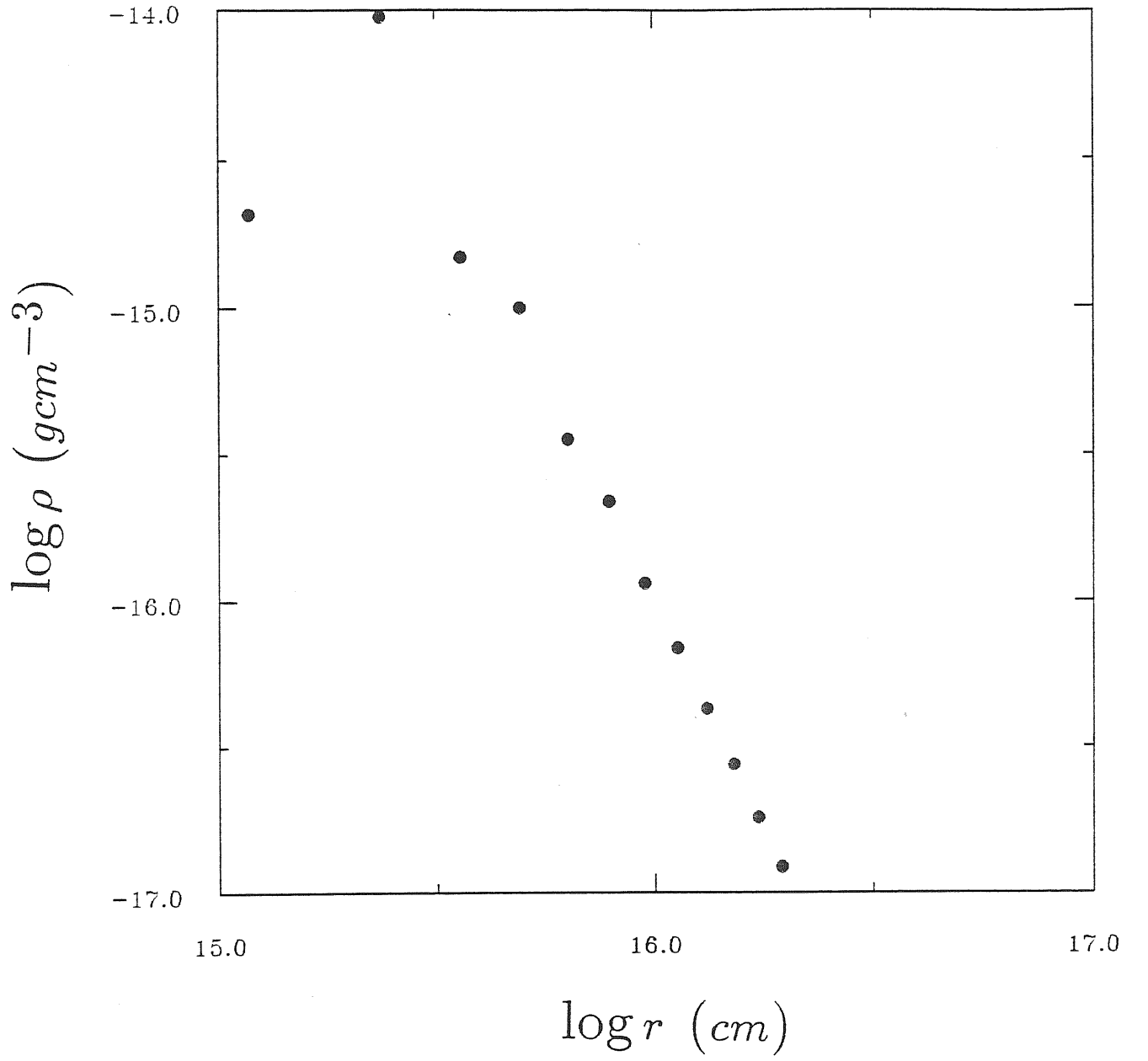


Figure 8.8: Equatorial density profile at $1.925t_{ff}$ for model 2D2 with 30 radial grid points.

observed to occur in a similar manner as described above for model 2D1. For both runs the global mass was again exactly conserved, while the total angular momentum was globally conserved to $6 \times 10^{-6}\%$ for the 20 point case and to $3.3 \times 10^{-5}\%$ for the 30 point run. The density profiles in Figures 8.8 and 8.9 were obtained after 1760 and 1801 steps, respectively, corresponding to nearly 2 hours of computational time on the Gould machine.

We now consider the axisymmetric collapse for model 2D3. This model represents a rapidly rotating protostellar cloud of low thermal energy ($\alpha = 0.251$) compared with the other two models. The collapse of such configurations is physically interesting because clouds with relatively low thermal energy have low thermal pressure and hence, the evolution should be rich in dynamical behaviour. The initial conditions for this model were chosen to allow comparisons with the Boss [12] case 2D-IV.

At the beginning, the collapse is dominated by a flattening phase similar to that experienced by models 2D1 and 2D2. After approximately $1.1t_{ff}$, the central regions bounce and an off-axis density maximum appears, as shown in Figure 8.9. The radial infall velocities in the inner regions near to the equator are so small ($\sim 0.03 \text{ km s}^{-1}$), that they can be easily reversed and a slight outflow is set up in the innermost equatorial cells. Meanwhile, the flow down the rotational axis is proceeding without experiencing any bounce and velocities in this direction are significantly higher than those for the equatorial flow. In contrast with the situation encountered for model 2D1, here the increasing centrifugal forces are sufficient to reverse the direction of the flow in the region of the equatorial plane before the formation of any clear shock perpendicular to the rotational axis. However, this is a merely transient feature. The immediately subsequent evolution is characterized by an oscillation of the central density about a

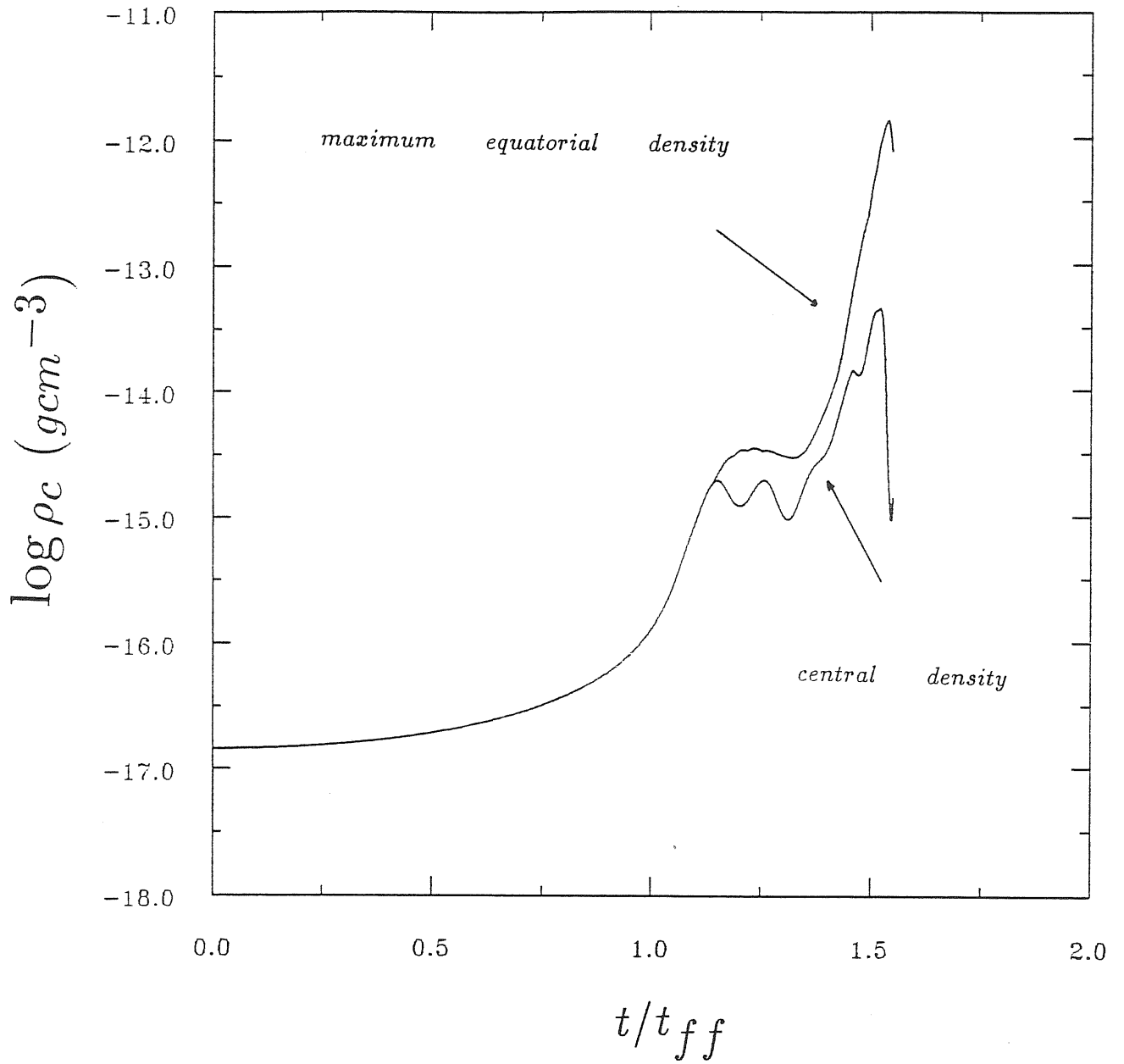


Figure 8.9: Evolution of the central density and maximum equatorial density for model 2D3.

preferred value of $\sim 1.6 \times 10^{-15} \text{ g cm}^{-3}$, with the maximum density of the weak ring remaining nearly constant until about $1.35t_{ff}$. In the meantime, by $\sim 1.25t_{ff}$, the rapid infall down the rotational axis has formed a shock front, which extends up to $\theta \sim 56^\circ$. The shock gives rise to an outwardly directed flow in the innermost five axial and main grid ($j \leq 7$) cells. At this time the maximum infall velocities ($\sim 1.04 \text{ km s}^{-1}$) are along the axis, while the equatorial matter is moving inwards with a maximum velocity of only 0.3 km s^{-1} . The flow in the innermost equatorial zone is no longer outwards although it is still proceeding at a reduced rate. At $\sim 1.35t_{ff}$, the flow pattern is such that the material in the innermost axial and main grid ($j \leq 8$) cells behind the shock reverses direction and starts collapsing towards the centre, while the that ahead the shock is being deflected towards the gravitational potential minimum (at the ring). Meanwhile, the flow in the innermost four equatorial cells has again reversed. This rather complicated flow pattern explains the increase of both the central density and the maximum ring density after $\sim 1.3t_{ff}$ as observed in Figure 8.9. At this time, the maximum ring density is located at the fifth inner radial grid point. The evolution will essentially proceed in this manner until $\sim 1.51t_{ff}$. After this time, the continued infall of material towards the centre (behind the first shock) gives rise to a steep pressure gradient which then reverses the flow. A second shock forms and the material bounces in almost all of the innermost cells. By $\sim 1.55t_{ff}$, the first shock front has essentially disappeared and a well defined flow pattern is established, with the matter in the innermost two shells flowing outwards roughly isotropically. This leads to a drastic reduction of the central density and the formation of a dominating ring structure.

In Figures 8.10, 8.11, and 8.12, we show equatorial density profiles at slightly different times illustrating the development of the ring. Finally, in Figure 8.13, we show

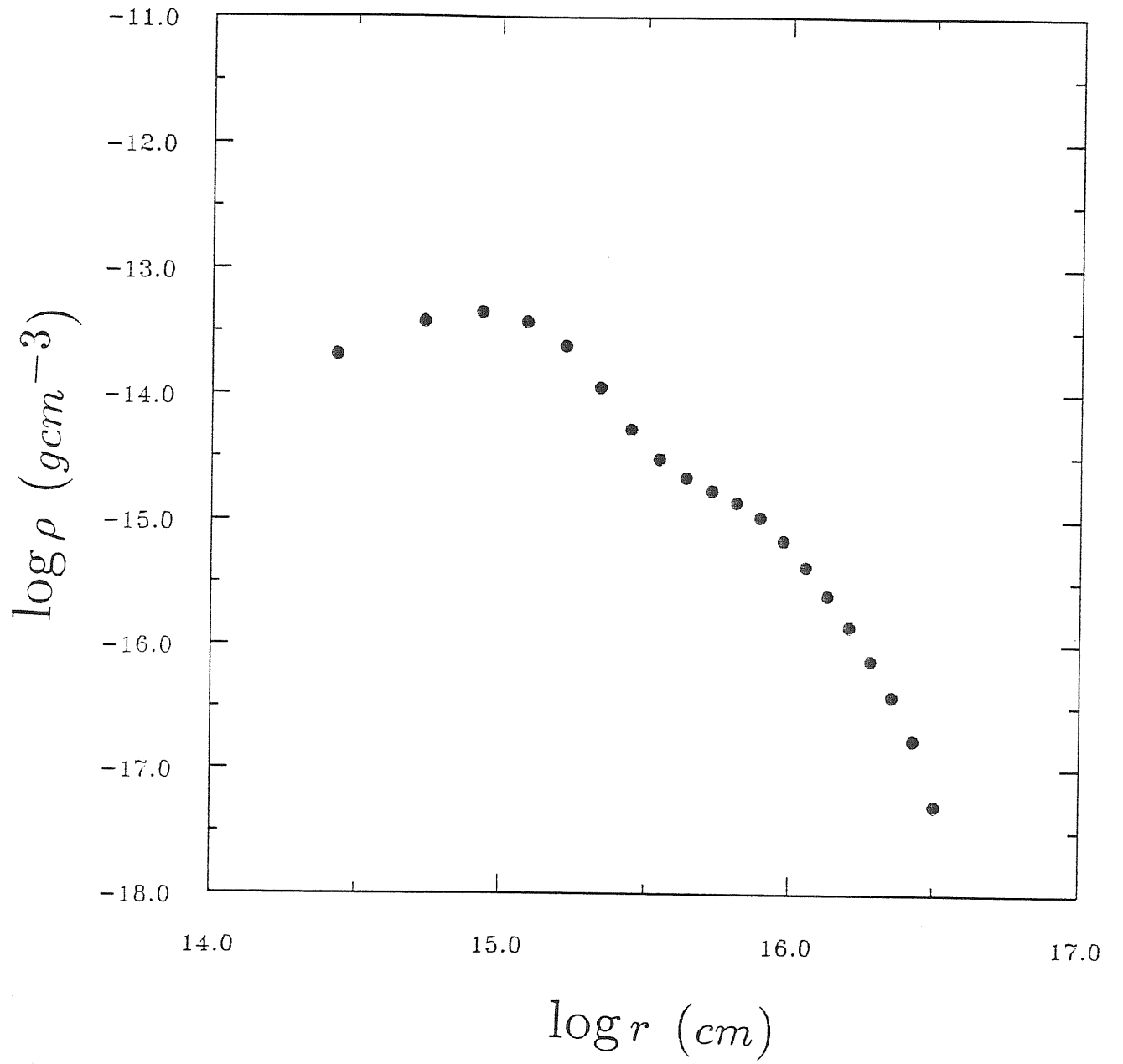


Figure 8.10: Equatorial density profile at $1.45t_{ff}$ for model 2D3.

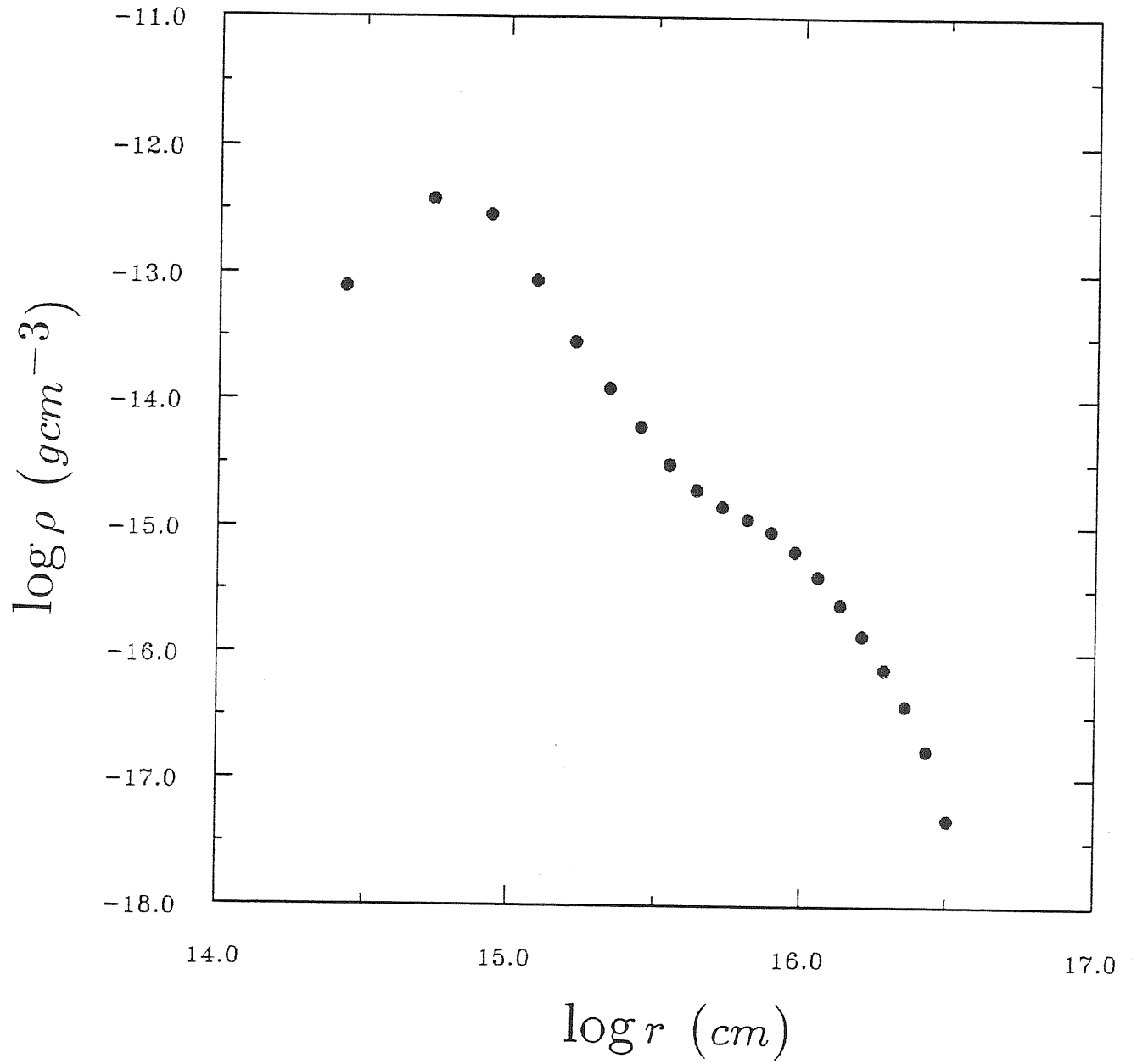


Figure 8.11: Equatorial density profile at $1.50t_{ff}$ for model 2D3.

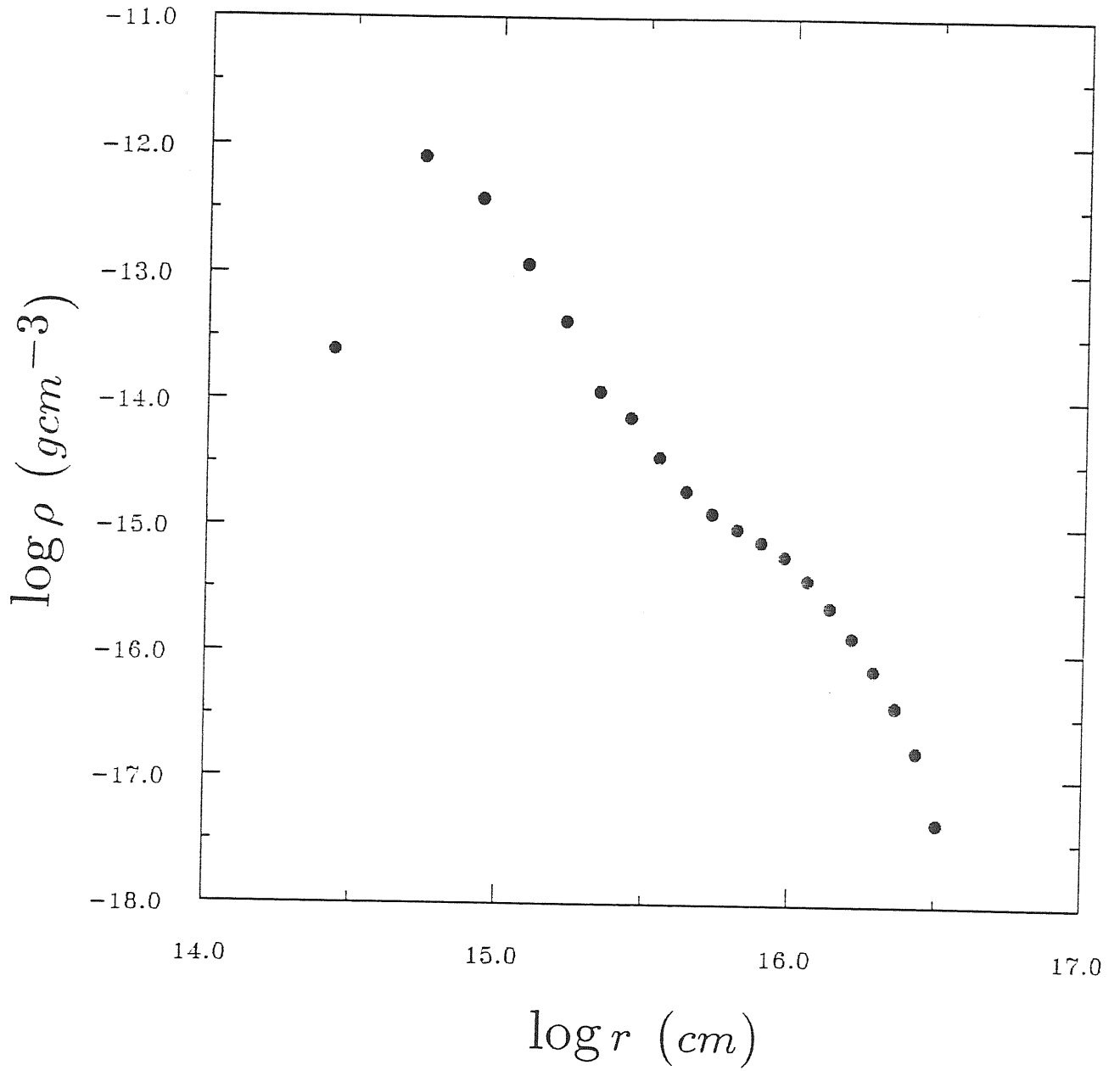


Figure 8.12: Equatorial density profile at $1.55t_{ff}$ for model 2D3.

a contour density plot (including the inner 7 shells) detailing the inner structure of the collapsing cloud at $1.55t_{ff}$. The final configuration is strongly flattened and the marked bunching of contour lines near the axis at $r \sim 5.4 \times 10^{14} cm$ indicates the presence of the shock front. At this time, also the outermost regions (near the boundary of the cloud) have also experienced a slight flattening. The calculation took 874 cycles to reach $1.55t_{ff}$ following which further evolution was inhibited because the ring mass became concentrated in only a few cells and the time step became extremely small. However, for this model we left the code running for about one day (7435 cycles) in order to observe the evolution of the maximum ring density. It was found that ring continued to evolve with the maximum density oscillating about a nearly constant value at constant radius. This is in agreement with the results obtained by Boss [12].

8.3 Conclusions

In this chapter, we have studied the response of the 2-dimensional version of the code to the question of ring formation. The sets of initial conditions were chosen to allow comparison with the results previously obtained by Black and Bodenheimer [4] and Boss [12,14]. We have observed the formation of ring structures similar to the ones that reported by these authors. In the numerical picture, ring formation occurs as a natural consequence of the interplay between the gravitational forces and the combined effects of pressure and centrifugal forces. The collapse is observed to be characterized by an overall flattening of the cloud during the first free-fall time, followed by a central bounce of the collapsing material and subsequent shock formation. An off-axis density maximum then appears as a consequence of the flow reversal in the innermost regions around the equatorial plane. The ring forms and develops by accreting mass from

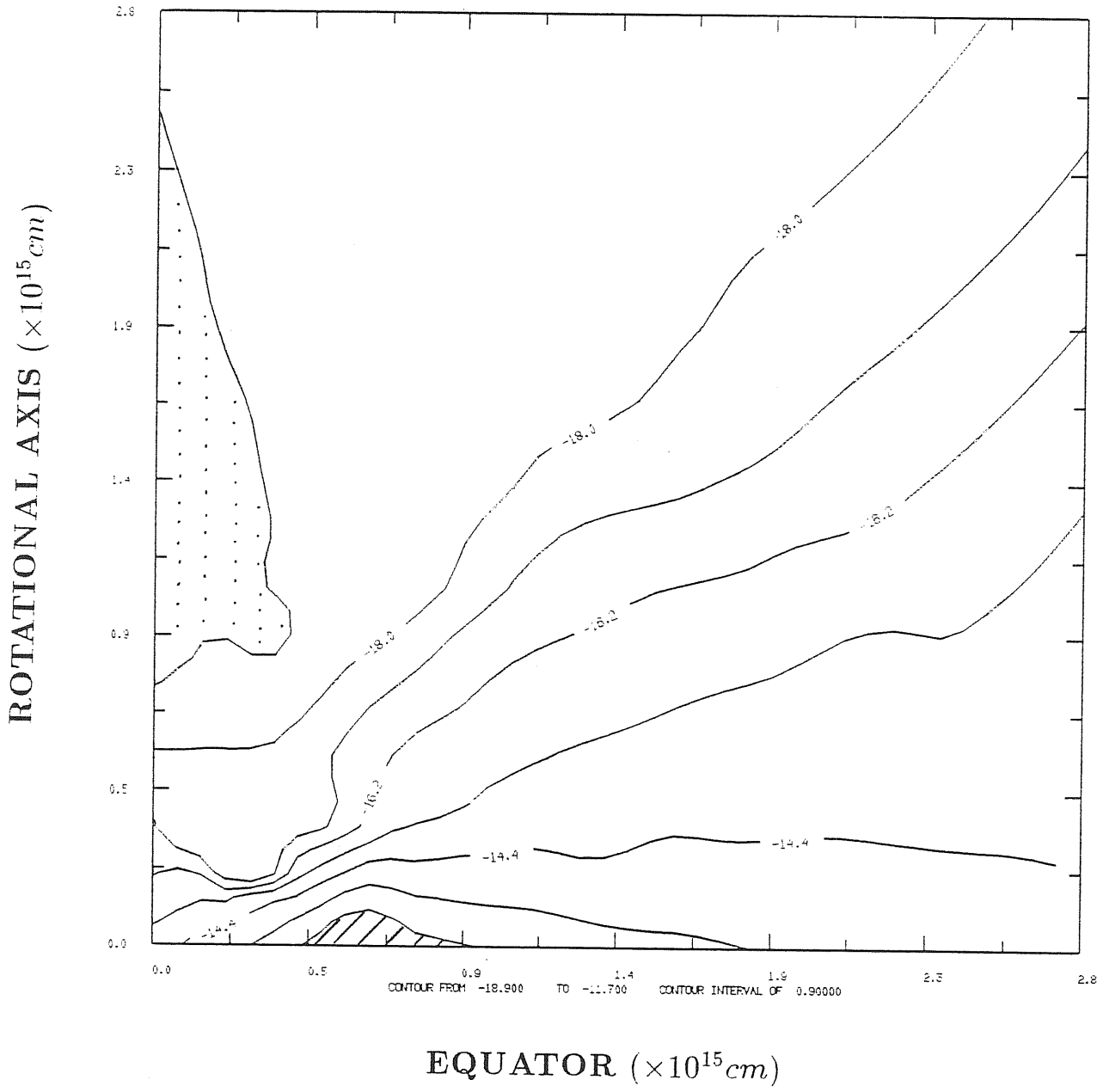


Figure 8.13: Contour density plot at $1.55t_{ff}$ for model 2D3. The contour factor of 0.9 corresponds to a real interval of 7.94. The cross-hatched region is a density maximum and the dotted region is a density minimum. The maximum density is $7.98 \times 10^{-13} gcm^{-3}$ and the central density is $1.42 \times 10^{-15} gcm^{-3}$.

the surrounding regions on a very short time-scale ($\sim 0.01 - 0.02t_{ff}$). At the end of each continued calculation, the outermost regions of the cloud were still infalling with roughly spherical symmetry but at a reduced rate. Only for initially rapidly rotating clouds with low thermal energy, was a substantial amount of flattening observed in the outermost layers.

The sensitivity of the numerical scheme to local conservation of angular momentum is improved when the specific angular momentum is properly centred at the computational cell borders. For initially slow rotators, the analytical law $\omega \propto \rho^{2/3}$ is reproduced numerically with an error of 0.001% showing that only a very small amount of inward transfer of angular momentum remains. Thus, the code is seen to have quite good local conservation of angular momentum. Global conservation of all advected quantities is ensured by the donor cell method. Furthermore, the axisymmetric code is also able to recognize (with a high accuracy) a spherically symmetric collapse when the rotational effects are removed.

Finally, when the number of grid points is varied only small differences are observed between the numerically calculated rings. Hence, the hydrodynamical approximation seems to converge satisfactorily to a unique solution. These results are important because they indicate that acceptable accuracy is maintained even with a relatively small number of mesh-points.

Chapter 9

Further Research

The Gould computer has been quite suitable for development work in 1- and 2-space dimensions, even though it has been necessary to carry out the runs with double precision accuracy in order to get results of comparable accuracy to those obtained by other workers on a CDC 7600 machine in single precision. However, under these circumstances runs of the 3-dimensional code become extremely expensive. A typical 3-dimensional test run needed about 12 hours of CPU time on the Gould machine to complete $\sim 1t_{ff}$ in double precision. After this time, the stretched computational grid required such small time steps that following the solution further became impossible. In practice, the smallest time step will generally occur in the innermost portions of the grid where

$$\Delta t_{CFL} = \Delta t_{\phi} \approx \frac{\Delta r \Delta \theta \Delta \phi}{(C_{ss} + |v_{\phi}|)}.$$

The product $\Delta \theta \Delta \phi$ is $1/20$ or smaller so that the Courant time for explicit 3-dimensional calculations is about $1/20$ of that allowed for the spherically symmetric case. In view of this, the 3-dimensional code was initially run with a large fraction ($f = 0.9$) of the Δt_{CFL} , and when a negative density occurred due to this rather large fraction, the calculation was stopped and then re-started with progressively smaller fractions of the

Δt_{CFL} . This strategy, however, has not significantly eased the computational time demand. For this reason, the 3-dimensional scheme has been only tested superficially. A run was carried out for an initial $1M_{\odot}$ molecular cloud ($\mu = 2$) at $T = 10K$ with uniform density $\rho_0 = 1.44 \times 10^{-17} gcm^{-3}$ and uniform angular velocity $\omega_0 = 1.56 \times 10^{-12} s^{-1}$. This set of initial conditions is the same as that of the Boss [15] case 3D-II. The calculation was carried out in single precision in order to reduce the computational time required to observe fragmentation into a binary system (as expected after $\sim 1.4t_{ff}$). Qualitatively, the results obtained were found to compare well with those of Boss [15] for the same test. However, this run cannot be considered as a definitive production run and, hence, it has not been described in the present thesis. With the single precision of the Gould machine, the Poisson solver is capable of recognizing a spherically symmetric distribution only up to the fifth significant figure instead of the fourteenth as previously. This obviously introduces errors in calculating the potential, of a level at which the hydrodynamical calculation could be prejudiced.

In the near future the 3-dimensional code will be tested on a faster machine having single precision accuracy at least comparable with the double precision accuracy of the Gould computer.

A further planned development is the inclusion of radiation transfer in each of the versions of the present code. This will then allow the calculations to follow the non-isothermal evolution of protostellar clouds. In this case, the calculations become more complicated because we must include radiative transfer in the energy equation and solve a coupled radiative equation. Furthermore, we need relations for the gas pressure, internal energy, and opacity as functions of the density, temperature, and chemical composition. The solution of the energy equation needs to be obtained implicitly in

contrast to what is done for the continuity and momentum equations, which are solved explicitly. The reason for this is that otherwise we shall run into a severe time-step restriction due to the presence of the radiative transfer term in the energy equation. The transport of internal energy through the computational grid will again be performed using the donor cell method.

Finally, the profiles shown in Chapters 7 and 8 could be substantially improved by calculating the hydrodynamics with a more sophisticated method. One way to do this is by correcting the donor-cell flow accros the cell borders [Boris and Book (1980)] by a technique generally referred to as the Flux Corrected Donor Cell Method. This could be tried first in 1- and 2-space dimensions with relatively small computational cost.

Appendix A

Solution of the Poisson Equation in Two Space Dimensions

In this appendix, we give details of the Poisson solver implemented in the 2-dimensional collapse calculations. The general solution method is seen as a restricted case of that described in Chapter 5 for the 3-dimensional problem.

For axisymmetric flows, the gravitational potential at each point of the spherical cloud is determined by equation (3.19). This equation can be solved by separation of variables, if we define the gravitational potential and the density as Legendre polynomial expansions of the form

$$\begin{aligned}\Phi(r, \theta) &= \sum_{l=0}^{\infty} \Phi_l(r) P_l(\cos \theta), \\ \rho(r, \theta) &= \sum_{l=0}^{\infty} \rho_l(r) P_l(\cos \theta),\end{aligned}\tag{A.1}$$

where $\Phi_l(r)$ and $\rho_l(r)$ are the Legendre coefficients of $\Phi(r, \theta)$ and $\rho(r, \theta)$, respectively.

If we substitute the expansions (A.1) into equation (3.19), perform the change of variable $x = \cos \theta$, and then use the identity

$$\frac{d}{dx} \left\{ (1 - x^2) \frac{d}{dx} P_l(x) \right\} = -l(l+1) P_l(x),\tag{A.2}$$

we obtain the following simplified differential equation for the potential coefficients

$$\frac{d^2\Phi_l(r)}{dr^2} + \frac{2}{r} \frac{d\Phi_l(r)}{dr} - \frac{l(l+1)}{r^2} \Phi_l(r) = 4\pi G \rho_l(r), \quad (\text{A.3})$$

which exhibits exactly the same mathematical form of equation (5.4).

The density coefficients $\rho_l(r)$ needed for the solution of equation (A.3) are determined by using the orthogonality condition for the Legendre polynomials. After a straightforward operation, we find that

$$\rho_l(r) = \frac{2l+1}{2} \int_{-1}^{+1} \rho(r, x) P_l(x) dx. \quad (\text{A.4})$$

The external boundary condition on the gravitational potential is then specified in terms of its Legendre coefficients $\Phi_l(r)$ by assuming that there are no masses outside the computational grid which alter the gravitational field inside the collapsing cloud. Then, setting $\rho_l(r) = 0$ in equation (A.3) and solving for $\Phi_l(r)$, we obtain only one solution which remains finite as $r \rightarrow \infty$. This solution is

$$\Phi_l(r) \propto r^{-(l+1)}, \quad (\text{A.5})$$

and it applies for any $r \geq R_0$. Differentiating expression (A.5) once, we get, at the spherical boundary

$$\left[\frac{d\Phi_l(r)}{dr} \right]_{r=R_0} + \left[\frac{(l+1)}{r} \Phi_l(r) \right]_{r=R_0} = 0. \quad (\text{A.6})$$

This boundary condition is basically the same as that used to solve equation (5.4) in the 3-dimensional case, and it is mathematically sufficient for a consistent solution of equation (A.3). The inner boundary condition is specified by demanding that $\Phi(r, \theta)$ and its first derivatives be continuous functions at the cloud centre ($r = 0$). Furthermore, the assumption of reflection symmetry about the equatorial plane ($\theta = \pi/2$) simplifies

the calculations because only the l -even terms are actually needed in the expansions (A.1). Therefore, the number of differential equations (A.3) that must be solved to determine the potential coefficients is reduced by half.

A.1 Determination of the Density and Potential Coefficients

In order to solve the differential equation (A.3), we must evaluate the integral in equation (A.4) for the density coefficients. This integral is similar to that given in (5.12) and hence, it may be conveniently evaluated by means of a Gauss-Legendre quadrature formula [42]. In analogy with equation (5.16), we may then write

$$\rho_l(r) = \frac{2l+1}{2} \int_{-1}^{+1} \rho(r, x) P_l(x) dx \approx \frac{2l+1}{2} \sum_{j=1}^N H_j \rho(r, a_j) P_l(a_j), \quad (\text{A.7})$$

where the discrete abscissae a_j are chosen as the roots of the Legendre polynomial $P_N(x)$, and their corresponding weights H_j as explicit functions of the roots [See equation (5.16)]. A more detailed discussion of this type of quadrature is given in Chapter 5, Section 5.2, for the case in which the integrand is formed by the product $\rho(r, x, \phi) P_l^m(x)$, with $P_l^m(x)$ being the associated Legendre functions. Exactly the same basic considerations and definitions also apply to the determination of the quadrature (A.7).

The non-zero roots of the Legendre polynomial $P_N(x)$ (which are symmetric with respect to the origin $x = 0$) determine the location of the θ -points on the top and bottom hemispheres of the spherical grid. Therefore, if reflection symmetry about the equatorial plane is applied so that, for any integer j , we have $\rho(r, a_j) = \rho(r, -a_j)$ and $P_l(a_j) = P_l(-a_j)$ (for l even), it follows from the symmetry relation for the weights, $H_j = H_{N-j+1}$ [42], that

$$\rho_l(r) \approx \frac{2l+1}{2} \sum_{j=1}^{(N+1)/2} H_j' \rho(r, a_j) P_l(a_j) \quad l = 0, 2, 4, \dots, \quad (\text{A.8})$$

for $a_j \geq 0$. The new weights H'_j are related to the old weights H_j via equations (5.19). The upper limit in the summation (A.8) gives the number of θ -cells filling the top hemisphere of the computational volume. In Appendix B, we give the computed abscissae and corresponding weights determining the quadrature (A.8), when a resolution of $N_\theta = 11$ is chosen to represent the calculations.

The next step in our numerical approach consists in replacing the exact differential equation (A.3) by a set of linear algebraic finite-difference equations, which are simultaneously solved by applying the tridiagonal matrix algorithm. The discretization technique and the solution method are fully described in Chapter 5, Section 5.3. In practice, we retain in the summations (A.1) terms up to and including $l = 6$. This limited number of terms provides sufficient accuracy in evaluating the gravitational potential.

The gravitational potential for the axial cells is readily obtained by setting $\theta = 0$ in the Legendre summation (A.1).

A.2 Gravitational Potential at the Cloud Centre

In the 3-dimensional case, the gravitational potential at the centre ($r = 0$) has been approximately computed from the Φ of the neighbouring main grid-cells by using a limiting form of equation (3.25) at $r = 0$. The same procedure is also adopted for the axisymmetric case.

If we evaluate equation (3.19) at $r = 0$, and then integrate each term over θ , we obtain the limiting form

$$\int_{-1}^{+1} \left. \frac{\partial^2 \Phi(r, x)}{\partial r^2} \right|_{r=0} dx = \frac{4\pi G}{3} \int_{-1}^{+1} \rho(0, x) dx, \quad (\text{A.9})$$

where for convenience we have made the change of variable $x = \cos \theta$. The second

spatial derivative of the potential in the integrand is evaluated by expanding in a Taylor series the potential of the first shell of cells about the centre [See Chapter 5, Section 5.6]. Neglecting derivatives higher than the second and using the condition $(\partial\Phi/\partial r)_{r=0} = 0$, we obtain a first-order accurate, forward finite-difference approximation for the second derivative at $r = 0$

$$\left. \frac{\partial^2 \Phi(r, x)}{\partial r^2} \right|_{r=0} \approx \frac{2[\Phi(r_1, x) - \Phi(0, x)]}{r_1^2}, \quad (\text{A.10})$$

where r_1 denotes the radius of the first shell of main grid-points. Inserting the difference replacement (A.10) into equation (A.9) and re-arranging terms, we get the approximate equation

$$\int_{-1}^{+1} \Phi(0, x) dx \simeq \int_{-1}^{+1} \Phi(r_1, x) dx - \frac{2}{3} \pi G r_1^2 \int_{-1}^{+1} \rho(0, x) dx. \quad (\text{A.11})$$

From the same considerations made in Chapter 5, Section 5.6, the integrals in equation (A.11) are evaluated by means of a Gauss-Legendre quadrature formula:

$$\begin{aligned} \int_{-1}^{+1} \Phi(0, x) &\approx \sum_{j=1}^{N_\theta} H'_j \Phi(0, a_j) = 2\Phi_c, \\ \int_{-1}^{+1} \Phi(r_1, x) &\approx \sum_{j=1}^{N_\theta} H'_j \Phi(r_1, a_j), \\ \int_{-1}^{+1} \rho(0, x) &\approx \sum_{j=1}^{N_\theta} H'_j \rho(0, a_j) = 2\rho_c, \end{aligned} \quad (\text{A.12})$$

where Φ_c and ρ_c denote the gravitational potential and the density, respectively, at the central cell ($r = 0$).

Substitution of the quadratures (A.12) into equation (A.11) yields

$$\Phi_c \approx \frac{1}{2} \sum_{j=1}^{N_\theta} H'_j \Phi(r_1, a_j) - \frac{2}{3} \pi G r_1^2 \rho_c, \quad (\text{A.13})$$

which is only an approximate relation for the central potential. Note that relation (A.13) follows from its 3-dimensional counterpart (5.64) if we take the potentials Φ_{1jk} in the first shell of cells to be uniform in ϕ .

Appendix B

Abscissae and Weight Coefficients of the 21-Point Gauss-Legendre Quadrature Formula

As previously noted in Chapter 5, Section 5.2, due to the almost complete lack of available information about the zeros of the Legendre polynomial $P_{21}(x)$, a root-finding routine - originally implemented by Davis and Rabinowitz [30] - has been slightly modified and then incorporated into the 2- and 3-dimensional versions of the code in order to determine the Gauss-Legendre quadratures (5.18) and (A.8), for a θ -grid resolution of $N_\theta = 11$. The routine can be also used for any other value of $N_\theta = (N + 1)/2$, with N odd.

The algorithm computes the zeros of $P_N(x)$ by means of a Newton-Raphson iteration scheme. Following Davis and Rabinowitz [30], we calculate starting values for the zeros $x_{jN}^{(0)}$ by using the formula

$$x_{jN}^{(0)} \approx \left(1 - \frac{1}{8}N^{-2} + \frac{1}{8}N^{-3}\right) \cos \left[\frac{4j-1}{4N+2} \pi \right] + O\left\{(N)^{-4}\right\}, \quad (\text{B.1})$$

where the integer j takes values in the range $(1, 2, \dots, (N + 1)/2)$. If we set $N = 21$, the

error in this approximation is $\sim 5 \times 10^{-6}$, which provides a good initial accuracy for our purposes.

A sequence of two approximations to each zero $x_{jN}^{(i)}$ (with $i = 1, 2$) is defined by first using a rapidly convergent, fifth-order Newton iteration scheme

$$x_{jN}^{(1)} = x_{jN}^{(0)} - \frac{P_N(x_{jN}^{(0)})}{P'_N(x_{jN}^{(0)})} \left\{ 1 + \frac{1}{2} \frac{P_N(x_{jN}^{(0)})}{P'_N(x_{jN}^{(0)})} \left[\frac{P''_N(x_{jN}^{(0)})}{P'_N(x_{jN}^{(0)})} + \frac{P_N(x_{jN}^{(0)})}{P'_N(x_{jN}^{(0)})} \left(\frac{P''_N(x_{jN}^{(0)})}{P'_N(x_{jN}^{(0)})} \frac{P''_N(x_{jN}^{(0)})}{P'_N(x_{jN}^{(0)})} - \frac{1}{3} \frac{P'''_N(x_{jN}^{(0)})}{P'_N(x_{jN}^{(0)})} \right) \right] \right\}. \quad (\text{B.2})$$

The terms $P_N(x_{jN}^{(0)})$, on the right-hand side of equation (B.2), are evaluated by using the well-known recurrence formula for the Legendre polynomials

$$\begin{aligned} P_0(x) &= 1, \\ P_1(x) &= x, \\ P_n(x) &= \frac{1}{n} [(2n-1)xP_{n-1}(x) - (n-1)P_{n-2}(x)] \quad \text{for } n \geq 2, \end{aligned} \quad (\text{B.3})$$

while the first derivatives $P'_N(x_{jN}^{(0)})$ can be obtained from the relation

$$(1-x^2)P'_n(x) = n[P_{n-1}(x) - xP_n(x)], \quad (\text{B.4})$$

in terms of the $P_N(x_{jN}^{(0)})$. Finally, to evaluate the higher-order derivatives, we use the second-order differential equation for the Legendre polynomials, which gives them as linear combinations of lower-order derivatives.

Owing to the high accuracy of the starting values $x_{jN}^{(0)}$ and to the very fast convergence of the iteration scheme (B.2), it is sufficient to use only a first-order iteration scheme

$$x_{jN}^{(2)} = x_{jN}^{(1)} - \frac{P_N(x_{jN}^{(1)})}{P'_N(x_{jN}^{(1)})}, \quad (\text{B.5})$$

to compute the zeros with double precision accuracy, in the next approximation. Defining $\hat{H}_j = x_{jN}^{(1)} - x_{jN}^{(0)}$ [from equation (B.2)], $P_N(x_{jN}^{(1)})$ and $P'_N(x_{jN}^{(1)})$ may be conveniently approximated by the Taylor series

$$\begin{aligned} P_N(x_{jN}^{(1)}) &\approx P_N(x_{jN}^{(0)}) + \hat{H}_j P'_N(x_{jN}^{(0)}) + \frac{1}{2} \hat{H}_j^2 P''_N(x_{jN}^{(0)}) + \\ &\quad + \frac{1}{6} \hat{H}_j^3 P'''_N(x_{jN}^{(0)}) + \frac{1}{24} \hat{H}_j^4 P^{(4)}_N(x_{jN}^{(0)}) + O\left\{(\hat{H}_j)^5\right\}, \\ P'_N(x_{jN}^{(1)}) &\approx P'_N(x_{jN}^{(0)}) + \hat{H}_j P''_N(x_{jN}^{(0)}) + \frac{1}{2} \hat{H}_j^2 P'''_N(x_{jN}^{(0)}) + \\ &\quad + \frac{1}{6} \hat{H}_j^3 P^{(4)}_N(x_{jN}^{(0)}) + O\left\{(\hat{H}_j)^4\right\}, \end{aligned} \quad (\text{B.6})$$

respectively. The use of these expansions in the iteration scheme (B.5) is then sufficient to give exactly $x_{jN}^{(2)} = a_j$, when fourteen digits are carried.

The weight coefficients H_j are then computed from an alternative relation to (5.16). That is, if the a_j are roots of $P_N(x) = 0$, from equation (B.4) we have that

$$P'_N(a_j) = \frac{N P_{N-1}(a_j)}{(1 - a_j^2)}. \quad (\text{B.7})$$

Substitution of relation (B.7) into equation (5.26) yields

$$H_j = \frac{2(1 - a_j^2)}{[N P_{N-1}(a_j)]^2}. \quad (\text{B.8})$$

To evaluate the terms $N P_{N-1}(a_j)$, we use relation (B.4) and expand each term independently in a Taylor series about $x_{jN}^{(1)}$, consistently with scheme (B.5). After some cumbersome algebra, we obtain

$$\begin{aligned} N P_{N-1}(a_j) &\approx N P_{N-1}(x_{jN}^{(1)}) - N x_{jN}^{(1)} P_N(x_{jN}^{(1)}) - N(N+1) \left\{ \tilde{H}_j P_N(x_{jN}^{(1)}) + \right. \\ &\quad + \frac{1}{2} \tilde{H}_j^2 P'_N(x_{jN}^{(1)}) + \frac{1}{6} \tilde{H}_j^3 P''_N(x_{jN}^{(1)}) + \frac{1}{24} \tilde{H}_j^4 P'''_N(x_{jN}^{(1)}) + \frac{1}{120} \tilde{H}_j^5 P^{(4)}_N(x_{jN}^{(1)}) \left. \right\} + \\ &\quad + O\left\{(\tilde{H}_j)^6\right\}, \end{aligned} \quad (\text{B.9})$$

where $\tilde{H}_j = a_j - x_{jN}^{(1)}$.

TABLE B1

Abscissae and Weight Coefficients of the 21 - Point

Gauss - Legendre Quadrature Formula

j	a_j	H_j	H'_j
1	0.95375217062039D+00	0.16317288257774D-01	0.32034456515549D-01
2	0.96722683856631D+00	0.36953789770853D-01	0.73907579541705D-01
3	0.92009933415040D+00	0.37136425426857D-01	0.11426885085371D+00
4	0.85336336458332D+00	0.76100113628379D-01	0.15220022725676D+00
5	0.76843496347568D+00	0.93444423456034D-01	0.18688884691207D+00
6	0.66713880419741D+00	0.10879729916715D+00	0.21759459833430D+00
7	0.55161883588722D+00	0.12183141605373D+00	0.24366283210746D+00
8	0.42434212020744D+00	0.13226893863334D+00	0.26453787726667D+00
9	0.28802131680240D+00	0.13988739479107D+00	0.27977478958215D+00
10	0.14556185416090D+00	0.14452440398997D+00	0.28904880797994D+00
11	0.00000000000000D+00	0.14608113364969D+00	0.14608113364969D+00

TABLE B2

Latitudes and θ - Grid Spacings Used in the

Difference Representations

j	$\theta_j = \cos^{-1} a_j$ (°)	$\Delta\theta_{j+1}$ (rad)	$\Delta\theta_{j+1/2}$ (rad)
1	0.64080397638705D+01	0.11184226514289D+00	0.12836229187244D+00
2	0.14709235145835D+02	0.14486231860200D+00	0.14531002237946D+00
3	0.23059391770460D+02	0.14573772615693D+00	0.14583422221807D+00
4	0.31420606029172D+02	0.14593071827922D+00	0.14596715055463D+00
5	0.39785795119122D+02	0.14600358283003D+00	0.14602101191623D+00
6	0.48153381435232D+02	0.14603844100244D+00	0.14604794728865D+00
7	0.56521857091500D+02	0.14605745357487D+00	0.14606302449952D+00
8	0.64890971128702D+02	0.14606859542416D+00	0.14607193482726D+00
9	0.73260467833224D+02	0.14607527423006D+00	0.14607718708210D+00
10	0.81630183734603D+02	0.14607909993384D+00	0.14607997577600D+00
11	0.90000000000000D+02	0.14608085161815D+00	0.14608085161815D+00

In Table B1, we list the positive abscissae and corresponding weights of the 21-point Gauss-Legendre quadrature formula, as calculated from (B.5) and (B.8). The accuracy of the root-finding routine has been tested against the tabulated data given by Kopal [57], for odd values of N . Identical results were obtained, even carrying fifteen decimal places. In Table B2, we give the polar location of the grid-points and the θ -spacings used in the difference representations, when $N_\theta = 11$ cells are included along the θ -direction.

Appendix C

Finite-Difference Approximations

In this appendix, we deal with the basic finite-difference formulae used in the discretization of the relevant differential equations.

In Section C.1, we deduce appropriate replacements for the first and second radial derivatives involved in the simplified Poisson equations (5.4) and (A.3). The difference approximations for the acceleration gradients in the momentum transfer equations are given in Section C.2. In Section C.3, we derive the basic differences for the fluid advective terms, and finally in Section C.4, we treat the explicit time integration.

C.1 A Three-Point Finite-Difference Scheme

Even for a variable radial grid, we can construct a second-order accurate finite-difference scheme for the numerical solution of equations (5.4) and (A.3) by deriving suitable approximations for the exact derivatives $d^2\Phi/dr^2$ and $d\Phi/dr$. In order to do so, let us consider Figure C.1 and denote the potential coefficients in equations (5.4) and (A.3), in the domain $r_1 \leq r_i \leq r_{N_r}$, by $\Phi_{lm}(r_i) = \Phi_i$ and $\Phi_l(r_i) = \Phi_i$.

The grid-spacings Δr_i , Δr_{i+1} , and $\Delta r_{i+1/2}$ are as defined in Chapter 4, Section 4.2,

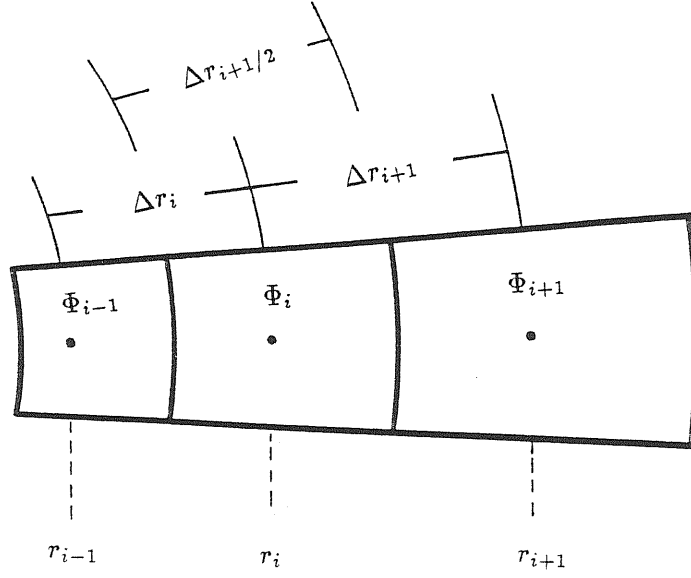


Figure C.1: Possible radial grid configuration at step n .

that is

$$\begin{aligned}
 \Delta r_i &= r_i - r_{i-1}, \\
 \Delta r_{i+1} &= r_{i+1} - r_i, \\
 \Delta r_{i+1/2} &= \frac{1}{2}(\Delta r_i + \Delta r_{i+1}).
 \end{aligned}
 \tag{C.1}$$

Expanding Φ_i in Taylor series forward and backward from the i th radial point at the time step n (the superscript for which is omitted for simplicity), we have that

$$\begin{aligned}
 \Phi_{i+1} &= \Phi_i + \left. \frac{d\Phi}{dr} \right|_i \Delta r_{i+1} + \frac{1}{2!} \left. \frac{d^2\Phi}{dr^2} \right|_i \Delta r_{i+1}^2 + \\
 &\quad + \frac{1}{3!} \left. \frac{d^3\Phi}{dr^3} \right|_i \Delta r_{i+1}^3 + \frac{1}{4!} \left. \frac{d^4\Phi}{dr^4} \right|_i \Delta r_{i+1}^4 + \dots, \\
 \Phi_{i-1} &= \Phi_i - \left. \frac{d\Phi}{dr} \right|_i \Delta r_i + \frac{1}{2!} \left. \frac{d^2\Phi}{dr^2} \right|_i \Delta r_i^2 -
 \end{aligned}
 \tag{C.2}$$

$$-\frac{1}{3!} \left. \frac{d^3 \Phi}{dr^3} \right|_i \Delta r_i^3 + \frac{1}{4!} \left. \frac{d^4 \Phi}{dr^4} \right|_i \Delta r_i^4 - \dots \quad (\text{C.3})$$

Multiplying the expansion (C.2) by Δr_i^2 and (C.3) by Δr_{i+1}^2 , and then subtracting the second from the first, we eliminate those terms containing second space derivatives. Grouping similar terms and solving for the first derivative, we finally obtain the approximation

$$\left\{ \frac{d\Phi}{dr} \right\}_i \approx \frac{\Phi_{i+1} + (\lambda_{i+1}^2 - 1)\Phi_i - \lambda_{i+1}^2 \Phi_{i-1}}{\Delta r_{i+1}(\lambda_{i+1} + 1)} + E_i, \quad (\text{C.4})$$

where the parameter $\lambda_{i+1} = \Delta r_{i+1}/\Delta r_i$ is always of order unity for smooth variations of the radial spacings. The error implied by the replacement (C.4) is

$$E_i = -\frac{1}{6} \lambda_{i+1} (\Delta r_i)^2 \left. \frac{d^3 \Phi}{dr^3} \right|_i - O \left\{ (\Delta r_i)^3 \right\}. \quad (\text{C.5})$$

Similarly, multiplying expansion (C.2) by Δr_i and (C.3) by Δr_{i+1} and adding the resulting expansions, we now eliminate the terms containing first spatial derivatives. Grouping terms as before and solving for the second derivative, we get

$$\left\{ \frac{d^2 \Phi}{dr^2} \right\}_i \approx \frac{\Phi_{i+1} - (\lambda_{i+1} + 1)\Phi_i + \lambda_{i+1} \Phi_{i-1}}{\frac{1}{2} \Delta r_{i+1} \Delta r_i (\lambda_{i+1} + 1)} + E'_i, \quad (\text{C.6})$$

with an error of the form

$$E'_i = -\frac{1}{3} (\lambda_{i+1} - 1) \Delta r_i \left. \frac{d^3 \Phi}{dr^3} \right|_i - O \left\{ (\Delta r_i)^2 \right\}. \quad (\text{C.7})$$

The first terms on the right-hand side of (C.4) and (C.6) approximate the first and second derivatives on the left-hand sides to second and first order accuracy, respectively. They are generally referred to as partially centred difference replacements. If we set $\lambda_{i+1} = 1$, as it should be for a uniformly spaced grid, the approximations (C.4) and (C.6) automatically reduce to second-order accurate centred differences of the form

$$\left\{ \frac{d\Phi}{dr} \right\}_i \approx \frac{\Phi_{i+1} - \Phi_{i-1}}{2\Delta r_i} - \frac{1}{6} (\Delta r_i)^2 \left. \frac{d^3 \Phi}{dr^3} \right|_i, \quad (\text{C.8})$$

$$\left\{ \frac{d^2\Phi}{dr^2} \right\}_i \approx \frac{\Phi_{i+1} - 2\Phi_i + \Phi_{i-1}}{\Delta r_i^2} - \frac{1}{12}(\Delta r_i)^2 \frac{d^4\Phi}{dr^4} \Big|_i. \quad (\text{C.9})$$

It is interesting to note that the replacement (C.6) can be made nearly second-order accurate by matching the dominant truncation errors (C.5) and (C.7) by setting [90]

$$\frac{1}{3}(\lambda_{i+1} - 1)\Delta r_i \frac{d^3\Phi}{dr^3} \Big|_i = \frac{1}{6}\lambda_{i+1}(\Delta r_i)^2 \frac{d^3\Phi}{dr^3} \Big|_i. \quad (\text{C.10})$$

This relation then leads to the following prescription

$$\Delta r_{i+1} = \Delta r_i[1 + \kappa\Delta r_i] \quad \text{with } \kappa = \text{constant},$$

or more explicitly

$$\Delta r_{i+1} = \xi\Delta r_i, \quad (\text{C.11})$$

where ξ is the so-called stretch parameter which is constant in space but is allowed to vary in time. For smooth grid variations, it is of order unity and positive if the non-uniform grid starts with small spacings in the central regions and gradually changes to larger and larger spacings towards the external boundary.

In the calculations, we use the finite-difference approximations (C.4) and (C.6) written in the alternative forms

$$\left\{ \frac{d\Phi}{dr} \right\}_i \approx \frac{1}{2\Delta r_{i+1/2}} \left[\frac{\Delta r_i}{\Delta r_{i+1}}(\Phi_{i+1} - \Phi_i) + \frac{\Delta r_{i+1}}{\Delta r_i}(\Phi_i - \Phi_{i-1}) \right], \quad (\text{C.12})$$

and

$$\left\{ \frac{d^2\Phi}{dr^2} \right\}_i \approx \frac{1}{\Delta r_{i+1/2}} \left[\frac{(\Phi_{i+1} - \Phi_i)}{\Delta r_{i+1}} - \frac{(\Phi_i - \Phi_{i-1})}{\Delta r_i} \right], \quad (\text{C.13})$$

respectively.

C.2 Acceleration Gradients

In this section, we show the finite-difference formulae used to approximate the r -, θ -, and ϕ -gradients in the momentum transfer equations (3.11), (3.16)-(3.17), and (3.22)-

(3.24).

For a variable non-uniform radial grid, the r -gradients are evaluated by using a second-order accurate replacement identical to that shown in expression (C.12). Then, defining for a typical main grid-cell $Y(r_i, \theta_j, \phi_k) = Y_{ijk}$, where Y may be the pressure p or the gravitational potential Φ , we may write

$$\left\{ \frac{\partial Y}{\partial r} \right\}_{ijk} \approx \frac{1}{2\Delta r_{i+1/2}} \left[\frac{\Delta r_i}{\Delta r_{i+1}} (Y_{i+1,jk} - Y_{ijk}) + \frac{\Delta r_{i+1}}{\Delta r_i} (Y_{ijk} - Y_{i-1,jk}) \right]. \quad (\text{C.14})$$

For evaluating the θ -gradients some comments are necessary. We may note from Table B2 in Appendix B, that the θ -grid is fairly uniform except for cells with $j = 1$ (near the rotational axis), where a sudden change in the grid spacing is evident. In this situation, a logical way of computing the θ -gradients could be to use a second-order central formula for points with $j \geq 3$ and a partially centred formula for points with $j = 1, 2$. However, a few simple tests made to investigate this, revealed that a little accuracy could be gained by applying a partially centred approximation everywhere. This is due to the fact that, even if the θ -spacings appear to be nearly uniform towards the equatorial plane, the θ -points are not exactly centred and a pure central approximation does not account for these small variations in the mesh size.

A partially centred finite-difference for the θ -gradients can be obtained by following the same procedure made to derive the radial three-point approximation (C.12). Defining

$$\begin{aligned} \Delta\theta_j &= \theta_j - \theta_{j-1}, \\ \Delta\theta_{j+1} &= \theta_{j+1} - \theta_j, \\ \Delta\theta_{j+1/2} &= \frac{1}{2}(\Delta\theta_{j+1} + \Delta\theta_j), \end{aligned} \quad (\text{C.15})$$

we may write for a typical main grid-cell

$$\left\{ \frac{1}{r} \frac{\partial Y}{\partial \theta} \right\}_{ijk} \approx \frac{1}{2r_i \Delta \theta_{j+1/2}} \left[\frac{\Delta \theta_j}{\Delta \theta_{j+1}} (Y_{i,j+1,k} - Y_{ijk}) + \frac{\Delta \theta_{j+1}}{\Delta \theta_j} (Y_{ijk} - Y_{i,j-1,k}) \right], \quad (\text{C.16})$$

which then introduces the dominant error

$$E_j = -\frac{1}{6} \frac{1}{r_i} \nu_{j+1} (\Delta \theta_j)^2 \left. \frac{\partial^3 Y}{\partial \theta^3} \right|_{ijk},$$

with $\nu_{j+1} = \Delta \theta_{j+1} / \Delta \theta_j$.

Since the ϕ -grid is exactly uniform, the ϕ -gradients are very conveniently evaluated by a second-order accurate central formula. Thus, in analogy with the radial replacement (C.8), we write

$$\left\{ \frac{\partial Y}{\partial \phi} \right\}_{ijk} \approx \frac{Y_{ij,k+1} - Y_{ij,k-1}}{2\Delta \phi_k} - \frac{1}{6} (\Delta \phi_k)^2 \left. \frac{\partial^3 Y}{\partial \phi^3} \right|_{ijk}. \quad (\text{C.17})$$

The finite-difference formulae (C.14), (C.16), and (C.17) have been written in the form used for the 3-dimensional calculations. Similar forms hold for the r - and θ -gradients in the 2-dimensional case and for the r -gradients in the 1-dimensional calculations.

C.3 Finite-Difference Representations for the Advective Terms

In any of the structural hydrodynamic equations, the fluid advection is represented by the following terms

$$\left\{ 3 \frac{\partial(r^2 X U)}{\partial(r^3)} \right\}; \quad \left\{ \frac{1}{r \sin \theta} \frac{\partial(\sin \theta X v_\theta)}{\partial \theta} \right\};$$

$$\left\{ \frac{1}{r \sin \theta} \frac{\partial(X v_\phi)}{\partial \phi} \right\}, \quad (\text{C.18})$$

for the r -, θ -, and ϕ -directions, respectively.

Following Tscharnuter and Winkler [115], the radial term has been written in compact form because when expressed in finite-differences, it provides a better approximation than the equivalent form

$$\left\{ \frac{1}{r^2} \frac{\partial(r^2 X U)}{\partial r} \right\}. \quad (\text{C.19})$$

Suitable finite-difference replacements for the quotients above are readily obtained with the help of control volumes, here defined by the intersection of the two mutually perpendicular planes (r, θ) and (r, ϕ) [See Figure 4.1].

Let us denote the generalized function $X(r, \theta, \phi)$ at a particular grid point (ijk) by X_{ijk} , and consider the quantities $(r^2 X U)$, $(\sin \theta X v_\theta)$, and $(X v_\phi)$ which are the fluxes accross the cell interfaces $(i \pm 1/2, jk)$, $(i, j \pm 1/2, k)$, and $(ij, k \pm 1/2)$, respectively. Expanding $(r^2 X U)_{i+1/2, jk}$ and $(r^2 X U)_{i-1/2, jk}$ in Taylor series about the common point (ijk) at the time step n , the superscript for which is again omitted for simplicity, and subtracting the second expansion from the first to eliminate $(r^2 X U)_{ijk}$, we obtain the finite-difference approximation for the radial advective term

$$\left\{ 3 \frac{\partial(r^2 X U)}{\partial(r^3)} \right\}_{ijk} \approx \frac{[(r^2 X U)_{i+1/2, jk} - (r^2 X U)_{i-1/2, jk}]}{\frac{1}{3}(r_{i+1/2}^3 - r_{i-1/2}^3)}, \quad (\text{C.20})$$

which introduces the dominant truncation error

$$E_r = -\frac{3}{2}(r_{i+1/2}^3 - 2r_i^3 + r_{i-1/2}^3) \left\{ \frac{\partial^2(r^2 X U)}{\partial(r^3)^2} \right\}_{ijk}.$$

The radial stretching of the computational grid destroys the second-order accuracy of the approximation. This fact is better observed from the truncation errors which arise in approximating the counterpart term (C.19). When this term is differenced on a non-uniform radial grid, the following dominant errors are introduced

$$E_r = -\frac{1}{4}(\lambda_{i+1} - 1)\Delta r_i \frac{1}{r_i^2} \left\{ \frac{\partial^2(r^2 X U)}{\partial r^2} \right\}_{ijk} -$$

$$-\frac{1}{24}(\lambda_{i+1}^2 - \lambda_{i+1} + 1)(\Delta r_i)^2 \frac{1}{r_i^2} \left\{ \frac{\partial^3(r^2 X U)}{\partial r^3} \right\}_{ijk},$$

where $\lambda_{i+1} = \Delta r_{i+1}/\Delta r_i$. The first term on the right-hand side is non-zero when $\lambda_{i+1} \neq 1$, as occurs for a non-uniform grid, and vanishes making the approximation second-order accurate when the grid is exactly uniform ($\lambda_{i+1} = 1$).

The finite-difference replacement for the θ -advective term is obtained in a similar way by expanding the fluxes $(\sin \theta X v_\theta)_{i,j\pm 1/2,k}$ about the grid-point (ijk) . Then, subtracting the resulting expansions to eliminate the quantity $(\sin \theta X v_\theta)_{ijk}$, we finally obtain

$$\left\{ \frac{1}{r \sin \theta} \frac{\partial(\sin \theta X v_\theta)}{\partial \theta} \right\}_{ijk} \approx \frac{[(\sin \theta X v_\theta)_{i,j+1/2,k} - (\sin \theta X v_\theta)_{i,j-1/2,k}]}{r_i \sin \theta_j \Delta \theta_{j+1/2}}, \quad (\text{C.21})$$

with the dominant errors

$$E_\theta = -\frac{1}{4} \frac{(\eta_{j+1} - 1) \Delta \theta_j}{r_i \sin \theta_j} \left\{ \frac{\partial^2(\sin \theta X v_\theta)}{\partial \theta^2} \right\}_{ijk} - \frac{1}{24} \frac{(\eta_{j+1}^2 - \eta_{j+1} + 1)}{r_i \sin \theta_j} (\Delta \theta_j)^2 \left\{ \frac{\partial^3(\sin \theta X v_\theta)}{\partial \theta^3} \right\}_{ijk},$$

where $\eta_{j+1} = \Delta \theta_{j+1}/\Delta \theta_j$. Although, the finite-difference (C.21) is formally first-order accurate, it becomes nearly second-order accurate for those main grid-cells with $j \geq 2$ [See Table B2]. The factor $(\eta_{j+1} - 1)$ (in the first error term) ranges from $\sim 6 \times 10^{-3}$ to $\sim 1.2 \times 10^{-5}$ for $j \geq 2$ and worsens (to ~ 0.3) for the first θ -cell $j = 1$.

Finally, expanding the ϕ -fluxes $(X v_\phi)_{ij,k\pm 1/2}$ in Taylor series about the point (ijk) and combining the resulting expansions, we find

$$\left\{ \frac{1}{r \sin \theta} \frac{\partial(X v_\phi)}{\partial \phi} \right\}_{ijk} \approx \frac{[(X v_\phi)_{ij,k+1/2} - (X v_\phi)_{ij,k-1/2}]}{r_i \sin \theta_j \Delta \phi_k} \quad (\text{C.22})$$

which approximates the partial derivative term on the left-hand side to second-order

accuracy due to the ϕ -grid being exactly uniform

$$E_\phi = -\frac{1}{24} \frac{1}{r_i \sin \theta_j} (\Delta \phi_k)^2 \left\{ \frac{\partial^3 (X v_\phi)}{\partial \phi^3} \right\}_{ijk}.$$

The finite-difference approximations (C.20), (C.21), and (C.22) have been derived for the general 3-dimensional case. For axisymmetric and spherically symmetric calculations, forms similar to (C.20) and (C.21) hold for the r - and θ -advective terms,

C.4 Time Differencing

The time derivative terms $\partial X / \partial t$ are evaluated by using a forward difference approximation. The use of this standard formula leads to a straightforward explicit time integration for the equations of motion.

If $(n + 1)$ is the new time level to which all of the hydrodynamical variables are advanced and we denote by X_{ijk}^{n+1} , the value of X for a typical main grid-cell at this time level, and by X_{ijk}^n , the value of X at the old time level, the new variables can be expressed in terms of the old ones by a Taylor expansion of the form

$$X_{ijk}^{n+1} = X_{ijk}^n + \left\{ \frac{\partial X}{\partial t} \right\}_{ijk}^n \Delta t + \frac{1}{2} \left\{ \frac{\partial^2 X}{\partial t^2} \right\}_{ijk}^n \Delta t^2 + \dots, \quad (\text{C.23})$$

where $\Delta t = t^{n+1} - t^n$ is the time step used for advancing the system. Solving for the first derivative, we then obtain

$$\left\{ \frac{\partial X}{\partial t} \right\}_{ijk}^n \approx \frac{X_{ijk}^{n+1} - X_{ijk}^n}{\Delta t} - \frac{1}{2} \Delta t \left\{ \frac{\partial^2 X}{\partial t^2} \right\}_{ijk}^n, \quad (\text{C.24})$$

which approximates the time derivative to first-order accuracy.

Bibliography

- [1] Abramowitz M. and Stegun I. A., *Handbook of Mathematical Functions*, (Dover Publications, Inc., New York), 1970, pp.916.
- [2] Aveni A. F. and Hunter J. H., *Astron. J.* **78** (1967), 1019.
- [3] Black D. C. and Bodenheimer P., *Ap. J.* **199** (1975), 619.
- [4] Black D. C. and Bodenheimer P., *Ap. J.* **206** (1976), 138.
- [5] Bodenheimer P. and Sweigart A., *Ap. J.* **152** (1968), 515.
- [6] Bodenheimer P. and Black D. C., in *Protostars and Planets*, ed. T. Gehrels (University of Arizona Press, Tucson, Arizona) (1978).
- [7] Bodenheimer P., *Ap. J.* **224** (1978), 488.
- [8] Bodenheimer P. and Tscharnuter W. M., *Astron. Astrophys.* **74** (1979), 288.
- [9] Bodenheimer P., Tohline J. E., and Black D. C. *Ap. J.* **242** (1980), 209.
- [10] Bodenheimer P., *Lectures in Applied Mathematics*, Vol. 20 (1983), 141.

- [11] Bonnor W. B., *Mon. Not. R. astr. Soc.* **116** (1956), 351.
- [12] Boss A. P., *Theoretical Models of Stellar Formation*, Ph. D. Dissertation, University of California, Santa Barbara (1979).
- [13] Boss A. P., *Ap. J.* **236** (1980), 619.
- [14] Boss A. P., *Ap. J.* **237** (1980), 563.
- [15] Boss A. P., *Ap. J.* **242** (1980), 699.
- [16] Boss A. P., *Ap. J.* **250** (1981), 636.
- [17] Boss A. P. and Haber G. J., *Ap. J.* **255** (1982), 240.
- [18] Boss A. P., *Ap. J.* **277** (1984), 768.
- [19] Boss A. P., *Mon. Not. R. astr. Soc.* **209** (1984), 543.
- [20] Brandshaft D., McLaren R. A., and Werner M. W., *Ap. J. (Letters)*, **199** (1975), L115.
- [21] Carvalho J. C. and Ter Haar D., *Astrophys. Space Sci.* **51** (1977), 385.
- [22] Cassinelli J. P. and Castor J. I., *Ap. J.* **179** (1973), 189.
- [23] Chu C. K. and Sereny A., *J. Comp. Phys.* **15** (1974), 476.
- [24] Chu C. K., in *Numerical Methods for Partial Differential Equations*, ed. S. V. Parter (Academic Press, New York), 1979, pp. 193-211.

- [25] Chuen-Yen C., *An Introduction to Computational Fluid Mechanics*
(Wiley, New York), 1979, pp. 74.
- [26] Clark F. O., Giguere P. T., and Crutcher R. M., *Ap. J.* **215** (1977),
511.
- [27] Cook T. L. and Harlow F. H., *Ap. J.* **225** (1978), 1005.
- [28] Craxton R. S. and McCrory R. L., *J. Comp. Phys.* **33** (1979), 432.
- [29] Crutcher R. M., Evans II N. J., Troland T., and Heiles C., *Ap. J.*
198 (1975), 91.
- [30] Davis P. J. and Rabinowitz P., *Methods of Numerical Integration*
(Academic Press, Inc.), 1984, chap. 2.
- [31] Deissler R. G., *Ap. J.* **209** (1976), 190.
- [32] Disney M. J., McNally D., and Wright A. E., *Mon. Not. R. astr.*
Soc. **146** (1969), 123.
- [33] Durisen R. H., Gingold R. A., Tohline J. E., and Boss A. P., *Ap.*
J. **305** (1986), 281.
- [34] Emery A. F., *J. Comp. Phys.* **2** (1968), 306.
- [35] Fallon F. W., Gerola H., and Sofia S., *Ap. J.* **217** (1977), 719.
- [36] de Felice F. and Yunqiang Yu, *J. Phys. A.: Math. Gen.* **15** (1982),
3341.
- [37] de Felice F., *Mem. S. A. It.*, Vol. 54, N°3, (1983), 725.

- [38] de Felice F., Miller J. C., and Yunqiang Yu, *Ap. J.* **298** (1985), 480.
- [39] de Felice F. and Yunqiang Yu, *Mon. Not. R. astr. Soc.* **220** (1986), 737.
- [40] de Felice F. and Sigalotti L., in *Gravitational Collapse and Relativity*, Proceedings of Yamada Conference XIV (World Scientific Publishing, Co. Pte. Ltd.), 1986, pp. 377.
- [41] Fleck R. C. and Hunter J. H., *Mon. Not. R. astr. Soc.* **175** (1976), 335.
- [42] Gentry R. A., Martin R. E., and Daly B. J., *J. Comp. Phys.* **1** (1966), 87.
- [43] Gerald C. F. and Wheatley P. O., *Applied Numerical Analysis* (Addison-Wesley Publishing Company), 1984, chap. 9.
- [44] Gerola H. and Sofia S., *Ap. J.* **196** (1975), 473.
- [45] Gillis J., Mestel L., and Paris R. B., *Astrophys. Space Sci.* **27** (1974), 167.
- [46] Gingold R. A. and Monaghan J. J., *Mon. Not. R. astr. Soc.* **184** (1978), 481.
- [47] Gordon C. P., *Astron. J.* **75** (1970), 914.
- [48] Hayashi C., *Ann. Rev. Astr. Astrophys.* **4** (1966), 171.

- [49] Hayashi C., Narita S., and Miyama S. M., *Prog. Theoret. Phys.* **68** (1982), 1949.
- [50] Heiles C., *Ap. J.* **160** (1970), 51.
- [51] Herbst W. and Assousa G. E., *Ap.J.* **217** (1977), 473.
- [52] Hirt C. W., *J. Comp. Phys.* **2** (1968), 339.
- [53] Hirt C. W., in *Numerical Methods for Partial Differential Equations*, ed. S. V. Parter (Academic Press, New York), 1979, pp. 149-175.
- [54] Hunter C., *Ap. J.* **136** (1962), 594.
- [55] Ibáñez M. H., *Mon. Not. R. astr. Soc.* **196** (1981), 13.
- [56] Kamiya Y., *Prog. Theoret. Phys.* **58** (1977), 802.
- [57] Kopal Z., *Numerical Analysis* (Chapman & Hall. Ltd.), 1961, chap. VII.
- [58] Kutner M. L. and Tucker K. D., *Ap. J.* **199** (1975), 79.
- [59] Landau L. D. and Lifshitz E. M., *Fluid Mechanics* (Pergamon Press), 1987, chap. I.
- [60] Lapidus L. and Pinder G. F., *Numerical Solution of Partial Differential Equations in Science and Engineering* (Wiley, New York), 1982, chap. 6.
- [61] Larson R. B., *Mon. Not. R. astr. Soc.* **145** (1969), 271.

- [62] Larson R. B. and Starrfield S., *Astron. Astrophys.* **13** (1971), 190.
- [63] Larson R. B., *Mon. Not. R. astr. Soc.* **156** (1972), 437.
- [64] Larson R. B., *Ann. Rev. Astron. Astrophys.* **11** (1973), 219.
- [65] Larson R. B., *Mon. Not. R. astr. Soc.* **184** (1978), 69.
- [66] Larson R. B., *Mon. Not. R. astr. Soc.* **206** (1984), 197.
- [67] Lin C. C. and Shu F. H., *Ap. J.* **140** (1964), 646.
- [68] Linke R. A. and Wannier P. G., *Ap. J. (Letters)*, **193** (1974), L41.
- [69] Loren R. B., *Ap. J.* **209** (1976), 466.
- [70] Loren R. B., *Ap. J.* **215** (1977), 129.
- [71] Loren R. B., *Ap. J.* **218** (1977), 716.
- [72] Loren R. B. and Wootten H. A., *Ap. J. (Letters)*, **225** (1978), L81.
- [73] Lucy L. B., *Astron. J.* **82** (1977), 1013.
- [74] McNally D., *Ap. J.* **140** (1964), 1088.
- [75] McNally D., *Mém. Soc. Roy. Sci., Liège.*, **9** (1976), 487.
- [76] Mestel L. and Spitzer L., *Mon. Not. R. astr. Soc.* **116** (1956), 503.
- [77] Miller G. E. and Scalo J. M., *Pub. Astr. Soc. Pac.* **90** (1978), 506.
- [78] Miller J. C. and de Felice F., *Ap. J.* **298** (1985), 474.
- [79] Milman A. S., *Ap. J.* **211** (1977), 128.

- [80] Mitchell A. R. and Griffiths D. F., *The Finite Difference Method in Partial Differential Equations* (Wiley, New York), 1985, chap. 4.
- [81] Miyama S. M., Hayashi C., and Narita S., *Ap. J.* **279** (1984), 621.
- [82] Mouschovias T. Ch., *Ap. J.* **211** (1977), 147.
- [83] Nakano T. and Tademaru E., *Ap. J.* **173** (1972), 87.
- [84] Nakazawa K., Hayashi C., and Takahara M., *Prog. Theoret. Phys.* **56** (1976), 515.
- [85] Narita S., Nakano T., and Hayashi C., *Prog. Theoret. Phys.* **43** (1970), 942.
- [86] Narita S., Hayashi C., and Miyama S. M., *Prog. Theoret. Phys.* **72** (1984), 1118.
- [87] Norman M. L. and Wilson J. R., *Ap. J.* **224** (1978), 497.
- [88] Norman M. L., Wilson J. R., and Barton R. T., *Ap. J.* **239** (1980), 968.
- [89] Norman M. L. and Winkler K.-H. A., in *Astrophysical Radiation Hydrodynamics* eds. K.-H. A. Winkler and M. L. Norman (D. Reidel Publishing Company), 1986, pp. 187-221.
- [90] Noye J., *Computational Techniques for Differential Equations* (North-Holland), 1984.
- [91] Ostriker J. P., *Ap. J.* **140** (1964), 1067.

- [92] Penston M. V., *R. Obs. Bull.* **117** (1966), 299.
- [93] Penston M. V., *Mon. Not. R. astr. Soc.* **144** (1969), 425.
- [94] Phillips T. G., Jefferts K. B., Huggings P. J., Ade P. A. R., and Clegg P. E., *Ap. J. (Letters)*, **201** (1975), L157.
- [95] Press W. H., Flannery B. P., Teukolsky S. A., and Vetterling W. T., *Numerical Recipes* (Cambridge University Press), 1986, pp. 180.
- [96] Reddish V. C., *Mon. Not. R. astr. Soc.* **135** (1967), 251.
- [97] Reddish V. C., *Stellar Formation* (Pergamon Press, New York), 1978.
- [98] Richtmyer R. D. and Morton K. W., *Difference Methods for Initial-Value Problems* (Interscience Publishers, Wiley), 1967, chap. 12 and 13.
- [99] Roberts W. W., *Ap. J.* **158** (1969), 123.
- [100] Scalo J. M., *Ap. J.* **213** (1977), 705.
- [101] Shu F. H., *Ap. J.* **214** (1977), 488.
- [102] Silk J., *Ap. J.* **214** (1977), 152.
- [103] Spitzer L. and Tomasko M. G., *Ap. J.* **152** (1968), 971.
- [104] Stoeckly R., *Ap. J.* **142** (1965), 208.
- [105] Strom K. M., Strom S. E., and Grasdalen G. L., *Ap. J. (Letters)*, **187** (1974), L83.

- [106] Strom K. M., Strom S. E., and Kinman T. D., *Ap. J. (Letters)*,
191 (1974), L93.
- [107] Strom S. E., Strom K. M., and Grasdalen G. L., *Ann. Rev. Astron. Astrophys.* **13** (1975), 187.
- [108] Takahara M., Nakazawa K., Narita S., and Hayashi C., *Prog. Theoret. Phys.* **58** (1977), 536.
- [109] Tassoul J.-L., *Theory of Rotating Stars* (Princeton University Press, Princeton, New Jersey), 1978, chap. 11.
- [110] Thompson R. I. and Tokunaga A. T., *Ap. J.* **229** (1979), 153.
- [111] Tohline J. E., *Ap. J.* **236** (1980), 160.
- [112] Tohline J. E., *Ap. J.* **248** (1981), 717.
- [113] Tscharnuter W. M., *Astron. Astrophys.* **39** (1975), 207.
- [114] Tscharnuter W. M., *The Moon and the Planets*, **19** (1978), 229.
- [115] Tscharnuter W. M. and Winkler K.-H., *Computer Phys. Commun.* **18** (1979), 171.
- [116] Tscharnuter W. M., in *Astrophysical Radiation Hydrodynamics* eds. K.-H. Winkler and M. L. Norman (D. Reidel Publishing Company), 1986, pp. 181-185.
- [117] Van den Bergh S., *Astron. J.* **71** (1966), 990.
- [118] Winkler K.-H. A. and Newman M. J., *Ap. J.* **236** (1980), 201.

[119] Winkler K.-H. A. and Newman M. J., *Ap. J.* **238** (1980), 311.

